LEABHARLANN CHOLÁISTE NA TRÍONÓIDE, BAILE ÁTHA CLIATH | TRINITY COLLEGE LIBRARY DUBLIN
Ollscoil Átha Cliath | The University of Dublin

Terms and Conditions of Use of Digitised Theses from Trinity College Library Dublin

Copyright statement

All material supplied by Trinity College Library is protected by copyright (under the Copyright and Related Rights Act, 2000 as amended) and other relevant Intellectual Property Rights. By accessing and using a Digitised Thesis from Trinity College Library you acknowledge that all Intellectual Property Rights in any Works supplied are the sole and exclusive property of the copyright and/or other IPR holder. Specific copyright holders may not be explicitly identified. Use of materials from other sources within a thesis should not be construed as a claim over them.

A non-exclusive, non-transferable licence is hereby granted to those using or reproducing, in whole or in part, the material for valid purposes, providing the copyright owners are acknowledged using the normal conventions. Where specific permission to use material is required, this is identified and such permission must be sought from the copyright holder or agency cited.

Liability statement

By using a Digitised Thesis, I accept that Trinity College Dublin bears no legal responsibility for the accuracy, legality or comprehensiveness of materials contained within the thesis, and that Trinity College Dublin accepts no liability for indirect, consequential, or incidental, damages or losses arising from use of the thesis for whatever reason. Information located in a thesis may be subject to specific use constraints, details of which may not be explicitly described. It is the responsibility of potential and actual users to be aware of such constraints and to abide by them. By making use of material from a digitised thesis, you accept these copyright and disclaimer provisions. Where it is brought to the attention of Trinity College Library that there may be a breach of copyright or other restraint, it is the policy to withdraw or take down access to a thesis while the issue is being resolved.

Access Agreement

By using a Digitised Thesis from Trinity College Library you are bound by the following Terms & Conditions. Please read them carefully.

I have read and I understand the following statement: All material supplied via a Digitised Thesis from Trinity College Library is protected by copyright and other intellectual property rights, and duplication or sale of all or part of any of a thesis is not permitted, except that material may be duplicated by you for your research use or for educational purposes in electronic or print form providing the copyright owners are acknowledged using the normal conventions. You must obtain permission for any other use. Electronic or print copies may not be offered, whether for sale or otherwise to anyone. This copy has been supplied on the understanding that it is copyright material and that no quotation from the thesis may be published without proper acknowledgement.

A THEORETICAL STUDY OF THE STRAIN-MODIFIED RKKY INTERACTION IN MAGNETICALLY DOPED CARBON MATERIALS



Paul D. Gorman

A THESIS SUBMITTED FOR THE DEGREE OF
DOCTOR OF PHILOSOPHY

SCHOOL OF PHYSICS
TRINITY COLLEGE DUBLIN

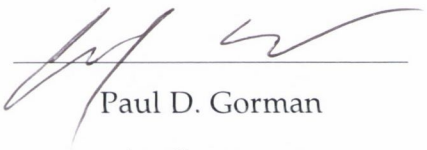
2015

TRINITY COLLEGE
2 9 JUL 2015
LIBRARY DUBLIN
Thesis 10636

DECLARATION

I, Paul Declan Gorman, hereby declare: This thesis has not been submitted as an exercise for a degree at this or any other university; That it comprises work performed entirely by myself during the course of my Ph.D. studies at Trinity College Dublin; That I was involved in a number of collaborations, and where it is appropriate my collaborators are acknowledged for their contributions.

A copy of this thesis may be lended or copied by the Trinity College Library upon request by a third party provided it spans single copies made for study purposes only, subject to normal conditions of acknowledgement.



Paul D. Gorman

April 23, 2015

I hate quotation. Tell me what you know.

— Ralph Waldo Emerson

SUMMARY

Graphene-related materials continue to be in the scientific limelight due to near-continuous discoveries regarding their properties and production. The applications envisaged for these super materials are numerous and varied across many disciplines. In addition to this, the simplicity with which the physical properties of these materials can be described makes them particularly popular in theoretical examinations, where the simple dispersion relation for their electrons is of key utility. In this thesis we will examine a number of topics relating to graphene systems, focusing on those doped with magnetic impurities. We will utilize a combination of analytical and numerical methods to explore these topics in graphene and carbon nanotubes.

There exists massive potential for magnetically-doped graphene systems in spintronic devices. Important to this endeavour is an understanding of the interactions between magnetic impurities embedded in graphene systems. Of particular interest is the Indirect Exchange Coupling which is mediated by the graphene conduction electrons. By further developing the analytic Green's functions for graphene and nanotubes we are able to explore the distance dependence of these interactions between a variety of impurities in a mathematically transparent fashion. We use our model to examine the method of mechanically induced strain to modify these interactions. We show that strain is capable of increasing the range of these interactions as well as modifying several properties of them in a controllable manner.

We then use the methods developed to examine two current questions. The first is the interaction between extended magnetic defects in graphene. Here we develop a method for examining the interactions between large linear magnetic objects. Our model provides a mathematically transparent description

of the magnitude and decay rate of this interaction. The second is the mechanism behind the sublattice-asymmetric nitrogen doping of graphene in chemical vapour deposition grown graphene. Here we use a simple model of the problem to show that the dopants themselves are one of the primary causes of the asymmetry. The explanation we provide should be testable experimentally with relative ease.

PUBLICATIONS

Publications resulting, partially or wholly, from this work:

- **P. D. Gorman**, J. M. Duffy, S. R. Power, and M. S. Ferreira
  Strain-Modified RKKY Interaction in Carbon Nanotubes
  In preparation.

- **P. D. Gorman**, J. M. Duffy, S. R. Power, and M. S. Ferreira
  RKKY Interaction Between Extended Magnetic Defect Lines in Graphene
  Physical Review B, 90, 125411, 2014.

- J. A. Lawlor, **P. D. Gorman**, S. R. Power, C. G. Bezerra, and M. S. Ferreira
  Sublattice Imbalance of Substitutionally Doped Nitrogen in Graphene
  Carbon 77, 645-650, 2014.

- J. M. Duffy, **P. D. Gorman**, S. R. Power, and M. S. Ferreira
  Variable Range of the RKKY Interaction in Edged Graphene
  Journal of Physics: Condensed Matter, 26, 055007, 2014.

- **P. D. Gorman**, J. M. Duffy, M. S. Ferreira, and S. R. Power
  RKKY Interaction Between Adsorbed Magnetic Impurities in Graphene: Symmetry and Strain Effects
  Physical Review B, 88, 085405, 2013.

- S. R. Power, **P. D. Gorman**, J. M. Duffy, and M. S. Ferreira
  Strain-Induced Modulation of Magnetic Interactions in Graphene
  Physical Review B, 86, 195423, 2012.

ACKNOWLEDGEMENTS

Over the last few years I have received incalculable help and guidance from numerable people. I would first like to thank Prof. Mauro Ferreira for his supervision and advice throughout this project, and for creating a friendly and collaborative environment in which to conduct research.

I would like to acknowledge the financial support this project received from the Irish Research Council for Science, Engineering and Technology under the EMBARK initiative and from Science Foundation Ireland under Grant No. SFI 11/RFP.1/MTR/3083, and also from the School of Physics Trinity College Dublin.

Throughout this project I have had many fruitful collaborations to whom I owe a debt. I would like to acknowledge my fellow graduate students John Duffy and James "Ringo" Lawlor, who have been of great assistance and provided much support throughout my research, and I would like to say that I'm sorry we never found our "George". I would also like to acknowledge Dr. Stephen Power who provided much assistance and supervision in the early years of my research and has continued to do so from his new home in Denmark. I would like to thank Tom, Awadhesh, and Amaury for useful discussions, and Eric for useless discussions. I would further like to thank Colin for being very milk-conscious, avoiding many milk-less catastrophes.

I would like to extend my thanks outside of Trinity to: Dr. Ali Mozaffari, for answering all of my dumb questions about black holes; Dr. Sinéad Griffin, for being kind, fun, and much smarter than me; Mr. James McHugh, wherever he may be; and to whoever has been cutting the grass outside my house for the last year. Finally, I would like to thank my wife, Sreeja, without her love and support this thesis would not have been possible.

CONTENTS

List of Figures xvii

Acronyms xxii

1 INTRODUCTION 1

1.1 Graphene-Related Materials 1

1.2 Spintronics and the Indirect Exchange Coupling 5

1.3 Magnetic Impurities and Interactions in Graphene Systems . . 7

1.4 Graphene and Nanotube Deformations 10

1.5 Thesis Layout 13

2 MATHEMATICAL METHODS 17

2.1 Green's Functions 18

2.2 Density of States 20

2.3 The Dyson Equation 22

2.3.1 Substitutional Impurities 24

2.3.2 Adsorbed Impurities 26

2.4 The Lloyd Formula Method 30

2.5 Stationary Phase Approximation 34

2.6 Energy Integrals of Green's Functions 39

2.7 Tight-Binding Model 42

2.8 Summary of Chapter 43

3 GRAPHENE-RELATED MATERIALS AND IMPURITIES 45

3.1 Electronic Structure of Graphene 47

3.1.1 Graphene Tight-Binding Model 47

3.1.2 Graphene Dispersion Relation 51

3.1.3 Graphene Green's Functions 54

3.1.4 Stationary Phase Approximation of Graphene 65

3.2 Carbon Nanotubes 72
3.2.1 Electronic Structure of Carbon Nanotubes 74
3.2.2 Green's Functions of Carbon Nanotubes 75
3.3 Other Graphene Derived Materials 82
3.3.1 Semi-infinite Graphene 83
3.3.2 Graphene Nanoribbons 84
3.4 Impurities in Graphene-Related Materials 86
3.4.1 Impurity Conformation in Graphene and Nanotubes . . 88
3.4.2 Magnetic Impurities (Electron-electron Interactions) . . . 95
3.5 Summary of Chapter 100

4 INDIRECT EXCHANGE COUPLING IN MAGNETICALLY DOPED GRAPHENE-BASED MATERIALS 101

4.1 Indirect Exchange Interaction 101
4.1.1 Quantum Well Method 102
4.1.2 Energy Difference Calculation 104
4.1.3 Moment Rotation Calculation 110
4.1.4 Numerical Calculation of the Coupling 111
4.1.5 The RKKY Formalism 112
4.1.6 Key Features of RKKY in Graphene-Based Materials . . 114
4.2 Evaluation of the RKKY in Graphene 115
4.2.1 Derivation of the RKKY in Graphene 116
4.2.2 Key Quantities for Graphene 119
4.2.3 RKKY Between Substitutional and Top-Adsorbed Impurities 122
4.2.4 RKKY Between Bridge-Adsorbed Impurities 125
4.2.5 RKKY Between Centre-Adsorbed Impurities 128
4.3 Evaluation of the RKKY in Carbon Nanotubes 134
4.3.1 Derivation of the RKKY in Carbon Nanotubes 134
4.3.2 RKKY Between Impurities in ACNT 136

4.3.3 RKKY Between Impurities in ZZNT 139
4.3.4 RKKY as a Function of Nanotube Circumference 142
4.4 Summary of Chapter 144
5 STRAIN EFFECTS ON MAGNETIC INTERACTIONS 147
5.1 Strain-Modified Electronic Structure of Graphene and Nanotubes 149
5.1.1 Modified Hamiltonian and Dispersion Relation 151
5.1.2 Modified Brillouin Zone 152
5.1.3 Modified Graphene Green's Functions 155
5.1.4 Modified Nanotube Green's Functions 159
5.1.5 Modified Hopping Integrals 161
5.1.6 Modified Impurities 163
5.2 Strain-Modified Interactions in Graphene 163
5.2.1 Substitutional and Top-Adsorbed 164
5.2.2 Bridge-Adsorbed 169
5.2.3 Centre-Adsorbed 174
5.3 Strain-Modified Interactions in Nanotubes 178
5.3.1 Modified Interactions in Armchair Nanotubes 179
5.3.2 Modified Interactions in Zigzag Nanotubes 182
5.4 Summary of Chapter 185
6 APPLICATION OF METHODS TO OTHER SYSTEMS 189
6.1 Extended Magnetic Defects 190
6.1.1 Coupling Between Lines of Defects 192
6.1.2 Comparison of Coupling Between Finite and Infinite Lines 198
6.2 Sublattice Asymmetry of Impurities in Graphene 201
6.2.1 Energetics of Dopants 203
6.2.2 Critical Concentration 208
6.2.3 Strain-Modified Critical Concentration 211
6.3 Summary of Chapter 213
7 SUMMARY AND FUTURE WORK 215

7.1 Summary 215

7.2 Extensions and Future Work 219

A IRREDUCIBLE GRAPHENE SECTOR: TRANSFORMATION ALGORITHM223

BIBLIOGRAPHY 227

LIST OF FIGURES

Figure 1.1 **Schematic:** Carbon Allotropes 2

Figure 2.1 **Schematic:** Substitutional Impurity in a 1D chain . . . 24

Figure 2.2 **Schematic:** Adsorbed Impurity in a 1D chain 27

Figure 2.3 **Plot:** Stationary Phase Approximation of Generic Integral 35

Figure 2.4 **Plot:** Comparison of the Green's Function Stationary Phase Approximation Green's Function 38

Figure 2.5 **Schematic:** Contour Integration 40

Figure 3.1 **Schematic:** Graphene Lattice 49

Figure 3.2 **Plot:** Fermi Surface Contour Plot and Brillouin Zone . 52

Figure 3.3 **Schematic:** Modified Brillouin Zone of Graphene . . . 59

Figure 3.4 **Schematic:** Graphene Green's Function - Contour Integral Over k_A 61

Figure 3.5 **Schematic:** Graphene Green's Function - Contour Integral Over k_Z 64

Figure 3.6 **Plot:** Integrands of Graphene Green's Function 65

Figure 3.7 **Plot:** Comparison of the Graphene Green's Function and the Stationary Phase Approximation Green's Function Between Sites Separated Along the Armchair Direction as a Function of Energy 69

Figure 3.8 **Plot:** Comparison of the Graphene Green's Function and the Stationary Phase Approximation Green's Function Between Sites Separated Along the Zigzag Direction as a Function of Energy 70

Figure 3.9 **Schematic:** Carbon Nanotube 73

Figure 3.10 **Schematic:** Armchair Carbon Nanotube and Brillouin Zone 77
Figure 3.11 **Plot:**Comparison of Analytic and Recursive Methods for Armchair Nanotube Green's Function 78
Figure 3.12 **Schematic:** Zigzag Carbon Nanotube and Brillouin Zone 79
Figure 3.13 **Plot:** Comparison of Analytic and Recursive Methods for Zigzag Nanotube Green's Function 81
Figure 3.14 **Schematic and Plot:** a) Armchair Semi-Infinite Graphene; b) Comparison of the Eigenstate and Recursive Methods for Semi-Infinite Graphene Green's Function 83
Figure 3.15 **Schematic and Plot:** Armchair Symmetric Nanoribbon; Comparison of the Eigenstate and Recursive Methods for Nanoribbon Graphene Green's Function 85
Figure 3.16 **Schematic:** Impurity Conformation Types in Graphene 87
Figure 3.17 **Schematic:** Spin Channel Band Splitting 99
Figure 4.1 **Schematic:** Quantum Well Interpretation of Indirect Exchange Coupling 103
Figure 4.2 **Plot:** Coupling Between Substitutional Impurities in Graphene Along the High-Symmetry Directions 124
Figure 4.3 **Plot:** Coupling Between Bridge-Adsorbed Impurities in Graphene Along the High-Symmetry Directions 126
Figure 4.4 **Schematic:** Origin of Additional Phase Term Arising From The Interaction of Centre-Adsorbed Impurities . 129
Figure 4.5 **Plot:** Coupling Between Centre-Adsorbed Impurities in Graphene Along the High-Symmetry Directions 132
Figure 4.6 **Plot:** Coupling on Armchair Nanotubes Between Substitutional, Bridge-adsorbed, and Centre-Adsorbed Impurities. 138

Figure 4.7 **Plot:** Coupling on Zigzag Nanotubes Between Substitutional, Bridge-adsorbed, and Centre-Adsorbed Impurities. 140
Figure 4.8 **Plot:** Decay Rate Versus Nanotube Circumference for Four Impurity Conformations 143
Figure 5.1 **Plot:** Lifshitz Transition for Graphene Under Strain . . 148
Figure 5.2 **Schematic:** Anisotropic Graphene Lattice 150
Figure 5.3 **Schematic:** Wigner-Seitz Cell for Strained Graphene . . 153
Figure 5.4 **Schematic:** Nanotube Brillouin Zone for Armchair and Zigzag Nanotubes 154
Figure 5.5 **Plot:** Comparison of the Strain-dependent GFs and SPA GFs as a Function of Energy 158
Figure 5.6 **Plot:** Comparison of Strained and Unstrained Coupling between Substitutional Impurities Separated Along the Armchair Direction of Graphene 166
Figure 5.7 **Plot:** Comparison of Strained and Unstrained Coupling between Substitutional Impurities Separated Along the Zigzag Direction of Graphene 168
Figure 5.8 **Plot:** Coupling between Bridge-Adsorbed Impurities in Graphene Separated Along the Armchair and Zigzag Directions of Graphene 170
Figure 5.9 **Plot:** Comparison of Strained and Unstrained Coupling between Bridge-Adsorbed Impurities in Graphene Separated Along the Armchair and Zigzag Directions of Graphene 171
Figure 5.10 **Plot:** Coupling between Centre-Adsorbed Impurities in Graphene Separated Along the Armchair Zigzag Directions of Graphene 175

Figure 5.11 **Plot:** Comparison of Strained and Unstrained Coupling Between Centre-Adsorbed Impurities in Graphene Separated Along the Armchair and Zigzag Directions of Graphene 177
Figure 5.12 **Plot:** Coupling between Substitutional and Bridge-Adsorbed Impurities in ACNTs 181
Figure 5.13 **Plot:** Comparison of Centre-Adsorbed Impurity RKKY for Isotropic and Anisotropic ACNTs 182
Figure 5.14 **Plot:** ZZNT DOS for Various Values of Strain 183
Figure 5.15 **Plot:** Coupling Between Adsorbed Impurities in Strained ZZNTs 185
Figure 5.16 **Plot:** Summary of Chapter 5 187
Figure 6.1 **Schematic:** Extended Magnetic Defects in Graphene . . 191
Figure 6.2 **Plot:** Comparison of the SPA of the Coupling Between Extended Magnetic Defects 197
Figure 6.3 **Plot:** Caparison of the Coupling Between Finite and Infinite Extended Magnetic Impurities 199
Figure 6.4 **Plot:** Numerical Evaluation of the Coupling Between Two Lines of Impurities as a Function of Their Separation 200
Figure 6.5 **Schematic:** Sublattice-Asymmetrically Doped Graphene 202
Figure 6.6 **Plot:** Correction to the Energy Change Due to the Introduction of Two Impurities as a Function of Separation 205
Figure 6.7 **Plot:** Functional Form of the Normalized Pairwise Interaction Energy Per Unit Area Against the Fraction of the Dopants Occupying a Single Sublattice 209
Figure 6.8 **Plot:** Onsite Dopant Energy as a Function of Critical Concentration 210
Figure 6.9 **Plot:** Critical Concentration as a Function of Strain . . . 212

Figure A.1 **Schematic:** Irreducible Graphene Sector 224

COMMON ACRONYMS

AC Armchair

ACNT Armchair Carbon Nanotube

AFM Antiferromagnetic

CNT Carbon Nanotube

CVD Chemical Vapour Deposition

DFT Density Functional Theory

DOS Density of States

FM Ferromagnetic

GF Green's Function

IEC Indirect Exchange Coupling

LDOS Local Density of States

RKKY Ruderman-Kittel-Kasuya-Yosida

SPA Stationary Phase Approximation

ZZ Zigzag

ZZNT Zigzag Carbon Nanotube

1

INTRODUCTION

In this thesis we wish to provide a theoretical analysis of the interactions between localized magnetic moments in graphene and nanotubes, and how they may be modified. We will approach this with the utmost of mathematical transparency throughout in the hopes of gaining insight into the underlying features of these interactions. As such, we will make heavy use of Green's function (GF) techniques due to the ease with which they can be exploited to deal with the addition of disorder into systems.

Here we will provide a brief introduction to graphene-related materials, including their discoveries, properties, and uses, before proceeding to discuss the exciting field of spintronics which possesses the ability to up-end the way we think about electronics and information processing. We will then show that these graphene-related materials may be useful components of this spintronic future due to their unique and interesting properties in the presence of magnetic moments. An important feature of which is the ability to tune and control those properties in a predictable way, which we discuss under the umbrella of impurity conformation and strain. We start with an overview of the materials in question.

1.1 GRAPHENE-RELATED MATERIALS

In 1985 fullerenes, a family of quasi zero-dimensional carbon allotropes, were discovered [1], pushing carbon-based materials to the forefront of material science. Carbon nanotubes (CNTs), a pseudo one-dimensional material, were

discovered shortly afterwards in 1991 [2]. The initial observation was of what would later be called multi-walled nanotubes (MWNTs), which are sets of concentric CNTs. Single-walled nanotubes (SWNTs), carbon cylinders a single layer thick, were successfully isolated not long afterwards [3]. These SWNTs were found to not only be mechanically robust and light-weight, but they also display uniquely sensitive and tunable electronic properties [4–6]. Graphene was first synthesized in 2004, when monolayers of graphene large enough to be studied using conventional techniques were produced by micromechanical cleavage [7, 8]. Graphene is the two-dimensional cousin of graphite, a three-dimensional solid consisting of stacked layers of graphene weakly coupled by van der Waals force. Its discoverers were acknowledged for their identification and subsequent investigations into graphene with the 2010 Nobel Prize for Physics [9, 10]. The method they used to isolate graphene is known as micromechanical cleavage, or the "scotch-tape method", and involves transferring the top layer of a high-quality graphite crystal onto a substrate via adhesive tape. Before this, graphene had been predicted not to exist in a free state [11–13]. Despite its simplicity, high quality graphene crystals can be produced in this manner. Graphene has also been produced by chemical exfoliation and using epitaxial growth mechanisms [14–16]. Figure 1.1 shows the graphene allotropes in order of increasing dimensionality.

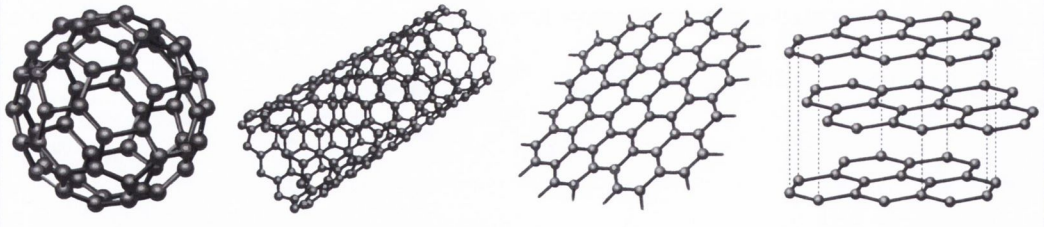


Figure 1.1: Representation of carbon allotropes in order of increasing dimensionality: quasi zero-dimensional fullerenes, quasi one-dimensional nanotubes, two-dimensional graphene, and three-dimensional graphite. Image is adapted from Ref. [17].

Since its discovery, experimental and theoretical interest in graphene has grown rapidly. However, much of the electronic theory had been previously formulated when it was used as a starting point for calculating the electronic structure of graphite [18, 19]. Graphene is a two-dimensional atomic crystal (the first of its kind, though several others have now been discovered [20–23]) consisting of a single sheet of sp^2 bonded carbon atoms arranged in a hexagonal lattice. It is the thinnest and strongest material ever obtained, with a breaking strength 200 times greater than steel [9, 24], and extraordinary elastic properties [24]. It is also found to be an extremely effective electrical and thermal conductor [25, 26], as well as being impermeable to molecules and gases [27].

Nanotubes can be produced with a high level of purity, *i.e.*, a low level of defects, where the quantity of defects depends on how they are grown. These defects do have an impact on the physical an electronic properties of nanotubes, and these defect-induced changes are themselves the subject of study. Nanotubes display remarkable mechanical properties, such as flexibility [28], and tend to buckle or kink when strained rather than break. The Young's Modulus for SWNTs is found to be 1TPa which is similar to that of graphene [29]. Experiments on the thermal properties of nanotubes have found a thermal conductivity comparable to that of diamond, which is one of the best know thermal conductors [30, 31]. Such structural robustness and thermal conductivity make nanotubes desirable components in a wide variety of technologies including atomic force microscope tips, liquid crystal displays, and future electronics. Nanotubes also have interesting optical properties and hold possibilities for ultra-small photonic devices [32, 33]. Experiments on the electrical conductivity of SWNT show that they behave as quantum wires, where their behaviour as ballistic conductors was demonstrated by the observed conduction plateaus as a function of the bias voltage [5, 34]. Such a robust quantum wire offers enormous potential for technological applications.

Nanotubes may have potential advantages over graphene as solid state devices as they possess a direct bandgap. However, it is the electronic properties of graphene that have garnered the most attention since its discovery [35]. Graphene is found to be a zero-gap semiconductor, or semi-metal. Its Fermi surface at zero Fermi energy consists of six discrete points, at the corners of the first Brillouin zone, where the conduction and valence bands touch; two of which are independent - the Dirac points. The Dirac points are so called because of the linearity of the dispersion relation around these points. Electrons at these energies lose their effective mass and behave more like relativistic particles than normal electrons which allows the Hamiltonian to be written in the form of a Dirac Hamiltonian for massless particles [36]. A consequence of which is that they can propagate without scattering over large distances [7]. Although not itself magnetic, graphene has many properties that suggest its possible use as a carrier of spin information including weak spin-orbit and hyperfine couplings, which are the main sources of relaxation and decoherence of electron spin [37–43]. Although not itself magnetic graphene has recently been shown to become magnetic in close proximity to yttrium iron garnet [44].

The bandstructure of graphene and nanotubes are found to be well described using a nearest-neighbour tight-binding approximation which restricts the Hamiltonian considered to a single p_z orbital per carbon atom. Throughout this work we will use this approximation as it allows us to maintain a good degree of mathematical transparency. It will be discussed in further detail in Chap. 3.

1.2 SPINTRONICS AND THE INDIRECT EXCHANGE COUPLING

Spintronics[1] has emerged as a promising alternative to conventional electronics. Traditional electronic information processes utilize the electron's charge to carry information. In contrast, spintronics is the idea that we may harness the potential of an electron's spin degrees of freedom, associated with their intrinsic angular momentum, to accomplish the same feat. Driven by the demand for smaller and faster computer components, spintronics has been the focus of much intensive research in recent years, and this research holds great promise for more efficient computer memories, magnetic sensors, and enhanced information storage capacity. The Giant Magnetoresistance (GMR) effect [45, 46], in which a significant change in the electrical resistance of a material can be induced by the parallel or anti-parallel magnetic alignment of adjacent ferromagnetic layers, has already found applications in hard-drives and is an example of a major technological advance in this field, and was awarded the Nobel Prize for Physics in 2007. Spintronics is expected to revolutionize the electronics industry, and graphene-based materials are expected to play a major role [47]. Spintronics allows for information storage, processing and communication at faster speeds and with lower energy consumption than is currently possible with conventional electronics [48–51].

One possible implementation of spintronics is found via the doping of low-dimensional systems with magnetic impurities. When the separation between these magnetic impurities is small enough for significant overlap of their electron wavefunctions then a direct exchange coupling can occur. In a large system, sparsely populated with impurities, this kind of interaction is rare. Indirect Exchange Coupling (IEC) occurs at larger distances, when the coupling

1 This is sometimes called magnetoelectronics.

is mediated by the conduction electrons of the host material, and is therefore host-dependent. The IEC allows us to measure the coupling between magnetic moments as the energy difference in the system between their ferromagnetic (FM) and antiferromagnetic (AFM) alignments. If the relative orientation of two magnetic moments does not affect the energy of a system then there is no coupling between them. The indirect exchange coupling is explained by *Quantum Well Theory*, and by the Ruderman-Kittel-Kasuya-Yosida (RKKY) theory, which was later found to be an approximation of the quantum well theory. The quantum well theory explains the IEC (and its oscillatory behaviour) as the result of quantum confinement, by the magnetic impurity, causing the allowed energy levels to change as a function of the impurity separation [52]. The oscillatory nature of the interaction arises from the fact that the allowed energy levels alternate with respect to the Fermi energy. The IEC is often calculated using the RKKY approximation, and the interaction often takes this name [53]. IEC was first observed in magnetic multilayer systems (2 thin FM layers embedded in, and separated by, a metallic host) [54], where at low temperatures the coupling was found to decay and to oscillate between FM and AFM as a function of the separation, D, of the magnetic layers [55]. The coupling was found to decay as D^{-2} and the period of oscillation was found to be almost independent of the magnetic material composing the layer [56].

The IEC requires the presence of magnetic moments in a non-magnetic material with conduction electrons to mediate the interaction - graphene and nanotubes doped with magnetic impurities fit these requirements perfectly. To realize the full potential of magnetoelectronics it is important to understand how the magnetic moments of atoms interact with each other and with host materials. The IEC can be characterized by its magnitude, oscillation, and decay rate. The aim of this project is to study these features of magnetic interactions in graphene and nanotubes, which have interesting and unusual properties due to their reduced dimensionality. Several of these features have

multiple and conflicting descriptions in the literature and we hope that our work here provides an explanation of the different effects seen and lead to a consensus. Of major interest is the exchange coupling of magnetic moments attached to graphene systems (both substitutional and adsorbed), as this coupling could facilitate the transfer of information between parts of future spintronic devices.

1.3 MAGNETIC IMPURITIES AND INTERACTIONS IN GRAPHENE SYSTEMS

An understanding of the coupling between magnetic moments is an essential step in the effort to exploit graphene-related systems for spintronic applications. How dopants and vacancies alter the properties of graphene has received much attention [57–62], and it is thought that they might lead to the appearance of band gaps, and in the substitutional case induce spin-polarized currents [63, 64]. This tunable reaction may pave the way to engineer the transport properties of doped graphene leading to a new species of transistor [60, 65, 66].

This coupling underpins many magnetic properties including the magnetic ordering and magnetoresistance of a magnetically-doped graphene device. We will examine the RKKY interaction, mentioned above, which is mediated by the conduction electrons of the host system, and is an approximation to the IEC. This type of long ranged interaction allows impurities to feel each other's presence and respond to magnetic perturbations. The favourable orientation of these moments is usually evaluated as the orientation that lowers the total energy of the system.

There is a strong interest in understanding the RKKY interaction in graphene-related systems, which has been intensively studied [67–84]. In carbon nan-

otubes the long-ranged interaction between moments was found to decay as D^{-1} where D is the separation between moments [83], as expected for a pseudo-one-dimensional material. Interestingly in graphene, a two-dimensional material, where one would expect the interaction to decay as D^{-2}, it is actually found to decay at D^{-3}, due to the peculiar properties of graphene at zero Fermi energy [68–80]. This was also found to affect the sign of the interaction and its decay rate for certain impurity configurations [84–87]. Although signatures of the IEC have been detected experimentally in carbon nanotubes [88], there exists no conclusive experimental evidence that could confirm the theoretical prediction of the decay rate for graphene.

We will therefore briefly discuss some of the experimental measurements that have been made for the indirect exchange coupling, and some of the estimates that have been made computationally. Here we look at DFT calculations of impurities on graphene, and combine these with experimental studies of various adatoms on substrates to get an idea of the magnitude of couplings that are required for spintronic devices. Since spintronic devices will likely operate on the nm length scale we will focus on studies that estimate the coupling near this range. Several DFT studies have been performed to attempt to estimate the interaction between adsorbed impurities on graphene and nanotubes. Although the two situations are not entirely analogous - we study pairwise interactions between two isolated impurities in an otherwise pristine graphene sheet whereas DFT calculations are usually performed with a doped supercell repeated to form an infinite sheet containing higher orders of interactions - for the purposes of finding a rough order of magnitude of the coupling they should suffice.

Another problem that hampers some of this DFT work is the representation of independent particles by single-impurity unit cells [89]. It had been shown [90] that the DFT assumption of independent unit cells in the case of magnetically doped low-dimensional graphene-based materials is fundamen-

tally inadequate, leading to the spurious suppression of an overall magnetic moment. It is further shown that this problem can be circumvented by using unit-cells that contain more than one impurity. Despite these inadequacies, calculations that use a single impurity per unit cell are probably sufficient to indicate the magnitude of the interaction.

Santos *et al.* [91] use SIESTA to examine the coupling of substitutional Co atoms in graphene sheets using a periodic distribution of Co atoms in 4x4 and 8x8 supercells. Using this method they are able to replicate the prediction of AFM interactions for opposite-sublattice sites, and FM interactions for same-sublattice site. They find that the indirect exchange coupling between impurities at a range of about 0.5 nm is ~20-50 meV. Gerber *et al.* [92] perform DFT calculations of bridge-adsorbed carbon adatoms on a graphene sheet, where they use multiple unit-cells to ensure that the coupling in not strongly correlated with the unit-cell size. They find that at a distance of about 0.5nm the coupling interaction is in the ~24-42 meV.

Until recently experimental work in this area has been hampered by spatial averaging techniques, which only provide fragmentary information on the distribution and do not enable a real-space study of the magnetic phases. However, the direct detection of such interactions is now feasible with the technique of measuring magnetisation curves of individual atoms using spin-polarised scanning tunnelling spectroscopy [93]. Recently Khajetoorians *et al.* [94] have studied the indirect exchange interaction between Fe atoms on a Cu(111) substrate. This is studied in real-space as a function of an external magnetic field by means of single-atom magnetometry (SAM) using spin-resolved scanning tunnelling spectroscopy. Here they are able to detect a sinusoidal pattern in the distance dependence of the magnetism. At separations under 1 nm they find couplings on the order of tens of meV, decaying to about 0.1 meV at 1 nm, and to 0.01 meV at 3 nm.

Zhou *et al.* [95] study experimentally well-defined pairs of Co adatoms with different orientations and distances on Pt(111). Here they find coupling magnitudes of the order of ~ 0.1meV in the range 0.75-1.25nm. They also conclude that exact knowledge of the RKKY interaction on the atomic scale can be essential even for systems showing a rather simple Fermi surface.

For some experimental work on the magnitudes of couplings that might be required for spintronic devices we look to Hirjibehedin *et al.* [96]. Here they have built 10 atom long chains of Mn on a thin insulating layer using STM techniques. They could then determine the AFM coupling strength, which could be set at either 3 or 6 meV depending on the exact atomic configuration.

Despite the small magnitude of the interaction it is important to note that due to the commensurability effect in graphene, which causes impurities occupying the same sublattice to be FM aligned, the combined coupling between many impurities may be vastly stronger. Based on the experimentally detectable values for the coupling in other materials, and on the computationally determined values for the coupling in graphene, it is likely that these experiments will be performed in graphene in the coming years and that they will yield useful coupling strengths for spintronic devices.

1.4 GRAPHENE AND NANOTUBE DEFORMATIONS

Numerous techniques have been examined that might alter the electronic properties of graphene-related systems, such as the effects of multiple layers of graphene and nanoribbons, concentric nanotubes, magnetic fields, nanomesh structures, grain boundaries, chemical functionalization, edges and many more [97–106]. Due to the ease with which graphene's properties can be tuned, the prospect of using strain to alter its electronic properties has come to much attention. Graphene has extraordinary elastic properties; withstand-

ing reversible deformations of approximately 20% (depending on direction of strain), more than any other crystal [24, 107–110], which may provide opportunities to tune the electronic, magnetic, optical and thermal properties of graphene systems [111–114]. The unusually large range of electronic response, combined with graphene's two-dimensionality and the peculiar coupling between electrons and deformations, makes graphene an excellent condensed matter system in which to explore uniaxial strain. As such, this thesis will explore the range of effects that strain has on the IEC in graphene and nanotubes.

Deformations in graphene may occur as a by-product of the growth method, or they may be intentionally introduced or exaggerated for the purpose of altering the electronic structure. Growth on substrates with different lattice constants will usually introduce strain into the graphene, which may be detected by Raman spectroscopy [115, 116]. However, even without this lattice mismatch, strain will still arise along the edges of the system, and can result in some interesting quantum features [117, 118]. During the transfer of graphene from one substrate to another, the relief of compressive strain can result in the formation of ridges and buckling [119]. It is possible to create many different types of deformations in graphene by growing it on shaped substrates: sinusoidally corrugated surfaces, steps, elongated trenches, spherical bubbles, Gaussian bumps, and Gaussian depressions [120]. Folding of graphene nanoribbons has been explored to allow for the connection of graphene nanoelectronic components, where it was found that for certain folding angles the conductance of the ribbon is only slightly perturbed [121]. Shear strain, that of pulling parallel lines in opposite directions, has been shown to create periodic ripples in graphene sheets [122], and to tune the electronic properties, opening and closing energy gaps [123]. The effects of strain on bilayer graphene (where two layers of graphene are coupled by the van der Waals

interaction) has also been explored, and it is shown to be able to open a band gap [124].

Stretching graphene has a profound effect on the material's electrical properties. The effects on the band structures of both graphene and graphene nanoribbons have been vigorously investigated using *ab initio* and tight-binding approaches [109, 112, 125–138]. However, it has been shown that uniaxial strain will not open a band gap in graphene for any reasonable physical strain. However, strain does cause the Dirac points to be displaced from the corners of the BZ [112, 130, 133, 134]. This is also true of nanotubes and has a profound effect on their electronic properties, as we shall see in Sec. 5.3. The gapless and conical nature of the energy dispersion in graphene remains robust, except when the deformation is so strong that the two equivalent Dirac points merge in a Lifshitz transition. However, this occurs at strain values approaching that of the limit of graphene, and likely the tight-binding description is not reliable at these deformations [139].

It has been proposed recently that strain could be used to modify graphene for use as various fundamental components in *all-graphene* electronics [57]. Mechanical deformations also open up prospects for studying the Dirac fermions in new regimes [140]. Recent experiments report that certain strain profiles can induce Landau quantization and effective pseudomagnetic fields over 300 T [113, 141–144]. One such experiment reports that the non-uniform strain produced by depositing graphene over pillars can induce pseudomagnetic fields up to 5000 T [145]. Another reports that subjecting graphene to mechanical strain can mimic the effects of magnetic fields and create a quantum dot, an exotic type of semiconductor with a wide range of potential uses in electronic devices [146]. Strain has also been suggested as a new route to realize robust topological states in mesoscopic graphene [140], and to create an electron lens, where deformation modifies the band structure, leading to a local decrease of electron group velocity [147] .

In order to expand the applicability of those systems we need to understand how the interactions may be modified to suit our needs. Much progress has been made explaining the intrinsic properties of nanotubes and nearly two decades after their discovery they are still the subject of intensive scientific research due to their intriguing physical properties. One such avenue that has been explored to alter the intrinsic properties of nanotubes is the introduction of strain. The effects of strain on the elastic, structural, and electronic properties of carbon nanotubes - including band gap and electron conductance - have been extensively studied [148–154]. Many uses have been suggested for strained nanotubes including strain sensors and Field-Effective Transistors [155, 156]. It has been shown that uniaxial strain can open a bandgap in metallic nanotubes and alter the bandgap in semi-conducing nanotubes [157, 158].

When a nanotube undergoes strain, the bonds between carbon atoms become stretched, which increases the overall energy of the atomic lattice. Some of this energy can be alleviated through the formation of local defects. One such defect, which transforms four hexagons into a pair of heptagons and a pair of pentagons, is know as a Stone-Wales defect, and may become energetically favourable in tubes experiencing as little as 5% strain [159]. Due to the local nature of such defects, and the difficulty of incorporating them in a realistic manner in our calculations, we will ignore them in this work.

1.5 THESIS LAYOUT

The IEC has been extensively studied in graphene-systems, as have the effects of strain. By combining these areas of work we hope to gain insight into the effects that strain has on the IEC between magnetic moments in graphene and nanotubes. This is the main topic of discussion that will be worked towards in the following chapters:

Chapter 2 presents the mathematical methods that will be used throughout this thesis. Here we review the Green's functions that form the backbone of this thesis. We then demonstrate how they they can be calculated, and how, in conjunction with the Dyson equation and Lloyd formula, they may be used to determine many properties of condensed matter systems. Central to the work in this thesis is how the Dyson equation may be used to describe perturbed systems, and we present two basic examples of that in this chapter. We also introduce here another concept central to this work, namely how the Lloyd formula may be used to calculate the change in energy of a system in the presence of an impurity. Several other mathematical methods important to this work are also briefly discussed here, and will be elaborated on in specific cases as they arise in later chapters.

In Chap. 3 we focus on the electronic structure of graphene, which we then extend to nanotubes. Both of these will be treated in the simple π-band model, which make it possible to examine the electronic properties of both systems in a mathematically transparent manner. We then derive closed-form analytic expressions for the high-symmetry Green's functions of both. These Green's functions are crucial in determining the electronic properties of disordered systems, and the existence of analytic expressions allows us to understand the underlying features of these properties. These analytic expressions are useful in understanding certain properties of these systems in a mathematically transparent manner, and offer advantages over numerical methods, which lack this transparency, and the linear dispersion approximation, which is only valid in a narrow energy range. We also briefly discuss the versatility of Green's functions in dealing with more difficult graphene-related materials such as semi-infinite graphene and graphene nanoribbons. We then extend our model to allow the introduction of magnetic moments into our systems.

In Chap. 4 we examine the magnetic interaction between impurities in graphene-related systems known as the Indirect Exchange Coupling. The

Green's functions of Chap. 3 allow us to calculate the separation dependence of this interaction. By examining the interaction between different impurity conformations we are able to show that conformation is one of the primary factors determining the form of the Indirect Exchange Coupling. We discuss the decay rate of this interaction in graphene and nanotubes, and how they can be related to each other by considering increasingly large nanotube circumferences.

In Chap. 5 we expand our Hamiltonian for graphene and nanotubes to allow for the inclusion of uniaxial strain, which allows us to consider how the electronic properties of both systems are modified by strain. We then derive strain-dependent versions of the Green's functions derived in Chap. 3. The strain-dependent effects on the decay rate of the RKKY interaction can be understood in purely mathematical terms, without regard for the strained lattice effect on the hopping integrals. To allow us to understand more subtle strain-dependent effects we discuss how the changes in these hopping integrals may be approximated. We then use this knowledge to examine the strain-dependent effects for each type of impurity conformation in graphene and nanotubes, and compare our results to the strain-independent results.

In Chap. 6 we examine two puzzles. The first involves the strength of the interaction between extended magnetic defects. We focus on one practical case where we examine the RKKY interaction between extended magnetic defect lines. Here we derive an analytic form of the interaction in the presence of infinite lines of magnetic defects and show that this method can be used to examine the properties of finite lines. The second is an examination of sublattice-asymmetric nitrogen dopants in the Chemical Vapour Deposition (CVD) grown graphene on copper substrates. We provide some background to the uses of asymmetrically doping graphene before discussing some of the possible explanations of the effect. We then present an argument that the nitrogen dopants themselves were responsible for the effect, rather than a

graphene edge as has been suggested by other works. We make use of the Lloyd formula to calculate how dopants modify the energy of the system, and then build a model which allows us to understand the criteria for sublattice asymmetry to occur. Though only a simple model it does allow us to define a critical concentration of dopants, which should be experimentally testable. As the copper substrate is known to induce some strain on graphene we further apply our strain-dependent Green's functions to this problem to define a strain-dependent critical concentration.

We now start with an introduction to the mathematical methods that will we used throughout this work.

2

MATHEMATICAL METHODS

This chapter will introduce the mathematical methods to be used throughout the remainder of this thesis. The most notable of these are the single particle Green's function and the Lloyd formula method. We place both of these in context by considering the altered electronic state of a host system with a localized perturbation.

Introducing an interaction between a foreign body and a host manifests itself as a change in the density of states. The density of states allows us to calculate a number of physical quantities such as charge transfer, occupation number, and the total energy. The Green's function (Sec. 2.1) is directly related to the density of states (Sec. 2.2), and for periodic systems calculating the local density of states via Green's functions is a reasonably straightforward task. The real strength of the Green's function method is that it is also capable of calculating the change in local density of states due to the introduction of a perturbation using the Dyson equation (Sec. 2.3). And further, using the Lloyd formula method (Sec. 2.4), we can rewrite the Dyson equation in a way that gives direct access to the change in energy of the system, due to a perturbation, without the need to calculate the total energy of either the initial or final system. We will also introduce a method that allows us to write the change of energy of the system in a completely analytic fashion, under some conditions, namely the Stationary Phase Approximation (Sec. 2.5), as well as a section that describes the method of integrating over Green's functions in the various forms they will be encountered in this work (Sec. 2.6).

Throughout the rest of this thesis we will use these methods to examine the effect of magnetic impurities on low dimensional carbon systems. However,

the methods introduced in the sections that follow are done in a general way with no particular reference to the type of system or perturbation. The goal of this work is to maintain as much mathematical transparency as possible so that the features of the physics may be examined. The methods we will now introduce are chosen for this reason, as such, much effort is put into maintaining analytic forms.

2.1 GREEN'S FUNCTIONS

In this section the concept of single particle Green's functions (GFs) will be introduced along with their relation to the Density of States (DOS). GFs are the most important concept introduced in this chapter, and underpin all of the calculations performed in this thesis. The GF is a solution to a linear differential equation, in our case the Schrödinger equation, relating an impulse response function to a source term. They are useful in electronic and optical transport calculations, field theory, and computing scattering cross-sections in high-energy physics, among others. In a general sense a GF is a two-point correlation function that allows us to express the response of a system to a perturbation.

A GF is a type of function used to solve inhomogeneous differential equations. Where z is a complex variable and $L(\mathbf{r})$ is a time-independent, linear, hermitian differential operator with a complete set of eigenfunctions, the GF, $G(\mathbf{r}, \mathbf{r}'; z)$, is defined as the solution to

$$[z - L(\mathbf{r})]G(\mathbf{r}, \mathbf{r}'; z) = \delta(\mathbf{r} - \mathbf{r}'). \tag{2.1.1}$$

In condensed matter physics the GF, $\hat{g}$, corresponding to the Schrödinger equation is typically defined as

$$\hat{g} = \lim_{\eta \to 0} \left[(E \pm i\eta)\hat{I} - \hat{\mathcal{H}} \right]^{-1}, \tag{2.1.2}$$

where $\hat{\mathcal{H}}$ is the Hamiltonian describing the system, $\hat{I}$ is the identity matrix, and E is the energy at which we wish to evaluate the system. A small imaginary part, $i\eta$, is added to ensure the GF is well defined around the eigenvalues of the Hamiltonian. The sign choice corresponds to two types of GF: $+i\eta$ refers to the *retarded* GF, which describes propagation away from a site; $-i\eta$ refers to the *advanced* GF, which describes propagation toward a site. The use of both *advanced* and *retarded* GF is required only when the time-reversal symmetry is broken, under the application of a magnetic field for example. For the calculation of the Indirect Exchange Coupling, which is a magnetic interaction mediated by the host electrons of a system (an important physical feature of this work that will be introduced in Sec. 4.1) either may be used, and unless otherwise stated it is to be assumed that we are using the *retarded* case throughout this work.

The GF itself is a very general operator. It is defined by the specific Hamiltonian, $\hat{\mathcal{H}}$, which may incorporate many physical effects depending on the level of complexity required. For the sake of the following derivation we will use the linear combination of atomic orbitals (LCAO), which allows us to express the molecular orbital as a linear sum of each of the atomic orbitals, and allows us to write a simplified Hamiltonian. In the next chapter we will introduce the full tight-binding Hamiltonian that is sufficient to describe the electronic properties of graphene.

2.2 DENSITY OF STATES

One of the main benefits of the GF methods is that it provides direct access to the DOS. The DOS is a fundamental quantity that describes the electronic structure of a system. In bulk systems the density distributions are not discrete, as they are in isolated atoms or molecules, but are instead continuous. The DOS describes the number of states per energy interval, at each energy level, that are available for electron occupation, where a high DOS is associated with many available states. The DOS is an average over the whole system, the local density of states (LDOS) describes the variation in the DOS at a particular site due to some local potential.

To derive the DOS we select a Hamiltonian, which we write in its eigenbasis, to insert into our GF Eq. 2.1.2

$$\hat{\mathcal{H}} = \sum_{\mu} |\psi_\mu\rangle \epsilon_\mu \langle\psi_\mu|, \tag{2.2.1}$$

with eigenvalues ϵ_μ, and where the state vectors, $|\psi_\mu\rangle$, form a complete set of eigenvectors of $\hat{\mathcal{H}}$. This yields a GF of the form

$$\hat{g} = \lim_{\eta \to 0} \sum_{\mu} |\psi_\mu\rangle \frac{1}{E + i\eta - \epsilon_\mu} \langle\psi_\mu|. \tag{2.2.2}$$

We can describe our LCAO type Hamiltonian, $\hat{\mathcal{H}}$, by a basis of localized orbitals $|\mathbf{r}\rangle$, centred on some site $\mathbf{r}$. We then project onto two orbitals, $|\mathbf{r}\rangle$ and $|\mathbf{r}'\rangle$

$$\langle\mathbf{r}|\hat{g}|\mathbf{r}'\rangle = \lim_{\eta \to 0} \sum_{\mu} \langle\mathbf{r}|\psi_\mu\rangle \frac{1}{E + i\eta - \epsilon_\mu} \langle\psi_\mu|\mathbf{r}'\rangle. \tag{2.2.3}$$

Multiplying and dividing across by a factor $E - i\eta - \epsilon_\mu$ allows us to separate this equation into a real and imaginary part

$$\langle \mathbf{r}|\hat{g}|\mathbf{r}'\rangle = \lim_{\eta\to 0} \sum_\mu \langle \mathbf{r}|\psi_\mu\rangle \left[\frac{E+\epsilon_\mu}{(E-\epsilon_\mu)^2+\eta^2} - \frac{i\eta}{(E-\epsilon_\mu)^2+\eta^2} \right] \langle \psi_\mu|\mathbf{r}'\rangle. \quad (2.2.4)$$

The imaginary part of which, for $\mathbf{r} = \mathbf{r}'$, is simply

$$Im\left(\langle \mathbf{r}|\hat{g}|\mathbf{r}\rangle\right) = \lim_{\eta\to 0} \sum_\mu \langle \mathbf{r}|\psi_\mu\rangle \frac{-\eta}{(E-\epsilon_\mu)^2+\eta^2} \langle \psi_\mu|\mathbf{r}\rangle. \quad (2.2.5)$$

The form of this is now identical to the definition for the Dirac Delta function

$$\delta(x) = \frac{1}{\pi} \lim_{a\to 0} \frac{a}{x^2+a^2}, \quad (2.2.6)$$

from which we can write

$$-\frac{1}{\pi} Im(\langle \mathbf{r}|\hat{g}|\mathbf{r}\rangle) = \lim_{\eta\to 0} \sum_\mu |\langle \mathbf{r}|\psi_\mu\rangle|^2 \delta((E-\epsilon_\mu)) = \rho_{\mathbf{r}}(E). \quad (2.2.7)$$

This is now precisely the definition for the LDOS at some site $\mathbf{r}$, $\rho_{\mathbf{r}}(E)$. To attain the (total) density of states we must sum over all sites in the system

$$\rho_{tot}(E) = \sum_{\mathbf{r}} \rho_{\mathbf{r}}(E) = -\sum_{\mathbf{r}} \frac{1}{\pi} Im(\langle \mathbf{r}|\hat{g}|\mathbf{r}\rangle) = -\frac{1}{\pi} Im(Tr(\hat{g})). \quad (2.2.8)$$

So we see that the total DOS can be written in terms of a trace over the GF matrix. This allows us to easily calculate physical quantities such as occupation number and energy changes. One caveat is that we have implicitly assumed that the system is translationally invariant. However, once translational invariance is broken, by the introduction of an impurity for example, then the Bloch wavevectors are no longer eigenvectors of the system and it is no longer valid.

In the following section we will introduce the Dyson equation which shows the true value of the GF approach since it allows us to introduce disorder into an otherwise periodic system without the need to determine the eigenvectors of the disordered system or construct large supercells which may introduce unwanted periodicity. It does so by relating the propagators of the disordered system to those of the pristine system.

2.3 THE DYSON EQUATION

The Dyson equation allows us to use perturbation theory to calculate the physical properties of a system by providing a simple method to introduce disorder into an otherwise periodic system. The GF of a system, $\hat{g}$, that displays translational invariance can often be calculated straightforwardly using Bloch's Theorem. To calculate the GF for a disordered or perturbed system, $\hat{G}$, is more difficult. The introduction of an impurity (or impurities) breaks this translational invariance so that the Bloch wavevectors are no longer eigenvectors of the system. Using the Dyson equation one requires only the GF of the pristine system and the perturbation, $\hat{V}$, to calculate the GF of the perturbed system. As there is no need to calculate the eigenvectors of the perturbed system, this allows for the easy calculation of the physical properties of perturbed systems.

The Dyson equation can be derived by applying the perturbation, $\hat{V}$, to the definition of a GF from Eq. 2.1.2, giving

$$\begin{aligned}\hat{G} &= \lim_{\eta \to 0} \left[(E + i\eta)\hat{I} - (\hat{\mathcal{H}} + \hat{V}) \right]^{-1} \\ &= \left[\hat{g}^{-1} - \hat{V} \right]^{-1} \\ &= \left[\hat{I} - \hat{g}\hat{V} \right]^{-1} \hat{g},\end{aligned} \tag{2.3.1}$$

where $\hat{\mathcal{H}}$ is the Hamiltonian and $\hat{g}$ is the retarded GF (though we could just as easily have used the advanced GF) of the pristine system. Multiplying from the left by $(\hat{I} - \hat{g}\hat{V})$ gives us the form

$$\hat{G} = \hat{g} + \hat{g}\hat{V}\hat{G}, \tag{2.3.2}$$

in which the Dyson equation is usually encountered. However, a form that collects all contributions from the perturbation into a single term is easier to use. Expanding the $\hat{G}$ term on the right hand side of the above equation gives

$$\begin{aligned}\hat{G} &= \hat{g} + \hat{g}\hat{V}\hat{g} + \hat{g}\hat{V}\hat{g}\hat{V}\hat{g} + \hat{g}\hat{V}\hat{g}\hat{V}\hat{g}\hat{V}\hat{g} + \dots \\ &= \hat{g} + \hat{g}\hat{V}\left[\hat{I} + \hat{g}\hat{V} + \hat{g}\hat{V}\hat{g}\hat{V} + \hat{g}\hat{V}\hat{g}\hat{V}\hat{g}\hat{V} + \dots\right]\hat{g} \\ &= \hat{g} + \hat{g}\hat{V}\left[\hat{I} - \hat{g}\hat{V}\right]^{-1}\hat{g}.\end{aligned} \tag{2.3.3}$$

This allows all the contributions arising from the perturbation to be collected in a single matrix, called the $\hat{T}$-matrix

$$\hat{T} = \hat{V}\left[\hat{I} - \hat{g}\hat{V}\right]^{-1}, \tag{2.3.4}$$

provided that the perturbation potential $\hat{V}$ affects a finite number of localized atomic orbitals $|\mathbf{j}\rangle$. In the case that $\hat{V}$ affects an infinite number of localized orbitals an exact solution of the T-matrix is not possible, and configurational averaging must be employed. The perturbed system can then be written simply as

$$\hat{G} = \hat{g} + \hat{g}\hat{T}\hat{g}. \tag{2.3.5}$$

The majority of perturbations introduced in this work will consist of either changes to onsite energy terms, to the hopping potentials connecting atomic orbitals in a lattice, or to both. These types of perturbations are sufficient to

work with a large class of impurities. A method will be demonstrated below for the cases of a single substitutional impurity and a single adsorbed impurity (adatom) attached to host, though these methods can be easily extended to multiple impurities.

2.3.1 *Substitutional Impurities*

The simplest type of impurity to model is a substitutional impurity, Fig. 2.1, which involves replacing an atom in our host system with an atom of another element. We model this type of impurity by changing the onsite energy term describing the relevant orbital at a particular site, since the energy orbital on the impurity atom will differ from that of the orbitals of the host. We may also need to modify the hopping parameters describing the overlap between the site and its neighbours, however, in the first approximation, we can neglect changes to the hopping parameters and consider only a single orbital on the impurity atom.

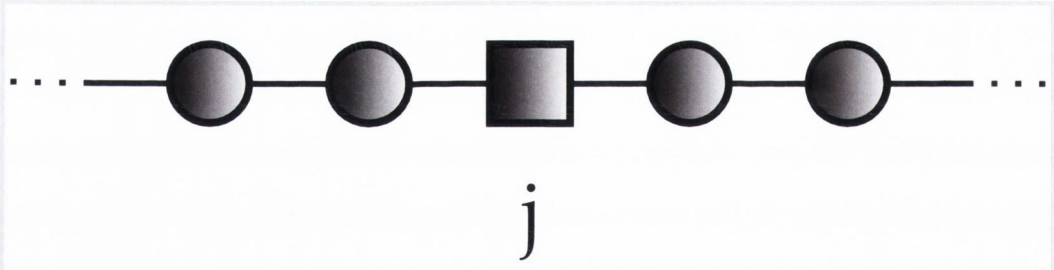


Figure 2.1: A schematic representation of a substitutional impurity (square), at a site **j**, in a one dimensional chain of atoms (circle).

The perturbing potential for such an impurity is

$$\hat{V} = |\mathbf{j}\rangle\lambda_{\mathbf{j}}\langle\mathbf{j}| = |\mathbf{j}\rangle(\varepsilon_A - \varepsilon_0)\langle\mathbf{j}|, \tag{2.3.6}$$

where ε_0 is the onsite energy for the host atoms, ε_A is that of the impurity atom, and $\mathbf{j}$ indexes the site of the impurity. In general we want to calculate some particular matrix element of the GF for our perturbed system, which we denote, $G_{\mathbf{r}\mathbf{r}'}$. To do this we apply the Dyson equation to the unperturbed GF, $\hat{g}$,

$$G_{\mathbf{r}\mathbf{r}'} = g_{\mathbf{r}\mathbf{r}'} + g_{\mathbf{r}\mathbf{j}}\lambda_{\mathbf{j}}G_{\mathbf{j}\mathbf{r}'}. \tag{2.3.7}$$

And then perform the same operation with the unknown GF $G_{\mathbf{j}\mathbf{r}'}$,

$$G_{\mathbf{j}\mathbf{r}'} = g_{\mathbf{j}\mathbf{r}'} + g_{\mathbf{j}\mathbf{j}}\lambda_{\mathbf{j}}G_{\mathbf{j}\mathbf{r}'} = \frac{g_{\mathbf{j}\mathbf{r}'}}{1 - g_{\mathbf{j}\mathbf{j}}\lambda_{\mathbf{j}}}. \tag{2.3.8}$$

Substituting this back into the Eq. 2.3.7 yields

$$G_{\mathbf{r}\mathbf{r}'} = g_{\mathbf{r}\mathbf{r}'} + \frac{g_{\mathbf{r}\mathbf{j}}\lambda_{\mathbf{j}}g_{\mathbf{j}\mathbf{r}'}}{1 - g_{\mathbf{j}\mathbf{j}}\lambda_{\mathbf{j}}}. \tag{2.3.9}$$

This form now allows us to extract our T-matrix element

$$T_{\mathbf{j}\mathbf{j}} = \frac{\lambda_{\mathbf{j}}}{1 - g_{\mathbf{j}\mathbf{j}}\lambda_{\mathbf{j}}}, \tag{2.3.10}$$

and write the GF of the perturbed system as

$$G_{\mathbf{r}\mathbf{r}'} = g_{\mathbf{r}\mathbf{r}'} + g_{\mathbf{r}\mathbf{j}}T_{\mathbf{j}\mathbf{j}}g_{\mathbf{j}\mathbf{r}'}. \tag{2.3.11}$$

This equation now describes the electron propagation between sites $\mathbf{r}$ and $\mathbf{r}'$ in the presence of an impurity at site j with onsite energy $\lambda_{\mathbf{j}}$, and can be thought of as the sum of electron propagation along two different paths. The first term, $g_{\mathbf{r}\mathbf{r}'}$, corresponds to the direct propagation of electrons between sites $\mathbf{r}$ and $\mathbf{r}'$. The second term, $g_{\mathbf{r}\mathbf{j}}T_{\mathbf{j}\mathbf{j}}g_{\mathbf{j}\mathbf{r}'}$, corresponds to the indirect propagation of the electrons - from site $\mathbf{r}$ to $\mathbf{j}$ and then from site $\mathbf{j}$ to $\mathbf{r}'$, where the scattering at this site introduces a factor $T_{\mathbf{j}\mathbf{j}}$.

From the previous section we know that the local density of states (LDOS) at some site $\mathbf{i}$ is defined as $-\frac{1}{\pi}\,\mathrm{Im}\,(g_{ii})$. This can be determined for the impurity site by setting $\mathbf{r} = \mathbf{r}' = \mathbf{j}$, and we can then write

$$\begin{aligned} G_{jj} &= g_{jj} + \frac{g_{jj}\lambda_j g_{jj}}{1 - g_{jj}\lambda_j}, \\ &= \frac{g_{jj}(1 - g_{jj}\lambda_j)}{1 - g_{jj}\lambda_j} + \frac{g_{jj}\lambda_j g_{jj}}{1 - g_{jj}\lambda_j}, \\ &= \frac{g_{jj}}{1 - g_{jj}\lambda_j}. \end{aligned} \tag{2.3.12}$$

So that the LDOS can be simply defined in terms of the diagonal GFs element of the pristine system, and the onsite energy of the impurity,

$$\rho_j(E) = -\frac{1}{\pi}\,\mathrm{Im}\left(\frac{g_{jj}}{1 - g_{jj}\lambda_j}\right). \tag{2.3.13}$$

And the LDOS for some site, $\mathbf{i}$, away from the site of the impurity, $\mathbf{j}$, is just

$$\rho_i(E) = -\frac{1}{\pi}\,\mathrm{Im}\left(g_{ii} + \frac{g_{ij}\lambda_j g_{ji}}{1 - g_{jj}\lambda_j}\right). \tag{2.3.14}$$

2.3.2 *Adsorbed Impurities*

An adsorbed impurity or adatom, Fig. 2.2, occurs when an impurity bonds to one or more atoms in a host system. We will initially consider only a single impurity, $\mathbf{A}$, with a single atomic orbital, that connects only to a single site in the host lattice, $\mathbf{j}$. We will again consider a pristine GF matrix, $\hat{g}$. The GF of the isolated impurity is given by g_{AA}, and may be derived from the definition of GF, Eq. 2.1.2, where we consider the Hamiltonian to simply contain the onsite energy of the impurity, ϵ_A

$$g_{AA} = \frac{1}{E - \epsilon_A}. \tag{2.3.15}$$

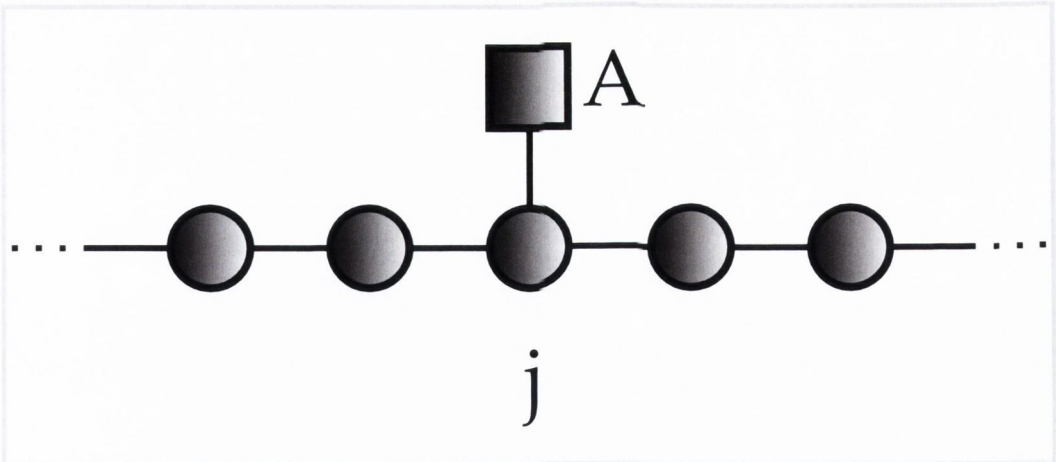


Figure 2.2: A schematic representation of an adsorbed impurity, A (square), connected at a site **j**, in a one dimensional chain of atoms (circle).

This type of impurity is fundamentally different to the substitutional case, where we were "modifying" an existing atom, in that we are now connecting two parts of the system which were previously separate. Our system contains two isolated components, the pristine host and the impurity, the GFs of which we will denote $\hat{g}_s$ and $g_{\mathbf{AA}}$ respectively. We are no longer modifying an on-site energy, but are instead using the Dyson equation to change the hopping between the impurity and the host from zero to a quantity we will call τ. The perturbation to add such an impurity is

$$V = |\mathbf{j}\rangle\tau_{\mathbf{jA}}\langle\mathbf{A}| + |\mathbf{A}\rangle\tau_{\mathbf{Aj}}\langle\mathbf{j}|, \tag{2.3.16}$$

which defines a hopping integral connecting the impurity, **A**, and host lattice site **j**, and where we assume that $\tau_{\mathbf{jA}} = \tau_{\mathbf{Aj}}$ for hermiticity.

The GF which describes the complete (disconnected) system can be written as

$$\hat{g} = \begin{pmatrix} g_{\mathbf{AA}} & 0 \\ 0 & \hat{g}_s \end{pmatrix}. \tag{2.3.17}$$

However, it may be best to illustrate the matrices in an expanded form, and though it is usually too cumbersome to do, it is useful here:

$$\hat{g} = \begin{pmatrix} g_{AA} & 0 & \cdots & 0 & \cdots & 0 \\ 0 & g_{11} & \cdots & g_{1j} & \cdots & g_{1N} \\ \vdots & \vdots & \ddots & \vdots & \ddots & \vdots \\ 0 & g_{j1} & \cdots & g_{jj} & \cdots & g_{jN} \\ \vdots & \vdots & \ddots & \vdots & \ddots & \vdots \\ 0 & g_{N1} & \cdots & g_{Nj} & \cdots & g_{NN} \end{pmatrix}. \tag{2.3.18}$$

Here **N** is the number of sites in the system. The perturbation matrix is of the form

$$\hat{V} = \begin{pmatrix} 0 & \cdots & 0 & \tau_{jA} & 0 & \cdots \\ \vdots & 0 & \cdots & 0 & \cdots & 0 \\ 0 & \vdots & \ddots & \vdots & \ddots & \vdots \\ \tau_{Aj} & 0 & \cdots & 0 & \cdots & 0 \\ 0 & \vdots & \ddots & \vdots & \ddots & \vdots \\ \vdots & 0 & \cdots & 0 & \cdots & 0 \end{pmatrix}. \tag{2.3.19}$$

If we are only concerned with the impurity and connecting site then we can treat this as a 2x2 matrix. This can be done more formally by rearranging the matrices above and separating them into block matrices. Starting with the

definition of Dyson's equation we introduce 2x2 versions of $\hat{V}$ and $\hat{g}$ so that we have

$$\begin{aligned}
\hat{G} &= \left[\begin{pmatrix} 1 & 0 \\ 0 & 1 \end{pmatrix} - \begin{pmatrix} g_{AA} & 0 \\ 0 & g_{jj} \end{pmatrix}\begin{pmatrix} 0 & \tau_{Aj} \\ \tau_{jA} & 0 \end{pmatrix}\right]^{-1}\begin{pmatrix} g_{AA} & 0 \\ 0 & g_{jj} \end{pmatrix} \\
&= \left[\begin{pmatrix} 1 & -\tau_{Aj}g_{AA} \\ -\tau_{jA}g_{jj} & 1 \end{pmatrix}\right]^{-1}\begin{pmatrix} g_{AA} & 0 \\ 0 & g_{jj} \end{pmatrix} \\
&= \frac{1}{1-\tau_{Aj}{}^2 g_{AA}g_{jj}}\begin{pmatrix} 1 & \tau_{Aj}g_{AA} \\ \tau_A g_{jj} & 1 \end{pmatrix}\begin{pmatrix} g_{AA} & 0 \\ 0 & g_{jj} \end{pmatrix} \\
&= \frac{1}{1-\tau_{Aj}{}^2 g_{AA}g_{jj}}\begin{pmatrix} g_{AA} & \tau_{Aj}g_{AA}g_{jj} \\ \tau_A g_{AA}g_{jj} & g_{jj} \end{pmatrix}.
\end{aligned} \tag{2.3.20}$$

From this we can get the modified diagonal GFs for the elements A and j, and the off-diagonal GF connecting them, namely

$$G_{AA} = \frac{g_{AA}}{1-\tau_{Aj}{}^2 g_{AA}g_{jj}}, \quad G_{jj} = \frac{g_{jj}}{1-\tau_{Aj}{}^2 g_{AA}g_{jj}}, \quad G_{Aj} = \frac{\tau_{Aj}{}^2 g_{AA}g_{jj}}{1-\tau_{Aj}{}^2 g_{AA}g_{jj}}. \tag{2.3.21}$$

To find the modified GF between any two sites we must use a more general method. Starting with the concise form of the Dyson equation, Eq. 2.3.2,

$$G_{\mathbf{r}\mathbf{r}'} = g_{\mathbf{r}\mathbf{r}'} + g_{\mathbf{r}j}\tau_{j\mathbf{A}}G_{\mathbf{A}\mathbf{r}'} + g_{\mathbf{r}\mathbf{A}}\tau_{\mathbf{A}j}G_{j\mathbf{r}'}, \tag{2.3.22}$$

we note two things. Firstly, that if $\mathbf{r} = \mathbf{A}$ then the second term must necessarily be zero, since in the initial system the impurity is disconnected, *i.e.*, $g_{\mathbf{A}j} = 0$. And secondly, that if $\mathbf{r} \neq \mathbf{A}$ then the third term must be zero since $g_{\mathbf{r}\mathbf{A}} = 0$

in the disconnected system. So for two general sites in the lattice $\mathbf{r}$ and $\mathbf{r}'$ we have

$$G_{\mathbf{r}\mathbf{r}'} = g_{\mathbf{r}\mathbf{r}'} + g_{\mathbf{r}\mathbf{j}}\tau_{\mathbf{j}A}G_{\mathbf{A}\mathbf{r}'}. \tag{2.3.23}$$

We continue calculating the new unknown modified GF that occurs at the end of each term until we arrive at one we have previously calculated and then can insert it back into our original equation

$$\begin{aligned} G_{\mathbf{A}\mathbf{r}'} &= \overbrace{g_{\mathbf{A}\mathbf{r}'}}^{=0} + g_{\mathbf{A}\mathbf{A}}\tau_{\mathbf{A}\mathbf{j}}G_{\mathbf{j}\mathbf{r}'}, \\ G_{\mathbf{j}\mathbf{r}'} &= g_{\mathbf{j}\mathbf{r}'} + g_{\mathbf{j}\mathbf{j}}\tau_{\mathbf{j}A}G_{\mathbf{A}\mathbf{r}'}. \end{aligned} \tag{2.3.24}$$

Here we are essentially just generating equations for unknown GFs until we have as many unique equations as unknowns. We can now combine and rearrange these two equations and then insert them into Eq. 2.3.23 to arrive at the form for the modified GF between two sites in the lattice in the presence of an adsorbed impurity connected to site $\mathbf{j}$,

$$G_{\mathbf{r}\mathbf{r}'} = g_{\mathbf{r}\mathbf{r}'} + \frac{g_{\mathbf{r}\mathbf{j}}\tau_{\mathbf{j}A}g_{\mathbf{A}\mathbf{A}}\tau_{\mathbf{A}\mathbf{j}}g_{\mathbf{j}\mathbf{r}'}}{1 - g_{\mathbf{A}\mathbf{A}}\tau_{\mathbf{A}\mathbf{j}}g_{\mathbf{j}\mathbf{j}}\tau_{\mathbf{j}A}} = g_{\mathbf{r}\mathbf{r}'} + \frac{\tau_{\mathbf{A}\mathbf{j}}{}^2 g_{\mathbf{r}\mathbf{j}}g_{\mathbf{A}\mathbf{A}}g_{\mathbf{j}\mathbf{r}'}}{1 - \tau_{\mathbf{A}\mathbf{j}}{}^2 g_{\mathbf{A}\mathbf{A}}g_{\mathbf{j}\mathbf{j}}}. \tag{2.3.25}$$

2.4 THE LLOYD FORMULA METHOD

Many of the calculations we will wish to perform involve calculating the change in energy of a system due to a perturbation, be this the addition of impurities, the rotation of an impurity's magnetic moment, or some other perturbation. The total change in energy of a system is given by,

$$\Delta E = E - E_0, \tag{2.4.1}$$

where E is the energy of the perturbed system, and E_0 is the energy of the pristine system. For a large, or infinite, system the energy difference would be extremely small for perturbations that affect only a few atomic orbitals. It is therefore difficult to directly evaluate the energies E and E_0. The Lloyd Formula [160] gives an expression for the total change in energy without requiring the total energy of either system to be calculated.

The total change in energy may be expressed in terms of changes in the density of states as

$$\Delta E(E_F) = \int_{-\infty}^{E_F} dE\ E\ (\rho(E) - \rho_0(E))\,. \tag{2.4.2}$$

The density of states is related to GFs as seen in Eq. 2.2.8, so we can therefore rewrite this equation as

$$\begin{aligned} \Delta E(E_F) &= -\frac{1}{\pi}\mathrm{Im} \int_{-\infty}^{E_F} dE\ E\ \sum_{\mathbf{r}} (G_{\mathbf{rr}}(E) - g_{\mathbf{rr}}(E))\,, \\ &= -\frac{1}{\pi}\mathrm{Im} \int_{-\infty}^{E_F} dE\ E\ \mathrm{Tr}\ \left(\hat{G}(E) - \hat{g}(E)\right), \end{aligned} \tag{2.4.3}$$

where the change in energy of a system is now directly related to the difference between the perturbed GF and the unperturbed GF. We wish to simplify the term inside the trace. To do this we rewrite the Dyson Equation, Eq. 2.3.5, as

$$\hat{G}(E) - \hat{g}(E) = \hat{g}\hat{T}\hat{g}. \tag{2.4.4}$$

It is then clear that

$$\mathrm{Tr}\ \left(\hat{G}(E) - \hat{g}(E)\right) = \mathrm{Tr}\ \left(\hat{g}\hat{T}\hat{g}\right), \tag{2.4.5}$$

and we may use the cyclical properties of the trace operator ($\mathrm{Tr}\,[\hat{X}\hat{Y}\hat{Z}] = \mathrm{Tr}\,[\hat{Z}\hat{X}\hat{Y}]$) to write

$$\mathrm{Tr}\,\left(\hat{G}(E) - \hat{g}(E)\right) = \mathrm{Tr}\,\left(\hat{g}^2\hat{T}\right). \tag{2.4.6}$$

Writing this in a more useful manner requires a little bit of work. Firstly, looking at our definition of the GF, Eq. 2.1.2, and taking the derivative with respect to energy we find that

$$\frac{d}{dE}\hat{g} = \frac{d}{dE}\left(E\hat{I} - \hat{H}\right)^{-1} = -\left(E\hat{I} - \hat{H}\right)^{-2} = -\hat{g}^2. \tag{2.4.7}$$

We can therefore replace $\hat{g}^2$ with $-\frac{d}{dE}\hat{g} \equiv -\hat{g}'$, so that we now have

$$\mathrm{Tr}\,\left(\hat{G}(E) - \hat{g}\,(E)\right) = -\mathrm{Tr}\,\left(\hat{g}'\hat{T}\right). \tag{2.4.8}$$

Using the definition of the $\hat{T}$-matrix we can expand this as

$$\mathrm{Tr}\,\left(\hat{G}(E) - \hat{g}(E)\right) = \mathrm{Tr}\,\left[-\hat{g}'\hat{V}\left(\hat{I} - \hat{g}\hat{V}\right)^{-1}\right]. \tag{2.4.9}$$

Further noting that

$$-\hat{g}'\hat{V} = \frac{d}{dE}\left(\hat{I} - \hat{g}\hat{V}\right) = \left(\hat{I} - \hat{g}\hat{V}\right)', \tag{2.4.10}$$

we may now write

$$\mathrm{Tr}\,\left(\hat{G}(E) - \hat{g}(E)\right) = \mathrm{Tr}\,\left[\left(\hat{I} - \hat{g}\hat{V}\right)'\left(\hat{I} - \hat{g}\hat{V}\right)^{-1}\right]. \tag{2.4.11}$$

We can now use another property of the trace operator, namely that $\mathrm{Tr}\,\left[\hat{X}'\,\hat{X}^{-1}\right] = \left(\mathrm{Tr}\,\left[\ln\hat{X}\right]\right)'$, to write

$$\mathrm{Tr}\,\left(\hat{G}(E) - \hat{g}(E)\right) = \frac{d}{dE}\,\mathrm{Tr}\,\left[\ln\left(\hat{I} - \hat{g}\hat{V}\right)\right]. \tag{2.4.12}$$

This now allows us to write our change in energy equation as

$$\Delta E\,(E_F) = -\frac{1}{\pi}\mathrm{Im}\int_{-\infty}^{E_F} dE\; E\;\frac{d}{dE}\;\ln\det\left(\hat{I}-\hat{g}\hat{V}\right), \tag{2.4.13}$$

where we have used the identity $\mathrm{Tr}\left[\ln\hat{X}\right] = \ln\det\hat{X}$. Finally, integrating by parts yields

$$\begin{aligned}\Delta E\,(E_F) = &-\frac{1}{\pi}\,E_F\,\mathrm{Im}\;\ln\det\left(\hat{I}-\hat{g}\hat{V}\right)\Big|_{E_F}\\ &+\frac{1}{\pi}\,\mathrm{Im}\int_{-\infty}^{E_F} dE\;\ln\det\left(\hat{I}-\hat{g}\hat{V}\right).\end{aligned} \tag{2.4.14}$$

To understand the first term we must look at the relationship between the DOS and GF given by Eq. 2.2.8. From this we can write the change in DOS as

$$\Delta\rho(E) = -\frac{1}{\pi}\mathrm{Im}\;\left(\hat{G}-\hat{g}\right), \tag{2.4.15}$$

and using the definition given above expand this as

$$\Delta\rho(E) = -\frac{1}{\pi}\mathrm{Im}\;\frac{d}{dE}\ln\det\left(\hat{I}-\hat{g}\hat{V}\right). \tag{2.4.16}$$

Now we note that the change in the occupation number, ΔN is defined as

$$\begin{aligned}\Delta N(E_F) &= \int_{-\infty}^{E_F} dE\;\Delta\rho(E),\\ &= -\frac{1}{\pi}\mathrm{Im}\;\frac{d}{dE}\ln\det\left(\hat{I}-\hat{g}\hat{V}\right)\Big|_{E_F}.\end{aligned} \tag{2.4.17}$$

This is almost exactly the first term of Eq. 2.4.14, which can now be simplified to

$$\Delta E(E_F) = E_F\, \Delta N(E_F) + \frac{1}{\pi}\mathrm{Im} \int_{-\infty}^{E_F} dE\ \ln\det\left(\hat{I} - \hat{g}\hat{V}\right). \tag{2.4.18}$$

Since no change in the total charge should occur by joining two systems we would expect that $\Delta N(E_F) = 0$. However, it may be necessary to allow a small nonphysical change in the Fermi Energy.

So, the final expression for the change in energy of a system, $\hat{g}$, due to a perturbation, $\hat{V}$, is

$$\Delta E(E_F) = \frac{1}{\pi}\mathrm{Im} \int_{-\infty}^{E_F} dE\ \ln\det\left(\hat{I} - \hat{g}\hat{V}\right). \tag{2.4.19}$$

This equation now allows us to directly calculate the change in energy of a system due to a perturbation, without the need to calculate the total energy of either system. This feature can be especially useful when dealing with small changes in energy relative to the energy of the system.

2.5 STATIONARY PHASE APPROXIMATION

The Stationary Phase Approximation (SPA) [161] is a method of describing the limiting behaviour of oscillatory integrals. Its main idea relies on the cancellation of sinusoids with rapidly varying phases. If the phases of these sinusoids are the same they will add together constructively, however if these phases vary rapidly as the frequency changes they will add together constructively and deconstructively at different times, in an overall incoherent manner. Only those regions where the phases add together coherently will therefore contribute to the integral.

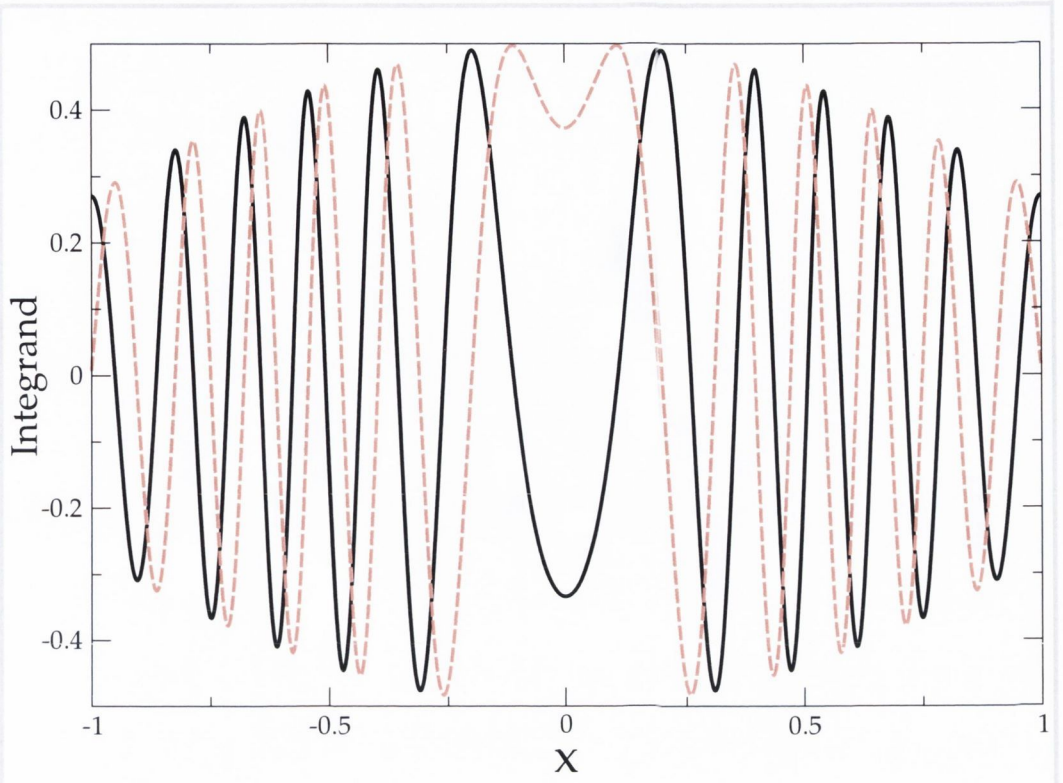


Figure 2.3: A plot of the real (black) and imaginary (red) parts of the integrand of Eq. 2.5.9, which satisfies the form of Eq. 2.5.1 necessary to perform the Stationary Phase Approximation. With a stationary point observed at $x = 0$.

To illustrate this, consider an integral of the form

$$I(y) = \int dx\, F(x)\, e^{iy\phi(x)}, \tag{2.5.1}$$

where ϕ is a rapidly-varying function of x, and F is slowly-varying function of x, relative to ϕ. We also require that these are smooth functions, that is to say differentiable at all orders. For large positive values of y the exponential term will be highly oscillatory. Figure 2.3 shows an example integrand of an equation satisfying the form of Eq. 2.5.1, for a moderate value of y. This oscillation around the x-axis for large sections of the integrand will cause the integration over x to mostly cancel out. Only those regions of x where the phase is stationary will have coherently adding phases, and it is thus only

these regions which contribute to the integral. It is from this region that the approximation gets its name.

The method of calculating the approximation is quite straightforward. The phase term is replaced with a Taylor expansion around some points x_j as

$$\phi(x) \approx \sum_j \left(\phi(x_j) + \left.\frac{d\phi}{dx}\right|_{x_j} (x - x_j) + \frac{1}{2}\left.\frac{d^2\phi}{dx^2}\right|_{x_j} (x - x_j)^2 + \dots \right). \tag{2.5.2}$$

We then require that these points, x_j, correspond to the stationary points. To do this we impose

$$\left.\frac{d\phi}{dx}\right|_{x_j} = 0, \tag{2.5.3}$$

thus simplifying the approximation of the phase term, which we now truncate to second order, giving

$$\begin{aligned} \phi(x) &\approx \sum_j \left(\phi(x_j) + \frac{1}{2}\left.\frac{d^2\phi}{dx^2}\right|_{x_j} (x - x_j)^2 \right) \\ &\approx \sum_j \left(\phi(x_j) + \frac{1}{2}\phi''(x_j)(x - x_j)^2 \right). \end{aligned} \tag{2.5.4}$$

Although there may be any number of stationary points we will consider for a moment just a single stationary point, x_0. Replacing the integrand in Eq. 2.5.1 with a Taylor expansion around the stationary point therefore gives

$$\begin{aligned} I(y)_{x_0} &= \int dx\, F(x_0)\; e^{iy\left(\phi(x_0) + \frac{1}{2}\phi''(x_0)(x - x_0)^2\right)} \\ &= F(x_0)\, e^{iy\phi(x_0)} \int dx\, e^{iy\frac{1}{2}\phi''(x_0)(x - x_0)^2}, \end{aligned} \tag{2.5.5}$$

where we have assumed the function $F(x)$ varies slowly around the stationary point. The remaining integral may by solved using the well known Gaussian integral identity

$$\int_{-\infty}^{+\infty} dx\, e^{-ix^2} = \sqrt{\pi}. \tag{2.5.6}$$

This therefore gives the contribution from a single stationary point to the integral as

$$I(y)_{x_0} = F(x_0)\, e^{iy\phi(x_0)} \sqrt{\frac{2i\pi}{\phi''(x_0)\, y}}. \tag{2.5.7}$$

To calculate the overall contribution from all stationary points we must sum over the stationary points as

$$I(y) \approx \sum_j I(y)_{x_j}. \tag{2.5.8}$$

By way of example we will now apply the SPA to the integral

$$I(y) = \int_{-1}^{+1} dx\, \frac{\cos(x)}{2} e^{iy(\cos^3(x))}, \tag{2.5.9}$$

where the integrand has been plotted as a function of x in Fig. 2.3. We have the phase term and its derivatives

$$\begin{aligned} \phi(x) &= \cos^3(x), \\ \phi'(x) &= -3\sin(x)\cos^2(x), \\ \phi''(x) &= -\frac{3}{4}(\cos(x) + 3\cos(3x)), \end{aligned} \tag{2.5.10}$$

and the remaining function is

$$F(x) = \frac{\cos(x)}{2}. \tag{2.5.11}$$

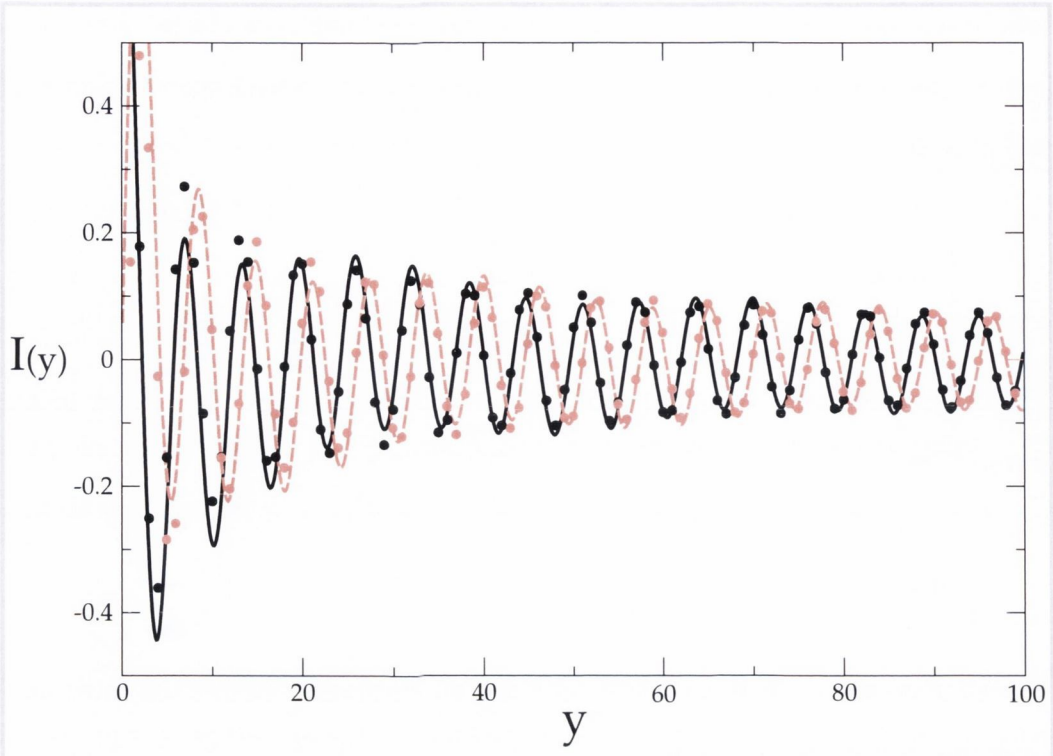


Figure 2.4: A comparison of the numerically integrated function Eq. 2.5.9 (lines) against the Stationary Phase Approximation given by Eq. 2.5.12 (dots). These are both plotted against the variable y for both the real (black) and imaginary (red) parts.

Setting $\phi'(x) = 0$ we find the stationary points $x_0 = n\pi, n\pi - \frac{\pi}{2}$ where $n \in \mathbb{Z}$. Since our integral is confined to a region near the origin we may restrict ourselves to using the single stationary point at $x_0 = 0$. We can now write the resulting SPA to this integral as

$$\begin{aligned} I(y)_{x_0} &= \frac{\cos(x_0)}{2} e^{i\cos^3(x_0)y} \sqrt{\frac{2i\pi}{y\left(-\frac{3}{4}(\cos(x_0) + 3\cos(3x_0))\right)}} \\ &= \frac{1}{2} e^{iy} \sqrt{\frac{2i\pi}{-3y}}. \end{aligned} \tag{2.5.12}$$

Figure 2.4 shows a plot of the SPA to the integral in Eq. 2.5.12 against the numerically evaluated integral, Eq. 2.5.9, as a function of y. When y is close to zero the SPA is in poor agreement with the numerically calculated values. However, as y increases the match improves until it is seen to be essentially

identical. The value of y at which the match becomes good will depend on the function and on the acceptable error.

In later chapters we will be using this approximation repeatedly to write GFs in analytic forms. However, there are many conditions that need to be met in order for this approximation to hold. These will be addressed as we come to them.

2.6 ENERGY INTEGRALS OF GREEN'S FUNCTIONS

Throughout this work we are confronted with numerous energy integrations of GFs. This can be troublesome, as the integrands frequently contain singularities. However, the difficulties in the integrands may be avoided by converting an integral over the real axis to one over the imaginary axis.

Typically we have integrals of the form

$$\int_{-\infty}^{E_F} dE\, G^N(E_F + i\eta), \tag{2.6.1}$$

where N is some integer power and we have shifted the poles of the GF off the real axis by an amount η. The value of N will depend on exactly what is being calculated and will be discussed at the end. This form is reasonably general provided $G \sim \frac{1}{E+i\eta}$, which is the case for all GFs used in this thesis.

Since retarded GFs are analytical in the upper half of the complex plane we may use contour integration to evaluate our integral. First by using the fact that a closed integral loop containing no poles sums to zero (Cauchy's Theorem),

$$\lim_{R\to\infty} \int_{-R}^{E_F} dE\, G^N(E + i\eta) + \int_{\eta}^{R} dy\, G^N(E_F + iy) + \int_{C} dz\, G^N(z) = 0. \tag{2.6.2}$$

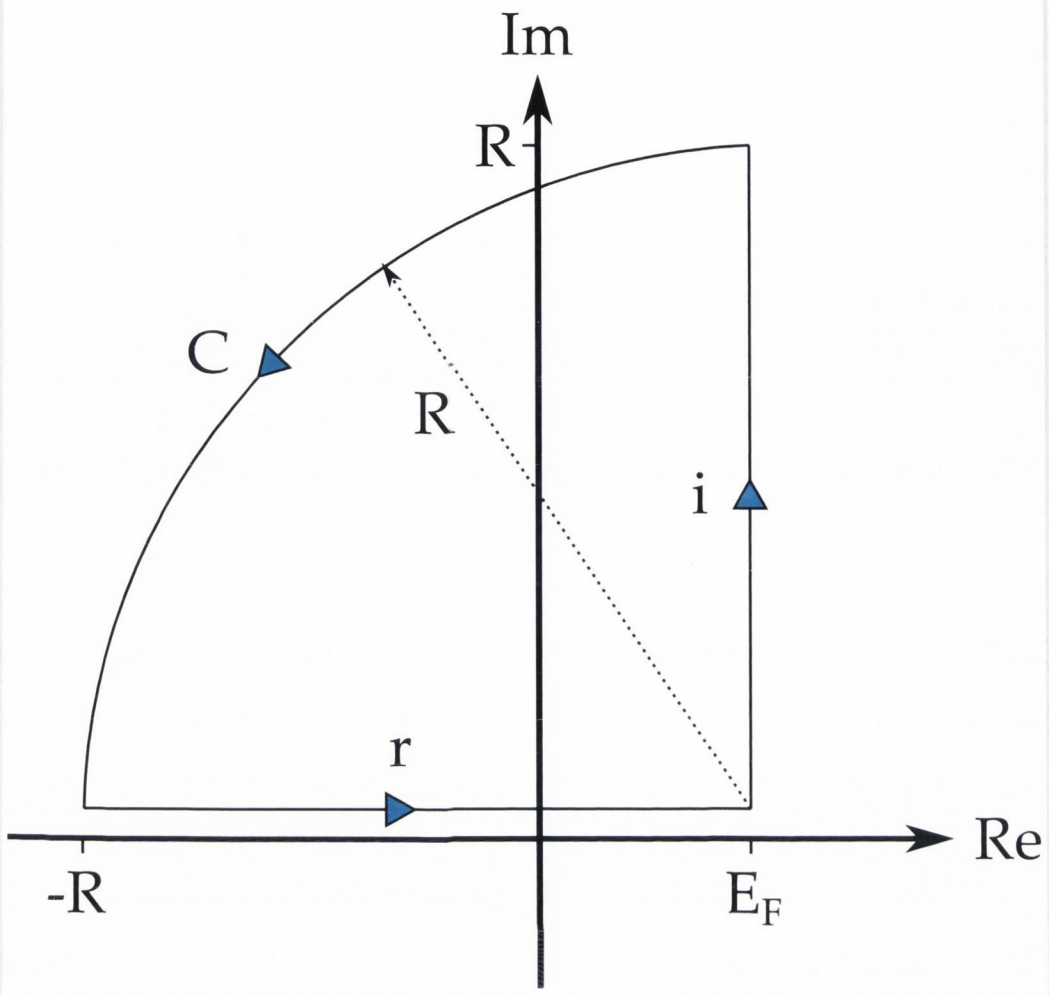


Figure 2.5: A closed contour with its three component parts: r, i, and C. Here r is the integral along the real axis (Re) from $-R$ to E_F, i is the integral along the imaginary axis (Im) from 0 to R, and C is the $\frac{\pi}{2}$ arc from R on the imaginary axis to $-R$ on the real axis. For each integral the direction of integration is indicated by the blue triangle.

This equation is shown diagrammatically in Fig. 2.5, where the first term, r, is the line perpendicular to the real axis extending from $-R$ to the Fermi energy, E_F, the second term, i, is the line perpendicular to the imaginary axis extending from η to R, and the third term is the curved line labelled C. It is the third term, the integral over the arc C, that we wish to focus our attention

on. We first treat the variable as a generic complex variable $z = E + i\eta$, so that our integral becomes

$$\lim_{R\to\infty} \int_C dz\, G^N(z) \sim \lim_{R\to\infty} \int_C dz\, \frac{1}{z^N}. \tag{2.6.3}$$

Converting this to polar coordinates $z = Re^{i\theta}$, where R is a constant, gives

$$\begin{aligned}
\lim_{R\to\infty} \int_C dz\, \frac{1}{z^N} &= \lim_{R\to\infty} \int_{\frac{\pi}{2}}^{\pi} d\theta\, iRe^{i\theta} \frac{1}{R^N e^{iN\theta}} \\
&= \lim_{R\to\infty} \int_{\frac{\pi}{2}}^{\pi} d\theta\, i \frac{1}{R^{N-1} e^{i(N-1)\theta}} \\
&= \lim_{R\to\infty} \frac{i}{R^{N-1}} \int_{\frac{\pi}{2}}^{\pi} d\theta\, \frac{1}{e^{i(N-1)\theta}} \\
&= \lim_{R\to\infty} \frac{i}{R^{N-1}}\, I_\theta(N)\,,
\end{aligned} \tag{2.6.4}$$

where $I_\theta(N)$ is the evaluated integral over θ for a given N. In the case $N = 1$ the function becomes $\frac{i\pi}{2}$, in the cases $N \geqslant 2$ it vanishes as $R \to \infty$. So provided our integrand is the product of 2 or more GFs we can consider this term to vanish, leaving us with precisely

$$\int_{-\infty}^{E_F} dE\, G^N(E + i\eta) = -\int_{\eta}^{\infty} dy\, G^N(E_F + iy)\,. \tag{2.6.5}$$

The majority of the integrals dealt with in this thesis are of a slightly more complicated form than this, but a similar method applies. When the original integral is of the form

$$\int_{-\infty}^{E} dE\, \ln\left[1 + sG^2(E + i\eta)\right], \tag{2.6.6}$$

and s is just some finite constant, we can apply a similar method as above,

$$\begin{aligned}\lim_{R\to\infty}\int_C dz\ \ln\left[1+\frac{s}{z^2}\right] &= \lim_{R\to\infty}\int_{\frac{\pi}{2}}^{\pi} d\theta\ Re^{i\theta}\ln\left[1+\frac{s}{R^2e^{i2\theta}}\right]\\ &\sim \lim_{R\to\infty}\int_{\frac{\pi}{2}}^{\pi} d\theta\ Re^{i\theta}\frac{s}{R^2e^{i2\theta}}\\ &\sim \lim_{R\to\infty}\frac{s}{R}\,I_\theta(2)\\ &\sim 0.\end{aligned} \tag{2.6.7}$$

Which now allows us to write the integral over the imaginary axis as

$$\int_{-\infty}^{E} dE\ \ln\left[1+sG^2(E+i\eta)\right] = \int_{\eta}^{\infty} dy\ \ln\left[1+sG^2(E+iy)\right]. \tag{2.6.8}$$

2.7 TIGHT-BINDING MODEL

Throughout this work we will be employing the tight-binding model to describe our systems. Specifically we will be employing the nearest-neighbour tight-binding (NNTB) approximation. This approximation simplifies a system by restricting the description of its Hamiltonian to the onsite energy of each atom, and the electron hopping probabilities to neighbouring sites. This model can be extended to include second-nearest neighbours, third-nearest neighbours and so on, usually with diminishing returns, and at the expense of mathematical transparency. How good of an approximation this is will be discussed in the next chapter when we discuss our specific systems.

A typical NNTB Hamiltonian is of the form

$$\hat{\mathcal{H}} = \sum_{\mathbf{r}} |\mathbf{r}\rangle\, \epsilon_{\mathbf{r}} \langle \mathbf{r}| + \sum_{\mathbf{r},\mathbf{r}'} |\mathbf{r}\rangle\, t_{\mathbf{r}\mathbf{r}'} \langle \mathbf{r}'|. \tag{2.7.1}$$

Here $|\mathbf{r}\rangle$ represents an atomic orbital at a lattice site $\mathbf{r}$, $\epsilon_{\mathbf{r}}$ represents its onsite energy, and $t_{\mathbf{r}\mathbf{r}'}$ represents the hopping integral between orbitals on sites $\mathbf{r}$ and $\mathbf{r}'$. The essence of the NNTB model is that $t_{\mathbf{r}\mathbf{r}'} \neq 0$ if sites $\mathbf{r}$ and $\mathbf{r}'$ are immediate neighbours, and $t_{\mathbf{r}\mathbf{r}'} = 0$ for all other pairs of sites. From this the band structure of the system may be found by calculating the eigenvalue solutions of the Schrödinger equation. For small systems this can be done using a matrix whose dimension is equal to the number of orbitals in the system. For larger systems we can make use of periodicity within the system. If this larger system can by generated by the translation, under a set of vectors, of a finite unit cell then we can express the problem in an easier form. This is the method that we use later in this work, and will be described in more depth in section 3.1.1.

2.8 SUMMARY OF CHAPTER

We have now covered most of the mathematical methods that we will require to introduce impurities in low dimensional carbon systems, and examine the energy changes of those systems. We began by introducing the Green's function, and defining its relationship to the density of states in Secs. 2.1 and 2.2. We then highlighted the advantages of Green's function methods for describing perturbed systems using the Dyson equation in Sec. 2.3, and examined the specific cases of substitutional and adsorbed impurities as perturbations in its subsections. Section 2.4 then provides a description for calculating the modification of various properties of a system in the presence of perturbation using the Lloyd formula. We finished our methods chapter with three brief sections, Secs. 2.5, 2.6, and 2.7, which respectively introduced a method to approximate Green's functions, a method for integrating over the general form of Green's function that we will encounter in later sections, and briefly

introduced the concept of the Tight-Binding method which will be elaborated in Chap. 3 for our particular system. In the cases of some minor methods they will be introduced as needed in later chapters.

In the next chapter we will talk more specifically about the low dimensional carbon systems that we will be working with for the rest of this thesis: graphene and carbon nanotubes. We will introduce the Hamiltonians for these systems, derive the Green's functions describing them, and calculate their electronic structures.

3

GRAPHENE-RELATED MATERIALS AND IMPURITIES

As previously mentioned in the introduction, graphene is in the scientific limelight due to its numerous possible applications in such fields as photonics, sensor technology, and spintronics [35, 162, 163]. Spintronics attempts to exploit the charge and spin degrees of freedom of electrons in order to develop the next generation of nanoscale devices. Graphene's weak spin-orbit and hyperfine interactions, which are the main sources of spin-relaxation and decoherence in other materials, make spintronic applications particularly attractive. Nanotubes display uniquely sensitive and tunable electronic properties which, along with increased interest in using the properties of low-dimensional systems, have lead them to be studied extensively for their uses in future electronic devices.

This chapter will introduce the two main systems to be used throughout this work, namely graphene (Sec. 3.1) and nanotubes (Sec. 3.2). In the case of graphene we will start from the nearest neighbour tight-binding model (Sec. 3.1.1), use this to derive the electronic structure (Sec. 3.1.2), and then further derive the Green's functions (Sec. 3.1.3). The precise form of these Green's functions is of central importance to this work and so this will be shown in quite some detail. Despite the simplicity with which the electronic structure of graphene can be described there exists no analytic form for the GF that is valid across the entire energy spectrum. To address this, we will show how the graphene Green's function can be written as a single integral using contour integration, and, under some conditions, may be written in an analytic form using the Stationary Phase Approximation (Sec. 3.1.4). It is this analytic form of the graphene Green's function that allows us to directly

examine some of the properties of interactions in magnetic impurities in later chapters. We use this analytic form because, as much as possible, we wish to maintain mathematical transparency. The Linear Dispersion regime, which approximates the band structure of graphene in a linear fashion around the Fermi energy, is used in other works to analytically examine the features of graphene. However, this approach is only valid in a small region around the Fermi energy. On the other hand, the Stationary Phase Approximation provides an excellent approximation to the Green's function throughout the entire energy band while maintaining mathematical transparency.

In the case of carbon nanotubes we will first examine the electronic structure (Sec. 3.2.1) before using the zone folding approximation to derive the Green's functions of two particular highly symmetric nanotubes that play an important role in later chapters (Sec. 3.2.2). The zone folding approximation allows us to consider nanotubes to be rolled up graphene sheets, so that we may work directly from graphene Green's function. However, the Green's functions for nanotubes contain only a single integral, which may be solved using contour integration, so that the Stationary Phase Approximation need not be applied in order to obtain an analytic form.

Green's functions are also very useful in examining the analytic properties of other graphene related materials (Sec. 3.3). We will briefly discuss particular examples of how Green's functions may be derived in semi-infinite graphene (Sec. 3.3.1), and nanoribbons (Sec. 3.3.2). Semi-infinite graphene is the name given to a sheet of graphene containing an edge, usually an edge along one of the high-symmetry directions, but continuing infinitely in all other directions, and graphene nanoribbons are a 1D strip of graphene containing two such edges, parallel to each other at a fixed distance. These will not be derived or examined in much detail, as we only wish to highlight the usefulness of Green's functions in graphene related materials, and these systems will not feature elsewhere in this work.

Finally, we will elaborate on the concept of impurities (Sec. 3.4), which were introduced briefly in Sec. 2.3, and how they conform to graphene and nanotubes (Sec. 3.4.1), before expanding our model Hamiltonian to allow the inclusion of magnetic impurities (Sec. 3.4.2). This is a necessary step to allow us to calculate the Indirect Exchange Coupling in Chap. 4.

3.1 ELECTRONIC STRUCTURE OF GRAPHENE

Graphene consists of a periodic two dimensional sheet of carbon atoms which may be sufficiently isolated from its environment to be considered free-standing. The carbon atoms are arranged in a hexagonal (honeycomb) lattice which is normally treated as a triangular Bravais lattice with a two atom unit cell. Each carbon atom in the lattice has three σ-bonds and a single π-bond. These σ-bonds form from the hybridisation of the $2p_x$, $2p_y$, and $2s$ orbitals of individual carbon atoms. This hybridization leads to a robust, hexagonal, planar lattice structure. The single π-bond forms from the remaining $2p_z$ orbitals, which stick out of the graphene plane. This π-bond leads to the half-filled band at the Fermi energy that permits free-moving electrons in graphene, which we shall study using the tight-binding model. Due to the simple nature of graphene's electronic structure the tight-binding model can provide a very good approximation, especially near the Fermi energy [35]. We may neglect the other energy bands which are sufficiently far from the Fermi energy as they play only a minor role in our calculations.

3.1.1 *Graphene Tight-Binding Model*

Here we employ a nearest-neighbour tight-binding (NNTB) approximation to describe the electronic band structure of graphene. Restricting the Hamilto-

nian describing the system to the p_z orbitals (which predominantly determine its electronic properties) and restricting the electron hopping probabilities to those between orbitals at neighbouring sites provides an excellent approximation to the band structure of graphene [35]. The Hamiltonian describing the system is of the form

$$\hat{\mathcal{H}} = \sum_{\mathbf{r},\gamma} |\mathbf{r},\gamma\rangle \epsilon_0 \langle \mathbf{r},\gamma| + \sum_{\mathbf{r},\mathbf{r}',\gamma} |\mathbf{r},\gamma\rangle t \langle \mathbf{r}',\gamma'|, \tag{3.1.1}$$

where $\mathbf{r}$ is the separation between unit cells, $\gamma = \{\alpha, \beta\}$ defines which sublattice (Fig. 3.1) the site occupies, $\epsilon_0 = \langle r, \alpha|\hat{\mathcal{H}}|\mathbf{r}, \alpha\rangle = \langle \mathbf{r}, \beta|\hat{\mathcal{H}}|\mathbf{r}, \beta\rangle$ defines the *onsite energy*, and the *hopping integral* is defined as $t = \langle \mathbf{r}, \gamma|\hat{\mathcal{H}}|\mathbf{r}', \gamma'\rangle$ if the sites are nearest neighbours, and is zero elsewhere.

The hopping integral for nearest neighbours in graphene is known to be well approximated by $t \approx -2.7eV$ [164], however we will generally quote values in terms of t, since we are usually interested in relative changes. The onsite energy is the same at each lattice site and defines the centre of the energy bands, and is set to zero in these calculations. To determine the band structure of the system we must find the eigenvalue solutions to the Schrödinger equation. For small systems we may attempt to solve this matrix equation directly, where the matrices have a dimension corresponding to the number of orbitals in the system. For large or infinite systems we may attempt to take advantage of periodicity within the system; if the system can be generated by the translation (under a set of vectors) of a finite cell, then we may be able to write the problem in a more easily solvable form.

The graphene lattice can be viewed as bipartite lattice composed of two interpenetrating triangular sublattices. The primitive cell of graphene consists of two adjacent atoms, one from each of the sublattices, $\gamma = \{\alpha, \beta\}$ as indicated by the blue rectangle in Fig. 3.1. We choose primitive lattice vectors $\mathbf{a}_1$ and $\mathbf{a}_2$ as functions of the interatomic separation $a = 1.42$ Å, however for ease

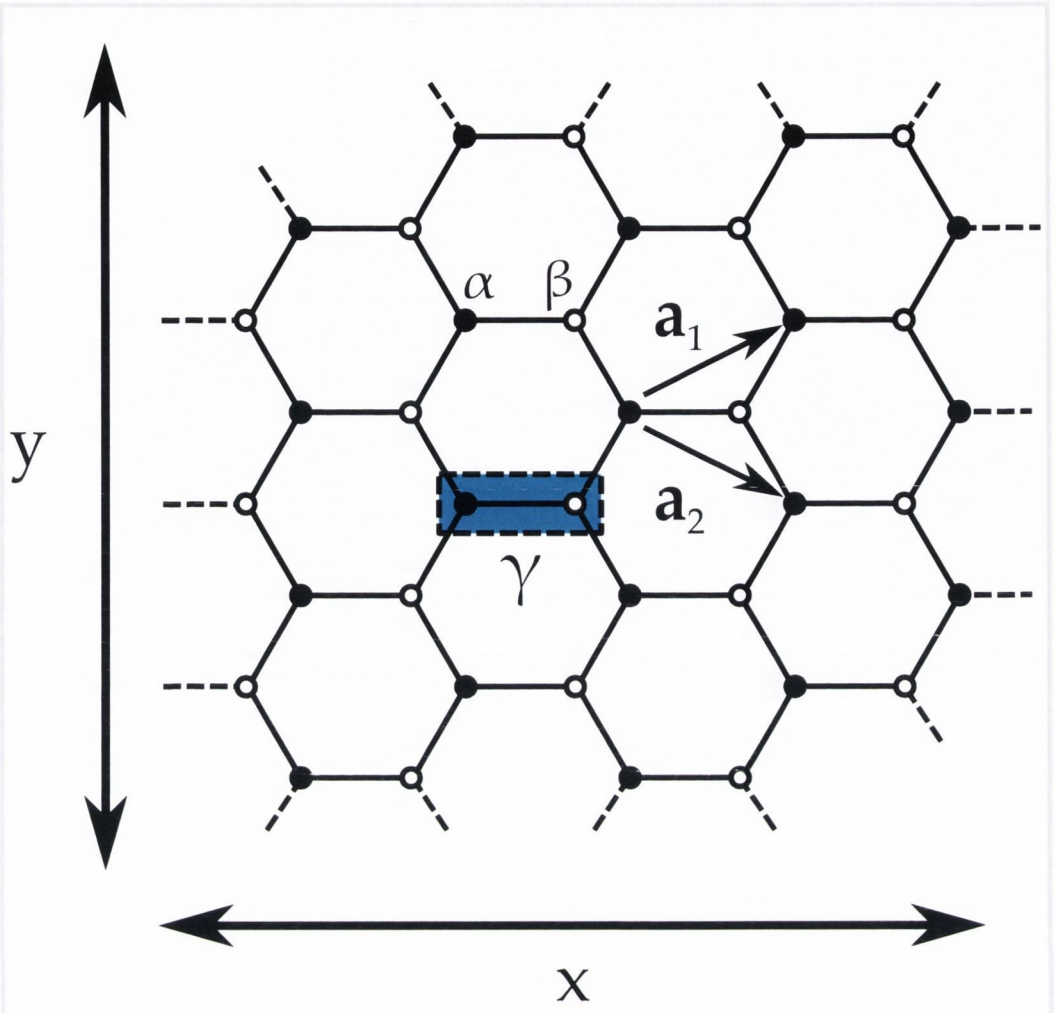


Figure 3.1: A schematic representation of a graphene lattice with the unit cell, γ, highlighted in blue, and the primitive lattice vectors $\mathbf{a}_1$ and $\mathbf{a}_2$. The sublattices, α and β, are denoted by filled circle and hollow circles respectively.

we will set the interatomic distance $a = 1$. The primitive lattice vectors are written in terms of the real space unit vectors $\hat{\mathbf{x}}$ along the armchair direction, and $\hat{\mathbf{y}}$ along the zigzag direction, as

$$\mathbf{a}_1 = \left(\frac{\sqrt{3}}{2}\hat{\mathbf{x}}, +\frac{1}{2}\hat{\mathbf{y}}\right), \quad \mathbf{a}_2 = \left(\frac{\sqrt{3}}{2}\hat{\mathbf{x}}, -\frac{1}{2}\hat{\mathbf{y}}\right), \tag{3.1.2}$$

such that any unit cell may be located by the linear combination $\mathbf{r} = m\mathbf{a}_1 + n\mathbf{a}_2$, where $m, n \in \mathbb{Z}$.

Including these specific vectors relating to graphene, the Hamiltonian can be written as a sum over $\mathbf{r}$ of all unit cells as

$$\begin{aligned}\hat{\mathcal{H}} = &\sum_{\mathbf{r}} |\mathbf{r},\alpha\rangle t \langle \mathbf{r},\beta| + |\mathbf{r},\beta\rangle t \langle \mathbf{r},\alpha| \\ &+|\mathbf{r},\alpha\rangle t \langle \mathbf{r}-\mathbf{a}_1,\beta| + |\mathbf{r},\alpha\rangle t \langle \mathbf{r}-\mathbf{a}_2,\beta| \\ &+|\mathbf{r},\beta\rangle t \langle \mathbf{r}+\mathbf{a}_1,\alpha| + |\mathbf{r},\beta\rangle t \langle \mathbf{r}+\mathbf{a}_2,\alpha|.\end{aligned} \tag{3.1.3}$$

To calculate the electronic structure we switch now to a reciprocal space Hamiltonian representation. To do this we project our real space Hamiltonian onto a basis set of Bloch waves using

$$\begin{aligned}|\mathbf{r},\gamma\rangle &= \frac{1}{\sqrt{N}} \sum_{\mathbf{k}} e^{i\mathbf{k}\cdot\mathbf{r}} |\mathbf{k},\gamma\rangle, \\ |\mathbf{k},\gamma\rangle &= \frac{1}{\sqrt{N}} \sum_{\mathbf{r}} e^{-i\mathbf{k}\cdot\mathbf{r}} |\mathbf{r},\gamma\rangle,\end{aligned} \tag{3.1.4}$$

which are Fourier transforms of each other, and N is the number of cells in the lattice. We now have a Hamiltonian

$$\begin{aligned}\hat{\mathcal{H}} &= \sum_{\mathbf{k}} |\mathbf{k},\alpha\rangle t \langle \mathbf{k},\beta| + |\mathbf{k},\beta\rangle t \langle \mathbf{k},\alpha| \\ &\quad +|\mathbf{k},\alpha\rangle t e^{-i\mathbf{k}\cdot\mathbf{a}_1} \langle \mathbf{k},\beta| + |\mathbf{k},\alpha\rangle t e^{-i\mathbf{k}\cdot\mathbf{a}_2} \langle \mathbf{k},\beta| \\ &\quad +|\mathbf{k},\beta\rangle t e^{+i\mathbf{k}\cdot\mathbf{a}_1} \langle \mathbf{k},\alpha| + |\mathbf{k},\beta\rangle t e^{+i\mathbf{k}\cdot\mathbf{a}_2} \langle \mathbf{k},\alpha| \\ &= \sum_{\mathbf{k}} |\mathbf{k},\alpha\rangle \left[t + t e^{-i\mathbf{k}\cdot\mathbf{a}_1} + t e^{-i\mathbf{k}\cdot\mathbf{a}_2} \right] \langle \mathbf{k},\beta| \\ &\quad +|\mathbf{k},\beta\rangle \left[t + t e^{+i\mathbf{k}\cdot\mathbf{a}_1} + t e^{+i\mathbf{k}\cdot\mathbf{a}_2} \right] \langle \mathbf{k},\alpha|,\end{aligned} \tag{3.1.5}$$

which is partially diagonal in k-space. Expanding out $\mathbf{k} = k_x\hat{\mathbf{x}} + k_y\hat{\mathbf{y}}$ we have

$$\begin{aligned}\mathbf{k}\cdot\mathbf{a}_1 &= \frac{\sqrt{3}}{2}k_x + \frac{1}{2}k_y, \\ \mathbf{k}\cdot\mathbf{a}_2 &= \frac{\sqrt{3}}{2}k_x - \frac{1}{2}k_y.\end{aligned} \tag{3.1.6}$$

We can now sum over the phase terms coming from each nearest neighbour atom, and write our Hamiltonian as

$$\begin{aligned}\hat{\mathcal{H}} = \sum_{\mathbf{k}} \Bigg[& |\mathbf{k},\gamma\rangle t \left(1 + 2\cos\left(\frac{1}{2}k_y\right) e^{-i\frac{\sqrt{3}}{2}k_x}\right) \langle \mathbf{k},\gamma'| \\ & + |\mathbf{k},\gamma'\rangle t \left(1 + 2\cos\left(\frac{1}{2}k_y\right) e^{+i\frac{\sqrt{3}}{2}k_x}\right) \langle \mathbf{k},\gamma| \Bigg].\end{aligned} \tag{3.1.7}$$

We then choose to define

$$\begin{aligned} f(\mathbf{k}) &= t \left(1 + 2\cos\left(\frac{1}{2}k_y\right) e^{-i\frac{\sqrt{3}}{2}k_x}\right), \\ f^*(\mathbf{k}) &= t \left(1 + 2\cos\left(\frac{1}{2}k_y\right) e^{+i\frac{\sqrt{3}}{2}k_x}\right), \end{aligned} \tag{3.1.8}$$

so that we can now write the NNTB Hamiltonian matrix describing our system in the simple form

$$\hat{\mathcal{H}} = \sum_{\mathbf{k}} \begin{pmatrix} 0 & f(\mathbf{k}) \\ f^*(\mathbf{k}) & 0 \end{pmatrix}. \tag{3.1.9}$$

We can now relate $\mathbf{k}$ to the energy eigenvalues of this diagonalizable Hamiltonian to calculate the graphene dispersion relation.

3.1.2 *Graphene Dispersion Relation*

To calculate our dispersion relation it is first necessary to diagonalize our Hamiltonian, and find the eigenvalues and corresponding eigenvectors. This is accomplished using the secular equation

$$\mathrm{Det}|\hat{\mathcal{H}} - \hat{I}\lambda| = 0, \tag{3.1.10}$$

where $\hat{I}$ is the identity matrix and which has eigenvalues $\lambda_\pm = \pm|f(\mathbf{k})|$. We choose to denote our dispersion relation as $\epsilon_\pm$, and the full form of the specific solution in the case of graphene is

$$\lambda_\pm = \epsilon_\pm = \pm t\sqrt{1 + 4\cos\left(\frac{\sqrt{3}}{2}k_x\right)\cos\left(\frac{1}{2}k_y\right) + 4\cos^2\left(\frac{\sqrt{3}}{2}k_x\right)}. \quad (3.1.11)$$

This equation defines the Fermi surface of graphene, as shown in Fig. 3.2, where the different signs correspond to the conduction and valence bands which touch each other at six discrete points at $E = 0$. Thus graphene is a zero bandgap semiconductor. These points are the peaks of the Dirac cones and are known as the K-points. They form the corners of the first Brillouin zone of graphene, which is the hexagon highlighted in Fig. 3.2. By symmetry we have only two unique K-points, **K** and **K′**, with the other four being two sets of equivalent pairs.

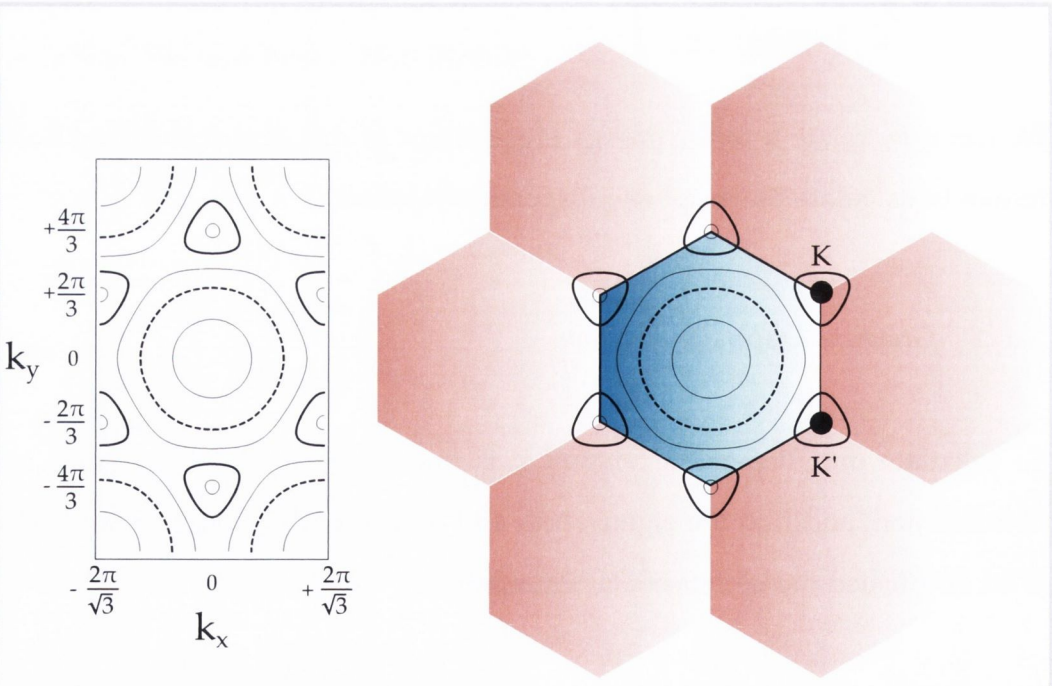


Figure 3.2: A contour plot of the Fermi surface of graphene with coordinates of the Dirac points labelled in k_x and k_y. The first Brillouin Zone of graphene is then highlighted (blue) along with the unique K-points **K** and **K′**.

In proximity to these K-points the energy depends linearly on the magnitude of the wavevector, so that the electrons can be described by an equation which is equivalent to the massless Dirac equation [165, 166]. This linear dispersion relation is given by

$$\epsilon = \hbar v_F \sqrt{k_1^2 + k_2^2}, \tag{3.1.12}$$

where k_1 and k_2 are centred on the Dirac points, v_F is the Fermi velocity in graphene, and $\hbar$ is the reduced Planck constant. This simple description of the graphene electrons allows us to understand their properties with a great level of mathematical transparency. However, it is only valid in a narrow range of energies around the Fermi level which restricts its use when an integral over energy is required. The Green's function (GF) is often calculated by approximating the band structure of graphene using this linear dispersion regime. However, here we show that the full dispersion relation may be used to obtain a fully analytic expression (*i.e.*, a closed-form expression) for the GF using the Stationary Phase Approximation (SPA). This analytic GF allows for mathematical transparency when calculating physical properties and is valid across nearly the entire energy band.

We now wish to find the eigenvectors corresponding to the eigenvalues of the full dispersion relation, Eq. 3.1.11. This is done by solving $(\hat{H} - \epsilon_{\pm}\hat{I})\,\mathbf{C} = 0$, where $\mathbf{C}$ is some 2D vector with coefficients c_1 and c_2. Firstly using the ϵ_+ eigenvalue we determine the corresponding eigenvector by letting

$$\begin{pmatrix} -|f| & f \\ f^* & -|f| \end{pmatrix} \begin{pmatrix} c_1 \\ c_2 \end{pmatrix} = 0, \tag{3.1.13}$$

which gives us the relation

$$c_2 = \frac{|f|}{f} c_1 = \frac{f^*}{|f|} c_1. \tag{3.1.14}$$

From this we can determine the eigenvector

$$|\mathbf{k},+\rangle = \frac{1}{\sqrt{2}} \begin{pmatrix} 1 \\ \frac{f^*}{|f|} \end{pmatrix}, \tag{3.1.15}$$

where $\frac{1}{\sqrt{2}}$ is the normalization constant, so that $\langle \mathbf{k},+|\mathbf{k},+\rangle = 1$. Similarly for the ϵ_- we can find the eigenvector

$$|\mathbf{k},-\rangle = \frac{1}{\sqrt{2}} \begin{pmatrix} 1 \\ -\frac{f^*}{|f|} \end{pmatrix}. \tag{3.1.16}$$

We now have everything we need to properly define the GF for graphene.

3.1.3 *Graphene Green's Functions*

Recall our definition for the GF from Sec. 2.1 ,

$$\hat{g} = \lim_{\eta \to 0} \left[(E \pm i\eta)\,\hat{I} - \hat{\mathcal{H}} \right]^{-1}. \tag{3.1.17}$$

We now have a diagonalized Hamiltonian that we can insert into this definition to obtain our GF,

$$\begin{aligned} \hat{g} &= \sum_k \frac{|\mathbf{k},+\rangle\langle\mathbf{k},+|}{E-\epsilon_+} + \frac{|\mathbf{k},-\rangle\langle\mathbf{k},-|}{E-\epsilon_-} \\ &= \sum_k \frac{|\mathbf{k},+\rangle\langle\mathbf{k},+|}{E-\epsilon_+} + \frac{|\mathbf{k},-\rangle\langle\mathbf{k},-|}{E+\epsilon_+}. \end{aligned} \tag{3.1.18}$$

On the last line we have used the fact that $\epsilon_+ = -\epsilon_-$. From section 3.1.2 we have the eigenvectors in terms of the sublattice of each site, where α and β

represent the black or white circles in Fig. 3.1, and these eigenvectors can be written

$$\begin{aligned} |\mathbf{k},+\rangle &= \frac{1}{\sqrt{2}}\left(|\mathbf{k},\alpha\rangle + \frac{f^*}{|f|}|\mathbf{k},\beta\rangle\right), \\ |\mathbf{k},-\rangle &= \frac{1}{\sqrt{2}}\left(|\mathbf{k},\alpha\rangle - \frac{f^*}{|f|}|\mathbf{k},\beta\rangle\right). \end{aligned} \tag{3.1.19}$$

We now wish to convert back into our real-space vector $\mathbf{r}$, to do this we use the inverse Fourier transform from Eq. 3.1.4, which gives

$$|\mathbf{k},\pm\rangle = \frac{1}{\sqrt{2}}\frac{1}{\sqrt{N}}\sum_{\mathbf{r}} e^{-i\mathbf{k}\cdot\mathbf{r}}\left(|\mathbf{r},\gamma\rangle \pm \frac{f^*}{|f|}|\mathbf{r},\gamma'\rangle\right). \tag{3.1.20}$$

We have four possible situations we wish to evaluate. These four situations stem from our two sublattices, α and β: $g^{\alpha\alpha}_{\mathbf{r}\mathbf{r}'}$, $g^{\beta\beta}_{\mathbf{r}\mathbf{r}'}$, $g^{\alpha\beta}_{\mathbf{r}\mathbf{r}'}$, and $g^{\beta\alpha}_{\mathbf{r}\mathbf{r}'}$. Where we have introduced the shorthand notation $g^{\alpha\beta}_{\mathbf{r}\mathbf{r}'} = \langle \mathbf{r},\alpha|g|\mathbf{r}',\beta\rangle$. Two of these cases are obviously degenerate by symmetry, namely $g^{\alpha\alpha}_{\mathbf{r}\mathbf{r}'}$ and $g^{\beta\beta}_{\mathbf{r}\mathbf{r}'}$. So we now want to work out our three unique cases. Starting with the case that both sites are on the same sublattice, we project onto our GF with

$$\begin{aligned} g^{\alpha\alpha}_{\mathbf{r}\mathbf{r}'}(E) &= \langle \mathbf{r},\alpha|g|\mathbf{r}',\alpha\rangle \\ &= \sum_{\mathbf{k}}\left(\frac{\langle \mathbf{r},\alpha|\mathbf{k},+\rangle\langle \mathbf{k},+|\mathbf{r}',\alpha\rangle}{E-\epsilon_+} + \frac{\langle \mathbf{r},\alpha|\mathbf{k},-\rangle\langle \mathbf{k},-|\mathbf{r}',\alpha\rangle}{E+\epsilon_+}\right) \\ &= \sum_{\mathbf{k}}\left(\frac{\frac{1}{2N}e^{i\mathbf{k}\cdot(\mathbf{r}'-\mathbf{r})}}{E-\epsilon_+} + \frac{\frac{1}{2N}e^{i\mathbf{k}\cdot(\mathbf{r}'-\mathbf{r})}}{E+\epsilon_+}\right) \\ &= \sum_{\mathbf{k}}\frac{2E\frac{1}{2N}e^{i\mathbf{k}\cdot(\mathbf{r}'-\mathbf{r})}}{E^2-\epsilon_+^2} \\ &= \frac{1}{N}\sum_{\mathbf{k}} E\frac{e^{i\mathbf{k}\cdot(\mathbf{r}'-\mathbf{r})}}{E^2-\epsilon_+^2}. \end{aligned} \tag{3.1.21}$$

Similarly

$$g^{\beta\beta}_{\mathbf{r}\mathbf{r}'}(E) = \langle \mathbf{r},\beta|g|\mathbf{r}',\beta\rangle = \frac{1}{N}\sum_{\mathbf{k}} E\frac{e^{i\mathbf{k}\cdot(\mathbf{r}'-\mathbf{r})}}{E^2-\epsilon_+^2}. \tag{3.1.22}$$

When separated precisely along the zigzag direction, $g^{\alpha\beta}_{\mathbf{r}\mathbf{r}'} = g^{\beta\alpha}_{\mathbf{r}\mathbf{r}'}$, however they are not generally equivalent and so we must treat them separately[1]. For the first inter-sublattice term, $\langle \mathbf{r}, \alpha | g | \mathbf{r}', \beta \rangle$, we can follow the same procedure as above,

$$\begin{aligned} g^{\alpha\beta}_{\mathbf{r}\mathbf{r}'}(E) &= \langle \mathbf{r}, \alpha | g | \mathbf{r}', \beta \rangle \\ &= \sum_{\mathbf{k}} \left(\frac{\langle \mathbf{r}, \alpha | \mathbf{k}, + \rangle \langle \mathbf{k}, + | \mathbf{r}', \beta \rangle}{E - \epsilon_+} + \frac{\langle \mathbf{r}, \alpha | \mathbf{k}, - \rangle \langle \mathbf{k}, - | \mathbf{r}', \beta \rangle}{E + \epsilon_+} \right) \\ &= \sum_{\mathbf{k}} \left(\frac{\frac{1}{2N} \frac{f}{|f|} e^{i\mathbf{k}\cdot(\mathbf{r}'-\mathbf{r})}}{E - \epsilon_+} - \frac{\frac{1}{2N} \frac{f}{|f|} e^{i\mathbf{k}\cdot(\mathbf{r}'-\mathbf{r})}}{E + \epsilon_+} \right) \\ &= \sum_{\mathbf{k}} \frac{2\epsilon_+ \frac{1}{2N} \frac{f}{|f|} e^{i\mathbf{k}\cdot(\mathbf{r}'-\mathbf{r})}}{E^2 - \epsilon_+^2} \\ &= \frac{1}{N} \sum_{\mathbf{k}} f \frac{e^{i\mathbf{k}\cdot(\mathbf{r}'-\mathbf{r})}}{E^2 - \epsilon_+^2}. \end{aligned} \tag{3.1.23}$$

The final case is then

$$\begin{aligned} g^{\beta\alpha}_{\mathbf{r}\mathbf{r}'}(E) &= \langle \mathbf{r}, \beta | g | \mathbf{r}', \alpha \rangle \\ &= \sum_{\mathbf{k}} \left(\frac{\langle \mathbf{r}, \beta | \mathbf{k}, + \rangle \langle \mathbf{k}, + | \mathbf{r}', \alpha \rangle}{E - \epsilon_+} + \frac{\langle \mathbf{r}, \beta | \mathbf{k}, - \rangle \langle \mathbf{k}, - | \mathbf{r}', \alpha \rangle}{E + \epsilon_+} \right) \\ &= \sum_{\mathbf{k}} \left(\frac{\frac{1}{2N} \frac{f^*}{|f|} e^{i\mathbf{k}\cdot(\mathbf{r}'-\mathbf{r})}}{E - \epsilon_+} - \frac{\frac{1}{2N} \frac{f^*}{|f|} e^{i\mathbf{k}\cdot(\mathbf{r}'-\mathbf{r})}}{E + \epsilon_+} \right) \\ &= \sum_{\mathbf{k}} \frac{2\epsilon_+ \frac{1}{2N} \frac{f^*}{|f|} e^{i\mathbf{k}\cdot(\mathbf{r}'-\mathbf{r})}}{E^2 - \epsilon_+^2} \\ &= \frac{1}{N} \sum_{\mathbf{k}} f^* \frac{e^{i\mathbf{k}\cdot(\mathbf{r}'-\mathbf{r})}}{E^2 - \epsilon_+^2}. \end{aligned} \tag{3.1.24}$$

1 Appendix A provides an algorithm for determining which graphene GFs are equivalent using a serious of reflections and rotations. This algorithm is useful for speeding up various calculations.

Examining the differences between these, namely the different prefactor inside the summation, we may define a sublattice dependent term $N_{\gamma\gamma'}(E, \mathbf{k})$ which encapsulates all sublattice dependent quantities,

$$N_{\gamma\gamma'}(E, \mathbf{k}) = \begin{cases} E & \text{if } \gamma = \gamma' \\ f(\mathbf{k}) = t\left(1 + 2\cos\left(\frac{1}{2}k_y\right) e^{-i\frac{\sqrt{3}}{2}k_x}\right) & \text{if } \gamma = \alpha, \gamma' = \beta \\ f^*(\mathbf{k}) = t\left(1 + 2\cos\left(\frac{1}{2}k_y\right) e^{+i\frac{\sqrt{3}}{2}k_x}\right) & \text{if } \gamma = \beta, \gamma' = \alpha \end{cases} . \tag{3.1.25}$$

This allows us to write the general GF for graphene as

$$g_{\mathbf{r}\mathbf{r}'} = \frac{1}{N} \sum_{\mathbf{k}} N_{\gamma\gamma'}(E, \mathbf{k}) \frac{e^{i\mathbf{k}\cdot(\mathbf{r}'-\mathbf{r})}}{E^2 - \epsilon_+^2}. \tag{3.1.26}$$

This sum over all $\mathbf{k}$ vectors can be replaced with an integral over the first Brillouin Zone (BZ). The first BZ of graphene consists of a hexagon with vertices corresponding to the discrete Fermi surface of graphene, however, for convenience, we may instead integrate over an equivalent rectangular area (Fig. 3.3). Focusing on the phase term, we see that this can be expanded as

$$\begin{aligned} \mathbf{k} \cdot (\mathbf{r}' - \mathbf{r}) &= (k_x, k_y) \cdot \left((m'\mathbf{a}_1 + n'\mathbf{a}_2) - (m\mathbf{a}_1 + n\mathbf{a}_2)\right) \\ &= (k_x, k_y) \cdot \left(\frac{\sqrt{3}}{2}(m' + n' - m + n), \frac{1}{2}(m' - n' - m + n)\right), \end{aligned} \tag{3.1.27}$$

where we have used the definition of the vectors $\mathbf{a}_1$ and $\mathbf{a}_2$ (Eq. 3.1.2) on the second line. To simplify our equations going forward we can use the translational invariance of graphene to set the vector $\mathbf{r}$ to the origin, such that $m = n = 0$ and the separation between the sites is the only important quantity.

So our GF, at some energy E, from a site at the origin to some site at $\mathbf{r}'$, can now be written

$$g_{\mathbf{r}\mathbf{r}'}(E) = \frac{\sqrt{3}}{4\pi}\frac{1}{2\pi}\int_{-\frac{2\pi}{\sqrt{3}}}^{+\frac{2\pi}{\sqrt{3}}} dk_x \int_{-\pi}^{+\pi} dk_y \, N_{\gamma\gamma'}(E, k_x, k_y)\, \frac{e^{i\left(\frac{\sqrt{3}k_x}{2}(m'+n')+\frac{k_y}{2}(m'-n')\right)}}{E^2 - \epsilon_+^2(E, k_x, k_y)}. \tag{3.1.28}$$

Note, that when dealing with several GFs between multiple sites, say $\mathbf{r}_1, \mathbf{r}_2, \mathbf{r}_3 \ldots$ *etc.*, that it is convenient to use the shorthand $g_{\mathbf{r}_i\mathbf{r}_j}$, but that we can always consider the GF to be between the origin and the site at $\mathbf{r}_j - \mathbf{r}_i$ using the fact that graphene is translationally invariant. To simplify some of expressions at this point it is useful to define the dimensionless wavevectors

$$k_A = \frac{\sqrt{3}}{2}k_x, \quad k_Z = \frac{1}{2}k_y. \tag{3.1.29}$$

The simplified BZs that we now have is shown in Fig. 3.3, where equivalent regions are labelled with the same number. And also, for convenience later, we can define the separation of sites in terms of the separation along the armchair direction and zigzag direction,

$$D_A = m' + n', \quad D_Z = m' - n'. \tag{3.1.30}$$

These now allow us to write our GF in a much simplified form

$$g_{\mathbf{r}\mathbf{r}'}(E) = \frac{1}{2\pi^2}\int_{-\pi}^{+\pi} dk_A \int_{-\pi/2}^{+\pi/2} dk_Z \, N_{\gamma\gamma'}\frac{e^{i(k_A D_A + k_Z D_Z)}}{E^2 - \epsilon_+^2}. \tag{3.1.31}$$

This is equivalent to the GF where the integration limits of k_A and k_Z have been swapped, as seen in Fig. 3.3. We have hidden some of the dependences here for neatness.

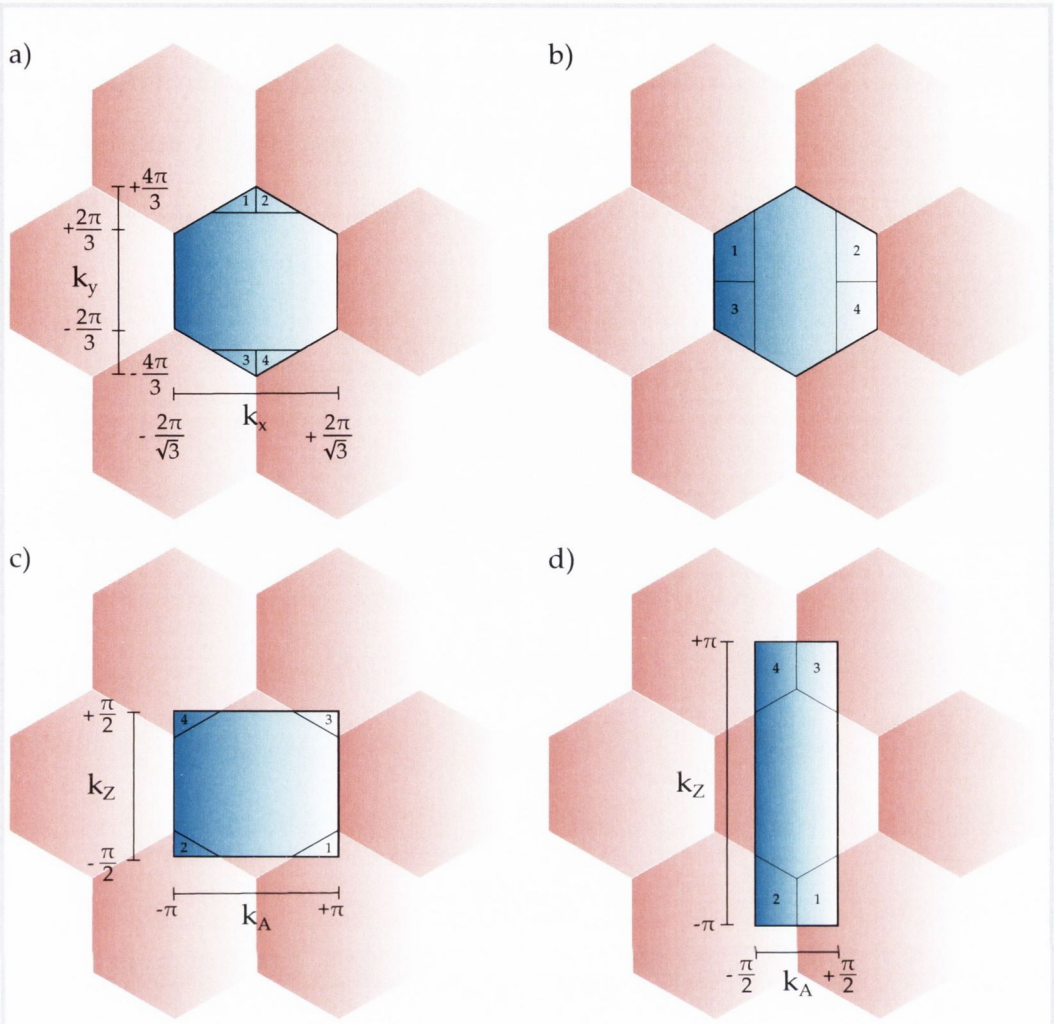


Figure 3.3: A schematic representation of the first Brillouin zone (BZ) of graphene (blue) with the original wavevectors (top), k_x and k_y, and the simplified wavevectors, k_A and k_Z (bottom). Subfigures c and d represent the BZs for use with the armchair integration and zigzag integration respectively. The regions labelled 1,2,3,4 indicate segments of the original hexagonal BZs (a and b) that are replaced by segments of neighbouring BZs to form the simplified rectangular BZs (c and d, respectively).

We now have our graphene GF in the form of a double integral. The numerical cost of evaluating this may be reduced by noting that either of the integrals may be solved using contour integration. However, both may not be solved, as will become clear, due to the complexity of the equations and difficulty of finding a contour. Therefore, it is necessary at this point to create two separate solutions, by solving one integral or the other. This is done so

that the SPA, which is explained in Sec. 3.1.4, can be applied equally to both. We will also need both forms when we move on to discussing nanotubes, and so we choose to perform them now, where they follow more logically, rather than later where it may be necessary to recap extensively. This will be done using Cauchy's Theorem which states that

$$\oint dz\, f(z) = 2\pi i \sum_{z_0} \mathrm{Res}(f_{z_0}), \tag{3.1.32}$$

where f is the integrand of one of the integrals, and z_0 are its poles.

Solving the armchair integral

We first choose to solve the integral in the armchair direction using contour integration. The armchair integral may be separated out from the rest of the GF as

$$I_A = \int_{-\pi}^{+\pi} dk_A\, N_{\gamma\gamma'} \frac{e^{i(k_A D_A + k_Z D_Z)}}{E^2 - t^2\left(1 + 4\cos(k_A)\cos(k_Z) + 4\cos^2(k_A)\right)}, \tag{3.1.33}$$

where we have expanded out ϵ_+ since we are interested in its full form. We now transpose the problem to the complex plane. For $D_A > 0$ we can consider the contour to be in the upper half of the complex plane ($\mathrm{Im}(k_A) > 0$) as shown in Fig. 3.4. Here, as $\mathrm{Im}(k_A) \rightharpoonup \infty$, its contribution goes to zero since the exponential now contains a term $e^{-\infty}$, and the net contribution from the left and right contours is likewise zero, arising from the 2π periodicity of the integrand. A similar argument can be made for the case $D_A < 0$ with a change of variables. So now the integral over the entire contour is just the sum of the residue around the pole of the integrand within the contour. The residue theorem states that if a function can be written as a composite function

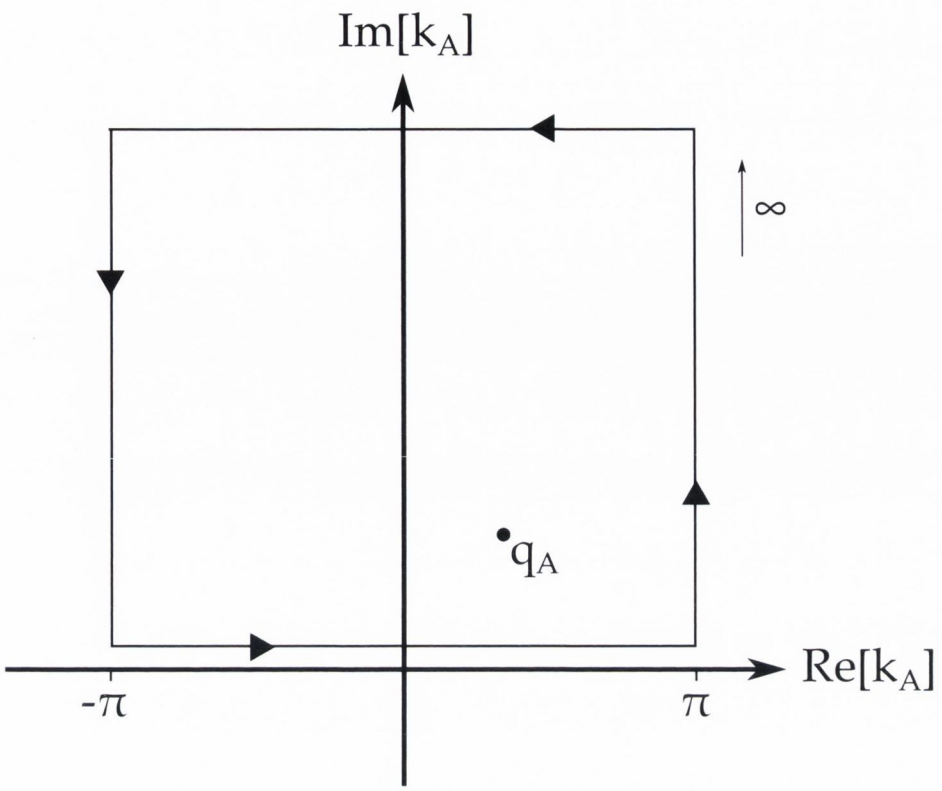


Figure 3.4: A contour integral over k_A, where a pole, q_A, is indicated by a dot, and the direction of the integration is indicated by the arrows.

of the form $f(z) = \frac{g(z)}{h(z)}$, then the residue, which is proportional to the contour integral, can be found as

$$\text{Res}(f(z)) = \frac{g(z_0)}{h'(z_0)}, \; h'(z_0) = \left.\frac{dh}{dz}\right|_{z_0}, \tag{3.1.34}$$

where z_0 is the value of z that satisfies the equation $h(z_0) = 0$, *i.e.*, the value that produces a simple pole in $f(z)$. So from our GF we have

$$\begin{aligned} h(k_A) &= E^2 - t^2(1 + 4\cos^2(k_Z) + 4\cos(k_Z)\cos(k_A)), \\ \frac{dh}{dk_A} &= 4t^2\cos(k_Z)\sin(k_A). \end{aligned} \tag{3.1.35}$$

We wish to find the specific value of k_A that creates a pole, *i.e.*, the value of k_A that satisfies

$$E^2 - t^2\left(1 + 4\cos(k_A)\cos(k_Z) + 4\cos^2(k_A)\right) = 0. \tag{3.1.36}$$

We call this pole q_A, where q is the general notation used to denote a pole, and the subscript A is to tie it to the integration performed over the armchair integral, k_A, and to differentiate it from the pole that will arise when performing the integration over the zigzag integral. Solving for q_A gives

$$q_A = \pm\cos^{-1}\left(\frac{\frac{E^2}{t^2} - 1 - 4\cos^2(k_Z)}{4\cos(k_Z)}\right), \tag{3.1.37}$$

where care must be taken to ensure that $\mathrm{Im}\,(q_A) > 0$, so that the pole remains in the contour, which in this case requires that it remain in the upper half of the complex plane. The denominator of our residue is then given by

$$h'(q_A) = 4t^2\cos(k_Z)\sin(q_A). \tag{3.1.38}$$

This now allows us to write the integral in a fully analytic form as

$$I_A = 2\pi i\left(N_{\gamma\gamma'}\frac{e^{i(q_A D_A + k_Z D_Z)}}{4t^2\cos(k_Z)\sin(q_A)}\right), \tag{3.1.39}$$

where this $2\pi i$ is the proportionality constant that relates the residue to the integral around a closed curve, Eq. 3.1.32, and $N_{\gamma\gamma'}$ is equivalent to Eq. 3.1.25 evaluated at q_A and k_Z. Our GF can now be written as a single integral

$$\begin{aligned} g_{\mathbf{r}\mathbf{r}'} &= \frac{1}{2\pi^2}\int_{-\pi/2}^{\pi/2} dk_Z\, 2\pi i\left(N_{\gamma\gamma'}\frac{e^{i(q_A D_A + k_Z D_Z)}}{4t^2\cos(k_Z)\sin(q_A)}\right) \\ &= \frac{i}{4\pi t^2}\int_{-\pi/2}^{\pi/2} dk_Z N_{\gamma\gamma'}\frac{e^{i(q_A D_A + k_Z D_Z)}}{\cos(k_Z)\sin(q_A)}. \end{aligned} \tag{3.1.40}$$

This is now in the simplest form that we can write it without making approximations or introducing further conditions.

Solving the zigzag integral

Note that we are not solving both integrals in the same equation. A similar process may be followed to solve the zigzag integral, however there exist some tripping points that differentiate the two. Attempting to use the same BZ as for the armchair integral leads to the sides not cancelling in the contour integration, so we instead use the BZ described by Fig. 3.3 d). Again, our contour is in the upper half plane as seen in Fig 3.5. Starting from Eq. 3.1.31, but with the limits of k_A and k_Z swapped, the integral we wish to solve is

$$I_Z = \int_{-\pi}^{+\pi} dk_Z \, N_{\gamma\gamma'} \frac{e^{i(k_A D_A + k_Z D_Z)}}{E^2 + t^2(1 + 4\cos^2(k_Z) + 4\cos(k_Z)\cos(k_A))}. \tag{3.1.41}$$

We again calculate a pole, now q_Z, as the zeros of the denominator

$$q_Z^{\pm} = \pm\cos^{-1}\left(-\frac{1}{2}\left(\cos(k_A) \pm \sqrt{\frac{E^2}{t^2} - \sin^2(k_A)}\right)\right). \tag{3.1.42}$$

Here the external $\pm$ corresponds to poles that are either in the upper or lower half plane. The internal $\pm$ corresponds to two different poles in that plane, where we have added a superscript to q_Z to indicate the existence of two poles. The external sign is taken care of by the condition that Im $(q_Z) > 0$ (for $D_Z \geqslant 0$). We take account of the internal sign by summing over both poles when calculating the residues. Where the residue with multiple poles is defined as

$$\mathrm{Res}(f(z)) = \frac{g(z_0)}{h'(z_0)} + \frac{g(z_1)}{h'(z_1)} + \cdots = \sum_j \frac{g(z_j)}{h'(z_j)}, \tag{3.1.43}$$

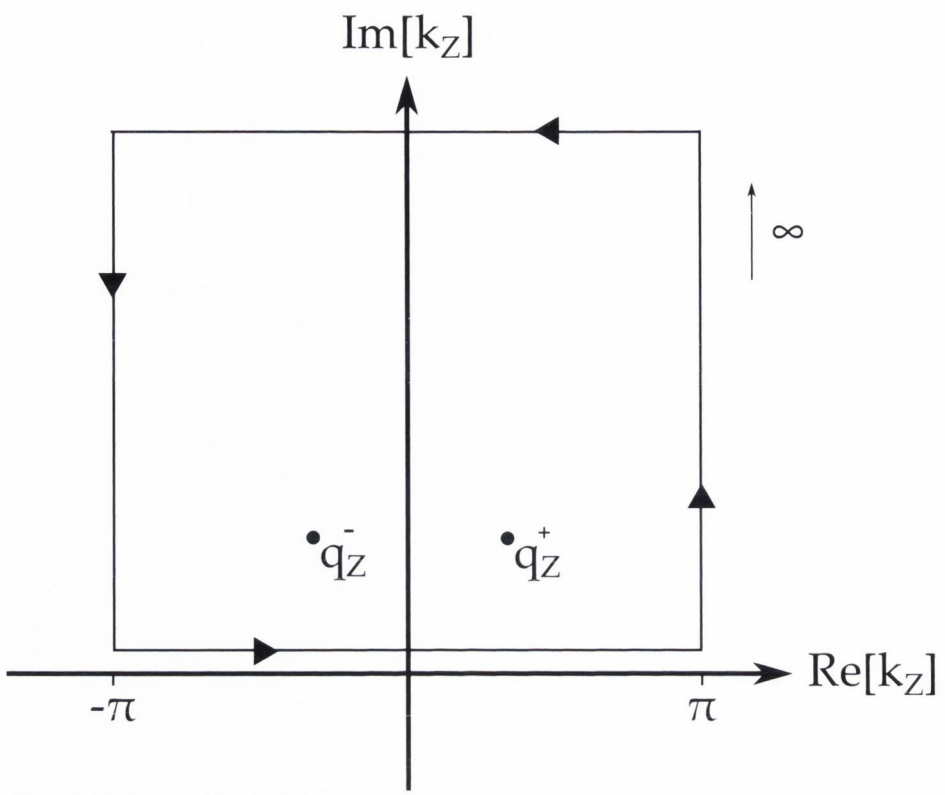


Figure 3.5: A contour integral over k_Z, where a poles, $q_Z^{\pm}$, are indicated by the dots, and the direction of the integration is indicated by the arrows.

and in principle we may have any number of poles. We can therefore express our integral as a sum over the poles

$$I_Z = \frac{2\pi i}{4t^2} \sum_{\pm} N_{\gamma\gamma'} \frac{e^{i(k_A D_A + q_Z^{\pm} D_Z)}}{\sin(2q_Z^{\pm}) + \sin(q_Z^{\pm}) \cos(k_A)}, \tag{3.1.44}$$

so that our GF has the form

$$g_{\mathbf{r}\mathbf{r}'} = \frac{i}{4\pi t^2} \sum_{\pm} \int_{-\frac{\pi}{2}}^{+\frac{\pi}{2}} dk_A \, N_{\gamma\gamma'} \frac{e^{i(k_A D_A + q_Z^{\pm} D_Z)}}{\sin(2q_Z^{\pm}) + \sin(q_Z^{\pm}) \cos(k_A)}. \tag{3.1.45}$$

3.1.4 *Stationary Phase Approximation of Graphene*

We have now shown how the first of the GF integrals can be performed, and our GFs are now tantalizingly close to being written in a fully analytic form. However, the remaining integral is not easily solvable without applying some restrictions to simplify the form and applying some approximations.

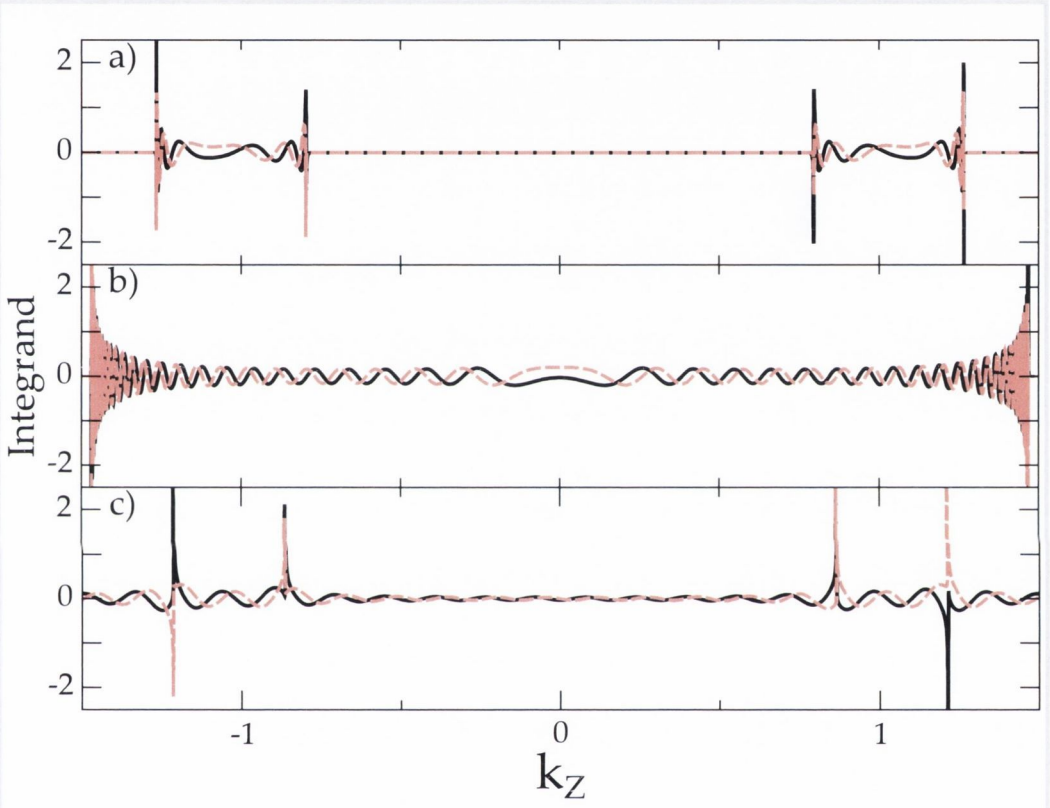


Figure 3.6: The integrand of the single integral GFs a) for $D_A = 20$, $D_Z = 0$ at $E = 0.4|t|$, b) for $D_A = 30$, $D_Z = 0$ at $E = 1.2|t|$, c) for $D_Z = 0$, $D_Z = 20$ at $E = 0.3|t|$. In all cases the real part of the integrand is solid-black, and the imaginary part is dashed-red.

In Sec. 2.5 we gave an overview of the SPA and how it is implemented in general. We showed that it can be used to approximate the integrals of highly oscillatory functions. The form of the equation that we considered there was

$$I(y) = \int dx\, F(x)\, e^{iy\phi(x)}. \tag{3.1.46}$$

Looking for a moment at just one of our single integral GFs, Eq. 3.1.40, (though it can equally be applied to the other GF, Eq. 3.1.45) we can rearrange this equation as

$$\begin{aligned} g_{\mathbf{r}\mathbf{r}'} &= \frac{i}{4\pi t^2} \int_{-\pi/2}^{\pi/2} dk_Z \, N_{\gamma\gamma'} \, \frac{e^{i(q_A D_A + k_Z D_Z)}}{\cos(k_Z)\sin(q_A)} \\ &= \frac{i}{4\pi t^2} \int_{-\pi/2}^{\pi/2} dk_Z \, \frac{N_{\gamma\gamma'}}{\cos(k_Z)\sin(q_A)} e^{iq_A(k_Z)D_A} \, e^{ik_Z D_Z} \\ &= \frac{i}{4\pi t^2} \int_{-\pi/2}^{\pi/2} dk_Z \, F(k_Z) \, e^{iq_A(k_Z)D_A} \, e^{ik_Z D_Z}. \end{aligned} \tag{3.1.47}$$

Which has the form we require in precisely three cases: $D_A = 0$, $D_Z = 0$, and $D_Z = D_A$. These three cases correspond to three values for ϕ: $\phi = k_Z$, $\phi = q_A(k_Z)$, and $\phi = 2(q_A(k_Z) + k_Z)$. However, the cases $D_A = 0$ and $D_Z = D_A$ correspond to separations along different zigzag directions, which are just rotations of each other so we can ignore the case $D_Z = D_A$, as it has the more complicated phase term. Figure 3.6 shows the integrand of our GF, Eq. 3.1.40, plotted for three different cases. Each of these cases is along either the armchair or zigzag direction, and has been performed at different energies. All three cases are oscillatory or zero for large sections of the integrand, and we note that the integrands of GFs in all directions will be highly oscillatory, but these are the only directions that also satisfy the form of Eq. 3.1.46. This behaviour is understood in terms of the exponential, which for large values of separation, D_A and D_Z, will oscillate rapidly. We can now use the SPA to write an analytic form for the graphene GF if the two sites are separated precisely along the armchair or zigzag directions, which we will now examine separately.

SPA Armchair direction

We first consider the case of sites separated along the armchair direction of graphene, *i.e.*, when $D_Z = 0$. The GF that we wish to solve using the SPA method, and component functions, are

$$\begin{aligned} g_{rr'} &= \frac{i}{4\pi t^2} \int_{-\pi/2}^{\pi/2} dk_Z \, F(k_Z) \, e^{iq_A(k_Z)D_A} \, , \\ F(k_Z) &= \frac{N_{\gamma\gamma'}}{\cos(k_Z)\sin(q_A)}, \\ q_A(k_Z) &= \pm\cos^{-1}\left(\frac{\frac{E^2}{t^2} - 1 - 4\cos^2(k_Z)}{4\cos(k_Z)}\right). \end{aligned} \tag{3.1.48}$$

We must necessarily use this version to calculate the SPA for sites along the armchair direction, since the other integral has no stationary points in this direction. And when calculating the SPA along the zigzag direction we must use the other integral for the same reasons.

Our first step is to replace the phase term, $q_A(k_Z)$, with a Taylor expansion around the stationary point, k_Z^0,

$$q(k_Z) \approx q\left(k_Z^0\right) + q'_A\left(k_Z^0\right) + q''_A\left(k_Z^0\right)\left(k_Z - k_Z^0\right)^2, \tag{3.1.49}$$

where the stationary point is defined by $q'_A\left(k_Z^0\right) = 0$. The precise forms of $q_A(k_Z)$ and $q''_A(k_Z)$ are quite messy and are omitted here, though reasonably straightforward to calculate. We only need to consider stationary solutions that yield real solutions for q_A, which are

$$k_z^0 = \begin{cases} \pm\cos^{-1}\left(\frac{\sqrt{t^2-E^2}}{2t}\right), & \text{if } |E| < |t| \\ 0, & \text{if } |E| > |t| \end{cases} . \tag{3.1.50}$$

In the region around $E = \pm t$ we may need to consider contributions from both stationary points. Using this we can find values for $q_A\left(k_Z^0\right)$ and $q_A''\left(k_Z^0\right)$,

$$q_A\left(k_Z^0\right) = \begin{cases} \pm\cos^{-1}\left(-\sqrt{1-\frac{E^2}{t^2}}\right), & \text{if } |E| < |t| \\ \pm\cos^{-1}\left(\frac{E^2-5t^2}{4t^2}\right), & \text{if } |E| > |t| \end{cases}, \tag{3.1.51}$$

and

$$q_A''\left(k_Z^0\right) = \begin{cases} \pm\frac{E^2+3t^3}{2E\sqrt{t^2-E^2}}, & \text{if } |E| < |t| \\ \pm\frac{E^2+3t^3}{2\sqrt{(t^2-E^2)(E^2-9t^2)}}, & \text{if } |E| > |t| \end{cases}, \tag{3.1.52}$$

where the factor of $\frac{1}{2}$ from the Taylor expansion has been absorbed into the definition of $q_A''\left(k_Z^0\right)$.

This now allows us to write our GF as

$$\begin{aligned} g_{\mathbf{r}\mathbf{r}'} &= \frac{i}{4\pi t^2}\int_{-\pi/2}^{+\pi/2} dkz \sum_{k_Z^0} F\left(k_Z^0\right)\, e^{i\left(q_A\left(k_Z^0\right)D_A + q_A''\left(k_Z^0\right)\left(k_Z-k_Z^0\right)^2 D_A\right)} \\ &= \frac{i}{4\pi t^2}\sum_{k_Z^0} F\left(k_Z^0\right)\, e^{iq_A\left(k_Z^0\right)D_A}\int_{-\pi/2}^{+\pi/2} dk_Z\, e^{iq_A''\left(k_Z^0\right)\left(k_Z-k_Z^0\right)^2 D_A} \\ &= \frac{i}{4\pi t^2}\sum_{k_Z^0} F\left(k_Z^0\right)\, e^{iq_A\left(k_Z^0\right)D_A}\sqrt{\frac{i\pi}{q_A''\left(k_Z^0\right)D_A}}, \end{aligned} \tag{3.1.53}$$

where all of the sublattice dependence is contained within the $F\left(k_Z^0\right)$ term. On the last line the integral is solved using the Gaussian integral.

At this point the GF subscript, $g_{\mathbf{r}\mathbf{r}'}$, makes little sense, as the vectors are highly restricted, so we switch to the notation, g_{D_A}, to make clear that this

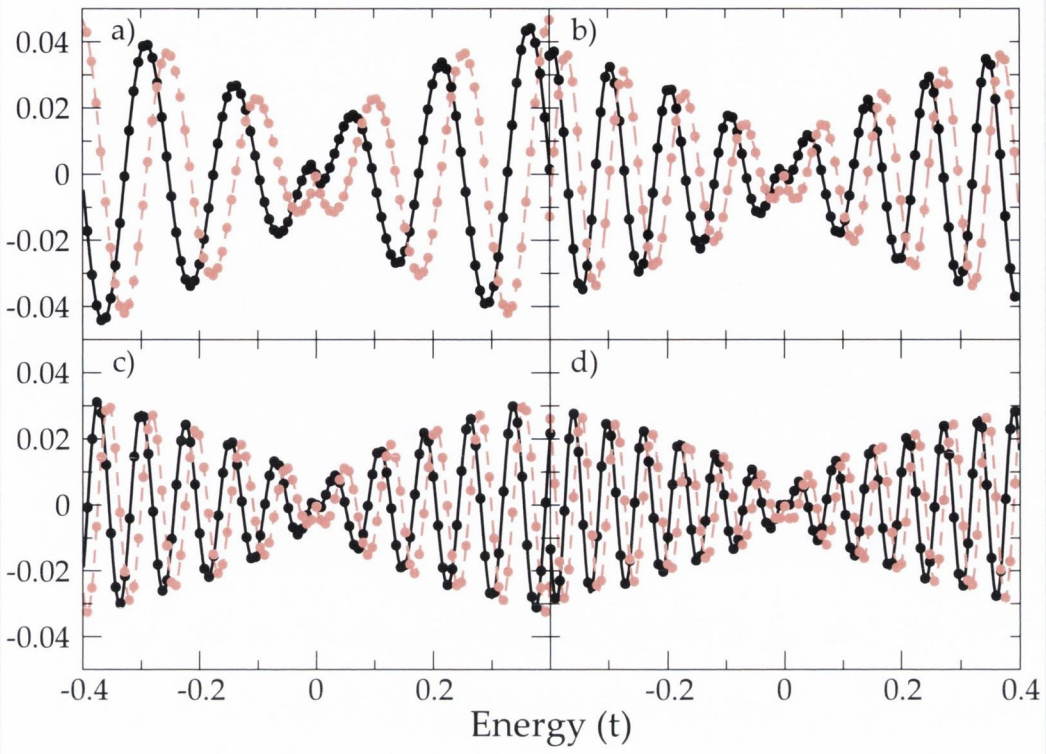


Figure 3.7: A comparison between the SPA GF g_{D_A} (dots) and the corresponding GF $g_{rr'}$ (lines) for a) $D_A = 20$, b) $D_A = 30$, c) $D_A = 40$, and d) $D_A = 50$. The real parts are in black, and the imaginary parts in red.

GF is only valid for separations along the D_A direction. For energies close to zero, *i.e.*, $|E| < |t|$, we get

$$g_{D_A} = N_{\gamma\gamma'}\left(k_Z^0\right)\sqrt{\frac{2i}{\pi D_A}}\,\frac{e^{iq_A(k_Z^0)D_A}}{\sqrt{E\left(E^2+3t^2\right)\sqrt{t^2-E^2}}}. \tag{3.1.54}$$

And for energies further from zero, $|E| > |t|$, we get

$$g_{D_A} = N_{\gamma\gamma'}\left(k_Z^0\right)\sqrt{\frac{2}{i\,\pi D_A}}\,\frac{e^{iq_A(k_Z^0)D_A}}{\sqrt{\left(E^2+3t^2\right)\sqrt{\left(t^2-E^2\right)\left(E^2-9t^2\right)}}}. \tag{3.1.55}$$

Figure 3.7 shows a comparison between the numerically calculated GF and the SPA GF, for a variety of separations. They are seen to be in excellent

agreement throughout the energy band, and the match is not limited only to the linear dispersion region around the Dirac points.

SPA Zigzag direction

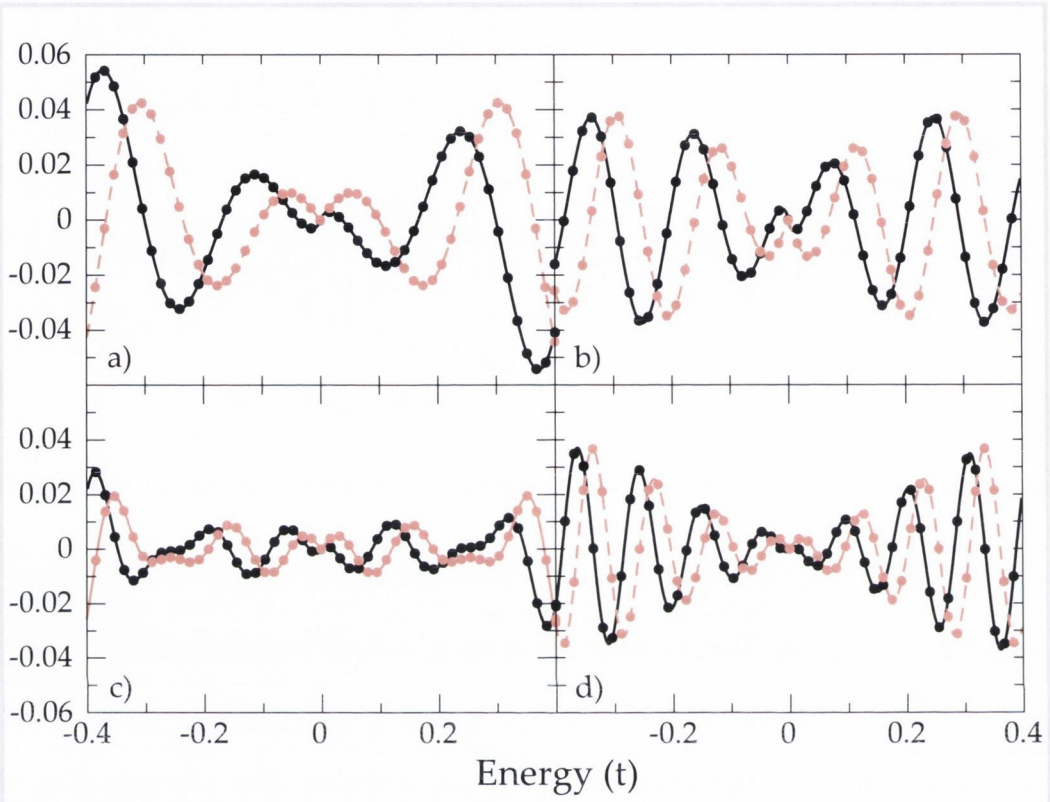


Figure 3.8: A comparison between the SPA GF, g_{D_Z}, (dots) and the corresponding GF $g_{rr'}$ (lines) for a) $D_Z = 20$, b) $D_Z = 30$, c) $D_Z = 40$, and d) $D_Z = 50$. The real parts are in black, and the imaginary parts in red.

We now consider sites separated along the zigzag direction, with $D_A = 0$. It is now necessary to use the GF where we have solved the k_Z integral, as,

roles now reversed, the other integral has no stationary points. We start by again defining exactly what we we are working with

$$\begin{aligned} g_{rr'} &= \frac{i}{4\pi t^2} \sum_{\pm} \int_{-\frac{\pi}{2}}^{+\frac{\pi}{2}} dk_A \; F(k_A) \, e^{iq_Z^{\pm}(k_A)D_Z} \, , \\ F(k_Z) &= \frac{N_{\gamma\gamma'}(k_A)}{\sin(2q_Z^{\pm}) + \sin\left(q_Z^{\pm}\right)\cos\left(k_A\right)} \, , \\ q_Z^{\pm}(k_A) &= \pm\cos^{-1}\left(-\frac{1}{2}\left(\cos\left(k_A\right) \pm \sqrt{\frac{E^2}{t^2} - \sin^2\left(k_A\right)}\right)\right) \, . \end{aligned} \tag{3.1.56}$$

Following a similar set of steps as above we now find just a single stationary point $k_A^0 = 0$. Since we have just one stationary point there is no need to consider the energy band as two separate regions. And from this we find the values of our pole at the stationary point $q_Z^{\pm}\left(k_A^0\right)$ and the second derivative of the pole at the same stationary point $q_Z^{\pm\prime\prime}\left(k_A^0\right)$,

$$q_Z^{\pm}\left(k_A^0\right) = \pm\cos^{-1}\left(\frac{-t \mp E}{2t}\right), \tag{3.1.57}$$

and

$$q_Z^{\pm\prime\prime}\left(k_A^0\right) = \mp\frac{t(E \pm t)}{E\sqrt{4t^2 - (-t \mp E)^2}}. \tag{3.1.58}$$

We can now use the method above to write our SPA GF, for impurities separated along D_Z as

$$g_{D_Z} = \frac{i}{4\pi t^2} N_{\gamma\gamma'}\left(k_A^0\right) \sum_{\pm} \sqrt{\frac{i\pi}{q_Z^{\pm\prime\prime}\left(k_A^0\right) D_Z}} \frac{e^{iq_Z^{\pm}(k_A^0)D_Z}}{\sin\left(2q_Z^{\pm}\left(k_A^0\right)\right) + \sin\left(q_Z^{\pm}\left(k_A^0\right)\right)}, \tag{3.1.59}$$

which can be simplified to

$$g_{D_Z} = N_{\gamma\gamma'}\left(k_A^0\right) \sqrt{\frac{1}{2i\pi D_Z}} \sum_{\pm} \frac{e^{iq_Z^{\pm}(k_A^0)D_Z}}{\sqrt{E|t|(t \pm E)\sqrt{4t^2 - (E \pm t)^2}}}. \tag{3.1.60}$$

As before, Fig. 3.8 shows a comparison between the numerically calculated GF and the SPA GF, for a variety of separations, which is seen to be in excellent agreement.

SPA application

We have now completed our derivation of the SPA of the GF between sites separated along the zigzag and armchair directions of graphene. Each of these GFs has the form

$$g_D(E) = \mathcal{A}(E)\frac{e^{iq(E)D}}{\sqrt{D}}, \tag{3.1.61}$$

where we omit the subscripts of D and q to show that it applies equally to both Eq. 3.1.55 and Eq. 3.1.60. This analytical expression for the real space GF is valid throughout the entire electronic energy band, and is especially useful when examining physical properties outside the linear dispersion regime.

However, it is the ability to easily separate the distance dependence that we make use of when examining the iterations between magnetic moments in Chap. 4. This simple form of the GF allows us to examine the distance dependence of the RKKY interaction between various magnetic moment conformations (Sec. 3.4), as well as their dependence on strain (Sec. 5.2). These concepts will be introduced in later chapters where we will demonstrate the ease and transparency with which these interactions and perturbations can be understood.

3.2 CARBON NANOTUBES

In this section, we will briefly discuss nanotubes and their electronic structure before moving on to derive closed form expressions for the GF between any two sites on an achiral nanotube as seen in Fig. 3.9. Initially discovered as co-

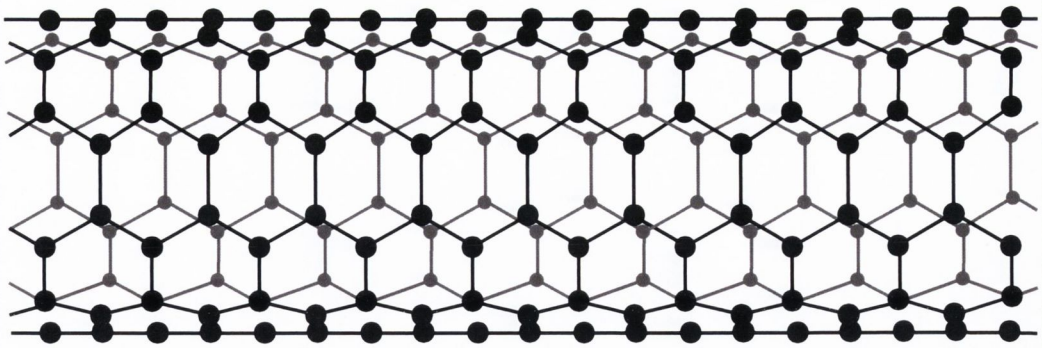


Figure 3.9: An armchair carbon nanotube (ACNT).

axially aligned tubes, multi-walled nanotubes (MWNT), and later isolated as single-walled nanotubes (SWNT), nanotubes consist of a single carbon atom thick cylindrical wall up to 1000 nm in length, and diameters ranging from 4-30 nm [2, 3]. Nanotubes display a host of remarkable mechanical properties. They are extremely flexible, and can be reversibly bent up to a large angle. They also exhibit high thermal conductivity, which is an especially desirable trait for transporting heat in modern electronics.

Like graphene the σ and π electrons are independent. Here too the σ band exists at energies far removed from the Fermi energy, and thus we will neglect them. The curvature of the tube results in non-zero overlap of the p_z orbitals, which may result in interesting spin-splitting effects [167]. We neglect this effect in our model, which should be minor in all but the smallest diameter nanotubes, which are structurally unstable and can be ignored without much loss of generality.

The derivation of these analytic expressions for the GF are made possible by the simple description of nanotubes in the tight-binding model, which may even be extended to include the GFs of semi-infinite nanotubes. Again we choose to neglect some characteristics in order to have GFs that provide a clear physical description of electron propagation.

3.2.1 *Electronic Structure of Carbon Nanotubes*

The structure of carbon nanotubes may be described in terms of the underlying graphene lattice. A carbon nanotube can be "derived" by rolling up a sheet of graphene along a particular direction, where the wrapping direction is defined by the vector $C_h = m\mathbf{a}_1 + n\mathbf{a}_2$, and all nanotubes are then defined by the tuplet (m, n), where m and n define an infinite number of wrapping directions. Nanotubes with (m, n) where $m \neq n$ and $m, n \neq 0$ are known as chiral nanotubes, and display a "twisting symmetry". A consequence of which is that the unit cell for chiral tubes is usually much larger than for the achiral tubes, making them harder to deal with analytically. In this work we will focus only on achiral nanotubes, those defined by (m, m) and $(m, 0)$. This focus is due to their high degree of symmetry which allows them to be treated analytically in a more simple fashion. These nanotubes are known as armchair and zigzag nanotubes. These names come from cross sectional profiles of the nanotube.

Imposing a boundary condition in the C_h direction reduces the two dimensional band structure of graphene to a series of one dimensional bands. This results from the quantisation of an electron's momentum along the nanotube's circumferential direction. Because of this the electronic properties of a nanotube are highly dependent on the tuplet (m, n), which determine whether the nanotube is metallic, $|n - m| \bmod 3 = 0$, or semi-conducting, $|n - m| \bmod 3 = 1, 2$. It is clear from this definition that two thirds of nanotubes will be semi-conducting and one third metallic. This dependence arises from the intersection of quantisation lines and the isolated points at the corners of the first Brillouin zone that make up the Fermi surface; if there is an intersection between the line and the point then the nanotube will be metallic, otherwise it will be semi-conducting. With this understanding we can determine that all armchair nanotubes (ACNT) will be metallic and that

every third zigzag nanotube (ZZNT) (as we increase m) will be metallic, with the remainder of the achiral ZZNT being semi-conducting. The metallicity of these one dimensional objects is not destroyed by the Peierls distortion, they are resistant to the effect which normally destroys the metallicity of one dimensional structures.

3.2.2 *Green's Functions of Carbon Nanotubes*

As stated above, the GFs for nanotubes can be best thought of in terms of the GFs of the underlying graphene lattice. To calculate the electronic structure, and hence the GF, of nanotubes we will use the zone-folding approximation. This approximation is made by taking the electronic states for graphene and accounting for a periodic boundary condition in the circumferential direction of the nanotube wavefunction, ψ_{nt}. This condition is

$$\psi_{nt}(\mathbf{r}) = \psi_{nt}(\mathbf{r} + \mathbf{C}_h), \tag{3.2.1}$$

where $\mathbf{C}_h = m\mathbf{a}_1 + n\mathbf{a}_2$, and is a Bravais lattice vector of graphene. This allows us to write, using Bloch's theorem, the graphene wavefunction, ψ_g, as

$$\psi_g(\mathbf{r} + \mathbf{C}_h) = e^{i\mathbf{k}\cdot\mathbf{C}_h}\psi_g(\mathbf{r}). \tag{3.2.2}$$

Equating these two leads us to the condition that $\mathbf{k} \cdot \mathbf{C}_h = 2\pi j$ where $j \in \mathbb{Z}$.

So, to derive the GFs for ACNT and ZZNT we start with the graphene GF. We may start with the final form of the GF in Eq. 3.1.31, where it contains a sum over all $\mathbf{k}$ vectors. This equation is written as

$$g_{\mathbf{r}\mathbf{r}'} = \frac{1}{N}\sum_{\mathbf{k}} N_{\gamma\gamma'}(E, \mathbf{k})\frac{e^{i\mathbf{k}\cdot(\mathbf{r}'-\mathbf{r})}}{E^2 - \epsilon_+^2}. \tag{3.2.3}$$

To obtain the integral form of GF for graphene we replaced both **k** vectors with integrals over the first BZ. Here we replace one of the **k** vectors with an integral and discretize the other, depending on whether we want ACNTs or ZZNTs. Due to the way that nanotubes are named, the armchair nanotube GF bears more resemblance to the zigzag graphene GF, and *vice versa*. In both cases the 2D Brillouin zones (BZ) will become a series of 1D lines in reciprocal space as indicated in Fig. 3.10 and Fig. 3.12. However, we may still use the modified rectangular BZs from Fig. 3.3 to keep the integration variables simple.

Armchair Nanotubes

For armchair nanotubes the circumferential direction $\mathbf{C}_h$ is defined as $\mathbf{C}_h = n_c(\mathbf{a}_1 + \mathbf{a}_2)$, Fig. 3.10, where the finite integer n_c describes the circumference of the tube. Using the discretization condition from above we arrive at the replacement

$$k_A = \frac{\pi j}{n_c}, \tag{3.2.4}$$

and the sum is now over j which runs from 1 to n_c. This, combined with the replacement of the other **k** vector with an integral over k_Z, gives us an expression for the GF

$$g_{\mathbf{r}\mathbf{r}'} = \frac{1}{2\pi}\frac{1}{n_c}\sum_{j=1}^{n_c}\int_{-\pi}^{+\pi} dk_Z \, \frac{N_{\gamma\gamma'}\, e^{i\frac{2\pi j}{n_c}D_A + ik_Z D_Z}}{E^2 - |f|^2}, \tag{3.2.5}$$

with

$$f = t + 2t\cos(k_Z)\, e^{i\frac{\pi j}{n_c}}. \tag{3.2.6}$$

Now D_Z describes the longitudinal position along the tube, and D_A describes a position around the circumference (these take on opposite meaning in zigzag nanotubes.).

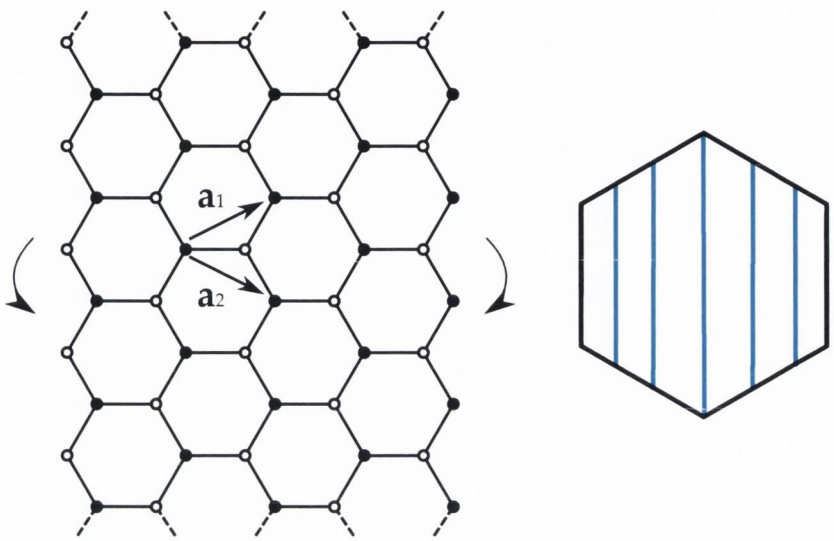


Figure 3.10: Armchair Carbon Nanotube with the wrapping direction indicated by the curved arrows, the extended edge indicated by dashed lines, and the basis vectors $\mathbf{a}_1$ and $\mathbf{a}_2$. The corresponding Brillouin Zone, where the reciprocal space is now a series of 1D lines (red).

Similar to graphene, the integral over k_Z may be solved using contour integration, where the pole q is obtained by solving the equation

$$E^2 - |f|^2 = 0, \tag{3.2.7}$$

for k_Z. This k_Z is then redefined as q_Z, and is given by

$$\begin{aligned} q_Z &= \pm\cos^{-1}\left(\frac{-2t^2\cos\left(\frac{\pi j}{n_c}\right) \pm \sqrt{2}\sqrt{2E^2t^2 - t^4 + t^4\cos\left(2\frac{\pi j}{n_c}\right)}}{4t^2}\right) \\ &= \pm\cos^{-1}\left(-\frac{1}{2}\cos\left(\frac{\pi j}{n_c}\right) \pm \frac{1}{2t}\sqrt{E^2 - t^2\sin^2\left(\frac{\pi j}{n_c}\right)}\right). \end{aligned} \tag{3.2.8}$$

We then use residue theorem to arrive at the simplest form for the armchair nanotube GF

$$
\begin{aligned}
g_{rr'} &= \frac{i}{n_c} \sum_j \sum_{\pm} \frac{N_{\gamma\gamma'}\, e^{i\frac{2\pi j}{n_c} D_A + iq_z|D_z|}}{4t^2 \cos\left(\frac{\pi j}{n_c}\right) \sin(q) + 8t^2 \sin(2q)} \\
&= \frac{i}{4t^2 n_c} \sum_j \sum_{\pm} \frac{N_{\gamma\gamma'}\, e^{i\frac{2\pi j}{n_c} D_A + iq_z|D_z|}}{\cos\left(\frac{\pi j}{n_c}\right) \sin(q_z) + 2\sin(2q_z)}.
\end{aligned}
\tag{3.2.9}
$$

Figure 3.11 shows a plot of this equation, calculated for specific values, against the same GF calculated using recursive techniques.

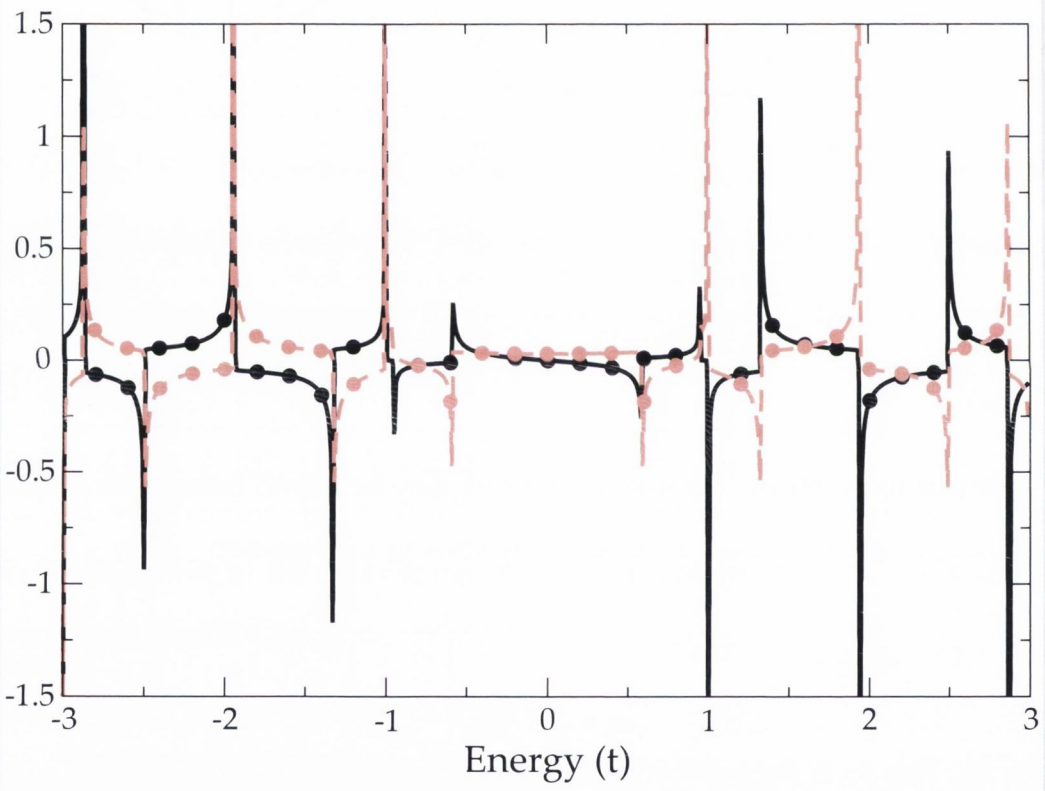


Figure 3.11: Comparison of the armchair nanotube graphene Green's function (lines) given in Eq. 3.2.9 and a standard recursive method (dots). Here the real part of the Green's function is given in red, and the imaginary part in black. The specific values used were $m = 2$, $n = 3$, $N_{\gamma\gamma'} = N_{\alpha\alpha}$, $n_c = 11$.

Zigzag Nanotubes

For zigzag nanotubes we have a very similar method as above. The circumferential direction is now defined as $\mathbf{C}_h = n_c(\mathbf{a}_1 - \mathbf{a}_2)$, Fig. 3.12, so that the wavevector k_Z is discretized as

$$k_Z = \frac{\pi j}{n_c}, \tag{3.2.10}$$

giving us

$$g_{rr'} = \frac{1}{2\pi}\frac{1}{n_c}\int_{-\pi}^{+\pi} dk_A \sum_j \frac{N_{\gamma\gamma'}\, e^{ik_A D_A + i\frac{\pi j}{n_c} D_Z}}{E^2 - |f|^2}, \tag{3.2.11}$$

with

$$f = t + 2t\cos\left(\frac{\pi j}{n_c}\right) e^{ik_A}. \tag{3.2.12}$$

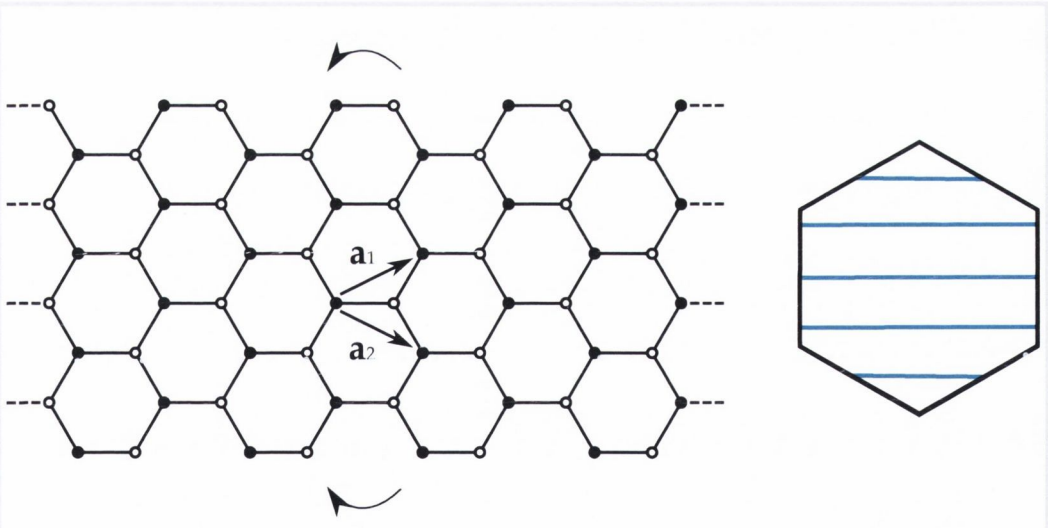


Figure 3.12: Zigzag Carbon Nanotube with the wrapping direction indicated by the curved arrows and the extended edge indicated by the dashed lines. The corresponding Brillouin Zone, where the reciprocal space is now a series of 1D lines (red).

Again we use contour integration to solve one of the integrals. Finding the zeros of the denominator gives

$$q_A = \pm\cos^{-1}\left(\frac{\frac{E^2}{t^2} - 1 - 4\cos^2\left(\frac{\pi j}{n_c}\right)}{4\cos\left(\frac{\pi j}{n_c}\right)}\right). \tag{3.2.13}$$

And the residue theorem now gives

$$\begin{aligned} g_{rr'} &= \frac{1}{2\pi}\frac{2\pi i}{n_c}\sum_j \frac{N_{\gamma\gamma'}\, e^{iq_A D_A + i\frac{\pi j}{n_c}D_Z}}{4t^2\cos\left(\frac{\pi j}{n_c}\right)\sin(q_A)} \\ &= \frac{i}{4t^2 n_c}\sum_j \frac{N_{\gamma\gamma'}\, e^{iq_A D_A + i\frac{\pi j}{n_c}D_Z}}{\cos\left(\frac{\pi j}{n_c}\right)\sin(q_A)}. \end{aligned} \tag{3.2.14}$$

We note here that we encounter a problem at $j = \frac{n_c}{2}$ where the integrand is undefined, as $\cos\left(\frac{\pi}{n_c}\frac{n_c}{2}\right) = 0$. To get around this we go back to Eq. 3.2.11 and solve this particular case separately. Setting $j = \frac{n_c}{2}$ in f, we get $f = t^2$, which simplifies our equation to

$$\begin{aligned} g_{rr'}\left(j = \frac{n_c}{2}\right) &= \frac{1}{2\pi}\frac{1}{n_c}\int_{-\pi}^{+\pi} dk_A\, \frac{N_{\gamma\gamma'}\, e^{ik_A D_A + i\frac{\pi}{2}D_Z}}{E^2 - t^2} \\ &= \frac{1}{2\pi}\frac{1}{n_c}\frac{N_{\gamma\gamma'} e^{i\frac{\pi}{2}D_Z}}{E^2 - t^2}\int_{-\pi}^{+\pi} dk_A\; e^{ik_A D_A}. \end{aligned} \tag{3.2.15}$$

The integral may now be solved easily and is equal to $2\pi\,\delta_{D_A,0}$, where $\delta_{D_A,0}$ is the standard Kronecker delta function, *i.e.* $\delta_{D_A,0} = 1$ if $D_A = 0$ and is zero for all other values of D_A. Since $D_Z \in \mathbb{Z}$, we may also make the simplification $e^{i\frac{\pi}{2}D_Z} = i^{D_Z}$. This now leaves us with the relatively simple form for this term of the sum

$$g_{rr'}\left(j = \frac{n_c}{2}\right) = \delta_{D_A,0}\,\frac{1}{n_c}\frac{N_{\gamma\gamma'}\left(j = \frac{n_c}{2}\right)\; i^{D_Z}}{E^2 - t^2}, \tag{3.2.16}$$

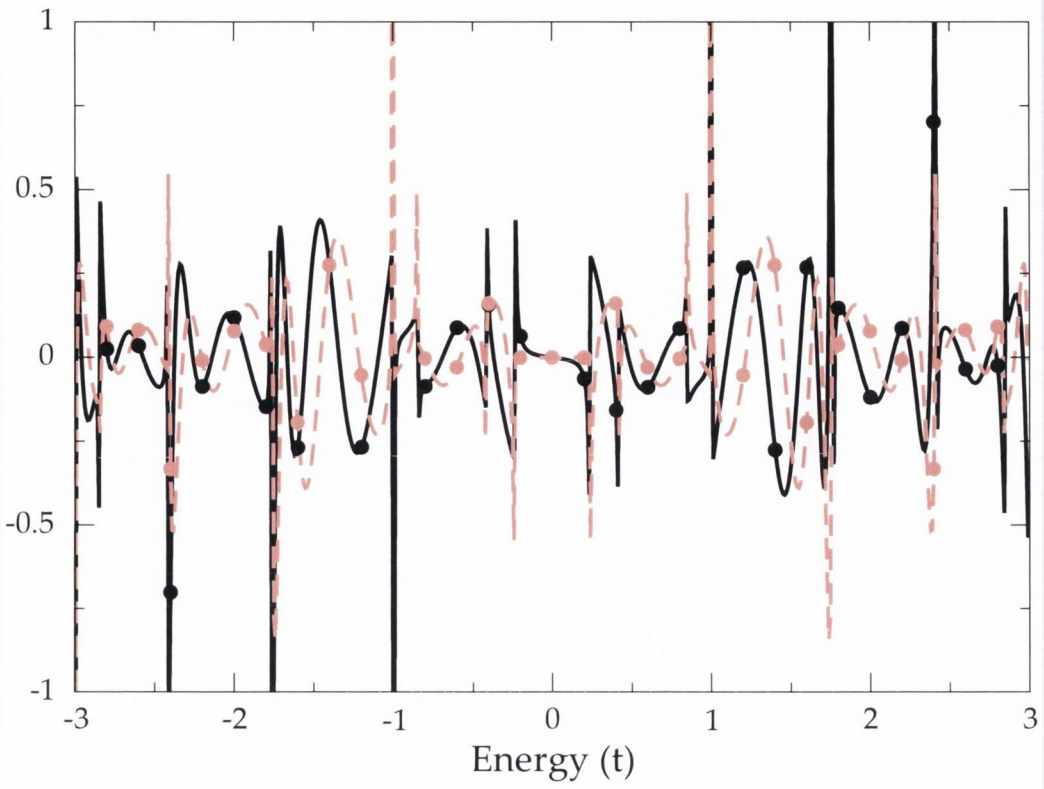


Figure 3.13: Comparison of the zigzag nanotube graphene Green's function (lines) given in Eq. 3.2.18 and a standard recursive method (dots). Here the real part of the Green's function is given in red, and the imaginary part in black. The specific values used were $m = 3$, $n = 6$, $N_{\gamma\gamma'} = N_{\alpha\alpha}$, $n_c = 8$.

where

$$N_{\gamma\gamma'}\left(j = \frac{n_c}{2}\right) = {N^0}_{\gamma\gamma'} = \begin{cases} E & \text{if } \gamma = \gamma' \\ t & \text{if } \gamma \neq \gamma' \end{cases} . \tag{3.2.17}$$

Our full GF may now be written as

$$g_{\mathbf{r}\mathbf{r}'} = \frac{i}{4t^2 n_c} \sum_{j \neq \frac{n_c}{2}} \frac{N_{\gamma\gamma'}\, e^{iq_A D_A + i\frac{\pi j}{n_c} D_Z}}{\cos\left(\frac{\pi j}{n_c}\right) \sin\left(q_A\right)} + \delta_{D_A,0}\, \frac{1}{n_c} \frac{{N^0}_{\gamma\gamma'}\, i^{D_Z}}{E^2 - t^2}. \tag{3.2.18}$$

Figure 3.13 shows of plot of this equation, calculated for specific values, against the same GF calculated using recursive techniques. In contrast to the

analytic GF for graphene we note that there is no distance dependence in the denominator, implying that the GF does not decay as a function of distance in a 1D material, which is one of the key signatures of 1D systems.

3.3 OTHER GRAPHENE DERIVED MATERIALS

Although not used in the rest of this thesis, at this point we choose to talk briefly about semi-infinite graphene (Fig. 3.14) and nanoribbons (Fig. 3.15) to emphasize the usefulness of the GF approach. Where we usually consider graphene to be a two-dimensional sheet that extends far enough in each direction that we can neglect any edge effect, we sometimes wish to examine these edge effects. Semi-infinite graphene is the name given to a graphene sheet that contains an edge, either armchair or zigzag. These have many of the same properties of graphene but do differ in some some significant ways. A nanoribbon can be thought of as a thin slice of graphene that contains two parallel edges at some fixed distance apart.

Semi-infinite graphene and nanoribbons may be approached computationally by a number of recursive techniques. These recursive techniques involve building up the system piece-by-piece, starting with a GF that defines an isolated block of the material and continually adding on new blocks and updating the GF until the variance in the GF between steps falls below a certainly arbitrary value. These blocks may be a single finite slice of a nanoribbon, or just a graphene unit cell.

Although these approaches are useful computationally, and for systems with large amounts of disorder, they lack the mathematical transparency of an analytic GF. However, it is possible to model some of these systems using analytic GFs, though not with the inclusion of the edge correction, which usu-

ally has a minor effect. We will briefly lay out those methods in the sections below.

3.3.1 *Semi-infinite Graphene*

The method for deriving an analytic semi-infinite graphene GF works in the presence of an armchair edge, as shown in Fig. 3.14 a), or a zigzag edge, though the introduction of the zigzag edge introduces some troubling complications. It involves selecting a linear combination of eigenstates from the eigenstates of graphene such that no states exist along a single line of the graphene sheet.

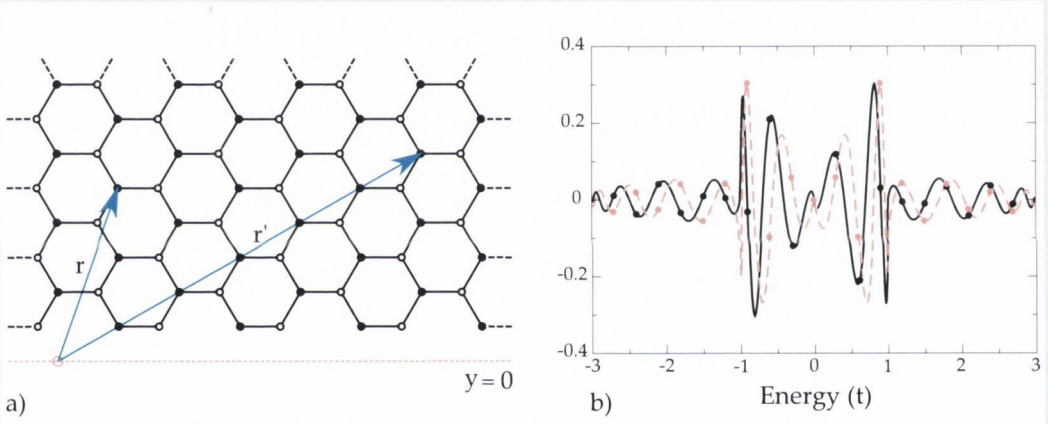


Figure 3.14: a) Armchair semi-infinite graphene with the stateless line $y = 0$ indicated by the dashed-red line, the red circle shows the origin (though it may be chosen at any such point along the dashed-red line), and vectors $\mathbf{r} = m\mathbf{a}_1 + n\mathbf{a}_2$ and $\mathbf{r}' = m'\mathbf{a}_1 + n'\mathbf{a}_2$ are indicated by the blue arrows.
b) Comparison of the semi-infinite graphene Green's function for the eigenstate method (lines) given in Eq. 3.3.3 and a standard recursive method (dots). Here the real part of the Green's function is given in red, and the imaginary part in black. The specific values used were $m = 1$, $n = 1$, $m' = 7$, $n' = 3$, $N_{\gamma\gamma'} = N_{\alpha\alpha}$.

This essentially separates a graphene sheet into two semi-infinite graphene sheets that cannot feel each other's presence and so can be thought of as a single isolated semi-infinite sheet. One such combination of eigenstates is

$$|\phi_k, \pm\rangle = \frac{1}{\sqrt{2}} \left(|(kx, ky), \pm\rangle - |(kx, -ky), \pm\rangle \right), \tag{3.3.1}$$

which results in a single stateless line at $y = 0$, which is just some arbitrary line along the armchair direction. Our GF for semi-infinite graphene is then given by

$$\hat{g}_{(SI)} = \frac{|\phi_k, +\rangle\langle\phi_k, +|}{E - \epsilon_+} + \frac{|\phi_k, -\rangle\langle\phi_k, -|}{E - \epsilon_-}. \tag{3.3.2}$$

Following the steps that we used for graphene we may derive a single integral form for the GF between any two sites on the sheet

$$g_{(SI)\mathbf{rr}'} = \frac{i}{2\pi t^2} \int_{-\frac{\pi}{2}}^{+\frac{\pi}{2}} dk_Z \, N_{\gamma\gamma'} \frac{e^{i2q_A(m'+n'-m-n)} \sin\left(k_Z(m-n)\right) \sin\left(k_Z(m'-n')\right)}{\cos\left(k_Z\right) \sin\left(q_A\right)}. \tag{3.3.3}$$

Here, q_A and $N_{\gamma\gamma'}$ are identical to those of an infinite graphene sheet. This equation may be further simplified to allow the SPA to be applied, and may even be written as a sum of GFs of a graphene sheet with certain restrictions [168]. This provides a great deal of information about the underlying mathematics that is unobtainable using recursive techniques, while at the same time giving identical results as seen in Fig. 3.14 b).

3.3.2 *Graphene Nanoribbons*

The derivation of the GF for nanoribbons is similar to that for semi-infinite graphene, Fig. 3.15 a). Conceptually however it is quite different. Instead of

thinking of an infinite graphene sheet being sliced in two, we instead imagine a nanotube, and a slice being made along its longitudinal direction so that it unfolds into a nanoribbon. To do this, first a boundary condition is applied

$$k_y = \frac{2\pi j}{n_c}, \tag{3.3.4}$$

which is equivalent to that applied for nanotubes. And then the same eigen-

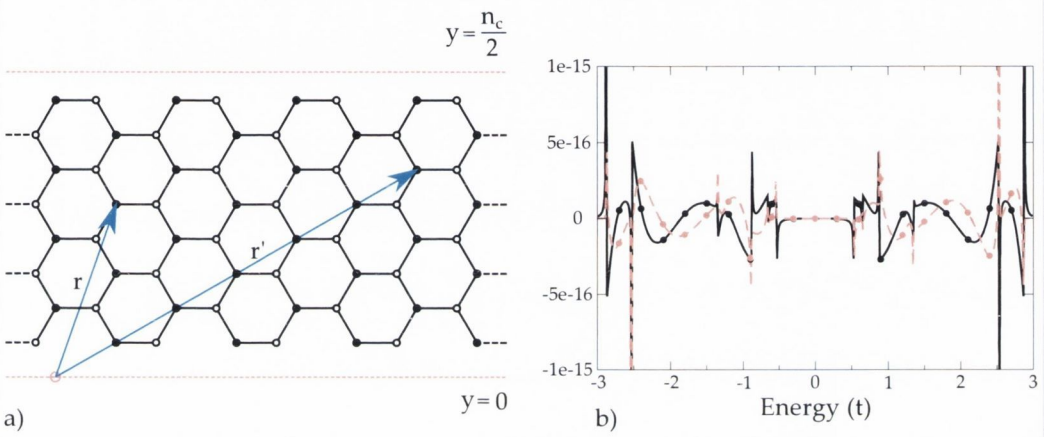


Figure 3.15: a) Armchair graphene nanoribbons with the stateless lines $y = 0$ and $y = \frac{n_c}{2}$ indicated by the dashed-red lines, the red circle shows the origin (though it may be chosen at any such point along the dashed-red line), and vectors $\mathbf{r} = m\mathbf{a}_1 + n\mathbf{a}_2$ and $\mathbf{r}' = m'\mathbf{a}_1 + n'\mathbf{a}_2$ are indicated by the blue arrows.
b) Comparison of the nanoribbon graphene Green's function for the eigenstate method (lines) given in Eq. 3.3.5 and a standard recursive method (dots). Here the real part of the Green's function is given in red, and the imaginary part in black. The specific values used were $m = 9$, $n = 3$, $m' = 0$, $n' = 8$, $N_{\gamma\gamma'} = N_{\alpha\beta}$, $n_c = 9$.

states that were used to describe semi-infinite graphene are introduced, which now produce stateless lines at $k_y \mathbf{y} = \pi j$. The GF may then be derived, in a similar manner, as

$$g_{(NR)_{\mathbf{r}\mathbf{r}'}} = \frac{i}{2\pi t^2} \sum_j N_{\gamma\gamma'} \frac{e^{i2q_A(m'+n'-m-n)} \sin\left(\frac{\pi j}{n_c}(m-n)\right) \sin\left(\frac{\pi j}{n_c}(m'-n')\right)}{\cos\left(\frac{\pi j}{n_c}\right) \sin(q_A)}. \tag{3.3.5}$$

Once again, this equation provides a great deal of information about the underlying mathematics that is unobtainable using recursive techniques, while at the same time giving identical results as seen in Fig. 3.15 b).

3.4 IMPURITIES IN GRAPHENE-RELATED MATERIALS

Unwanted impurities in graphene can be a nuisance for various properties, including transport, however they can also be thought of as a way to tailor the properties of graphene. As such, there is currently a large and growing interest in nanopatterning graphene. The advantage of graphene is that it is possible to tailor absorbants in an atomically precise fashion with atomic force microscopy [169]. Such tailoring allows for a complex manipulation of the electronic properties of the material, and is not currently possible in three-dimensional materials.

There are four types of small impurity conformations in graphene and nanotubes, defined by how they attach to the system, that we will examine in this work. These types are shown in Fig. 3.16 and are substitutional, top-adsorbed, bridge-adsorbed, and centre-adsorbed. It is our goal in Chap. 4 to analytically model the Indirect Exchange Coupling (IEC) between pairs of each of these conformation types in graphene and nanotubes. There we will make the argument that it is the conformation that determines the long range IEC behaviour of impurities, and not the atom type directly, as such we will deal with the magnetic moments in a generic fashion. However, we will briefly discuss now how various atom types are thought to conform in graphene and nanotubes.

Much effort has been expended to calculate the energetically favourable conformations of elements in graphene and nanotubes. The majority of these theoretical studies have used Density Functional Theory (DFT) techniques. Ex-

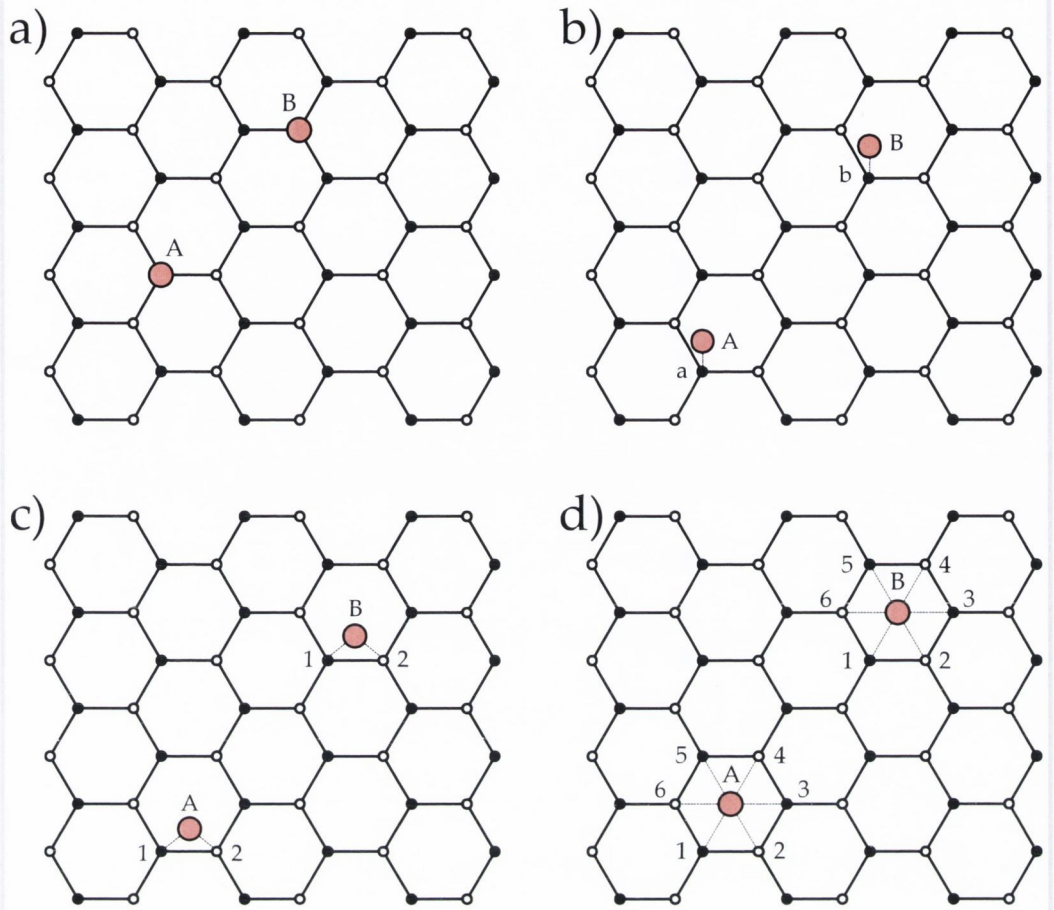


Figure 3.16: This is a schematic representation of two impurities A and B indicated by the red circles for a) substitutional impurities, b) top-adsorbed impurities, c) bridge-adsorbed impurities, and d) centre-adsorbed impurities.

perimental studies have been carried out with scanning tunnelling microscopy and spectroscopy [170]. Substitutional doping of graphene and nanotubes is fundamentally different to the three adsorbed types we will study, as the substitutions are usually added at the time of formation, though they may be added after this by creating vacancies in the lattice via ion irradiation [171]. Graphene and CNTs have been substitutionally doped with a variety of atoms including N, Al, P, Ga, and As [170, 172, 173]. However, it is centre-adsorbed impurities that are of particular interest since they are energetically favourable for many transition-metal atoms, including Mn, Fe, Co, and Ni [174–178]. In

DFT studies, transition metal elements are almost always found to be centre-adsorbed, and are usually found to have a large energy barrier to migration. Non-metallic elements are almost always found to be bridge-adsorbed, with certain elements shown to have a large bonding energy such as C, N, O [179, 180]. Interestingly, Si has been found to adsorb in all three conformations in CNTs, and may have some dependence on whether it is an armchair nanotube (ACNT) or zigzag nanotube (ZZNT) [181]. It has been suggested that top-adsorbed impurities can be determined by the number of valence electrons, as certain elements that are found to top-adsorb, such as H, F, Cl, Br, and I, all have a single valence electron [182].

3.4.1 *Impurity Conformation in Graphene and Nanotubes*

In this work we will discuss 4 types of impurity: substitutional, top-adsorbed, bridge-adsorbed, and centre-adsorbed (Fig 3.16). For most cases the top-adsorbed and substitutional impurities are found to display very similar behaviours, so we will generally discuss them together.

In Sec. 2.3 we introduced the idea of adding impurities to a material using the Dyson equation. We will now discuss this in more detail for graphene and nanotubes. Since the conformations of single impurities are extremely local, and since graphene and nanotubes have the same underlying hexagonal lattice, we will talk about impurity conformation to a hexagonal lattice, which applies equally to both systems.

In Chap. 4 we will introduce the IEC which describes the interaction of magnetic impurities. This interaction may be calculated in the presence of many magnetic moments, however when considering the behaviour of the interaction, we will consider it in the simplest case, *i.e.*, the interaction between two such impurities. As such we will now consider the addition of two impurities to the graphene lattice.

Substitutional Impurities

Substitutional impurities are the simplest kind of impurity to model. A substitutional impurity occurs when a carbon atom in the lattice is replaced by an atom of a different type, as represented by Fig. 3.16 a). This is modelled by making changes to the electronic structure parameters of graphene, such as the hopping integral to the nearest neighbour atoms or by changing the onsite energy. We will assume that the nearest neighbour hopping integral is not modified, though this can be included in our model it complicates the expressions somewhat. It will instead suffice to change the onsite energy. For two impurities, embedded in a graphene sheet, which have replaced the carbon atoms at some sites a and b, the perturbing potential is

$$\begin{aligned}\hat{V} &= |a\rangle(\varepsilon_1 - \varepsilon_0)\langle a| + |b\rangle(\varepsilon_1 - \varepsilon_0)\langle b| \\ &= |a\rangle\Delta\varepsilon\langle a| + |b\rangle\Delta\varepsilon\langle b|,\end{aligned} \tag{3.4.1}$$

where $|a\rangle$ is the atomic orbital at site a. Here ε_0 is the onsite energy for the host atoms, ε_1 is that of the impurity atom, and we generally choose to denote the difference between them $\Delta\varepsilon$. Each carbon atom in the graphene lattice is equivalent in pristine graphene and so the onsite energies are identical. The assumption that onsite energy of the impurity atoms is the same merely restricts us to the assumption that they are the same type of atom. The GF that connects them can then be calculated using the Dyson equation, Eq. 2.3.1, as

$$\hat{G}_{AB} = \left(\begin{pmatrix} 1 & 0 \\ 0 & 1 \end{pmatrix} - \begin{pmatrix} g_{aa} & g_{ab} \\ g_{ba} & g_{bb} \end{pmatrix}\begin{pmatrix} \Delta\varepsilon & 0 \\ 0 & \Delta\varepsilon \end{pmatrix}\right)^{-1}\begin{pmatrix} g_{aa} & g_{ab} \\ g_{ba} & g_{bb} \end{pmatrix}. \tag{3.4.2}$$

So far we have used lower case g_{ab} to refer to the GF between sites a and b of the pristine lattice, we now use capital G_{AB} to indicate that we are looking at the GF between two impurities A and B in a perturbed lattice. Since

g_{aa},g_{bb},g_{ab}, and g_{ba} are GFs of the pristine lattice, they have some equivalences, and we can make the simplification $g_{aa} = g_{bb}$ and $g_{ab} = g_{ba}$. The perturbed GF matrix, containing the modified interactions between these two impurities can now be written

$$\hat{G}_{AB} = \frac{1}{(g_{aa}\Delta\varepsilon - 1)^2 - g_{ab}^2\Delta\varepsilon^2} \begin{pmatrix} g_{aa} - g_{aa}^2\Delta\varepsilon + g_{ab}^2\Delta\varepsilon & g_{ab} \\ g_{ab} & g_{aa} - g_{aa}^2\Delta\varepsilon + g_{ab}^2\Delta\varepsilon \end{pmatrix}. \tag{3.4.3}$$

The symmetries of this matrix reflect the obvious underlying symmetries of the graphene sheet. We will generally focus our attention on the GF element between the two impurities, namely

$$G_{AB} = \frac{g_{ab}}{(g_{aa}\Delta\varepsilon - 1)^2 - g_{ab}^2\Delta\varepsilon^2}, \tag{3.4.4}$$

as this term contains all the separation dependence. Where we note that if the change in energy is zero, $\Delta\varepsilon = 0$, then we just recover the pristine graphene GF.

Top-Adsorbed Impurities

Adsorbed impurities are slightly more complicated to calculate than substitutional. Adsorbed impurities do not replace a carbon atom in the lattice, but instead sit above the lattice and bond to one or more sites. The simplest form of adsorbed impurity is the top-adsorbed impurity. The top-adsorbed impurity sits directly above a single carbon atom in the lattice, and bonds only to that atom, as represented by Fig. 3.16 b). The perturbing potential for two such impurities, one bonding to site a and the other bonding to site b, is

$$\hat{V} = |A\rangle\tau\langle a| + |a\rangle\tau\langle A| + |B\rangle\tau\langle b| + |b\rangle\tau\langle B|, \tag{3.4.5}$$

where τ defines the hopping integral between the impurity and a host lattice site, where we again assume that A and B are the same type of impurity. Our initial system consists of a graphene sheet and two isolated impurities. Each of these impurities has a self-energy ε_1, and a GF

$$g_{AA} = g_{BB} = \frac{1}{E - \varepsilon_1}, \tag{3.4.6}$$

that comes from the definition of the GF, Eq. 2.1.2. The GF matrix that describes all the relevant sites in the system is

$$\hat{g} = \begin{pmatrix} g_{AA} & 0 & 0 & 0 \\ 0 & g_{BB} & 0 & 0 \\ 0 & 0 & g_{aa} & g_{ab} \\ 0 & 0 & g_{ba} & g_{bb} \end{pmatrix}, \tag{3.4.7}$$

and the perturbation in matrix form is

$$\hat{V} = \begin{pmatrix} 0 & 0 & \tau & 0 \\ 0 & 0 & 0 & \tau \\ \tau & 0 & 0 & 0 \\ 0 & \tau & 0 & 0 \end{pmatrix}. \tag{3.4.8}$$

Again using the Dyson equation we can calculate the relevant matrix element corresponding to the GF between the two impurities

$$G_{AB} = \frac{g_{AA}^2 g_{ab} \tau^2}{1 - g_{AA} g_{aa} \tau^2 + g_{AA}^2 \tau^4 (g_{aa}^2 - g_{ab}^2)}, \tag{3.4.9}$$

where we have used the same symmetries as in the substitutional case, as well as the fact that $g_{AA} = g_{BB}$ to simplify the expression.

Bridge-Adsorbed and Centre-Adsorbed Impurities

A bridge-adsorbed impurity sits above the bond between two adjacent carbon atoms in the graphene lattice, as represented by Fig. 3.16 c). Again, this impurity is modelled by adding a hopping integral to the two nearest neighbour atoms, with the perturbing potential for two such impurities being

$$\hat{V} = \sum_{j=1}^{2} |A\rangle\tau\langle a_j| + |a_j\rangle\tau\langle A| + |B\rangle\tau\langle b_j| + |b_j\rangle\tau\langle B|. \tag{3.4.10}$$

Since the bridge-adsorbed impurities now bond to two sites we choose to label them with a subscript j, where j runs from 1 to the number of connected sites.

Centre-adsorbed impurities sit in the centre of a hexagon with a carbon atom at each vertex, as represented by Fig. 3.16 d). We will consider our impurities to be bonded equally to all six, and the perturbing potential describing two such impurities is

$$\hat{V} = \sum_{j=1}^{6} |A\rangle\tau\langle a_j| + |a_j\rangle\tau\langle A| + |B\rangle\tau\langle b_j| + |b_j\rangle\tau\langle B|. \tag{3.4.11}$$

The similarity between these two perturbing potentials allows us to approach the calculation of the GF between two adsorbed impurities using a slightly different method. This method will allow us to define a GF for bridge- and centre-adsorbed impurities in a unified manner, it can also be used to describe top-adsorbed impurities, but is needlessly complicated for that simple case. Using a different form of the Dyson equation we can write the Green's Function between two top-adsorbed impurities as

$$G_{AB} = g_{AB} + \langle A|\hat{g}\hat{V}\hat{G}|B\rangle, \tag{3.4.12}$$

where $g_{AB} = 0$ since A and B are disconnected in the initial system, and $\hat{V}$ is a generic perturbing potential of the form above, over some number of sites n. Expanding out the remaining term gives

$$\begin{aligned} G_{AB} &= \tau \sum_{j,k=1}^{n} \left(g_{AA} G_{a_j B} + g_{A a_j} G_{AB} + g_{AB} G_{b_k B} + g_{A b_k} G_{BB} \right) \\ &= \tau \sum_{j=1}^{n} g_{AA} G_{a_j B}, \end{aligned} \tag{3.4.13}$$

where the GFs $g_{A b_k}$ and $g_{A a_j}$ also go to zero since there is no connection between the impurities and any lattice site in the initial system. We now follow a process of applying the Dyson equation to any unknown perturbed GFs that arise in each equation. This gives

$$\begin{aligned} G_{a_j B} &= \underbrace{g_{a_j B}}_{=0} + \tau \sum_{k=1}^{n} \left(\underbrace{g_{a_j A}}_{=0} G_{a_j B} + g_{a_j a_k} G_{AB} + \underbrace{g_{a_j B}}_{=0} G_{b_j B} + g_{a_j b_k} G_{BB} \right) \\ &= \tau \sum_{k=1}^{n} \left(g_{a_j a_k} G_{AB} + g_{a_j b_k} G_{BB} \right), \end{aligned} \tag{3.4.14}$$

$$\begin{aligned} G_{BB} &= g_{BB} + \tau \sum_{k=1}^{n} \left(\underbrace{g_{BA}}_{=0} G_{a_k B} + \underbrace{g_{B a_k}}_{=0} G_{AB} + g_{BB} G_{b_k B} + \underbrace{g_{B b_k}}_{=0} G_{BB} \right) \\ &= g_{BB} + \tau \sum_{k=1}^{n} g_{BB} G_{b_k B}, \end{aligned} \tag{3.4.15}$$

$$\begin{aligned} G_{b_k B} &= \underbrace{g_{b_k B}}_{=0} + \tau \sum_{j=1}^{n} \left(\underbrace{g_{b_k A}}_{=0} G_{a_k B} + g_{b_k a_j} G_{AB} + \underbrace{g_{b_k B}}_{=0} G_{b_k B} + g_{b_k b_j} G_{BB} \right) \\ &= \tau \sum_{j=1}^{n} \left(g_{b_k a_j} G_{AB} + g_{b_k b_j} G_{BB} \right). \end{aligned} \tag{3.4.16}$$

Now combining Eqs. 3.4.15 and 3.4.16 yields

$$G_{BB} = g_{BB} + \tau^2 g_{BB} \sum_{j,k=1}^{n} \left(g_{b_k a_j} G_{AB} + g_{b_k b_j} G_{BB} \right), \tag{3.4.17}$$

and rearranging gives us the perturbed GF for the B impurity

$$\begin{aligned} G_{BB} &= \frac{g_{BB} + \tau^2 g_{BB} G_{AB} \sum g_{b_k a_j}}{1 - \tau^2 g_{BB} \sum g_{b_k b_j}} \\ &= \frac{g_{BB}(1 + G_{AB}\Gamma_{ba})}{(1 - g_{BB}\Gamma_{bb})}. \end{aligned} \tag{3.4.18}$$

Here we have defined the Gamma-sum function

$$\Gamma_{ab} = \tau^2 \sum_{j,k=1}^{n} g_{a_j b_k}. \tag{3.4.19}$$

Now looking at Eqs. 3.4.13 and 3.4.14 we have

$$\begin{aligned} G_{AB} &= \tau \sum_{j=1}^{n} g_{AA} G_{a_j B} \\ &= \tau^2 g_{AA} \sum_{j,k=1}^{n} \left(g_{a_j a_k} G_{AB} + g_{a_j b_k} G_{BB} \right) \\ &= g_{AA} G_{AB} \Gamma_{aa} + G_{AA} G_{BB} \Gamma_{ab}. \end{aligned} \tag{3.4.20}$$

Filling in for G_{BB} from Eq. 3.4.18, we have

$$\begin{aligned} G_{AB} &= g_{AA} G_{AB} \Gamma_{aa} + g_{AA} \Gamma_{ab} \left[\frac{g_{BB}(1 + \Gamma_{ba} G_{AB})}{(1 - g_{BB}\Gamma_{bb})} \right] \\ G_{AB}(1 - g_{AA}\Gamma_{aa}) &= g_{AA}\Gamma_{ab} \left[\frac{g_{BB}(1 + \Gamma_{ba} G_{AB})}{(1 - g_{BB}\Gamma_{bb})} \right] \\ G_{AB}(1 - g_{AA}\Gamma_{aa})(1 - g_{BB}\Gamma_{bb}) &= g_{AA}\Gamma_{ab} g_{BB}(1 + \Gamma_{ba} G_{AB}) \\ G_{AB}(1 - g_{AA}\Gamma_{aa})(1 - g_{BB}\Gamma_{bb}) - g_{AA}\Gamma_{ab} g_{BB}\Gamma_{ba} G_{AB} &= g_{AA}\Gamma_{ab} g_{BB} \\ G_{AB}(1 - g_{AA}\Gamma_{aa})(1 - g_{BB}\Gamma_{bb}) \left(1 - \frac{g_{AA}\Gamma_{ab} g_{BB}\Gamma_{ba}}{(1 - g_{AA}\Gamma_{aa})(1 - g_{BB}\Gamma_{bb})} \right) \\ = g_{AA}\Gamma_{ab} g_{BB}. \end{aligned} \tag{3.4.21}$$

So that we end up with

$$G_{AB} = g_{AA}\Gamma_{ab}g_{BB}\times \\ \times\left[(1-g_{AA}\Gamma_{aa})(1-g_{BB}\Gamma_{bb})\left(1-\frac{g_{AA}\Gamma_{ab}g_{BB}\Gamma_{ba}}{(1-g_{AA}\Gamma_{aa})(1-g_{BB}\Gamma_{bb})}\right)\right]^{-1}, \tag{3.4.22}$$

which is our GF between two impurities embedded in a graphene sheet, each connected to n lattice sites. That was quite a long and messy calculation, but the benefit of which is that we can describe all adsorbed impurities in this way. A simple check for this is to let all of the Gamma-sum functions in the previous expressions be a sum to $n = 1$, which recovers exactly the top-adsorbed impurity case of Eq. 3.4.9.

3.4.2 *Magnetic Impurities (Electron-electron Interactions)*

In Sec. 4.1 we will move on to discuss the interactions between magnetic impurities. However, the model we introduced in Sec. 3.1 to describe the electronic structure of graphene was single-body, tight-binding Hamiltonian, which does not take into account electron-electron interactions. And although this model is sufficient for many calculations it is not sufficient to describe magnetic impurities. The electron-electron interaction may be accounted for by including an additional many body term in the Hamiltonian using the Hubbard model approach.

Our simple tight-binding Hamiltonian is of the form

$$\hat{\mathcal{H}} = \sum_{i,j} |i\rangle t_{ij} \langle j|, \tag{3.4.23}$$

where, t_{ij} is the hopping integral between orbitals on sites i and j when these sites are nearest neighbours, is equal to the onsite energy of the site when $i = j$,

and is zero elsewhere. Starting from this we may rewrite the Hamiltonian to include the spin degree of freedom, σ,

$$\hat{\mathcal{H}} = \sum_{i,j,\sigma} t_{ij}\, \hat{c}^{\dagger}_{j\sigma}\, \hat{c}_{i\sigma}, \tag{3.4.24}$$

where we have introduced creation and annihilation operator notation such that $\hat{c}^{\dagger}_{j\sigma}$ creates an electron on site j with spin state σ, and $\hat{c}_{i\sigma}$ annihilates an electron on site i with spin state σ. This Hamiltonian is spin degenerate, which means that it cannot lead to the formation of moments. Magnetic moments result from an exchange term arising from the Coulomb repulsion between electrons. The Coulomb interaction term, which breaks the degeneracy between up and down spin electrons, is given by

$$\mathcal{H}_C = \sum_{i,j} \frac{e^2}{|\mathbf{r}_i - \mathbf{r}_j|}, \tag{3.4.25}$$

and allows for the formation of a moment. Here $\mathbf{r}_i$ is the position vector for site i and e is the single electron charge. This term may be written in a general operator form, between two arbitrary sites a and b, as

$$\mathcal{H}_{ab} = \frac{1}{2} \sum_{i,j,k,l} \langle i,j|\frac{e^2}{\mathbf{r}_{ab}}|k,l\rangle \sum_{\sigma,\sigma'} \hat{c}^{\dagger}_{i\sigma}\, \hat{c}^{\dagger}_{j\sigma'}\, \hat{c}_{k\sigma'}\, \hat{c}_{l\sigma}. \tag{3.4.26}$$

Here $\langle i,j|\frac{e^2}{\mathbf{r}_{ab}}|k,l\rangle = U_{i,j,k,l}$ is the expectation value of the Coulomb term. A basic assumption of the Hubbard model is that screening restricts the interaction to one site. This applies the restriction that $i = j = k = l$, so that the only term we need to consider corresponds to the Coulomb repulsion between electrons sharing the same orbital. By the Pauli exclusion principle this imposes

the further constraint that $\sigma \neq \sigma'$, and so we adopt the notation that $\overline{\sigma}$ is the opposite spin to σ. From this we can rewrite Eq. 3.4.26 as

$$\begin{aligned} \mathcal{H}_{\text{hub}} &= \frac{U}{2} \sum_{i\sigma} \hat{c}^{\dagger}_{i\sigma}\, \hat{c}_{i\sigma}\, \hat{c}^{\dagger}_{i\overline{\sigma}}\, \hat{c}_{i\overline{\sigma}} \\ &= \frac{U}{2} \sum_{i\sigma} \hat{n}_{i\sigma}\, \hat{n}_{i\overline{\sigma}}, \end{aligned} \tag{3.4.27}$$

which is now known as the Hubbard Hamiltonian. We have here introduced the notation $\hat{n}_{i\sigma} = \hat{c}^{\dagger}_{i\sigma}\, \hat{c}_{i\sigma}$, where $\hat{n}_{i\sigma}$ is known as the *number operator* and gives the occupation of a state at site i with spin σ.

However, to treat the exchange interaction as a single particle effect we must make a further approximation. We choose to apply the Mean-Field Approximation, which is done by trivially expanding the *number operator* in terms of its expectation value, $(\hat{n}_{i\sigma} - \langle n_{i\sigma}\rangle)$, as

$$\hat{n}_{i\sigma} = \langle n_{i\sigma}\rangle + (\hat{n}_{i\sigma} - \langle n_{i\sigma}\rangle)\,. \tag{3.4.28}$$

Making the assumption that $(\hat{n}_{i\sigma} - \langle n_{i\sigma}\rangle)$ is small, we may make an approximation that neglects terms of the form $(\hat{n} - \langle n\rangle)^2$. We may now write

$$\hat{n}_{i\sigma}\, \hat{n}_{i\overline{\sigma}} \approx \hat{n}_{i\sigma}\langle n_{i\overline{\sigma}}\rangle + \hat{n}_{i\overline{\sigma}}\langle n_{i\sigma}\rangle - \langle n_{i\sigma}\rangle\langle n_{i\overline{\sigma}}\rangle. \tag{3.4.29}$$

We now note that we have managed to express the many-particle term from the Hamiltonian as a sum of single-particle terms, where the last term applies a spin-independent shift to the band-centre of the magnetic atoms.

Now we define the average occupation on a site i as

$$\langle n_{i\sigma}\rangle = \langle n_{i\uparrow}\rangle + \langle n_{i\downarrow}\rangle = n_i \tag{3.4.30}$$

and the average magnetic moment on a site i as

$$\langle m_{i\sigma} \rangle = \langle n_{i\uparrow} \rangle - \langle n_{i\downarrow} \rangle = m_i, \tag{3.4.31}$$

i.e., the difference between up and down spins at a site. We may now write the Hubbard Hamiltonian as

$$\begin{aligned} \mathcal{H}_{hub} &= \sum_{i\sigma} \left(U \left(\frac{n_i}{2} - \langle n_{i\sigma} \rangle \langle n_{i\bar{\sigma}} \rangle \right) \mp \frac{1}{2} U m_i \right) \hat{n}_{i\sigma} \\ &= \sum_{i\sigma} \left(\delta_i \mp \frac{\Delta_i}{2} \right) \hat{n}_{i\sigma}, \end{aligned} \tag{3.4.32}$$

where the sign choice is $-$ for $\sigma = \uparrow$ and $+$ for $\sigma = \downarrow$. We have now simplified this expression into its spin-dependent and spin-independent components where $\frac{\Delta}{2}$ defines the exchange splitting, which we usually denote V_{ex}, between the up- and down-spin bands, and δ gives the shift in the bandcentre for the magnetic site. This band splitting leads to a greater occupation of one of the spin channels and hence the formation of a magnetic moment. Fig. 3.17 shows how the bands are split under the Hubbard Hamiltonian.

Using this Hamiltonian we can now calculate the GF of a system in the presence of magnetic moments. Within a simple model arbitrary values of Δ and δ may be used. However, in certain circumstances it may be necessary to apply a self-consistent procedure to calculate these values. For example, when doping graphene systems with objects that contain a magnetic moment. Applying this self-consistent procedure requires knowledge of the occupation number of the site and magnetic impurity to be added. For graphene and nanotubes the p_z orbital is half full, which corresponds to $n_i = 1$ for each site. For a specific magnetic impurity the occupation number can be found by comparison to *ab initio* calculations. Alternatively, this value can be varied over a range of values to simulate a variety of different magnetic impurities. The self-consistent procedure is implemented by first making an initial guess

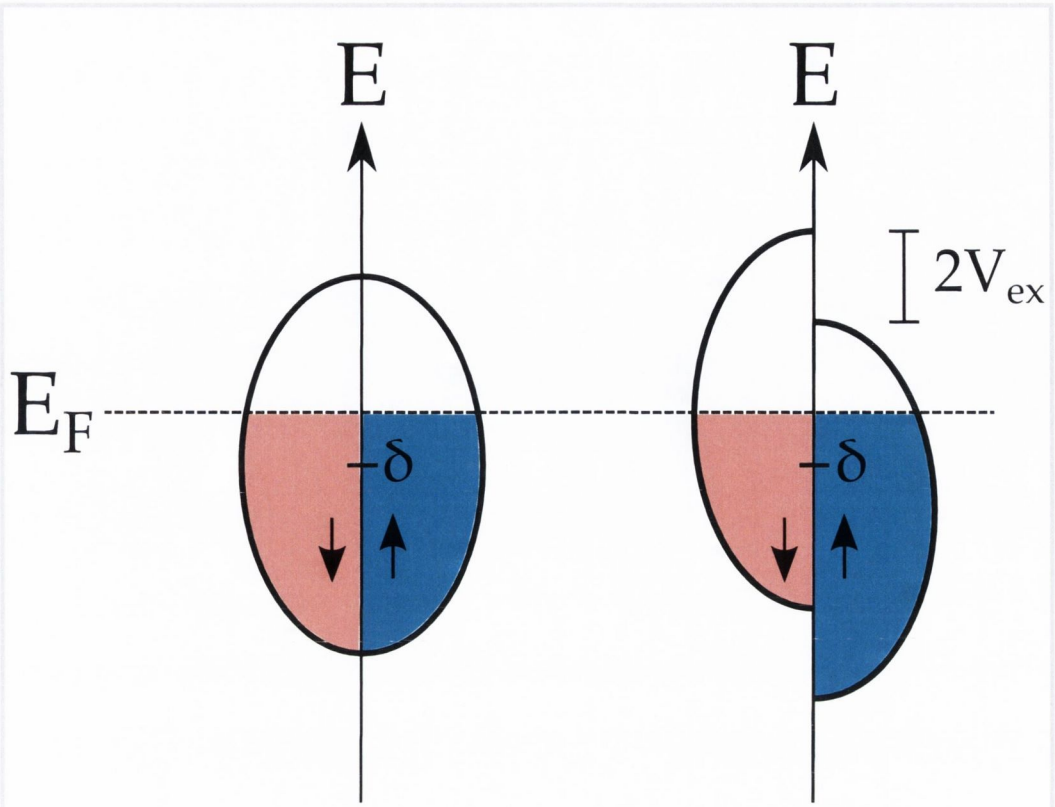


Figure 3.17: A diagram showing how the spin channels are altered in the new Hamiltonian, with the left image being before the bands are split and the right image after. The up-spin (down-spin) channel is shown with an up (down) arrow and coloured blue (red), with the bandcentre δ, the exchange splitting V_{ex}, and the Fermi energy E_F.

for the magnetic moments m_0 and bandcentres δ_0. These are then used to calculate the onsite potentials. Next applying the onsite potentials to the GF, the occupation of the up- and down- spin bands are calculated by integrating over the DOS. We then adjust the new bandcentre guess, δ_1, until the equation $n = n_\uparrow(\delta_1) - n_\downarrow(\delta_1)$ is satisfied, from which we can calculate our new guess for the magnetic moments m_1. This process can then be repeated until it is sufficiently converged. Once the converged values for m and δ have been calculated we may use them in our Hamiltonian to calculate our GF.

3.5 SUMMARY OF CHAPTER

We have now introduced the two main systems, and their corresponding Green's functions, that we will need throughout the remainder of this thesis: graphene in Sec. 3.1 and carbon nanotubes in Sec. 3.2.

We started with an examination of the properties and electronic structure of graphene in Sec. 3.1, which we examined in some depth before performing a detailed derivation of the graphene Green's function in Sec. 3.1.3. We then showed that these Green's functions may be written in a single integral form. In Sec. 3.1.4 we showed that the Stationary Phase Approximation may be applied to the graphene Green's function, under certain conditions, to write them in an analytic form. We then performed a similar set of examinations of the electronic structure of carbon nanotubes in Sec. 3.2.1, before deriving the nanotubes Green's functions for armchair and zigzag carbon nanotubes in Sec. 3.2.2. We also briefly discussed the use of Green's functions in the study of semi-infinite graphene and nanoribbons in Sec. 3.3.

In Sec. 3.4 we introduced the four impurity conformation types that we wish to examine, we then expanded our Hamiltonian to allow for the inclusion of magnetic moments. In the next chapter we will discuss how the change in system energy, caused by the interactions of these impurities, may be calculated. We will show how the methods introduced in Chaps. 2 and 3 will allow us to describe these changes in energy in a mathematically transparent manner. We will discuss these interactions for each impurity type, and as a function of various parameters.

4

INDIRECT EXCHANGE COUPLING IN MAGNETICALLY DOPED GRAPHENE-BASED MATERIALS

In this chapter we will discuss the Indirect Exchange Coupling between magnetic impurities in graphene and carbon nanotubes. We will begin with an introduction to the Indirect Exchange Coupling (Sec. 4.1), followed by a detailed discussion of how we may use the methods provided in Chap. 2 to calculate this coupling in a general system (Secs. 4.1.2 and 4.1.3). We will progress to show how the Indirect Exchange Coupling can be calculated using the Ruderman-Kittel-Kasuya-Yosida approximation (RRKY) in Sec. 4.1.5. We will then provide a detailed description of how we may use the Green's functions derived in Chap. 3 to write the RKKY approximation to the coupling between impurities in graphene and carbon nanotubes in an analytic fashion, and then use these analytic expressions to examine the coupling between various impurities in both systems (Secs. 4.2 and 4.3).

4.1 INDIRECT EXCHANGE INTERACTION

Recently, there has been much investment in the field of spintronics which has tremendous potential for technological applications. Low-dimensional structures such as graphene, nanowires, nanotubes, nanoribbons, silicene (and many more) are expected to be very useful when combined with spintronics, possibly leading to the production of extremely efficient magnetic sensors, high capacity memory storage, and non-volatile computer memories.

Important to spintronics is the mechanism of interaction between embedded impurities known as the indirect exchange interaction.

The direct exchange coupling between two magnetic objects depends on an overlap of the electron orbitals and, as such, decays rather abruptly with separation. In contrast to this the Indirect Exchange Coupling (IEC) between two magnetic objects embedded in a material is mediated solely by the conduction electrons of the host. The IEC was initially discovered in ultra-thin multilayered systems consisting of regions of the ferromagnetic material (Fe or Gd) separated by a region of the non-magnetic materials (Cr, Au, or Y), where the non-magnetic region is referred to as a spacer [54, 183]. Although the preliminary findings were of antiferromagnetic (AFM) coupling, later experiments with both Fe/Cr and Ru/Co systems found that the coupling actually oscillates as a function of the width of the spacer material [55] and that the oscillation period was mostly unaffected by the choice of magnetic material [56]. The coupling was also found to decay quite slowly, as approximately the inverse square of the separation, which is the expected decay rate for an essentially two-dimensional system [56], though we will see that graphene is an exception to this. The discovery of this coupling led directly to the discovery of the Giant Magnetoresistance Effect (GMR), which now forms the basis of most modern computer memories [45, 46].

4.1.1 *Quantum Well Method*

An indirect exchange interaction mediated by the conduction electrons of a host medium manifests as an energy difference between different alignments of the localized moments. Such an interaction is usually calculated within the RKKY approximation [53, 184, 185], and the interaction itself frequently takes this name [1].

1 Will we often use these terms synonymously throughout this work.

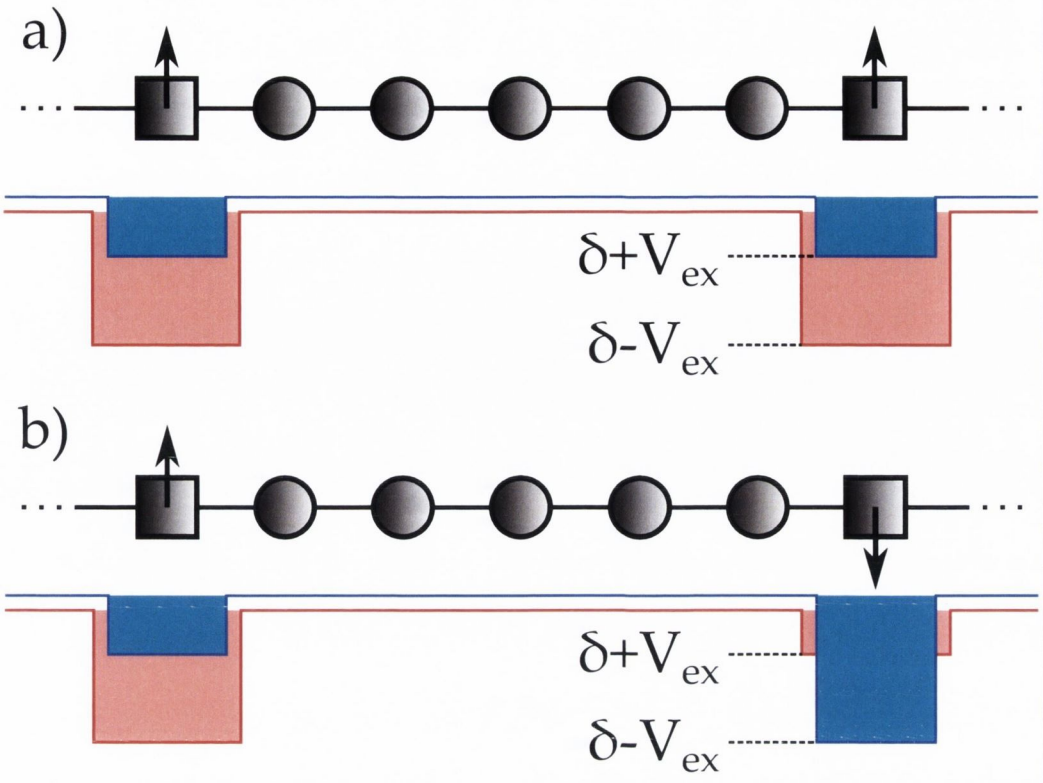


Figure 4.1: An illustration of a quantum well for a) parallel and b) anti-parallel alignments of magnetic moments (squares), embedded in a 1D chain of non-magnetic atoms (circles). The red and blue wells illustrate the spin-splitting potential, V_{ex}, from some bandcentre δ, experienced by up- and down-spin electrons respectively.

The IEC can be explained in terms of the Quantum Well Theory [52, 186]. This states that the spin-dependent potentials present in the system subject the electrons to one potential in the magnetic regions and another potential in the non-magnetic regions, as seen in Fig. 4.1. The spin-dependent potentials can be thought of as wells, and the presence of these wells quantises the allowed electron energies in the system. These allowed energies have a direct dependence on the width of the spacer material separating the magnetic moments. Changing the width of this spacer shifts these allowed energies of the system up and down relative to the Fermi energy. This relative energy shift gives rise to the observed oscillatory coupling as the allowed energies cross the Fermi energy in a decaying cyclical fashion. The Quantum Well The-

ory therefore explains the observed phenomenon that the alignment of the magnetic moments depended only on the width of the spacer.

4.1.2 *Energy Difference Calculation*

The coupling can be calculated by summing over all energies below the Fermi energy for two distinct systems - one with a spin potential corresponding to parallel aligned moments and one with a spin potential corresponding to anti-parallel aligned moments. Thus we define the coupling as $J = E^{\uparrow\uparrow} - E^{\downarrow\uparrow}$. We may now use the Lloyd formula method from Sec. 2.4 to calculate this as

$$\Delta E\,(E_F) = \frac{1}{\pi}\,\mathrm{Im}\int dE\; f(E)\,\ln\left(\det\left(\hat{I} - \hat{g}(E)\hat{V}\right)\right), \tag{4.1.1}$$

where $f(E)$ is the Fermi function, $\hat{g}$ is the GF matrix of our system, and $\hat{V}$ is the applied perturbation matrix. We first wish to look at the energy change in a system from adding the spin potential corresponding to two aligned moments at sites a and b, $\hat{V}^{\uparrow\uparrow}_{ab}$. When discussing GFs we previously found it useful to describe the GF propagator between two sites defined by vectors, $\mathbf{r}$ and $\mathbf{r}'$, however we will now switch to subscripts that reflect named sites, here a and b, to allow us to more easily consider operations on them. This energy is given by

$$\Delta E^{\uparrow\uparrow}_{ab} = \frac{1}{\pi}\,\mathrm{Im}\int dE\; f(E)\,\ln\left(\det\left(\hat{I} - \hat{g}(E)\hat{V}^{\uparrow\uparrow}_{ab}\right)\right). \tag{4.1.2}$$

The choice of $\Delta E^{\uparrow\uparrow}_{ab}$ is arbitrary and we may also have chosen $\Delta E^{\downarrow\downarrow}_{ab}$ with no distinction between the two. The quantity $\hat{g}$ is technically an infinite matrix containing the GF from all sites to all other sites, but since our perturbation is only applied to sites a and b we can reduce the GFs we have to deal with

to just the GFs at each site, g_{aa} and g_{bb}, and those between each site, g_{ab} and g_{ba}, as

$$\hat{g} = \begin{pmatrix} g_{aa} & g_{ab} \\ g_{ba} & g_{bb} \end{pmatrix}. \tag{4.1.3}$$

However, the magnetic moments break the spin degeneracy of the electrons so such a matrix does not allow us to deal with each spin channel separately. To allow us to deal with this we further define a new GF which is equal to the tensor product of our original GF with the identity matrix

$$\hat{G} = \hat{g} \otimes \hat{I} = \begin{pmatrix} g_{aa} & g_{ab} & 0 & 0 \\ g_{ba} & g_{bb} & 0 & 0 \\ 0 & 0 & g_{aa} & g_{ab} \\ 0 & 0 & g_{ba} & g_{bb} \end{pmatrix}. \tag{4.1.4}$$

The resulting matrix is block diagonal with the upper-left corresponding to the up-spin channel, and the lower right corresponding to the down-spin channel. The perturbation, $\hat{V}_{ab}^{\uparrow\uparrow}$, is then chosen such that it affects both spin channels symmetrically by adding (or subtracting) an exchange splitting V_{ex} (which was introduced in section 3.4.2) to the onsite potential,

$$\hat{V}_{ab}^{\uparrow\uparrow} = \begin{pmatrix} -V_{ex} & 0 & 0 & 0 \\ 0 & -V_{ex} & 0 & 0 \\ 0 & 0 & V_{ex} & 0 \\ 0 & 0 & 0 & V_{ex} \end{pmatrix}. \tag{4.1.5}$$

This shifts the band center of the onsite potential down by a quantity V_{ex} for the up-spin channel, and up by the same quantity for the down-spin channel.

Since the resulting matrix of $\hat{I} - \hat{G}(E)\hat{V}_{ab}^{\uparrow\uparrow}$ is block diagonal, we may use the property of matrices that

$$\det\begin{pmatrix} \hat{Y} & 0 \\ 0 & \hat{Z} \end{pmatrix} = \det(\hat{Y})\det(\hat{Z}), \tag{4.1.6}$$

to write the change in energy as

$$\begin{aligned} E_{ab}^{\uparrow\uparrow} = & \frac{1}{\pi}\,\mathrm{Im}\int dE\, f(E)\,\ln \\ & \left[\det\left(\hat{I} - \begin{pmatrix} g_{aa} & g_{ab} \\ g_{ba} & g_{bb} \end{pmatrix}\begin{pmatrix} -V_{ex} & 0 \\ 0 & -V_{ex} \end{pmatrix}\right)\right. \\ & \left.\times \det\left(\hat{I} - \begin{pmatrix} g_{aa} & g_{ab} \\ g_{ba} & g_{bb} \end{pmatrix}\begin{pmatrix} +V_{ex} & 0 \\ 0 & +V_{ex} \end{pmatrix}\right)\right]. \end{aligned} \tag{4.1.7}$$

Which can then be reduced to

$$\begin{aligned} E_{ab}^{\uparrow\uparrow} = & \frac{1}{\pi}\,\mathrm{Im}\int dE\, f(E)\,\ln \\ & \left[\left(1 + g_{aa}^2 V_{ex}^2 - 2g_{aa}V_{ex} - g_{ab}g_{ba}V_{ex}^2\right)\right. \\ & \left.\times\left(1 + g_{aa}^2 V_{ex}^2 + 2g_{aa}V_{ex} - g_{ab}g_{ba}V_{ex}^2\right)\right], \end{aligned} \tag{4.1.8}$$

where we have included the fact that $g_{aa} = g_{bb}$, since both represent the GFs at two particular sites which we assume to be equivalent in our unperturbed system. This equation represents the change in energy of the system from the initial system with two non-magnetic sites at a and b to a system where a and b are ferromagnetically (FM) aligned.

To calculate $E_{ab}^{\downarrow\uparrow}$, which represents the change in energy of the system from the initial system with two non-magnetic sites at a and b to a system where

a and b are magnetic and AFM aligned, we must introduce an asymmetric perturbation, $\hat{V}_{ab}^{\downarrow\uparrow}$,

$$\hat{V}_{ab}^{\downarrow\uparrow} = \begin{pmatrix} -V_{ex} & 0 & 0 & 0 \\ 0 & V_{ex} & 0 & 0 \\ 0 & 0 & V_{ex} & 0 \\ 0 & 0 & 0 & -V_{ex} \end{pmatrix}. \tag{4.1.9}$$

This shifts the band center of the onsite potential down by a quantity V_{ex} for the up-spin channel for the impurity at site a and up by the same quantity for the impurity at site b, and by the reverse for the down-spin channels. Again, we make no distinction between this and calculating $E_{ab}^{\uparrow\downarrow}$ with the perturbation $\hat{V}_{ab}^{\uparrow\downarrow}$. The Lloyd formula now yields

$$E_{ab}^{\uparrow\downarrow} = \frac{1}{\pi} \operatorname{Im} \int dE\, f(E) \ln \left[\left(1 - g_{aa}^2 V_{ex}^2 + g_{ab} g_{ba} V_{ex}^2 \right)^2 \right]. \tag{4.1.10}$$

Which now represents the change in energy from the initial system with two non-magnetic sites at a and b to a system where a and b are magnetic and AFM aligned.

To find the energetically favourable orientation these two can now be compared with

$$J = E_{ab}^{\uparrow\uparrow} - E_{ab}^{\uparrow\downarrow}, \tag{4.1.11}$$

where an overall negative sign corresponds to ferromagnetically (FM) aligned impurities being the lower energy state, and an overall positive sign corresponds to AFM aligned impurities being the lower energy state.

This method, though straightforward, requires the calculation of both changes to the system independently. To derive a simpler expression for the coupling we now look more closely at the equation

$$\begin{aligned} J &= E_{ab}^{\uparrow\uparrow} - E_{ab}^{\uparrow\downarrow} \\ &= \frac{1}{\pi}\,\mathrm{Im}\int dE\; f(E)\,\ln\left[\zeta^{\uparrow\uparrow}\right] - \frac{1}{\pi}\,\mathrm{Im}\int dE\; f(E)\,\ln\left[\zeta^{\uparrow\downarrow}\right] \\ &= \frac{1}{\pi}\,\mathrm{Im}\int dE\; f(E)\,\ln\left[\frac{\zeta^{\uparrow\uparrow}}{\zeta^{\uparrow\downarrow}}\right] \\ &= -\frac{1}{\pi}\,\mathrm{Im}\int dE\; f(E)\,\ln\left[\frac{\zeta^{\uparrow\downarrow}}{\zeta^{\uparrow\uparrow}}\right]. \end{aligned} \tag{4.1.12}$$

Where we have simplified the term inside the log from $E_{ab}^{\uparrow\downarrow}$ as $\zeta^{\uparrow\downarrow}$ and from $E_{ab}^{\uparrow\uparrow}$ as $\zeta^{\uparrow\uparrow}$, used the property of logarithms $\ln[Y] - \ln[Z] = \ln\left[\frac{Y}{Z}\right]$, and inverted the argument of the logarithm by extracting an overall minus sign. More closely examining the term,

$$\frac{\zeta^{\uparrow\downarrow}}{\zeta^{\uparrow\uparrow}} = \frac{\left(V_{ex}^2\left(g_{aa}^2 - g_{ab}g_{ba}\right) - 1\right)^2}{1 + V_{ex}^4\left(g_{aa}^2 - g_{ab}g_{ba}\right)^2 - 2V_{ex}^2\left(g_{aa}^2 + g_{ab}g_{ba}\right)}, \tag{4.1.13}$$

we see that the numerator can be expanded as

$$\begin{aligned} &= 1 + g_{aa}^4 V_{ex}^4 - 2g_{aa}^2 g_{ab}g_{ba}V_{ex}^4 - 2g_{aa}^2 V_{ex}^2 + g_{ab}^2 g_{ba}^2 V_{ex}^4 + 2g_{ab}g_{ba}V_{ex}^2 \\ &= \left(1 + V_{ex}^4\left(g_{aa}^2 - g_{ab}g_{ba}\right)^2 - 2V_{ex}^2\left(g_{aa}^2 + g_{ab}g_{ba}\right)\right) + 4g_{ab}g_{ba}V_{ex}^2, \end{aligned} \tag{4.1.14}$$

where we have added $2g_{ab}g_{ba}V_{ex}^2 - 2g_{ab}g_{ba}V_{ex}^2$ to allow the simplification. We now see that this is precisely the denominator plus another term, which allows us to write

$$\frac{\zeta^{\uparrow\downarrow}}{\zeta^{\uparrow\uparrow}} = 1 + \frac{4V_{ex}^2 g_{ab}g_{ba}}{1 + V_{ex}^4\left(g_{aa}^2 - g_{ab}g_{ba}\right)^2 - 2V_{ex}^2\left(g_{aa}^2 + g_{ab}g_{ba}\right)}. \tag{4.1.15}$$

This expression can be written more concisely by considering the modification of GFs spin channels. Such a perturbation is applied to the GF using the

Dyson equation. When we only consider the up-spin channel we see that the spin-dependent GF matrix, $\hat{g}^{\uparrow}$, can be written as

$$\hat{g}^{\uparrow} = \left(\hat{I} - \hat{g}\hat{V}^{\uparrow}\right)^{-1}\hat{g} = \begin{pmatrix} g^{\uparrow}_{aa} & g^{\uparrow}_{ab} \\ g^{\uparrow}_{ba} & g^{\uparrow}_{bb} \end{pmatrix}, \tag{4.1.16}$$

and where we can extract the following term

$$g^{\uparrow}_{ab} = \frac{g_{ab}}{1 + V_{ex}^2\left(g_{aa}^2 - g_{ab}g_{ba}\right) + 2g_{aa}V_{ex}}. \tag{4.1.17}$$

Similarly looking only at the down-spin channel (applying the $V^{\downarrow}$ perturbation) we may extract the term

$$g^{\downarrow}_{ba} = \frac{g_{ab}}{1 + V_{ex}^2\left(g_{aa}^2 - g_{ab}g_{ba}\right) - 2g_{aa}V_{ex}}. \tag{4.1.18}$$

We can therefore see that

$$g^{\uparrow}_{ab}g^{\downarrow}_{ba} = \frac{g_{ab}g_{ba}}{1 + V_{ex}^4\left(g_{aa}^2 - g_{ab}g_{ba}\right)^2 - 2V_{ex}^2\left(g_{aa}^2 + g_{ab}g_{ba}\right)}, \tag{4.1.19}$$

which enables us to rewrite Eq. 4.1.15 in the more simplified from

$$\frac{\zeta^{\uparrow\downarrow}}{\zeta^{\uparrow\uparrow}} = 1 + 4V_{ex}^2 g^{\uparrow}_{ab}g^{\downarrow}_{ba}. \tag{4.1.20}$$

So that the coupling equation, that determines the energetic alignment preference, can now be written simply as

$$J_{ab} = -\frac{1}{\pi}\,\mathrm{Im}\int_{-\infty}^{E_F} dE\,\ln\left[1 + 4V_{ex}^2 g^{\uparrow}_{ab}(E)g^{\downarrow}_{ba}(E)\right]. \tag{4.1.21}$$

Bearing in mind the definition of J, the energy difference between the FM and AFM alignments, we note that $J < 0$ corresponds to preferential parallel alignment, and $J > 0$ corresponds to preferential anti-parallel alignment.

4.1.3 *Moment Rotation Calculation*

This result can be generalized to allow a rotation of any angle by instead considering a rotation of one impurity relative to the other. We choose a spin perturbation which rotates the magnetic moment at b, by an angle ϕ, with respect to the magnetic moment at a. This perturbation is

$$\begin{aligned} V(\phi) &= -V_{ex}\left[(\cos(\phi)-1)\hat{\sigma}_z + \sin(\phi)\hat{\sigma}_x\right] \\ &= -V_{ex}\begin{bmatrix} \cos(\phi)-1 & \sin(\phi) \\ \sin(\phi) & 1-\cos(\phi) \end{bmatrix}, \end{aligned} \tag{4.1.22}$$

where $\hat{\sigma}_z$ and $\hat{\sigma}_x$ are the Pauli matrices.

The determinant term of the Lloyd formula is then written as

$$\begin{aligned} &\det\left[\hat{I} - g_{bb}(E)\hat{V}(\phi)\right] \\ &= \det\left[\hat{I} + V_{ex}\begin{pmatrix} g^{\uparrow}_{bb} & 0 \\ 0 & g^{\downarrow}_{bb} \end{pmatrix}\begin{pmatrix} \cos(\phi)-1 & \sin(\phi) \\ \sin(\phi) & 1-\cos(\phi) \end{pmatrix}\right] \\ &= 1 + V_{ex}\left(g^{\uparrow}_{bb} - g^{\downarrow}_{bb}\right)(\cos(\phi)-1) + 2V^2_{ex}g^{\uparrow}_{bb}g^{\downarrow}_{bb}(\cos(\phi)-1) \\ &= 1 + V_{ex}(\cos(\phi)-1)\left[\left(g^{\uparrow}_{bb} - g^{\downarrow}_{bb}\right) + 2V_{ex}g^{\uparrow}_{bb}g^{\downarrow}_{bb}\right]. \end{aligned} \tag{4.1.23}$$

To write this equation in a form that explicitly portrays the distance dependence we need to consider the relationship between $g^{\uparrow}_{bb}$ and $g^{\downarrow}_{bb}$. This can be done in the same manner as for $g^{\uparrow}_{ab}$ and $g^{\downarrow}_{ba}$ in Sec. 4.1.2 to determine the relationship

$$\left(g^{\uparrow}_{bb} - g^{\downarrow}_{bb}\right) + 2V_{ex}g^{\uparrow}_{bb}g^{\downarrow}_{bb} = g^{\uparrow}_{ab}g^{\downarrow}_{ba}. \tag{4.1.24}$$

We can then write the angle specific coupling equation as

$$J_{ab}(\phi) = -\frac{1}{\pi}\,\mathrm{Im}\int_{-\infty}^{E_F} dE\; f(E)\,\ln\left[1 - 2V_{ex}^2 g^{\uparrow}_{ab} g^{\downarrow}_{ba}(\cos(\phi) - 1)\right]. \tag{4.1.25}$$

In the case corresponding to perfect anti-parallel alignment, $\phi = \pi$, this of course reduces to Eq. 4.1.21 derived in Sec. 4.1.2.

4.1.4 *Numerical Calculation of the Coupling*

We will be using the form of the coupling presented in Eq. 4.1.25 in the remainder of this thesis. However, we may ease the numeric calculation of the coupling with some slight adjustments. Firstly, GFs over the real axis tend to be harder to calculate than those over the imaginary axis, as low dimensional systems can exhibit Van Hove singularities at certain energies. The first thing we wish to do is to use contour integration to rewrite the our integral over the imaginary axis, using the method described in Sec. 2.6. This allows us to write

$$\begin{aligned} J_{ab} &= -\frac{1}{\pi}\,\mathrm{Im}\int_{-\infty}^{E_F} dE\;\; \ln\left[1 + 4V_{ex}^2 g^{\uparrow}_{ab}(E) g^{\downarrow}_{ba}(E)\right] \\ &= \frac{1}{\pi}\mathrm{Im}\int_{0}^{\infty} dy\;\; i\ln\left(1 + 4V_{ex}^2 g^{\uparrow}_{ab}(E_F + iy) g^{\downarrow}_{ba}(E_F + iy)\right). \end{aligned} \tag{4.1.26}$$

To further reduce this, we consider our integral to be a general integral of the form

$$I = \frac{1}{\pi}\mathrm{Im}\left[\int i\; dy\,\ln(z(y))\right]. \tag{4.1.27}$$

Then, using the fact that $\mathrm{Im}[z] = \frac{1}{2i}(z - z^*)$, we can write

$$\begin{aligned} I &= \frac{1}{2\pi i}\left[\int i\ dy \ln(z) - \int -i\ dy \ln(z^*)\right] \\ &= \frac{1}{2\pi i}\left[\int i\ dy \ln(zz^*)\right] \\ &= \frac{1}{2\pi}\left[\int dy \ln|z|^2\right] \\ &= \frac{1}{\pi}\left[\int dy \ln|z|\right]. \end{aligned} \tag{4.1.28}$$

Which leads us finally to

$$J_{ab} = \frac{1}{\pi}\int_0^\infty dy\ \ln\left|1 + 4V_{ex}^2 g_{ab}^{\uparrow}(E_F + iy)\, g_{ba}^{\downarrow}(E_F + iy)\right|. \tag{4.1.29}$$

It is not always easy or convenient to integrate with infinities. Modern integrators can usually handle infinities just fine, however if we do wish to rescale the limits of our integral to get finite limits we may do so with the replacement $y = \frac{1-s}{s}$. So that our integral is now

$$\begin{aligned} J_{ab} = &\frac{1}{\pi}\int_0^1 ds\ \frac{1}{s^2} \\ &\times \ln\left|1 + 4V_{ex}^2 g_{ab}^{\uparrow}\left(E_F + i\left(\frac{1-s}{s}\right)\right) g_{ba}^{\downarrow}\left(E_F + i\left(\frac{1-s}{s}\right)\right)\right|, \end{aligned} \tag{4.1.30}$$

where we have flipped the integration limits to remove the minus sign that arises.

4.1.5 *The RKKY Formalism*

The coupling between magnetic objects embedded in a metallic host may also be accounted for using the Ruderman-Kittel-Kasuya-Yosida (RKKY) formalism. Originally developed as a way to describe the coupling mechanism of nuclear magnetic moments [53] it was generalized to provide a model capa-

ble of reproducing a whole range of experimental observations of indirect coupling phenomena [184, 185, 187]. This formalism uses the spin polarization of the conduction electrons of the host by the magnetic objects to explain the coupling between them. This approach gives a value for the coupling strength as

$$J_{ab} = -\frac{1}{4}\frac{1}{4\pi^2}\lambda^2 \hbar^2 \chi_{ab}, \tag{4.1.31}$$

which is an effective direct coupling. Here, $\hbar$ is Planck's constant and λ represents the magnitudes of the coupling between localized spins and conduction electrons. The χ term represents the static magnetic susceptibility, and may have a complicated form as it relates the response of the host magnetisation to a static magnetic field. We may understand how this relates to the IEC by looking at Eq. 4.1.21. Expanding the logarithm to first order in V_{ex} yields

$$\begin{aligned} J_{ab} &= \frac{4{V_{ex}}^2}{\pi}\mathrm{Im}\int dE\ f(E)\ [g_{ab}(E)g_{ba}(E)] \\ &= \left(-2{V_{ex}}^2\right)\left(-\frac{2}{\pi}\mathrm{Im}\int dE\ f(E)\ [g_{ab}(E)g_{ba}(E)]\right) \\ &= -2{V_{ex}}^2\,\chi^0_{ab}. \end{aligned} \tag{4.1.32}$$

Here χ^0_{ab} is the non-interacting static-susceptibility. This result is essentially the RKKY result that is obtained in the limit of small exchange splitting, so the RKKY formalism can be considered an approximation to the IEC. Both methods agree very well except for a few cases where the metallic host has peculiarities in their Fermi surfaces [188, 189]. In contrast to the Lloyd formula approach, which uses spin dependent GF, $g^{\uparrow}_{ab}$ and $g^{\downarrow}_{ab}$, this approach uses spin independent GFs, g_{ab} and g_{ba}. This provides a good approximation at large separations [189–191].

4.1.6 *Key Features of RKKY in Graphene-Based Materials*

The only requirement for the IEC to exist is the presence of localized magnetic moments in a metallic material that has conduction electrons to mediate the interaction. Graphene and metallic carbon nanotubes, embedded with magnetic impurities, fit this requirement. Coupled with the relative ease with which their electronic structures can be described makes them interesting materials in which to examine the IEC.

The IEC has been intensively studied in graphene and CNTs, where the focus has been on the sign, magnitude, and rate of decay of the interaction [67–84]. The consensus from these studies is that the interaction strength decays asymptotically as D^{-3} in undoped graphene, where D is the separation between magnetic moments. This decay rate is faster than the D^{-2} decay expected for conventional two-dimensional materials and arises from the vanishing density of states at the Fermi energy in graphene [78]. The usual sign-changing oscillations predicted for such interactions are masked by the coincidence of the Fermi surface and Brillouin zone. This unusual feature of graphene also causes this slower than expected decay rate. This causes the sign of the IEC - which determines the FM or AFM alignment of the moments - to only depend on whether the two moments occupy the same or opposite sublattices, and not on their separation. When graphene is doped or gated such that the Fermi surface no longer coincides with the Brillouin zone, sign-changing oscillations are recovered and the interaction is found to decay as D^{-2}.

The growing interest in carbon-based spintronics has stimulated a number of recent theoretical studies on the IEC in graphene with the aim of determining the most energetically favourable alignments between embedded magnetic moments. Recent studies suggest that the adsorption configurations favoured by many transition-metal impurities may lead to even shorter

ranged decays and possible sign-changing oscillations. Here we show that these features emerge in a mathematically transparent manner when the symmetry of the configurations is included in the calculation. Centre-adsorbed impurities are of particular interest since they are energetically favourable for many transition-metal atoms [174, 179, 182]. There is some discrepancy in the literature about the basic features of the interaction between centre-adsorbed impurities. Some studies suggest an interaction which is always AFM and decays as D^{-3} (the same decay rate predicted for substitutional) while others suggest a decay rate of D^{-7} with a FM interaction at some separations [70, 75, 76]. This discrepancy is similar to the related case of carbon nanotubes, where centre-adsorbed impurities are predicted to display a decay rate of D^{-5} instead of D^{-1} found for substitutional, top- and bridge-adsorbed impurities [83, 84, 86].

In the following sections we explore these features in a mathematically transparent manner for the four types of impurities that we have introduced. This will be carried out in both high-symmetry directions for graphene, and longitudinally for both ACNTs and ZZNTs.

4.2 EVALUATION OF THE RKKY IN GRAPHENE

With the motivation of understanding the functional form of the RKKY interaction we will now examine this in graphene. In this two-dimensional material the expected decay rate of the coupling is D^{-2} with separation D. However, we will show that at zero Fermi energy the coupling actually decays as D^{-3}, and for centre-adsorbed impurities as D^{-7}. We will examine it for the four impurity conformations types we introduction in Sec. 3.4, with the understanding that substitutional and top-adsorbed impurities have very similar properties in our model and we will usually discuss them together.

4.2.1 *Derivation of the RKKY in Graphene*

In Sec. 4.1.5 we derived the RKKY approximation to the IEC for a generic GF. Here we will use the Stationary Phase Approximation (SPA) GFs from Sec. 3.1.4 to derive an analytic expression for the coupling along the high-symmetry directions of graphene. To derive this form of the coupling within the RKKY we start with the expression for the coupling from Eq. 4.1.32,

$$J_{ab} \sim \mathrm{Im} \int dE\, f(E)\, V_{ex}^2 g_{ab}(E) g_{ba}(E), \tag{4.2.1}$$

where g_{ab} and g_{ba} are the pristine graphene GFs between two sites a and b. To obtain an analytic form for the coupling we must use the SPA of the GF, g_D, from Eq. 3.1.61,

$$g_D(E) = \mathcal{A}(E) \frac{e^{iq(E)D}}{\sqrt{D}}. \tag{4.2.2}$$

This describes the GF between two sites separated by a distance D_A in the armchair direction or D_Z in the zigzag direction. We neglect the subscript in our GFs here to maintain generality. Using the SPA GF we can write the coupling as

$$\begin{aligned} J_D &\sim \mathrm{Im} \int dE\, V_{ex}^2 \, \frac{1}{1 + e^{\frac{E-E_F}{k_B T}}} \frac{\mathcal{A}^2(E) e^{2iq(E)D}}{D} \\ &\sim \frac{V_{ex}^2}{D} \mathrm{Im} \int dE\, \frac{\mathcal{B}(E) e^{2iq(E)D}}{1 + e^{\frac{E-E_F}{k_B T}}}, \end{aligned} \tag{4.2.3}$$

where we have replaced the J_{ab} subscript with J_D to denote that this is now only valid under the same conditions as the SPA GF, g_D, *i.e.*, along the high symmetry directions. We have also defined a function $\mathcal{B} = \mathcal{A}^2$ for simplicity, and written the Fermi function in its full form, where k_B is the Boltzmann

constant and T is the temperature. This can now be solved using contour integration where the poles are given by the zeros of the denominator, in this case the Matsubara frequencies $E_p = E_F + i(2p+1)\pi k_B T$ where p is an integer labelling the poles. We can now write the coupling as

$$J_D \sim \frac{V_{ex}^2}{D} \text{ Im } 2\pi i \text{ Res} \sum_p \left[\frac{\mathcal{B}(E) e^{2iq(E)D}}{1 + e^{\frac{E-E_F}{k_B T}}} \right] \Bigg|_{E=E_p} . \tag{4.2.4}$$

Applying the residue theorem, the derivative of the denominator is

$$\frac{d}{dE}\left(e^{\frac{E-E_F}{k_B T}}\right)\Big|_{E=E_p} = \frac{1}{k_B T} e^{\frac{E-E_F}{k_B T}}\Big|_{E=E_p} = \frac{1}{k_B T} \underbrace{e^{\frac{1}{k_B T}(i\pi(2p+1)k_B T)}}_{=-1}. \tag{4.2.5}$$

So that the coupling is now given by

$$J_D \sim 2\pi \frac{V_{ex}^2 k_B T}{D} \text{Im} \sum_p \left[i\mathcal{B}(E_p)\, e^{2iq(E_p)D} \right]. \tag{4.2.6}$$

We can now expand $\mathcal{B}$ as a Taylor series around the Fermi energy, and $q(E)$ as a first order expansion,

$$\begin{aligned} \mathcal{B}(E) &= \sum_\ell \frac{1}{\ell!} \mathcal{B}^{(\ell)} (E - E_F)^\ell, \\ q(E) &= q^{(0)} + q^{(1)}(E - E_F). \end{aligned} \tag{4.2.7}$$

Here we have introduced the notation

$$\mathcal{B}^{(\ell)} = \frac{d^l \mathcal{B}}{dE^\ell}\Big|_{E=E_F}, \tag{4.2.8}$$

that defines the ℓth derivative of a function with respect to E evaluated at the Fermi energy. So that the expression for the coupling now becomes

$$\begin{aligned} J_D &\sim 2\pi \frac{V_{ex}^2 k_B T}{D} \mathrm{Im} \sum_\ell \sum_p \frac{i}{\ell!} \mathcal{B}^{(\ell)} (E_p - E_F)^\ell \, e^{2i\left(q^{(0)} + q^{(1)}(E_p - E_F)\right)D} \\ &\sim 2\pi \frac{V_{ex}^2 k_B T}{D} \mathrm{Im} \sum_\ell \frac{i}{\ell!} \mathcal{B}^{(\ell)} e^{2iq^{(0)}D} \sum_p e^{2iq^{(1)}(E_p - E_F)D} (E_p - E_F)^\ell \\ &\sim 2\pi \frac{V_{ex}^2 k_B T}{D} \mathrm{Im} \sum_\ell \frac{i}{\ell!} \mathcal{B}^{(l)} e^{2iq^{(0)}D} \frac{1}{\left(2iq^{(1)}\right)^\ell} \frac{d^\ell}{dD^\ell} \left[\sum_p e^{2iq^{(1)}(E_p - E_F)D} \right]. \end{aligned} \tag{4.2.9}$$

Where, in the last line, we have used the fact that $\frac{d^\ell}{dD^\ell} e^{YZD} = e^{YZD} Y^{(\ell)} Z^{(\ell)}$. Focusing on the term inside the square brackets for a moment, we may use the Matsubara frequencies to write

$$\begin{aligned} \sum_p e^{2iq^{(1)}(E_p - E_F)D} &= \sum_p e^{-2q^{(1)}(2p+1)\pi k_B T D} \\ &= e^{-2q^{(1)}\pi k_B T D} \sum_p \left(e^{-4q^{(1)}\pi k_B T D} \right)^p \\ &= \frac{e^{-2q^{(1)}\pi k_B T D}}{1 - e^{-4q^{(1)}\pi k_B T D}} \\ &= \frac{1}{2\sinh(2q^{(1)}\pi k_B T D)}, \end{aligned} \tag{4.2.10}$$

which in the low temperature limit, $T \rightharpoonup 0$, is $2\sinh(2q^{(1)}\pi k_B T D) \rightharpoonup 4q^{(1)}\pi k_B T D$. So we now have

$$\begin{aligned} J_D &\sim 2\pi \frac{V_{ex}^2}{D} \mathrm{Im} \sum_\ell \frac{i}{\ell!} \mathcal{B}^{(\ell)} e^{2iq^{(0)}D} \frac{1}{\left(2iq^{(1)}\right)^\ell} \frac{d^\ell}{dD^\ell} \left[\frac{1}{4q^{(1)}\pi D} \right] \\ &\sim 2\pi V_{ex}^2 \mathrm{Im} \left(e^{2iq^{(0)}D} \sum_\ell \left[\frac{i}{\ell!} \mathcal{B}^{(\ell)} \frac{1}{D} \frac{1}{(i)^\ell \left(2q^{(1)}\right)^\ell} \frac{1}{2\pi \left(2q^{(1)}\right)^1} \frac{d^\ell}{dD^\ell} \left(\frac{1}{D} \right) \right] \right) \\ &\sim V_{ex}^2 \mathrm{Im} \left(e^{2i\left(q^{(0)}\right)D} \sum_\ell \left[\frac{i}{\ell!} \mathcal{B}^{(\ell)} \frac{1}{D} \frac{1}{(i)^\ell \left(2q^{(1)}\right)^{\ell+1}} \left(\frac{(-1)^\ell \ell!}{D^{\ell+1}} \right) \right] \right) \\ &\sim V_{ex}^2 \ \mathrm{Im} \left(e^{2i\left(q^{(0)}\right)D} \sum_\ell \left[\mathcal{B}^{(\ell)} (i)^{\ell+1} \frac{1}{\left(2q^{(1)}\right)^{\ell+1}} \frac{1}{D^{\ell+2}} \right] \right). \end{aligned} \tag{4.2.11}$$

The final form of which is

$$J_D = -V_{ex}^2 \, \mathrm{Im}\left(e^{2iq^{(0)}D} \sum_{\ell} \left[\frac{\mathcal{B}^{(\ell)}}{\left(2iq^{(1)}\right)^{\ell+1}} \frac{1}{D^{\ell+2}} \right] \right). \tag{4.2.12}$$

In this form the oscillation period and decay rate of the interaction at different Fermi energies can be easily extracted. The decay rate in the asymptotic limit is determined by the leading order term, which is determined by the first non-vanishing $\mathcal{B}^{(\ell)}$. The oscillation period is determined by the term $e^{2iq^{(0)}D}$. The above equation suggests that $J \sim D^{-2}$,however we will show in the next sections that the decay rate has both a dependence on the Fermi energy, and on the conformation of magnetic impurities. We will also show that our model can not only capture the $J \sim D^{-3}$ behaviour but that it can also show, in a mathematically transparent manner, why the coupling between centre-adsorbed impurities goes as D^{-7}. Furthermore, it is the simple form of this expression that will allow us to clearly understand the effects of uniaxial strain on the RKKY in Chap. 5.

4.2.2 *Key Quantities for Graphene*

There are certain key quantities that arise again and again when attempting to evaluate the coupling between impurities, namely $\mathcal{B}$, $q^{(0)}$, and $q^{(1)}$, which can be seen from Eq. 4.2.12. Of these, $\mathcal{B}$ has separation, conformation, energy, and sublattice dependence, whereas $q^{(0)}$ and $q^{(1)}$ only have separation and energy dependence. However, we find it useful to evaluate these here in a generic way to avoid as much repetition as possible in the following sections. Where necessary we will use the subscripts A and Z to denote the separation along which the term is valid, standing for armchair and zigzag respectively.

The term $\mathcal{B}$ is actually just $\mathcal{A}^2$. For armchair separated impurities this term is

$$\mathcal{A}_A = N_{\gamma\gamma'}\sqrt{\frac{2i}{\pi}}\frac{1}{\sqrt{E(E^2+3t^2)\sqrt{t^2-E^2}}}, \tag{4.2.13}$$

and for zigzag separated impurities it is

$$\mathcal{A}_Z = N_{\gamma\gamma'}\sqrt{\frac{1}{2i\pi}}\frac{1}{\sqrt{E|t|(t\pm E)\sqrt{4t^2-(E\pm t)^2}}}, \tag{4.2.14}$$

where, in the zigzag direction, the sign chosen will depend on which pole we are summing over, though in practice we can consider either pole as they will both lead to the same decay rate. The term $N_{\gamma\gamma'}$ is the sublattice dependent term introduced in Eq. 3.1.25, and only applies to the substitutional and top-adsorbed cases. For bridge- and centre-adsorbed impurities, which adsorb to multiple sites, we have seen in Sec. 3.4.1 that the separation dependent behaviour of the full GF is determined by that of Γ_{ab} and so we can make the additional approximation to the coupling

$$J_D \sim -V_{ex}^2\,\mathrm{Im}\int dE\, f(E)\,\Gamma_{ab}^2(E)\,, \tag{4.2.15}$$

which encapsulates all the relevant separation-dependent behaviour of the interaction between adsorbed impurities. This Γ_{ab} term contains a sum over GFs between connected lattice sites

$$\Gamma_{ab} = g_{a_1b_1} + g_{a_1b_2} + \cdots, \tag{4.2.16}$$

and assuming these sites are located in the same unit cell we may write

$$\begin{aligned}\Gamma_{ab} &= N_{\gamma_1\gamma_1'}\,\overline{\mathcal{A}}(E)\,\frac{e^{iq(E)D}}{\sqrt{D}} + N_{\gamma_1\gamma_2'}\,\overline{\mathcal{A}}(E)\,\frac{e^{iq(E)D}}{\sqrt{D}} + \cdots \\ &= \left(N_{\gamma_1\gamma_1'} + N_{\gamma_1\gamma_2'} + \cdots\right)\,\overline{\mathcal{A}}(E)\,\frac{e^{iq(E)D}}{\sqrt{D}} \\ &= N_\Gamma\,\overline{\mathcal{A}}(E)\,\frac{e^{iq(E)D}}{\sqrt{D}}.\end{aligned} \tag{4.2.17}$$

Here we have defined two new terms: $\overline{\mathcal{A}}(E)$ which we define as $\mathcal{A}(E) = N_{\gamma\gamma'}\overline{\mathcal{A}}(E)$, is just the $\mathcal{A}(E)$ term with the sublattice dependence extracted, and N_Γ is just the sum over the sublattice terms that arises when summing over GF. For sites not located in the same unit cell we must make a slight variation to this method. This occurs in when looking at the interaction between centre-adsorbed impurities and we will discuss it in Sec. 4.2.5.

Looking at the form of Eq. 4.2.12 we see that the most important term in determining the decay behaviour of the coupling is the first non-zero derivative of $\mathcal{B}$ with respect to energy. For armchair separations this is

$$\mathcal{B}_A = \frac{2iN_{\gamma\gamma'}^2}{\pi(E^2+3t^2)\sqrt{t^2-E^2}}, \tag{4.2.18}$$

and for zigzag separations it is

$$\mathcal{B}_Z = -\frac{iN_{\gamma\gamma'}^2}{2\pi tE(E+t)\sqrt{4t^2-(E+t)^2}}. \tag{4.2.19}$$

The terms $q^{(0)}$ and $q^{(1)}$ represent, respectively, the Fermi vector evaluated at the Fermi energy and the first derivative of the Fermi vector also evaluated at the Fermi energy. For impurities separated along the armchair direction the Fermi vector is given by Eq. 3.1.51,

$$q_A = \pm\cos^{-1}\left(-\sqrt{1-\frac{E^2}{t^2}}\right) = \pi - \sin^{-1}\left(\sqrt{\frac{E^2}{t^2}}\right), \tag{4.2.20}$$

so that the zero-th and first derviatives with respect to energy, evaluated at $E_F = 0$, are given by

$$q_A^{(0)} = \pi, \quad q_A^{(1)} = \pm\frac{1}{t}. \tag{4.2.21}$$

For impurities separated along the zigzag direction the Fermi vector is, from Eq. 3.1.57,

$$q_Z^{\pm} = \pm\cos^{-1}\left(\frac{-t \mp E}{2t}\right), \tag{4.2.22}$$

and just considering one of the poles we find

$$q_Z^{+(0)} = \frac{2\pi}{3}, \quad q_Z^{+(1)} = \frac{1}{\sqrt{3}t}. \tag{4.2.23}$$

We will now proceed to evaluate the first non-vanishing $\mathcal{B}^{(l)}$ for each impurity type, and in each high symmetry direction, and hence determine the expected decay rates of the coupling between them.

4.2.3 *RKKY Between Substitutional and Top-Adsorbed Impurities*

We will begin by examining substitutional impurities, *i.e.*, those that replace a single carbon atom in the graphene lattice. For substitutional and top-adsorbed impurities we will restrict our derivation to sites on the same sublattice so that $N_{\gamma\gamma'} = E$, although it can be easily evaluated for sites on opposite sublattices. We will choose an energy shift of $\epsilon_A = 0$ for neatness. Under our approximation the RKKY interaction between top-adsorbed impurities is very similar to that of substitutional impurities. The only difference being a prefactor of τ^4 coming from the hopping integral of the disconnected impurity to the host site. As such, what follows applies to both substitutional and top-adsorbed impurities.

Armchair Separation

We start with the term

$$\mathcal{B}_A = \frac{2iE}{\pi(E^2+3t^2)\sqrt{t^2-E^2}}. \tag{4.2.24}$$

From this it is obvious that $\mathcal{B}_A^{(0)} = 0$ so the first term in the sum disappears. We now look at $l = 1$, this gives

$$\mathcal{B}_A^{(1)} = \frac{2i}{\pi}\frac{1}{3t^3}. \tag{4.2.25}$$

So the coupling, which is given by Eq. 4.2.12, can now be evaluated as

$$\begin{aligned} J_D &\sim -V_{ex}^2 \mathrm{Im}\left(\left(\cos\left(2q_A^{(0)}D_A\right)+i\sin\left(2q_A^{(0)}D_A\right)\right)\frac{\mathcal{B}^{(1)}}{\left(2iq_A^{(1)}\right)^2}\frac{1}{{D_A}^3}\right) \\ &\sim -V_{ex}^2 \mathrm{Im}\left(\frac{2i\left(\cos\left(2\pi D_A\right)+i\sin\left(2\pi D_A\right)\right)}{-12\pi t^3\left(q_A^{(1)}\right)^2{D_A}^3}\right) \\ &\sim V_{ex}^2\frac{1}{6\pi t}\frac{1}{{D_A}^3}, \end{aligned} \tag{4.2.26}$$

where $\cos(2\pi D_A) = 1$ as $D_A \in \mathbb{Z}$. So that the coupling decay rate, as a function of distance is $J_D \sim D^{-3}$, and there is no oscillation period indicating a linear function. This decay rate is a unique feature of graphene where the coupling is expected to decay with the dimensionality of the system. When evaluated at $E_F \neq 0$ we find that $\mathcal{B}^{(0)} \neq 0$, hence the decay rate of J_D goes as D^{-2}, and an oscillation period is introduced into the coupling.

Zigzag Separation

For zigzag separations we start with the term

$$\mathcal{B}_Z = -\frac{iE}{2\pi t(E+t)\sqrt{4t^2-(E+t)^2}}, \tag{4.2.27}$$

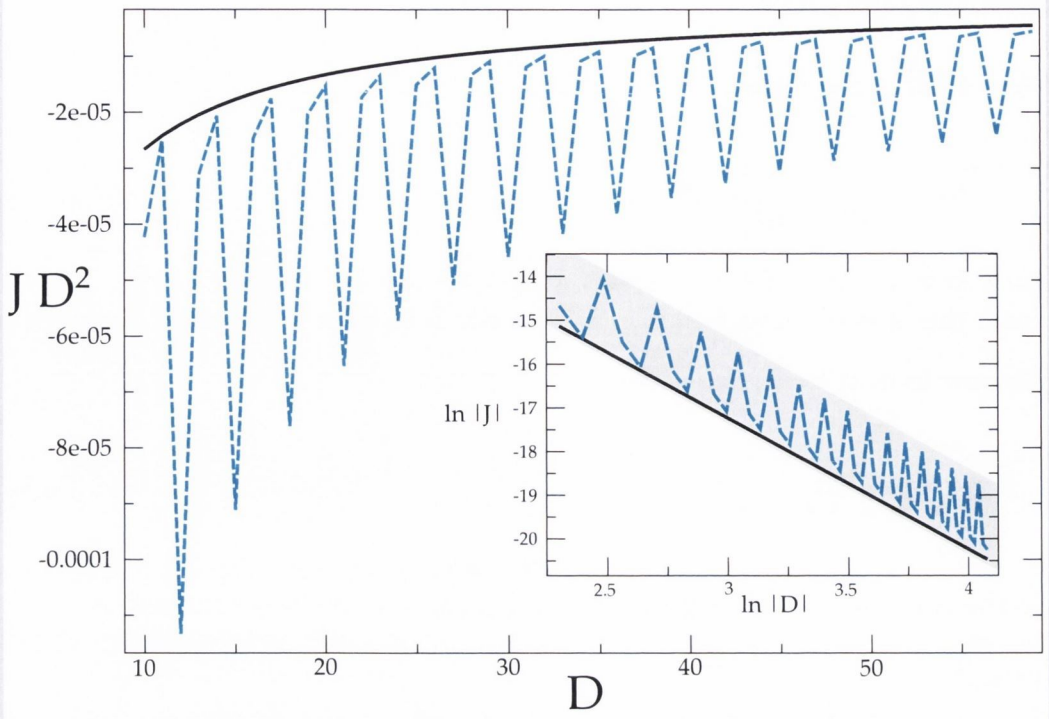


Figure 4.2: Plot of the Indirect Exchange Coupling (J) between substitutional impurities on the same sublattice in graphene along the high-symmetry directions: armchair (solid-black), zigzag (dashed-blue). The main plot shows the coupling scaled by the distance squared (D^2) to exaggerate the features. The inset shows a log-log plot of the coupling against the separation with a D^{-3} decay rate indicated by the grey band.

where again it is obvious that $B_Z^{(0)} = 0$, so that the first non-vanishing derivative is

$$\mathcal{B}_Z^{(1)} = -\frac{i}{\sqrt{3}\pi t^3}. \tag{4.2.28}$$

From this we can directly determine the coupling to be

$$J_D \sim -V_{ex}^2 \cos\left(\frac{4\pi}{3} D_Z\right) \frac{\sqrt{3}}{4\pi t} \frac{1}{{D_Z}^3}. \tag{4.2.29}$$

Again the coupling is found to decay as $J_D \sim D^{-3}$, but we now find a oscillation term $\cos\left(\frac{4\pi}{3} D_Z\right)$.

Figure 4.2 plots the full numerical calculation of the coupling between two substitutional impurities on the same sublattice for $V_{ex} = 0.2$ and $t = -1$, in both the armchair and zigzag directions. Here the solid-black line shows the smooth decay of the coupling for armchair separations, as well as the D^{-3} decay rate in the inset. Here we see an excellent match between the analytic results, Eq. 4.2.26, and the numerically evaluated results. The dashed-blue line shows the distinctive triplet pattern arising from the oscillation term in Eq. 4.2.29 for zigzag separations, where again the D^{-3} behaviour is seen in the inset.

4.2.4 *RKKY Between Bridge-Adsorbed Impurities*

For bridge-adsorbed impurities we need to replace the $N_{\gamma\gamma'}$ term in Eqs. 4.2.13 and 4.2.14. These are replaced by Eq. 4.2.17, which is defined as the sum of the sublattice terms of the connected sites, $N_\Gamma = N_{\alpha\alpha} + N_{\beta\beta} + N_{\alpha\beta} + N_{\beta\alpha}$. We note that by symmetry $N_{\alpha\beta} = N_{\beta\alpha}$ for zigzag separated impurities, which is not true for armchair separations.

Armchair Separation

For armchair separated bridge-adsorbed impurities, we have the sublattice term

$$\begin{aligned} N_\Gamma &= N_{\alpha\alpha} + N_{\beta\beta} + N_{\alpha\beta} + N_{\beta\alpha} \\ &= E + E + f(k) + f^*(k) \\ &= \frac{2E(E+t)}{t}. \end{aligned} \tag{4.2.30}$$

This gives us

$$\mathcal{B}_A = \frac{2i}{\pi} \frac{4E(E+t)^2}{t^2(E^2+3t^2)\sqrt{t^2-E^2}}. \tag{4.2.31}$$

Once again we find $\mathcal{B}^{(0)} = 0$, and that

$$\mathcal{B}_A^{(1)} = \frac{8i}{3\pi t^3}, \tag{4.2.32}$$

is the first non-vanishing term in the series. We can now write the coupling as

$$J_D \sim V_{ex}^2 \frac{2}{3\pi t} \frac{1}{D_A{}^3}. \tag{4.2.33}$$

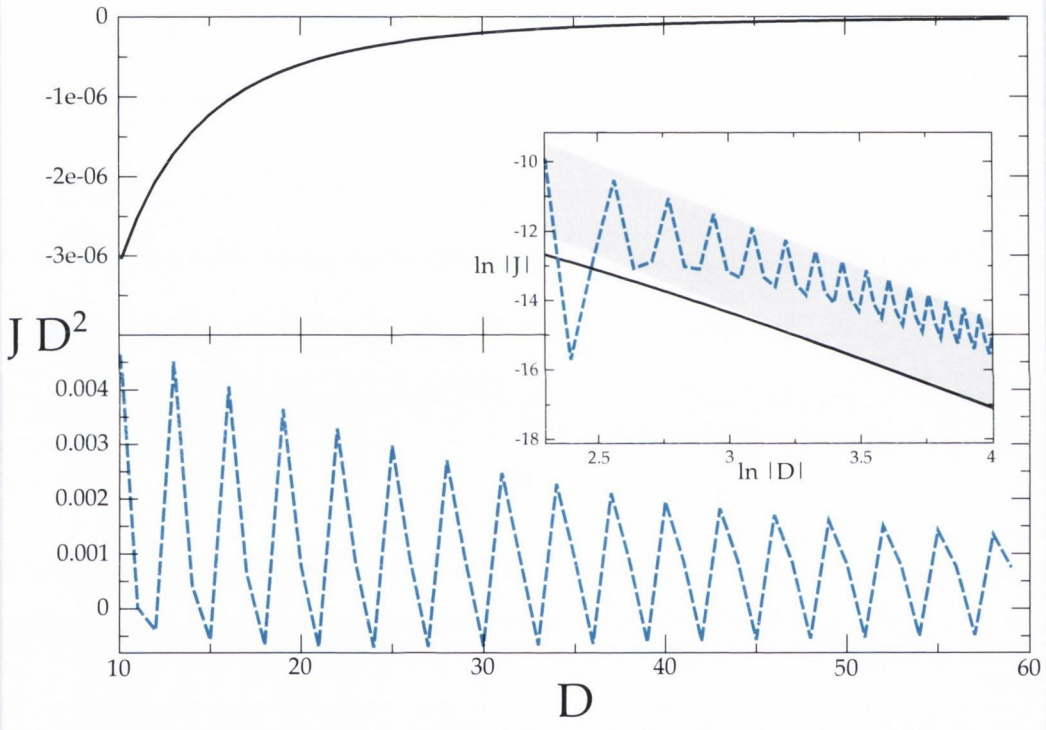


Figure 4.3: Plot of the Indirect Exchange Coupling (J) between bridge-adsorbed impurities in graphene along the high-symmetry directions: armchair (solid-black), zigzag (dashed-blue). The main plot shows the coupling scaled by the distance squared (D^2) to exaggerate the features. The inset shows a log-log plot of the coupling against the separation with a D^{-3} decay rate indicated by the grey band.

Zigzag Separation

For zigzag separated impurities we find

$$N_\Gamma = 4E. \tag{4.2.34}$$

Which gives us

$$\mathcal{B}_Z = \frac{1}{2i\pi} \frac{16E}{(E+t)\sqrt{4t^2-(E+t)^2|t|}}, \tag{4.2.35}$$

with derivatives

$$\mathcal{B}_Z^{(0)} = 0, \quad \mathcal{B}_Z^{(1)} = -\frac{8i}{\pi\sqrt{3}t^2|t|}. \tag{4.2.36}$$

So that the coupling is given by

$$J \sim -V_{ex}^2 \cos\left(\frac{4\pi}{3}D_Z\right) \frac{2\sqrt{3}}{\pi|t|} \frac{1}{{D_Z}^3}. \tag{4.2.37}$$

Figure 4.3 shows the numerical calculation of the coupling between bridge-adsorbed impurities in the armchair and zigzag directions. We note that in both cases the correct decay rate is predicted. The smooth behaviour of the interaction between armchair separated impurities is captured here, however, the oscillation seen in zigzag separated impurities is not captured by our model, which predicts it to go as $\cos\left(\frac{4\pi}{3}D_Z\right)$. This prediction is based on the approximation that $G_{AB} \sim \Gamma_{ab}(D)$, where $\Gamma_{ab}(D)$ contains all the distance-dependence of the interaction, and a denominator containing functions of GFs has been omitted (see Eq. 3.4.22). Although this can accurately reflect the decay rate it does not capture all the features of the oscillation. These oscillations are better described by a term $1 - 2\cos\left(2\frac{2\pi}{3}D_Z + \phi_B\right)$, which was previously derived by Sherafati *et al.* [75]. Here ϕ_B is a phase term which is dependent on the hopping integral connecting the impurity to the two neighbouring carbon

atoms, implying that different impurity species may have different oscillation phases.

4.2.5 *RKKY Between Centre-Adsorbed Impurities*

Working with centre-adsorbed impurities introduces a slight further complication. Each centre-adsorbed impurity attaches to six sites, and several of the GFs between these sites no longer lie precisely along the armchair or zigzag direction, but are slightly offset, as seen in Fig. 4.4. The fact that these sites are slightly out of alignment introduces an additional phase term into our SPA GF so that it is now of the form

$$g_D = \overline{\mathcal{A}} N_{\gamma\gamma'} \left(e^{\pm i\mathbf{k}.\mathbf{v}} \right) \frac{e^{iqD}}{\sqrt{D}}, \tag{4.2.38}$$

where $\mathbf{v}$ is a linear combination of our real-space vectors. Here we have used $\overline{\mathcal{A}}$ to denote $\mathcal{A}$ with the sublattice dependence, $N_{\gamma\gamma'}$, extracted such that $\mathcal{A} = N_{\gamma\gamma'}\overline{\mathcal{A}}$. This is to allow for neatness in the following calculation. Figure 4.4 shows an example of this problem where the GF $g_{a_1 b_1}$ can be well approximated by the SPA, but the GF $g_{a_1 b_5}$ requires an additional phase term, where $\mathbf{v} = \mathbf{a}_1 - \mathbf{a}_2$. This method is found to increase in accuracy as the separation of the sites increases, in a similar manner to the SPA, so that a good approximation can still be found.

Again we must make the approximation that the decay rate can be determined by the approximation $G_{AB} \sim \Gamma_{ab}$, where G_{AB} is the GF between the impurities in the perturbed system. The Gamma-sum term now defines the relation between the six neighbours of impurity A with the six neighbours of impurity B, for a total of 36 terms. It is defined as

$$\Gamma_{ab} = \sum_{ij}^{6} g_{a_i b_j}. \tag{4.2.39}$$

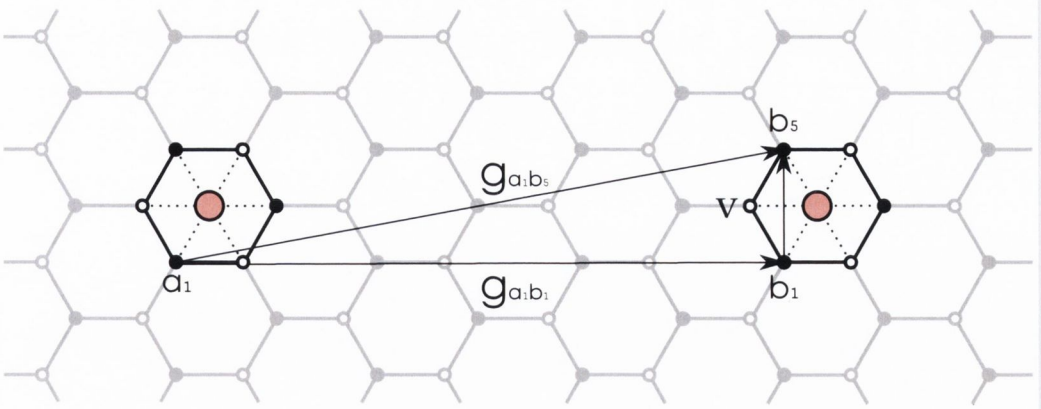


Figure 4.4: Schematic representation of the additional phase term arising from the interaction of centre-adsorbed impurities (red circles). Here we show that the Green's function between sites a_1 and b_1, $g_{a_1b_1}$, lie precisely along the armchair separation, and the Green's function between sites a_1 and b_5, $g_{a_1b_5}$, are not precisely along the armchair direction. The correction vector, $\mathbf{v}$, in this case is given by $\mathbf{v} = \mathbf{a}_1 - \mathbf{a}_2$, where $\mathbf{a}_1$ and $\mathbf{a}_2$ are our real space primitive lattice vectors.

Looking at the integrand of each GF, $g_{a_ib_j}$, we can group together the terms depending on their sublattice interaction $g^{\alpha\alpha}, g^{\beta\beta}, g^{\alpha\beta}, g^{\beta\alpha}$, where each contains nine terms. First considering impurities on the same sublattice we have

$$\begin{aligned}
\sum_{ij}^{6} g_{ij}^{\alpha\alpha} &= g_{11} + g_{13} + g_{15} + g_{31} + g_{33} + g_{35} + g_{51} + g_{53} + g_{55} \\
&= \frac{\overline{\mathcal{A}}}{\sqrt{D}} \Big[E e^{iqD} \left(1 + e^{i\mathbf{k}\cdot\mathbf{a}_1} + e^{i\mathbf{k}\cdot(\mathbf{a}_1 - \mathbf{a}_2)} \right) \\
&\qquad + E e^{iqD} \left(e^{-i\mathbf{k}\cdot\mathbf{a}_1} + 1 + e^{-i\mathbf{k}\cdot\mathbf{a}_2} \right) \\
&\qquad\qquad + E e^{iqD} \left(e^{i\mathbf{k}\cdot(\mathbf{a}_2 - \mathbf{a}_1)} + e^{i\mathbf{k}\cdot\mathbf{a}_2} + 1 \right) \Big] \\
&= \overline{\mathcal{A}} \, \frac{e^{iqD}}{\sqrt{D}} \left(\frac{E}{t^2} f(k) f^*(k) \right).
\end{aligned} \tag{4.2.40}$$

By symmetry we can see that $\sum_{ij}^{6} g_{ij}^{\alpha\alpha} = \sum_{ij}^{6} g_{ij}^{\beta\beta}$. We now consider one set of GFs between sites on opposite sublattices

$$\begin{aligned}\sum_{ij}^{6} g_{ij}^{\alpha\beta} &= g_{12} + g_{14} + g_{16} + g_{32} + g_{34} + g_{36} + g_{52} + g_{54} + g_{56} \\ &= \frac{\overline{\mathcal{A}}}{\sqrt{D}}\Big[f(k)e^{iqD}\left(1 + e^{i\mathbf{k}\cdot(\mathbf{a}_1-\mathbf{a}_2)} + e^{-i\mathbf{k}\cdot\mathbf{a}_2}\right) \\ &\qquad + f(k)e^{iqD}\left(e^{-i\mathbf{k}\cdot\mathbf{a}_1} + e^{-i\mathbf{k}\cdot\mathbf{a}_2} + e^{-i\mathbf{k}\cdot(\mathbf{a}_1+\mathbf{a}_2)}\right) \\ &\qquad + f(k)e^{iqD}\left(e^{i\mathbf{k}\cdot(\mathbf{a}_2-\mathbf{a}_1)} + 1 + e^{-i\mathbf{k}\cdot\mathbf{a}_1}\right)\Big] \\ &= \overline{\mathcal{A}}\,\frac{e^{iqD}}{\sqrt{D}}\left(\frac{1}{t^2}f^3(k)e^{-i\mathbf{k}\cdot(\mathbf{a}_1+\mathbf{a}_2)}\right).\end{aligned} \tag{4.2.41}$$

And by symmetry we find

$$\sum_{ij}^{6} g_{ij}^{\beta\alpha} = \overline{\mathcal{A}}\,\frac{e^{iqD}}{\sqrt{D}}\left(\frac{1}{t^2}f^{*3}(k)e^{+i\mathbf{k}\cdot(\mathbf{a}_1+\mathbf{a}_2)}\right), \tag{4.2.42}$$

where the additional term is now the conjugate of the previous term. So our expression for Γ_{ab} is now

$$\Gamma_{ab} = N_\Gamma\,\overline{\mathcal{A}}\,\frac{e^{iqD}}{\sqrt{D}}, \tag{4.2.43}$$

with

$$N_\Gamma = \frac{2E}{t^2}|f(k)|^2 + \frac{2}{t^2}\mathrm{Re}\left(tf^3(k)e^{-i2k_A}\right). \tag{4.2.44}$$

We can now use this expression to work out the coupling along armchair and zigzag separations.

Armchair Separation

For armchair separated impurities we must evaluate N_Γ by replacing k_Z with the stationary point k_Z^0 and k_A with the Fermi vector q_A, evaluated at that stationary point, Eq. 3.1.51 , which are

$$k_Z^0 = \pm\cos^{-1}\left(\frac{\sqrt{t^2-E^2}}{2t}\right), \quad q_A\left(k_Z^0\right) = \pm\cos^{-1}\left(-\frac{\sqrt{t^2-E^2}}{t}\right), \tag{4.2.45}$$

for energies where $|E| < |t|$. This gives us,

$$\mathcal{A}_A = \sqrt{\frac{2i}{\pi}}\sqrt{\frac{1}{E(E^2+3t^2)\sqrt{t^2-E^2}}}\frac{2E^3(t-E)}{t^3}. \tag{4.2.46}$$

From this we can now easily determine

$$\mathcal{B}_A = \frac{8iE^5(t-E)^2}{\pi t^6\sqrt{t^2-E^2}\,(E^2+3t^2)}. \tag{4.2.47}$$

Once again we want to find the derivatives of $\mathcal{B}$ with respect to energy, evaluated at the Fermi energy. Here we find that $\mathcal{B}^{(0)} = \mathcal{B}^{(1)} = \mathcal{B}^{(2)} = \mathcal{B}^{(3)} = \mathcal{B}^{(4)} = 0$, and that the first non-vanishing term occurs at $l = 5$,

$$\mathcal{B}_A^{(5)} = \frac{320i}{\pi t^7}. \tag{4.2.48}$$

And our expression for the coupling is

$$J \sim V_{ex}^2\,\frac{5}{\pi t}\,\frac{1}{D^7}. \tag{4.2.49}$$

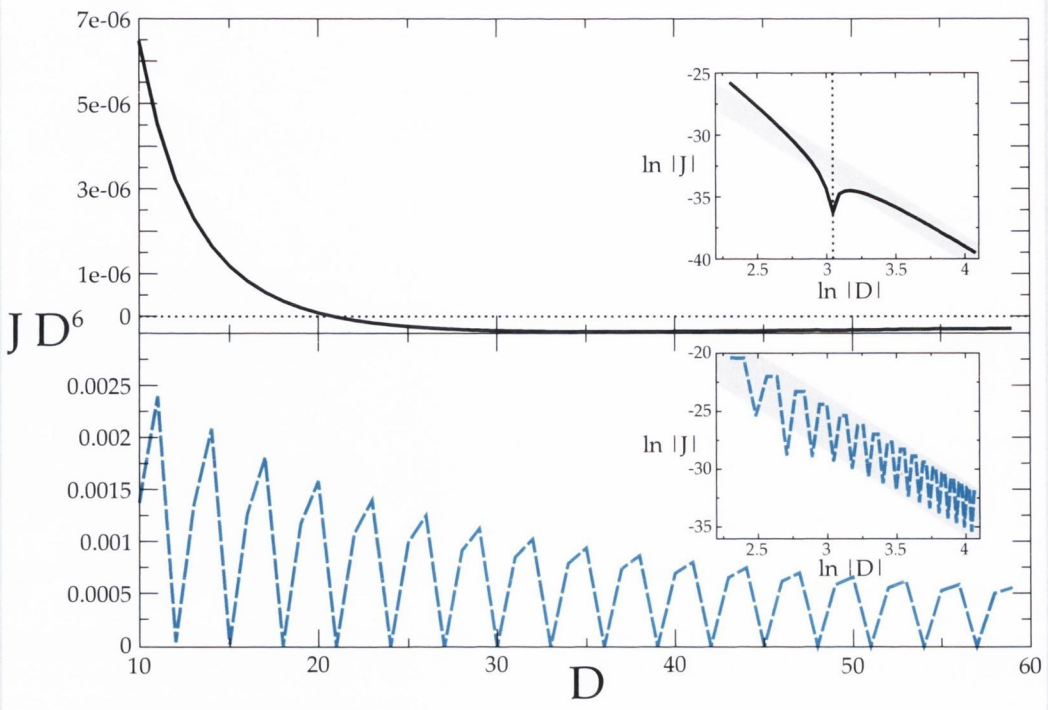


Figure 4.5: Plot of the Indirect Exchange Coupling (J) between centre-adsorbed impurities in graphene along the high-symmetry directions: armchair (solid-black), zigzag (dashed-blue). The main plot shows the coupling scaled by the distance to the sixth power (D^6) to exaggerate the features. The inset shows a log-log plot of the coupling against the separation with a D^{-7} decay rate indicated by the grey band.

Zigzag Separation

For zigzag separated impurities we now evaluate N_Γ by replacing k_A with the stationary point k_A^0 and k_Z with the Fermi vector q_Z evaluated at that point, Eq. 3.1.57. These are

$$k_A^0 = 0, \quad q_Z(k_A^0) = \pm\cos^{-1}\left(\frac{\pm E - t}{2t}\right), \tag{4.2.50}$$

which gives us

$$N_\Gamma = \frac{4E^3}{t^2}. \tag{4.2.51}$$

From this we can now simply derive

$$\mathcal{B}_Z = -\frac{i8E^5}{\pi(E-t)t^5\sqrt{(E-3t)(E+t)}}. \tag{4.2.52}$$

Again we wish to find the derivatives of $\mathcal{B}$ with respect to E at $E_F = 0$, to determine the first non-vanishing derivative. This is found to be

$$\mathcal{B}_Z^{(5)} \sim \frac{i320\sqrt{3}}{\pi t^7}, \tag{4.2.53}$$

so that the coupling goes as

$$J \sim -V_{ex}^2 \cos\left(\frac{4\pi}{3}D\right) \frac{135\sqrt{3}}{\pi t}\frac{1}{D^7}. \tag{4.2.54}$$

In Fig. 4.5 we plot a numerical evaluation of the coupling between centre-adsorbed impurities separated along the high-symmetry directions of graphene. Initially the decay of armchair separated impurities is seen to decay faster than the expected $J \sim D^{-7}$. This can be explained by the sign-change which occurs at approximately $D = 22$, and is indicated by the horizontal dotted line in Fig. 4.5. The corresponding point in the log-log inset is indicated by a vertical dotted line, where the sharp peak downward indicates the sign-change. The coupling between impurities separated along the zigzag direction displays the usual triplet pattern, and is also seen to decay as D^{-7}.

We have now shown that our method for modelling the coupling between various impurity conformations is very powerful. It provides a great deal of mathematical transparency, and correctly predicts the decay rate of the coupling for each impurity. It also helps to explain some of the discrepancies in the literature where decay rates of D^{-2}, D^{-3}, and D^{-7} are predicted, and provides a clear picture of when an how these different decay rates arise.

4.3 EVALUATION OF THE RKKY IN CARBON NANOTUBES

With the motivation of understanding the functional form of the RKKY interaction we will now examine this in nanotubes. We will examine it for the four impurity conformations types we introduced in Sec. 3.4, with the understanding that substitutional and top-adsorbed impurities have very similar properties in our model and we will usually discuss them together. We will divide our examination between armchair nanotubes (ACNTs) and zigzag nanotubes (ZZNTs). In this quasi-one-dimensional material the expected decay rate of the coupling is D^{-1} with separation D. However, we will show that in certain cases the coupling may decay much more rapidly than this as D^{-5}.

4.3.1 *Derivation of the RKKY in Carbon Nanotubes*

In Sec. 4.1.5 we derived the RKKY approximation to the IEC for a generic GF. Here we will use the analytic forms for the GFs in ACNTs and ZZNTs, derived in Sec. 3.2.2, to derive the form of the RKKY interaction in these systems.

The coupling in the RKKY approximation is again calculated as

$$J \sim \mathrm{Im} \int dE\ V_{ex}^2\ g_{ab}(E) g_{ba}(E). \tag{4.3.1}$$

However, now g_{ab} and g_{ba} are the GFs for nanotubes which are of the form

$$g_{ab} = \sum_j \mathcal{A}(E, j) e^{iq(E,j)D}, \tag{4.3.2}$$

which comes from Eqs. 3.2.9 and 3.2.18. So with nanotube GFs the coupling has the form

$$\begin{aligned} J &\sim \mathrm{Im}\int dE\; V_{ex}^2 \left(\sum_j \mathcal{A}(E,j)e^{iq(E,j)D}\right)\left(\sum_k \mathcal{A}(E,k)e^{iq(E,k)D}\right) \\ &\sim \mathrm{Im}\int dE\; V_{ex}^2 \sum_j\sum_k \underbrace{\mathcal{A}(E,j)\mathcal{A}(E,k)}_{\mathcal{B}(E,j,k)} e^{i\overbrace{(q(E,j)+q(E,k))}^{2q(E,j,k)}D} \\ &\sim \mathrm{Im}\int dE\; V_{ex}^2 \sum_{j,k} \mathcal{B}(E,j,k)e^{i2q(E,j,k)D} \\ &\sim \sum_{j,k} \mathrm{Im}\int dE\; V_{ex}^2\, \mathcal{B}(E,j,k)e^{i2q(E,j,k)D}. \end{aligned} \tag{4.3.3}$$

The inclusion of a sum over j,k here introduces a slight complication in evaluating the decay rate analytically. To circumvent this we consider a single pair of j and k values, j_0 and k_0 and work under the (reasonable) assumption that all the summed terms have the same decay rate, or at least that we can identify the lowest order term that will dominate in the asymptotic limit. So we can write a generic term of our coupling as

$$J_0 \sim \mathrm{Im}\int dE\; V_{ex}^2\, \mathcal{B}(E,j_0,k_0)e^{i2q(E,j_0,k_0)D}. \tag{4.3.4}$$

The calculation can then be carried out in a nearly identical manner as the RKKY SPA for graphene, Sec. 4.2.1. This leads to a form for the coupling between two magnetic impurities on a nanotube

$$J \sim -V_{ex}^2 \sum_{j,k} \mathrm{Im}\left(e^{2iq^{(0)}D}\sum_l\left[\frac{\mathcal{B}^{(l)}}{\left(2iq^{(1)}\right)^{l+1}}\frac{1}{D^{l+1}}\right]\right), \tag{4.3.5}$$

where q and $\mathcal{B}$ have a dependence on j and k. Note here that the decay rate as a function of distance goes as $\frac{1}{D^{l+1}}$ and not $\frac{1}{D^{l+2}}$ as it does for the graphene RKKY case.

This equation will now allow us to examine the decay rates of the four impurity conformations in ACNTs and ZZNTs. However, this equation does not capture all of the features of the coupling, but makes the generalization that the overall decay rate can be thought of as a sum over all orders. In fact, if we confine ourselves to the asymptotic limit we can be satisfied by finding the slowest decaying term, as this will dominate. Much of the derivation of decay rates is similar to those we performed in graphene, Sec. 4.2, and so we will consider it sufficient to just look at the first non-vanishing $\mathcal{B}$ term in each case.

4.3.2 *RKKY Between Impurities in ACNT*

We will first focus on ACNT, where sublattice dependent terms are given by

$$N_{\gamma\gamma'} = \begin{cases} E & \text{if } \gamma = \gamma' \\ f, f^* = t + 2t\cos(q_\pm)e^{i\left(\frac{j_0\pi}{n_c}\right)} & \text{if } \gamma \neq \gamma' \end{cases}. \tag{4.3.6}$$

We will consider the four impurity conformation types, where we again treat substitutional and top-adsorbed impurities in conjunction as they display similar behaviours

Substitutional and Top-Adsorbed Impurities

For impurities on the same sublattice, and considering for a moment just one of the poles, the value of $\mathcal{A}$ comes straight from our GF, Eq. 3.2.9, and is given by

$$\mathcal{A}(j_0) = \frac{i}{4t_2 n_c} \frac{E}{\sin(q_+)(t + 2t\cos(q_+))}, \tag{4.3.7}$$

where we have made note that this is just for a single j value. The form for $\mathcal{B}$ is now given trivially by $\mathcal{A}^2$, as

$$\mathcal{B} = \frac{-1}{16t^2n_c^2}\frac{E^2}{\sin^2(q_+)(t+2t\cos(q_+))^2}. \tag{4.3.8}$$

In the simplest case, $j = 0$, we can use the fact that $E^2 = t + 2t\cos(q_+)$ to simplify the equation and show that

$$\mathcal{B} = -\frac{1}{12n_c{}^2t^2}. \tag{4.3.9}$$

Considering the other pole, q_-, we get the same answer. Therefore the first non-vanishing term occurs at $l = 0$, and the decay rate is expected to go as D^{-1}. For impurities on opposite sublattices, similar steps will produce the same result but with an overall sign change.

Bridge-adsorbed impurities on armchair Nanotubes

Again considering just one pole and a single j_0. The bridge-adsorbed impurity contains a term

$$\begin{aligned} N_\Gamma &= N_{\alpha\alpha} + N_{\beta\beta} + N_{\alpha\beta} + N_{\beta\alpha} \\ &= 2E + 2t + 4t\cos(q_+). \end{aligned} \tag{4.3.10}$$

For impurities separated on the zigzag direction, $N^{\alpha\alpha} = N^{\beta\beta}$ and $N^{\alpha\beta} = N^{\beta\alpha}$. The full forms of $\mathcal{A}$ and $\mathcal{B}$ become cumbersome at this point, and will be omitted, however they may be calculated exactly as in Sec. 4.2.1. The first non-vanishing $\mathcal{B}^{(l)}$ is

$$\mathcal{B}^{(0)} = -\frac{4}{3n_c^2t^2}, \tag{4.3.11}$$

which again implies an asymptotic decay rate of D^{-1}.

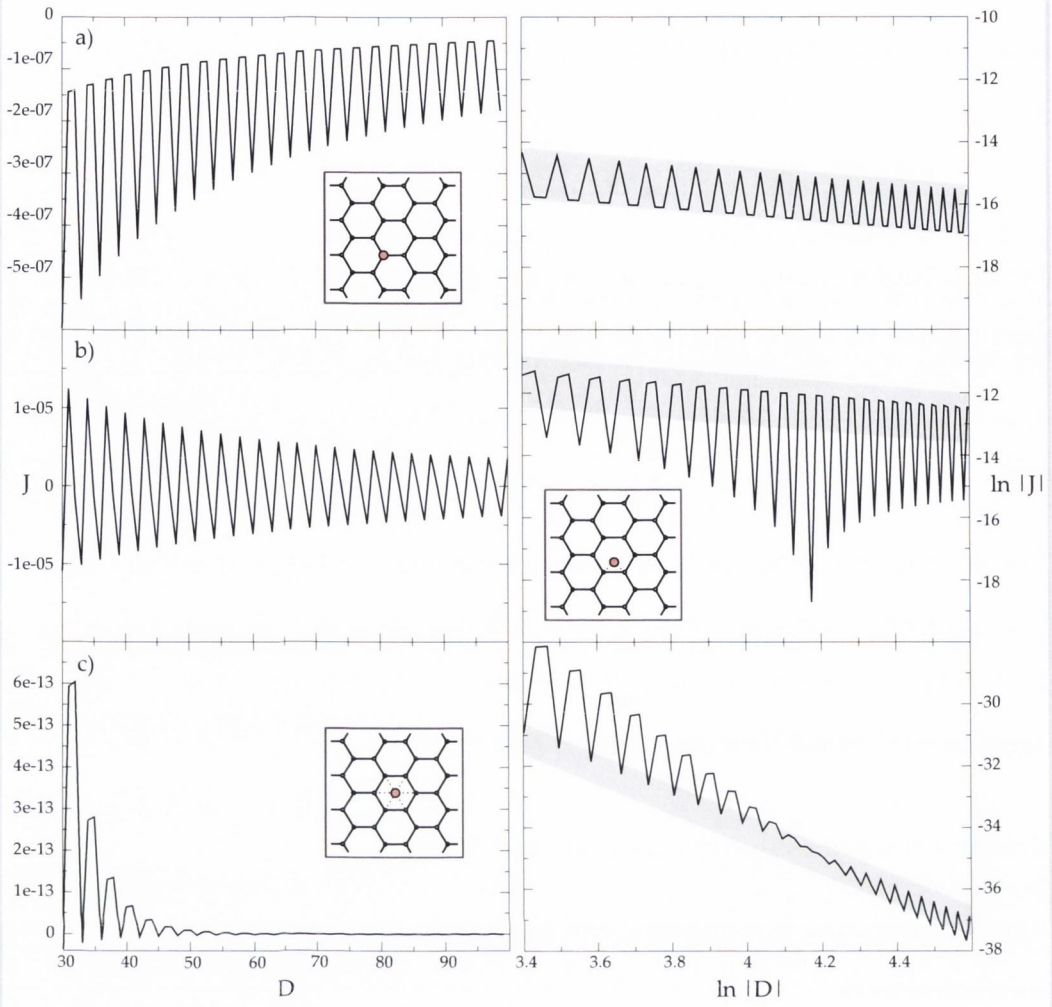


Figure 4.6: Plot of the Indirect Exchange Coupling (J) on armchair nanotubes between a) substitutional impurities, b) bridge-adsorbed impurities, and c) centre-adsorbed impurities. In each case the main plot shows the coupling, the offset plot shows a log-log plot of the coupling against the separation with the grey band indicating the decay rates a) D^{-1}, b) D^{-1}, and c) D^{-5}, and the inset boxes display the impurity type.

Centre-adsorbed impurities on armchair Nanotubes

As with the centre-adsorbed impurities for graphene, we now must account for a sum of 36 terms. This is done in a similar manner to those in graphene and can be simplified to

$$N_\Gamma = 2\frac{E}{t^2}f^2 + \frac{1}{t^2}f^3e^{(-i2q_+)} + \frac{1}{t^2}f^3e^{(i2q_+)}. \tag{4.3.12}$$

From this our terms for $\mathcal{A}$ and $\mathcal{B}$ can be easily found, though again they are cumbersome so we choose to omit them. In contrast to the previous impurity types, and in agreement with the centre-adsorbed in graphene, $l = 0$ is no longer the first non-vanishing $\mathcal{B}$ term found. What is found is that $\mathcal{B}^{(0)} = \mathcal{B}^{(1)} = \mathcal{B}^{(2)} = \mathcal{B}^{(3)} = 0$ and that the first non-zero term is $\mathcal{B}^{(4)}$ indicating a decay rate of D^{-5}, instead of D^{-1} as one might expect from a 1D system [83, 84, 86]. The exact form of $\mathcal{B}^{(4)}$ is too long to reproduce here. This behaviour is similar to that of centre-adsorbed behaviour in graphene where the decay rate is D^{-7} instead of the expected D^{-3}.

Figure 4.6 shows the IEC on ACNTs for substitutional, bridge-adsorbed, and centre-adsorbed impurities. In each case the coupling exhibits a period three behaviour as we expect. This is slightly masked in the bridge-adsorbed case where one of the values is much smaller than the others. For each impurity type we have also plotted the log of the coupling against the log of the separation. The overall decay rates are seen to be in excellent agreement, though we cannot capture the more complex features of the interaction.

4.3.3 *RKKY Between Impurities in ZZNT*

We will now perform the same analysis for ZZNTs, which can be done in exactly the same manner. As previously mentioned the metallicity of ZZNTs can be determined based on their circumference, where they are metallic only if $n_c = 3a$, where $a \in \mathbb{Z}$. The IEC between impurities on semi-conducting ZZNTs decays exponentially, and thus we will restrict ourselves to examining the IEC on metallic ZZNTs. In ACNT the axial separation is along the zigzag direction, which is known to feature a repeating triplet pattern of interaction strength: strong, strong, weak. To find a smooth decay rate, steps of three were taken.

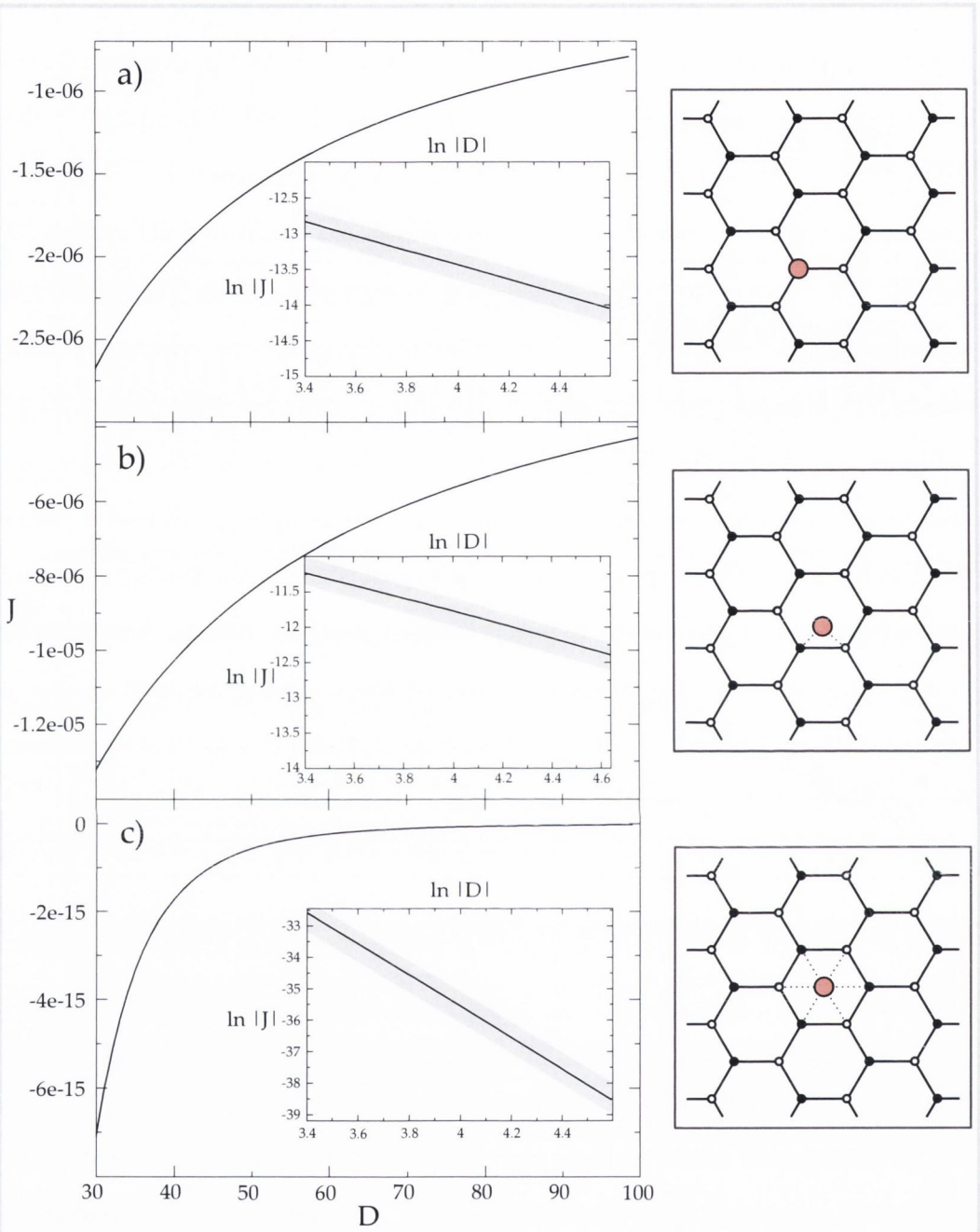


Figure 4.7: Plot of the Indirect Exchange Coupling (J) on zigzag nanotubes between a) substitutional impurities, b) bridge-adsorbed impurities, and c) centre-adsorbed impurities. In each case the main plot shows the coupling, the inset shows a log-log plot of the coupling against the separation with the grey band indicating the decay rates a) D^{-1}, b) D^{-1}, and c) D^{-5}, and the offset box displays the impurity type.

Substitutional and Top-adsorbed Impurities in ZZNTs

For substitutional and top-adsorbed impurities the sublattice dependent terms are

$$N_{\gamma\gamma'} = \begin{cases} E & \text{if } \gamma = \gamma' \\ f = t + 2te^{+iq} & \text{if } \gamma\gamma' = \alpha\beta \cdot \\ f^* = t + 2te^{-iq} & \text{if } \gamma\gamma' = \beta\alpha \end{cases} \tag{4.3.13}$$

Where now the case $\gamma\gamma' = \alpha\beta$ is no longer equivalent to $\gamma\gamma' = \beta\alpha$. So for sites on the same sublattice we have

$$\mathcal{A} = \frac{i}{2t^2 n_c} \frac{E}{\sin(q)}, \tag{4.3.14}$$

which gives

$$\mathcal{B} = \frac{1}{n_c{}^2 (E^2 - 4t^2)}, \qquad \mathcal{B}^{(0)} = \frac{1}{-4t^2 n_c{}^2}. \tag{4.3.15}$$

So that the first non-vanishing term is determined by $l = 0$. This is also found for impurities on the opposite sublattice.

Bridge-adsorbed Impurities in ZZNTs

In exactly the same manner as for bridge-adsorbed impurities in ACNT we can calculate

$$\mathcal{B}^{(0)} = -\frac{1}{n_c{}^2 t^2}, \tag{4.3.16}$$

indicating a decay rate of D^{-1}.

Centre-adsorbed Impurities in ZZNTs

Again the centre-adsorbed case contains a N_Γ term that is the sum of 36 sublattice terms. Which, in this case, can be simplified to

$$N_\Gamma = 2\frac{E}{t^2}ff^* + \frac{1}{t^2}f^3e^{(-i2q)} + \frac{1}{t^2}f^{*3}e^{(i2q)}, \tag{4.3.17}$$

where

$$f = t + 2t\cos\left(\frac{\pi j}{n_c}\right)e^{iq}. \tag{4.3.18}$$

The forms of $\mathcal{A}$ and $\mathcal{B}$ are too complicated to reproduce here. We find $\mathcal{B}^{(0)} = \mathcal{B}^{(1)} = \mathcal{B}^{(2)} = \mathcal{B}^{(3)} = 0$ and that the first non-zero term is $\mathcal{B}^{(4)}$ indicating a decay rate of D^{-5}, as with armchair nanotubes. Figure 4.7 shows the IEC on ZZNTs for substitutional, bridge-adsorbed, and centre-adsorbed impurities. In each case the coupling is a smooth decay, and the decay rate is in perfect agreement with our predicted decay rates.

4.3.4 *RKKY as a Function of Nanotube Circumference*

We have just shown that our model predicts a general decay rate of D^{-3} for the coupling in graphene, which is two-dimensional, and a general decay rate of D^{-1} in nanotubes which are pseudo-one-dimensional. This is, of course, neglecting the decay of the coupling of centre-adsorbed impurities, which is faster in both cases but still has some dependence on the dimensionality of the system. These have been calculated without much regard for the effect that the circumference of the nanotube has on the interaction. In this section we examine the role of the nanotube circumference, n_c, for both armchair nanotubes and metallic zigzag nanotubes, to understand how the RKKY interaction transitions from the behaviour predicted in nanotubes to that predicted

in bulk graphene as its dimensionality essentially changes from a pseudo-one-dimensional system to a two-dimensional system. This is done for all four impurity types, where pairs are separated along the length of the tube, and have no circumferential offset. Since nanotubes are not stable at these sizes this is, to some extent, purely an intellectual exercise to examine the self-consistency of our own model.

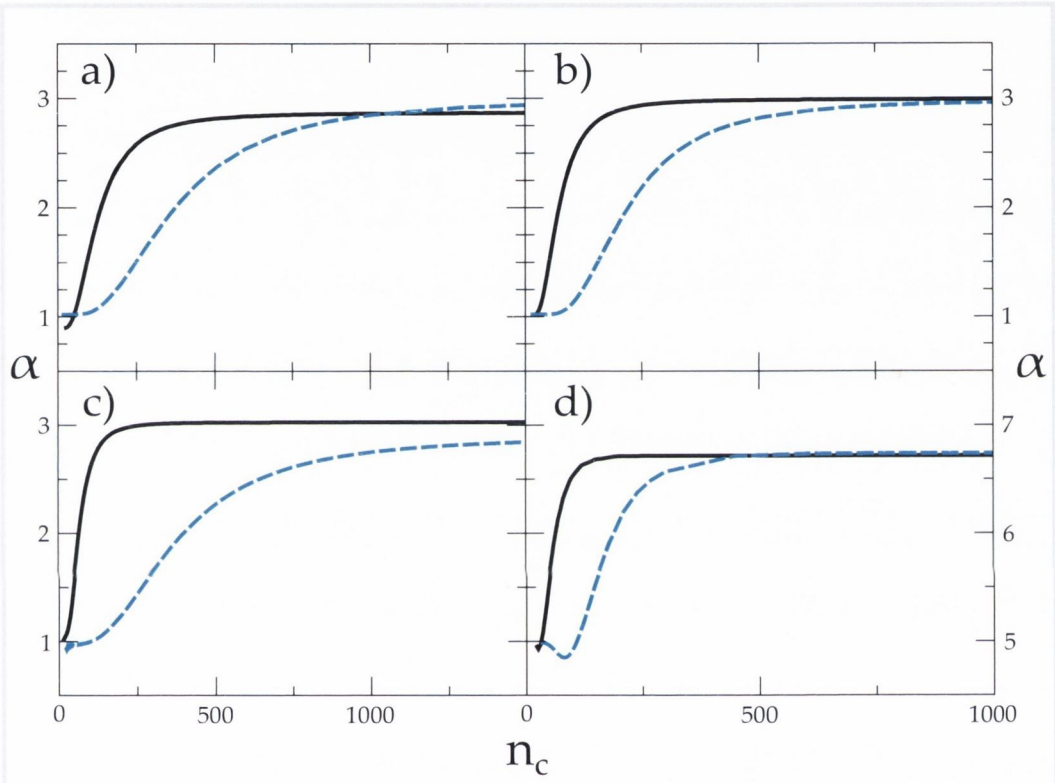


Figure 4.8: Plot of the decay rate (α) of the Indirect Exchange Coupling versus circumference (n_c) in armchair nanotubes (solid-black) and zigzag nanotubes (dashed-blue) for a) substitutional impurities, same-sublattice, b) substitutional impurities, opposite-sublattice, c) bridge-adsorbed impurities, and d) centre-adsorbed impurities.

Figure 4.8 shows the change in decay, α, between impurities as a function of the circumference for both ACNT and ZZNT at zero Fermi energy. For same-sublattice substitutional impurities, opposite-sublattice substitutional impurities, and bridge-adsorbed impurities we see that the greatest predictor of behaviour is whether the nanotube is an ACNT or a ZZNT. On ACNTs the

interaction very quickly decays away from the nanotube case of D^{-1} to the graphene case of D^{-3}. This is seen in Fig. 4.8 a), b), c) as the black line, which resembles graphene by about $n_c = 200$. On ZZNT the interaction has a plateau of NT-like behaviour before moving gradually to the behaviour seen in graphene, this is shown as the blue line, and does not resemble graphene until about $n_c = 1000$.

Figure 4.8 d) shows the same effect for centre-adsorbed impurities. By increasing the circumference of the NT we show that both ACNT and ZZNT decay rates go from D^{-5} to D^{-7}. Again, impurities on ACNT decay much more rapidly towards the bulk case and on ZZNT exhibit a plateau and a slow decay towards bulk.

4.4 SUMMARY OF CHAPTER

We have now introduced everything we need to start examining the effects of mechanical strain on the magnetic interaction between impurities in graphene and nanotubes. In Sec. 4.1 we explained how the Indirect Exchange Interaction could be calculated in an analytic fashion in graphene and nanotubes [67, 78, 83, 84]. This was then used to derive the specific expressions for the coupling in graphene in Sec. 4.2 and to determine the coupling decay rates between impurities in nanotubes in Sec. 4.3. We also showed here how the two are related by examining the effect of increasing nanotube circumference on coupling decay rate. Specifically, we have shown that the RKKY interaction between adsorbed magnetic moments in graphene depends on the exact conformation of the impurities. With the coupling between centre-adsorbed impurities decaying as D^{-7} in graphene and D^{-5} in nanotubes. The coupling between substitutional, top-adsorbed, and bridge-adsorbed D^{-3} in graphene and D^{-1} in nanotubes, with bridge-adsorbed impurities also displaying a sign

changing behaviour as a function of separation in the zigzag direction. We have demonstrated that using our prescription, the decay, along with other features of the interaction, may be derived in a mathematically transparent fashion.

5

STRAIN EFFECTS ON MAGNETIC INTERACTIONS

In Chap. 4 we used a combination of analytic and numerical techniques to show that the RKKY interaction between localized moments in undoped graphene decays faster than expected for conventional two-dimensional materials. We also showed in graphene and nanotubes that the impurity conformation, favoured by many transition-metal impurities, may lead to even shorter ranged decays and possible sign-changing oscillations. Our work was motivated by the hope of controlling the interaction between magnetic objects in graphene and carbon nanotubes (CNTs) to open up the possibility of implementing the technologically promising area of spintronics.

We will now examine the role that mechanical strain can play in modifying these interactions in graphene and nanotubes. Strain is known to have a profound effect on the electronic properties of graphene, shifting the Dirac cones, and leading to a Lifshitz transition (a topological transition of the Fermi surface), Fig. 5.1, though this transition is likely beyond any physically realizable strain. It has also been shown that uniaxial strain can open a bandgap in metallic nanotubes and alter the bandgap in semi-conducing nanotubes [157, 158], and that Coulomb repulsion may cause a similar effect [192]. We will show that by breaking the symmetry of the lattice, via uniaxial strain, a range of interesting features are uncovered depending on the separation and strain directions. We report that strain can significantly amplify or suppress features of the interaction between substitutional magnetic moments embedded in graphene (Sec. 5.2.1) [193, 194]. Furthermore we demonstrate that inter- and intra-sublattice couplings can be switched on and off independently, suggesting a wide range of possible applications. Ampli-

fication, suppression, and oscillatory behaviour are reported as a function of the strain. Mathematically transparent expressions predicting these features are derived for bridge and centre configurations, which are the preferred sites for a number of transition-metal atoms (Secs. 5.2.2 and 5.2.3). We will show that strain takes on a similar role to graphene as in ACNTs (Sec. 5.3.1), however the effects of strain in ZZNTs are much more pronounced since it can profoundly modify the electronic structure by distorting the Brillouin zone (Sec. 5.3.2).

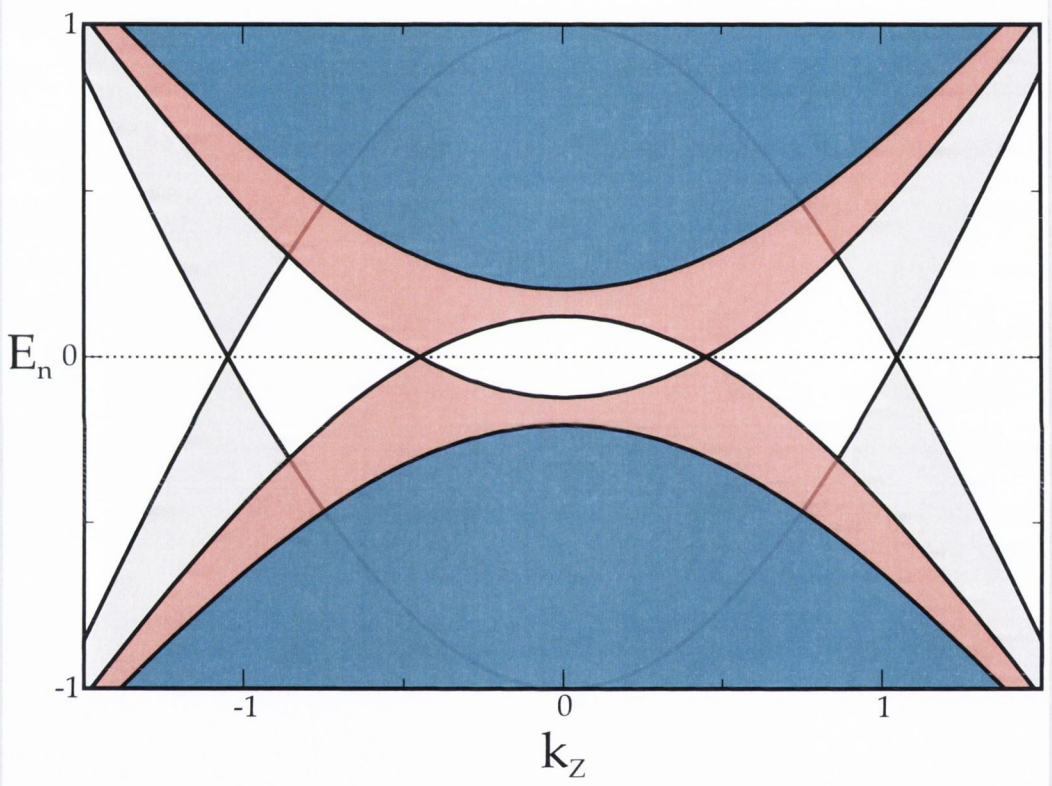


Figure 5.1: Graphene dispersion relation as a function of k_Z for $k_A = \frac{\pi}{3}$, for three values of strain for a) $\varepsilon = 0$ (grey), b) $\varepsilon = 0.2$ (red), and c) $\varepsilon = 0.3$ (blue). The Dirac cones merge with increasing strain until the Lifshitz Transition occurs at $\varepsilon \approx 0.22$. E_n is the normalized energy.

Because the IEC can be characterized by the magnitude, oscillation, and rate of decay, we wish to examine the strain effects on these features. If they

are found to be sensitive to strain this might be a clear indication that strain could be useful to control the interaction.

5.1 STRAIN-MODIFIED ELECTRONIC STRUCTURE OF GRAPHENE AND NANOTUBES

To allow the introduction of strain into graphene and nanotubes we must re-evaluate our tight-binding model, introduced in Sec. 3.1.1, with this goal in mind. Since graphene and nanotubes have the same underlying hexagonal lattice we may start with a joint treatment, which can then be further considered in each case. Again we will restrict our Hamiltonian describing the system to the p_z orbitals, and the electron hopping integrals to neighbouring sites. The Hamiltonian introduced in Eq. 3.1.1,

$$\hat{\mathcal{H}} = \sum_{\mathbf{r},\gamma} |\mathbf{r},\gamma\rangle \epsilon_0 \langle \mathbf{r},\gamma| + \sum_{\mathbf{r},\mathbf{r}',\gamma} |\mathbf{r},\gamma\rangle t \langle \mathbf{r},'\gamma'|, \tag{5.1.1}$$

describes a system where the hopping integral between each carbon atom and its three nearest-neighbours has the same value t. This comes from the fact that in unstrained graphene the vectors, $\mathbf{R}_1$, $\mathbf{R}_2$, and $\mathbf{R}_3$, shown in Fig. 5.2, describing the carbon-carbon bond lengths, are identical. When a tensile strain, ε (the fractional increase in length of the material), is applied to a graphene sheet (or CNT) the lattice bond lengths and hence the hopping values are altered such that the above Hamiltonian does not apply and we must rederive another that is capable of modelling strain.

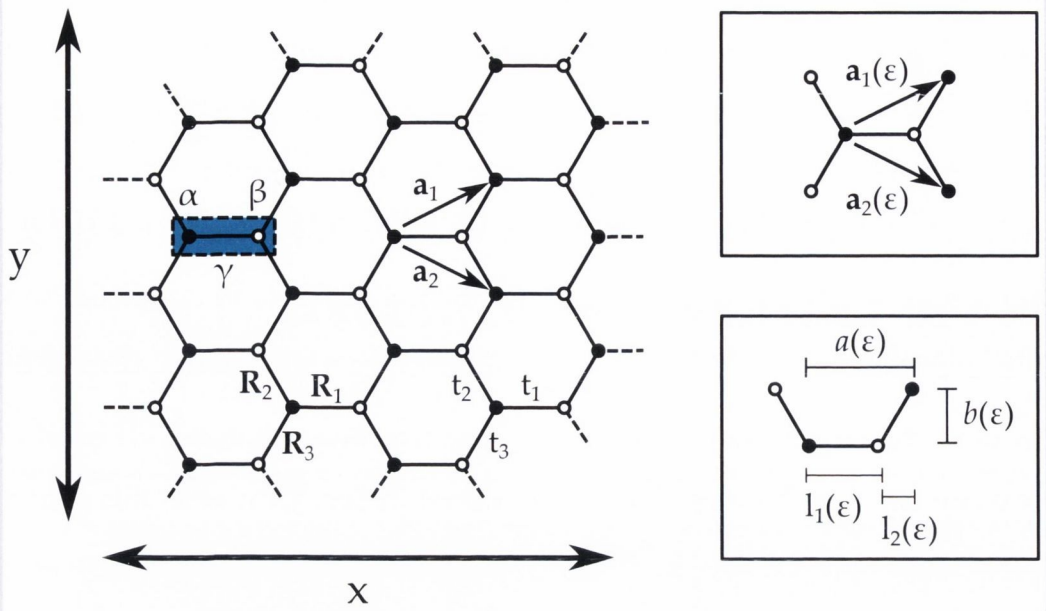


Figure 5.2: A graphene lattice with the unit cell, γ, highlighted in blue, and the sublattices, α and β, denoted by filled circle and hollow circle respectively. Also indicated are the lattice vectors $\mathbf{a}_1$ and $\mathbf{a}_2$, the nearest-neighbour vectors $\mathbf{R}_1$, $\mathbf{R}_2$, and $\mathbf{R}_3$, and the corresponding hopping integrals t_1, t_2, and t_3. The offset images show the strain-dependent primitive vectors $\mathbf{a}_1(\varepsilon)$ and $\mathbf{a}_2(\varepsilon)$, and the strain-dependent real-space lengths $a(\varepsilon)$, $b(\varepsilon)$, $l_1(\varepsilon)$ and $l_2(\varepsilon)$, where $a(\varepsilon) = l_1(\varepsilon) + l_2(\varepsilon)$.

The first step is to define strain dependent primitive lattice vectors $\mathbf{a}_1(\varepsilon)$ and $\mathbf{a}_2(\varepsilon)$,

$$\begin{aligned} \mathbf{a}_1(\varepsilon) &= a(\varepsilon)\mathbf{x} + b(\varepsilon)\mathbf{y}, \\ \mathbf{a}_2(\varepsilon) &= a(\varepsilon)\mathbf{x} - b(\varepsilon)\mathbf{y}, \end{aligned} \tag{5.1.2}$$

in terms of the strain-dependent real-space lengths $a(\varepsilon)$ and $b(\varepsilon)$ as shown in Fig. 5.2, where we also further define $a(\varepsilon) = l_1(\varepsilon) + l_2(\varepsilon)$ to allow the carbon-carbon bond lengths to be easily determined. As described here the lattice is now capable of capturing all the distortions of strain along the two high-symmetry directions. It is possible to allow variation in the lattice such that strain can be applied from any direction, however this complicates the calculation of strain-modified BZ and GF, and provides little additional information

about the strain effects on the indirect exchange coupling, the extremes of which are seen in the high-symmetry directions. This immediately adds the simplification that $|\mathbf{R}_2| = |\mathbf{R}_3|$ and $t_2 = t_3$. The vectors describing the carbon-carbon bond lengths are now given by

$$\begin{aligned}\mathbf{R}_1 &= l_1(\varepsilon)\mathbf{x},\\ \mathbf{R}_2 &= -l_2(\varepsilon)\mathbf{x} + b(\varepsilon)\mathbf{y},\\ \mathbf{R}_3 &= -l_2(\varepsilon)\mathbf{x} - b(\varepsilon)\mathbf{y}.\end{aligned} \tag{5.1.3}$$

These can now be used to derive a strain-dependent Hamiltonian for the underlying hexagonal lattice.

5.1.1 *Modified Hamiltonian and Dispersion Relation*

We now move on to derive the strain-modified Hamiltonian. This is done by rewriting our Hamiltonian from Sec. 3.1.1 with our strain-dependent hopping integrals $t_1(\varepsilon)$ and $t_2(\varepsilon)$, and strain-dependent vectors $\mathbf{a}_1(\varepsilon)$ and $\mathbf{a}_2(\varepsilon)$,

$$\begin{aligned}\hat{\mathcal{H}} = &\sum_{\mathbf{r}} |\mathbf{r},\alpha\rangle t_1(\varepsilon)\langle\mathbf{r},\beta| + |\mathbf{r},\beta\rangle t_1(\varepsilon)\langle\mathbf{r},\alpha|\\ &+ \sum_{\mathbf{r}} |\mathbf{r},\alpha\rangle t_2(\varepsilon)\langle\mathbf{r}-\mathbf{a}_1(\varepsilon),\beta| + |\mathbf{r},\alpha\rangle t_2(\varepsilon)\langle\mathbf{r}-\mathbf{a}_2(\varepsilon),\beta|\\ &+ \sum_{\mathbf{r}} |\mathbf{r},\beta\rangle t_2(\varepsilon)\langle\mathbf{r}+\mathbf{a}_1(\varepsilon),\alpha| + |\mathbf{r},\beta\rangle t_2(\varepsilon)\langle\mathbf{r}+\mathbf{a}_2(\varepsilon),\alpha|.\end{aligned} \tag{5.1.4}$$

In a similar manner to before we may write our Hamiltonian as

$$\hat{\mathcal{H}} = \sum_{\mathbf{k}} \begin{pmatrix} 0 & f(\mathbf{k},\varepsilon) \\ f^*(\mathbf{k},\varepsilon) & 0 \end{pmatrix}, \tag{5.1.5}$$

where $f(\mathbf{k}, \varepsilon)$ is calculated by summing over the phase term coming from each nearest neighbour atom,

$$f(\mathbf{k}, \varepsilon) = \sum_{i=1}^{3} e^{i\mathbf{k}\cdot\mathbf{R}_i(\varepsilon)}. \tag{5.1.6}$$

Using Eq. 5.1.3 we now have

$$\begin{aligned} f(\mathbf{k}, \varepsilon) &= t_1 e^{il_1 k_x} + t_2 e^{i(-l_2 k_x + b k_y)} + t_2 e^{i(-l_2 k_x - b k_y)} \\ &= t_1 e^{il_1 k_x} + 2t_2 \cos(b k_y) e^{-il_2 k_x}, \end{aligned} \tag{5.1.7}$$

where we have dropped some of the strain-dependent notation for neatness. The dispersion relation can then be found as

$$\begin{aligned} |f(\mathbf{k}, \varepsilon)| &= \pm\sqrt{f(\mathbf{k}, \varepsilon) f^*(\mathbf{k}, \varepsilon)} \\ &= \pm\sqrt{t_1^2 + 2t_1 t_2 \cos(b k_y) e^{il_1 k_x} e^{il_2 k_x} + 2t_1 t_2 \cos(b k_y) e^{-il_1 k_x} e^{-il_2 k_x} + 4t_2^2 \cos^2(b} \\ &= \pm\sqrt{t_1^2 + 4t_1 t_2 \cos(b(\varepsilon) k_y) \cos(a(\varepsilon) k_x) + 4t_2^2 \cos^2(b(\varepsilon) k_y)}, \end{aligned} \tag{5.1.8}$$

where we have used the fact that $a(\varepsilon) = l_1(\varepsilon) + l_2(\varepsilon)$, by definition.

5.1.2 *Modified Brillouin Zone*

Before moving on to derive the strain-dependent GFs for graphene and nanotubes we need to briefly discuss the Brillouin zone (BZ). In Sec. 3.3 we simply presented the well-known BZ of graphene without mentioning its origin. This may be derived using the Wigner-Seitz method which can be used to create a primitive cell spanning the entire space, and in reciprocal space this cell is known as the first BZ. To create this cell we first choose a lattice point, then draw lines to all neighbouring lattice points, and then draw perpendicular bisectors to each of these lines. This process is shown diagrammatically in

Fig. 5.3 in reciprocal space, where the reciprocal vectors $\mathbf{A}_1$ and $\mathbf{A}_2$ are chosen such that

$$\begin{aligned} \mathbf{A}_1 \cdot \mathbf{a}_1 &= \mathbf{A}_2 \cdot \mathbf{a}_2 = 2\pi, \\ \mathbf{A}_1 \cdot \mathbf{a}_2 &= \mathbf{A}_2 \cdot \mathbf{a}_1 = 0, \end{aligned} \tag{5.1.9}$$

and are therefore

$$\mathbf{A}_1 = \left(\frac{\pi}{a(\varepsilon)}, \frac{\pi}{b(\varepsilon)}\right), \quad \mathbf{A}_2 = \left(\frac{\pi}{a(\varepsilon)}, -\frac{\pi}{b(\varepsilon)}\right). \tag{5.1.10}$$

Our rectangular BZ is therefore determined to span $k_x = \left(-\frac{\pi}{a(\varepsilon)}, \frac{\pi}{a(\varepsilon)}\right)$ and $k_y = \left(-\frac{\pi}{2b(\varepsilon)}, \frac{\pi}{2b(\varepsilon)}\right)$, as shown in Fig. 5.3. Where we have implicitly transformed our BZ into a rectangular BZ for ease of integration in later steps. This is done in manner identical to that shown in Fig. 3.3.

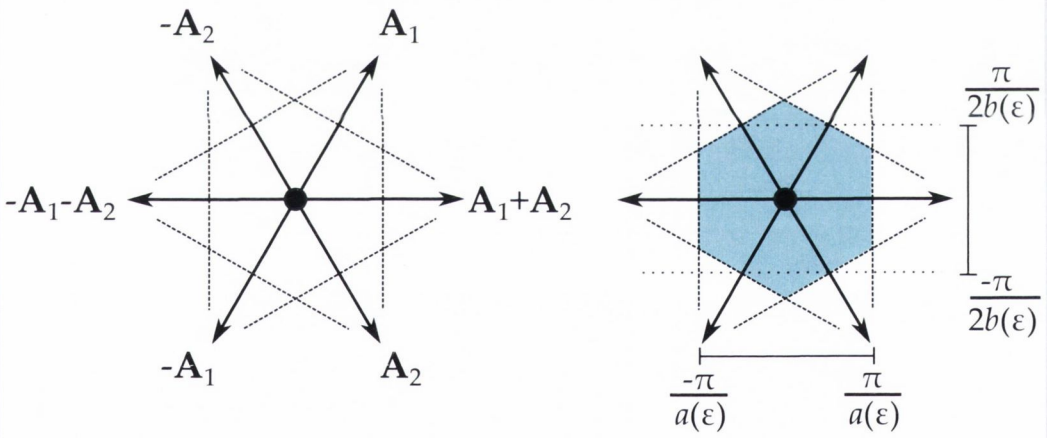


Figure 5.3: Schematic representation of the Wigner-Seitz cell for strained graphene with reciprocal vectors $\mathbf{A}_1$ and $\mathbf{A}_2$, the hexagonal Brillouin zone shown in blue, and the boundaries of the rectangular Brillouin, $\left(\frac{-\pi}{a(\varepsilon)}, \frac{\pi}{a(\varepsilon)}\right)$ and $\left(\frac{-\pi}{2b(\varepsilon)}, \frac{\pi}{2b(\varepsilon)}\right)$, indicated by the dotted lines.

In Sec. 3.2.1 we introduced the BZ of nanotubes and noted that armchair nanotubes are always metallic, and the ZZNTs are metallic or semi-conducting depending on the circumference n_c. This is understood in terms of lines of the discretized BZ intersecting with the Dirac points, $\mathbf{K}$ and $\mathbf{K}'$. Fig. 5.4 a)

shows the discretized BZ (blue lines) for an armchair nanotube. It is obvious from this image that the central line will always intersect with a Dirac point. As strain is introduced into the system, the relative positions of the Dirac points and lines will change, however this central line will always cross a Dirac point, so that even under strain ACNTs will remain metallic. Fig. 5.4 b) shows the discretized BZ (blue lines) for a semi-conducting zigzag nanotube. In this case the blue line will only intersect with the Dirac points under the condition $\mathrm{mod}(n_c, 3) = 0$, and thus only these nanotubes will be metallic. In contrast to ACNTs, strain shifts the Dirac points of ZZNTs in such a way that a semi-conducting NT may transition to being metallic, and vice-verse. This is very important as the coupling between magnetic moments in undoped semi-conducting ZZNTs decay exponentially and therefore becomes too small for practical purposes, as we shall see in Sec. 5.3.

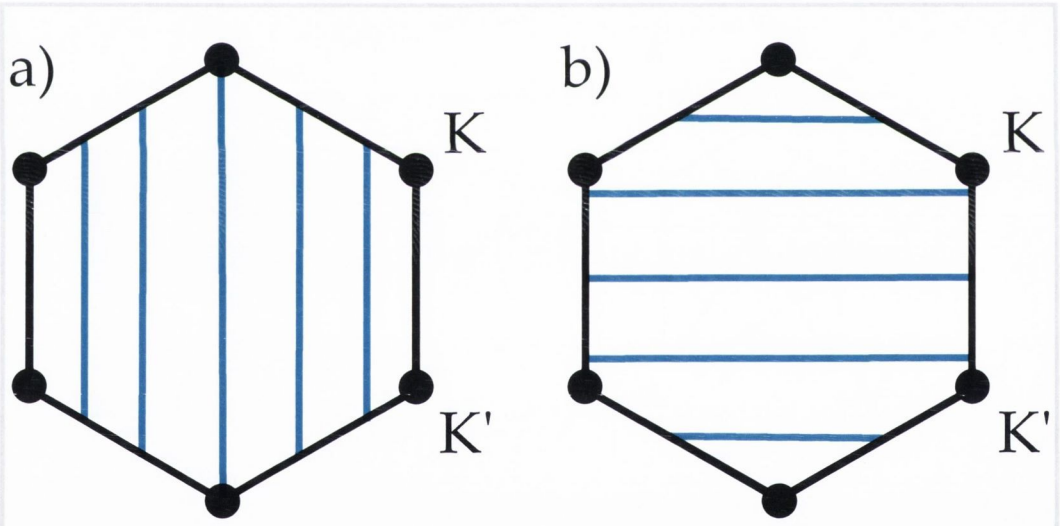


Figure 5.4: Schematic Representation of the Brillouin zone for a) an armchair nanotube, and b) a semi-conducting zigzag nanotube. With the Dirac points highlighted as black dots, and the unique Dirac points labelled K and K′.

5.1.3 *Modified Graphene Green's Functions*

Most of the work of deriving these GFs has been covered in Sec. 3.1.3. By combining that work with the two previous sections, we may now write the strain modified GF as

$$g_{\mathbf{r}\mathbf{r}'}(\varepsilon) = \frac{a(\varepsilon)}{2\pi}\frac{b(\varepsilon)}{\pi}\int_{-\pi/a(\varepsilon)}^{\pi/a(\varepsilon)} dk_x \int_{-\pi/2b(\varepsilon)}^{\pi/2b(\varepsilon)} dk_y \times N_{\gamma\gamma'}\frac{e^{i(a(\varepsilon)k_x(m+n)+b(\varepsilon)k_y(m-n))}}{E^2-\left(t_1^2+4t_1t_2\cos(b(\varepsilon)k_y)\cos(a(\varepsilon)k_x)+4t_2^2\cos^2(b(\varepsilon)k_y)\right)}. \tag{5.1.11}$$

This is can be simplified by making the substitutions $k_A = a(\varepsilon)k_x$ and $k_Z = b(\varepsilon)k_y$, giving us

$$f(\mathbf{k},\varepsilon) = t_1 + 2t_2\cos(k_Z)e^{-ik_A}, \tag{5.1.12}$$

and

$$|f(\mathbf{k},\varepsilon)| = \pm\sqrt{t_1^2+4t_1t_2\cos(k_Z)\cos(k_A)+4t_2^2\cos^2(k_Z)}. \tag{5.1.13}$$

This allows us to write the strain-dependent GF in a similar manner to strain-independent GF, Eq. 3.1.31, where all the strain dependence is now contained within the sublattice term $N_{\gamma\gamma'}$ and the dispersion relation,

$$g_{\mathbf{r}\mathbf{r}'}(\varepsilon) = \frac{1}{2\pi^2}\int_{-\pi}^{\pi} dk_A \int_{-\pi/2}^{\pi/2} dk_Z N_{\gamma\gamma'}(\varepsilon)\frac{e^{i(k_AD_A+k_ZD_Z)}}{E^2-|f(\mathbf{k},\varepsilon)|^2}, \tag{5.1.14}$$

The sublattice term has a similar form

$$N_{\gamma\gamma'}(E,\mathbf{k}) = \begin{cases} E & \text{if } \gamma = \gamma' \\ f(\mathbf{k},\varepsilon) & \text{if } \gamma = \alpha, \gamma' = \beta \\ f^*(\mathbf{k},\varepsilon) & \text{if } \gamma = \beta, \gamma' = \alpha \end{cases}. \tag{5.1.15}$$

We will now use this base form to derive strain dependent versions of the semi-analytic and SPA GFs for graphene, and analytic GFs for carbon nanotubes. For graphene we will examine four cases for each impurity: armchair separation with armchair strain (that is, parallel to the separation), armchair separation with zigzag strain (perpendicular to the separation), zigzag separation with armchair strain, and zigzag separation with armchair strain. For nanotubes we will only examine longitudinal separation with longitudinal strain, that is, separated and strained along the length of the nanotube.

Graphene Armchair Single Integral Green's function and SPA Green's function

We may now write the semi-analytic (single integral) GF for anisotropic graphene by following the same steps as in Sec. 3.1.4. This is now

$$g_{\mathbf{r}\mathbf{r}'}(\varepsilon) = \frac{i}{4\pi t_1 t_2} \int_{-\pi/2}^{+\pi/2} dk_Z \, N_{\gamma\gamma'}(\varepsilon) \frac{e^{i(q_A D_A + k_Z D_Z)}}{\cos(k_Z)\sin(q_A)}, \tag{5.1.16}$$

where the pole q_A is now

$$q_A(\varepsilon) = \pm\cos^{-1}\left(\frac{E^2 - t_1^2 - 4t_2^2\cos^2(k_Z)}{4t_1 t_2 \cos(k_Z)}\right). \tag{5.1.17}$$

From this, and following the steps laid out in Sec. 3.1.4 we may also easily derive the strain-dependent version of the SPA GF as

$$g_{D_A}(\varepsilon) = N_{\gamma\gamma'}\sqrt{\frac{2i}{\pi D_A}}\frac{e^{iq_A(k_Z^0)D_A}}{\sqrt{E(E^2-t_1^2+4t^2)\sqrt{t_1^2-E}}}, \tag{5.1.18}$$

where we have now evaluated the pole at a stationary point

$$q_A(\varepsilon, k_Z^0) = \cos^{-1}\left(\frac{\sqrt{t_1^2-E^2}}{t_1}\right). \tag{5.1.19}$$

Graphene Zigzag Single Integral Green's function and SPA Green's function

In a similar manner we can derive

$$g_{\mathbf{rr}'}(\varepsilon) = \frac{-i}{4\pi t_2}\sum_{\pm}\int_{-\frac{\pi}{2}}^{+\frac{\pi}{2}} dk_A\, N_{\gamma\gamma'}(\varepsilon)\frac{e^{i(qk_AD_A+q_Z^{\pm}D_Z)}}{t_2\sin(2q_Z^{\pm})+t_1\cos(k_A)\sin(q_Z^{\pm})}, \tag{5.1.20}$$

where the poles $q_Z^{\pm}$ are now

$$q_Z^{\pm}(\varepsilon) = \pm\cos^{-1}\left(-\frac{1}{2}\left(\frac{t_1\cos(k_A)}{t_2}\pm\sqrt{\frac{E^2}{t_2^2}-\frac{t_1^2}{t_2^2}\sin^2(k_A)}\right)\right). \tag{5.1.21}$$

And from this we may derive the SPA GF as

$$g_{D_Z} = N_{\gamma\gamma'}(\varepsilon)\left(k_A^0\right)\sqrt{\frac{1}{2i\pi D_Z}}\sum_{\pm}\frac{e^{iq_Z^{\pm}(k_A^0)D_Z}}{\sqrt{E|t_1|(t_1\pm E)\sqrt{-(E-t_1-2t_2)(E-t_1+2t_2)}}}, \tag{5.1.22}$$

where we now have the pole evaluated at a stationary point

$$q_Z^{\pm}(\varepsilon, k_A^0) = \cos^{-1}\left(\frac{-t_1\mp E}{2t_2}\right). \tag{5.1.23}$$

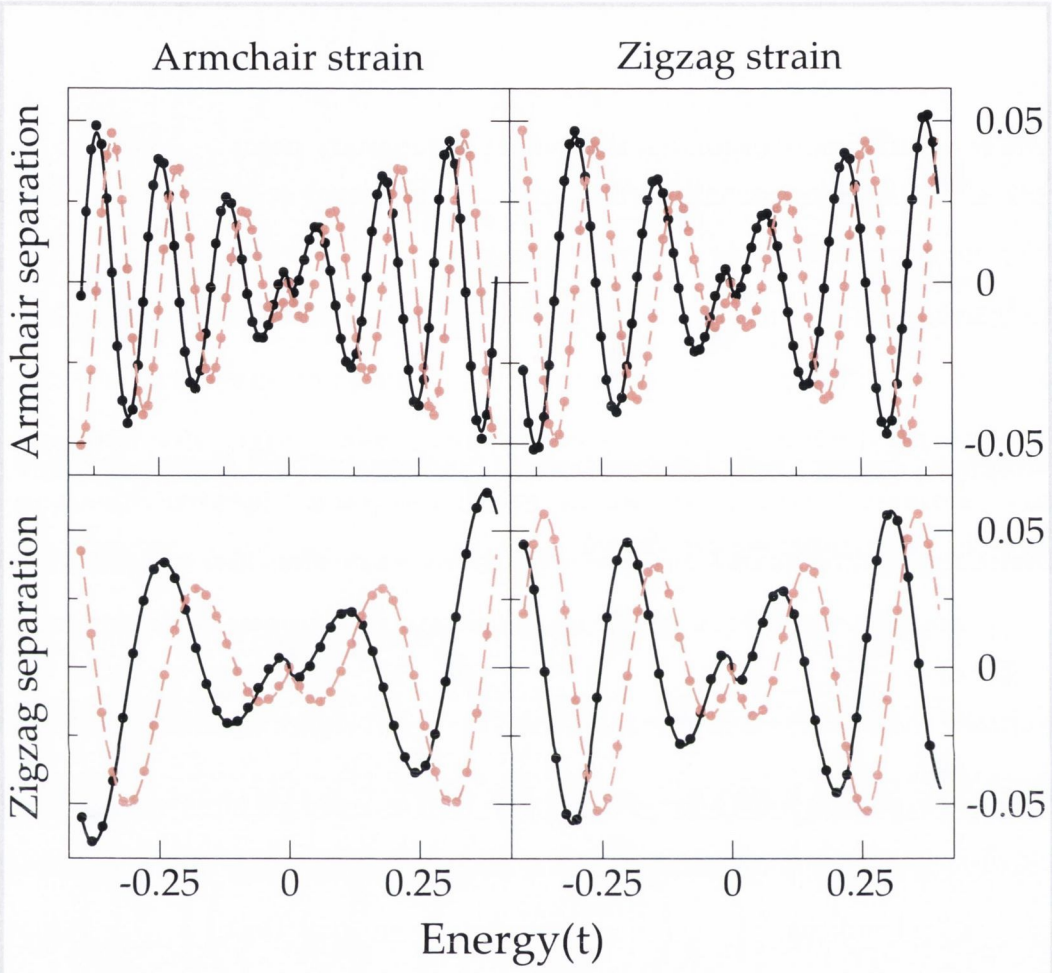


Figure 5.5: Plot comparing the numerically calculated (dots) and analytic expressions (lines) for the GF between two sites on the same sublattice in strained graphene systems. In all cases solid-black represent the real parts, and dashed-red represent the imaginary parts, of the GF. The upper panels represent the GF for a separation of $D_A = 20$ in the armchair direction and the lower panels a separation of $D_Z = 20$ in the zigzag direction. The left (right) panel in each case represents the GF for a strain in the armchair (zigzag) direction of $\varepsilon = 0.05$. An excellent agreement is seen for each.

A comparison between the strain-dependent GFs of Eqs. 5.1.16 and 5.1.20, and the SPA to these GFs, Eqs. 5.1.18 and 5.1.22, can be seen for each site separation and direction of strain in Fig. 5.5.

5.1.4 *Modified Nanotube Green's Functions*

The strain-dependent GFs for nanotubes can be derived in a similar manner as in Sec. 3.2.2. That is, discretizing one of the integrals in the circumferential direction.

ACNT

The GF we get from discretizing the strain-dependent GF, Eq. 5.1.14, over K_A, is

$$g_{rr'}(\varepsilon) = \frac{1}{2\pi}\frac{1}{n_c}\int_{-\pi/2}^{+\pi/2} dk_Z \sum_j N_{\gamma\gamma'}(\varepsilon)\frac{e^{i\frac{2\pi j}{n_c}D_A + ik_Z D_Z}}{E^2 - |f(\varepsilon)|^2} \tag{5.1.24}$$

where

$$f(\varepsilon) = t_1 + 2t_2\cos(k_Z)\, e^{i\frac{\pi j}{n_c}}. \tag{5.1.25}$$

Following the same procedure as before, we now find the pole to be

$$q_Z^{\pm}(\varepsilon) = \pm\cos^{-1}\left(-\frac{t_1}{2t_2}\cos\left(\frac{\pi j}{n_c}\right) \pm \frac{1}{2t_2}\sqrt{E^2 - t_1^2\sin^2\left(\frac{\pi j}{n_c}\right)}\right) \tag{5.1.26}$$

and the GF can be simply derived as

$$g_{rr'}(\varepsilon) = \frac{i}{4t_2 n_c}\sum_j\sum_{\pm} N_{\gamma\gamma'}\frac{e^{i\frac{2\pi j}{n_c}D_A + iq_Z^{\pm}|D_Z|}}{t_1\cos\left(\frac{\pi j}{n_c}\right)\sin\left(q_Z^{\pm}\right) + 2t_2\sin\left(2q_Z^{\pm}\right)}. \tag{5.1.27}$$

ZZNT

For ZZNTs we find the strain-dependent GF by discretizing Eq. 5.1.14 over k_Z. This gives us

$$g_{rr'}(\varepsilon) = \frac{1}{2\pi}\frac{1}{n_c}\int_{-\frac{\pi}{2}}^{+\frac{\pi}{2}} dk_A \sum_j N_{\gamma\gamma'}\frac{e^{ik_A D_A + i\frac{\pi j}{n_c}D_Z}}{E^2 - |f(\varepsilon)|^2} \tag{5.1.28}$$

with

$$f(\varepsilon) = t_1 + 2t_2\cos\left(\frac{\pi j}{n_c}\right)e^{ik_A}. \tag{5.1.29}$$

Again, we solve the integral in the same way as for graphene, using residue theory. Expanding the denominator as

$$|f(\varepsilon)|^2 = t_1^2 + 4t_1t_2\cos(k_A)\cos\left(\frac{\pi j}{n_c}\right) + 4t_2^2\cos\left(\frac{\pi j}{n_c}\right) \tag{5.1.30}$$

and solving for $E^2 - |f(\mathbf{k}, \varepsilon)|^2 = 0$ we find the pole

$$q_A = \pm\cos^{-1}\left(\frac{E^2 - t_1^2 - 4t_2^2\cos^2\left(\frac{\pi j}{n_c}\right)}{4t_1t_2\cos\left(\frac{\pi j}{n_c}\right)}\right). \tag{5.1.31}$$

Which now gives us the GF

$$g_{rr'}(\varepsilon) = \frac{i}{4t_1t_2n_c}\sum_j N_{\gamma\gamma'}\frac{e^{iq_A D_A + i\frac{2\pi j}{n_c}D_Z}}{\cos\left(\frac{\pi j}{n_c}\right)\sin(q_A)}. \tag{5.1.32}$$

Exactly as before we encounter a problem at $j = \frac{n_c}{2}$ where the denominator goes to zero. To get around this we go back and solve this particular case separately, with

$$f\left(j = \frac{n_c}{2}\right) = t_1^2. \tag{5.1.33}$$

So we have

$$\begin{aligned} I &= \frac{1}{2\pi n_c} \int_{-\frac{\pi}{2}}^{+\frac{\pi}{2}} dk_A \; N_{\gamma\gamma'} \frac{e^{ik_A D_A + i\frac{2\pi j}{n_c} D_Z}}{E^2 - t_1^2} \\ &= \delta_{m+n,0} \, N_{\gamma\gamma'} \frac{e^{i\frac{2\pi j}{n_c} D_Z}}{n_c (E^2 - t_1^2)}, \end{aligned} \tag{5.1.34}$$

where now

$$N_{\gamma\gamma'} = \begin{cases} E & \text{if } \gamma = \gamma' \\ \\ t_1 & \text{if } \gamma \neq \gamma' \end{cases} . \tag{5.1.35}$$

5.1.5 *Modified Hopping Integrals*

We now have everything we need to understand the effects of an arbitrary magnitude strain on the coupling between magnetic impurities in graphene and carbon nanotubes. We generally wish to treat the tensile strain, ε, as the relevant parameter rather than the tension applied. The strain can be more easily related to the hopping integrals, t_1 and t_2, the relative values of which will determine all of our effects. To examine the effects of specific values of strain it is important to know the relative values of the hopping parameters t_1 and t_2, which vary as a function of the change in bond length, $\Delta|R|$. We will follow the method laid out by Pereira *et al.* [112].

To start we must define the change in a general vector, $\mathbf{v}$, in graphene caused by some strain value, ε. This is given as

$$\Delta \mathbf{v} = \hat{\varepsilon} \cdot \mathbf{v}, \tag{5.1.36}$$

where $\hat{\varepsilon}$ is the strain tensor in the lattice coordinate system, and is given by

$$\hat{\varepsilon} = \varepsilon \begin{pmatrix} \cos^2(\theta) - \sigma\sin^2(\theta) & (1+\sigma)\cos(\theta)\sin(\theta) \\ (1+\sigma)\cos(\theta)\sin(\theta) & \sin^2(\theta) - \sigma\cos^2(\theta) \end{pmatrix}. \tag{5.1.37}$$

Here, θ is the angle of applied strain, and $\sigma = 0.165$ is the Poisson ratio for graphite, giving the level of contraction perpendicular to the direction of applied strain [195]. In graphene we will take the values of applied strain to be either along the armchair or zigzag direction, that is, either $\theta = \frac{\pi}{2}$ or $\theta = 0$, and in nanotubes we will always take the strain direction to be longitudinal. From this we may now calculate the change in magnitude of the interatomic vectors, $\mathbf{R}_1$ and $\mathbf{R}_2$, for both armchair and zigzag direction strain, as

$$\begin{aligned} \text{AC}: \Delta\left|\frac{\mathbf{R}_1}{\mathbf{R}_0}\right| &= -\varepsilon, \qquad \Delta\left|\frac{\mathbf{R}_2}{\mathbf{R}_0}\right| = \frac{1}{4}\varepsilon - \frac{3}{4}\varepsilon\sigma, \\ \text{ZZ}: \Delta\left|\frac{\mathbf{R}_1}{\mathbf{R}_0}\right| &= -\varepsilon\sigma, \qquad \Delta\left|\frac{\mathbf{R}_2}{\mathbf{R}_0}\right| = \frac{3}{4}\varepsilon - \frac{1}{4}\varepsilon\sigma, \end{aligned} \tag{5.1.38}$$

where $\mathbf{R}_0$ is the vector determining the unstrained interatomic distance. Determining the change in the hopping integral from the change in the interatomic distances is not a trivial matter, and several methods are used in the literature [196–198]. Here we choose to follow the exponential decay model [112, 199], such that

$$t_i = t_0 e^{-\alpha\Delta\left|\frac{\mathbf{R}_i}{\mathbf{R}_0}\right|}, \tag{5.1.39}$$

where t_0 is the hopping integral in the unstrained case, and the rate of decay, $\alpha = -3.37$, is determined from experiment [200].

5.1.6 *Modified Impurities*

Before looking at strain-modified interactions we note that straining the lattice may have an effect on the magnitude of an impurity moment. This topic has been discussed by several recent studies for a wide range of impurities in graphene and related materials [201–204]. For some impurities, a sudden change in the magnitude of the moment occurs when the impurity changes its hybridisation at critical strain values. For other impurities, for example substitutional Mn, the magnitude of the moment only varies very slightly with strain. Recall that the coupling goes as V_{ex}^2, where V_{ex} is the exchange splitting, which is proportional to value of the moment. As such, changes in the moment value, caused by strain, could influence the coupling, but should not qualitatively affect the results presented in this chapter.

5.2 STRAIN-MODIFIED INTERACTIONS IN GRAPHENE

The behaviour of coupling in response to strain can now easily be extracted by comparing the coupling equation, J_D, which was calculated in Eq. 4.2.12 using the strain-independent GFs of Sec. 3.1.3, with $J_D(\varepsilon)$ which can be calculated in the same manner using the strain-dependent GFs from Sec. 5.1.3. Calculating this coupling in the presence of strain, in an identical manner to Sec. 4.2.1 we get

$$J_D(\varepsilon) = -V_{ex}^2 \,\mathrm{Im}\left\{ e^{2iq^{(0)}(\varepsilon)D} \sum_{\ell} \frac{\mathcal{B}^{(\ell)}(\varepsilon)}{(2iq^{(1)}(\varepsilon))^{\ell+1}} \frac{1}{D^{\ell+2}} \right\}, \tag{5.2.1}$$

Which is identical, except that it now contains strain-dependent versions of the terms q and $\mathcal{B}$. For clarity we choose to write this in such a way that we can extract the distance independent terms. The full expression is given as

$$J_D \sim \mathrm{Im} \sum_{\ell} \frac{\mathcal{J}_\ell(E_F, \varepsilon)}{D^{\ell+2}} e^{2iq^{(0)}(E_F,\varepsilon)D}, \tag{5.2.2}$$

where

$$\mathcal{J}_\ell(E_F, \varepsilon) = -\frac{V_{ex}^2 \mathcal{B}^{(\ell)}(E_F, \varepsilon)}{(2iq^{(1)}(E_F, \varepsilon))^{\ell+1}} \tag{5.2.3}$$

is the distance-independent coefficient for the ℓ-th term in the power series, ℓ is a non-negative integer and $\mathcal{B}^{(\ell)}(E_F, \varepsilon)$ is the ℓ-th order energy derivative of $\mathcal{B}(E, \varepsilon)$ evaluated at E_F, resulting from its Taylor expansion.

5.2.1 *Substitutional and Top-Adsorbed*

In general the leading term in the series, in Eq. 5.2.2, should determine the asymptotic decay rate of the coupling. For substitutional and top-adsorbed impurities, in the undoped case, we showed for unstrained graphene that the coefficient $\mathcal{B}^{(0)} = 0$, so that the $\ell = 1$ term dominates and $J_D(E_F = 0) \sim D^{-3}$. For the strained case we can similarly show that $\mathcal{B}^{(0)}(\varepsilon) = 0$ and that

$$\begin{aligned} J_{D_A}(E_F = 0, \varepsilon) &\sim \frac{V_{ex}^2}{\pi} \frac{2t_1}{4t_2^2 - t_1^2} \frac{1}{D_A^3}, \\ J_{D_Z}(E_F = 0, \varepsilon) &\sim -\frac{V_{ex}^2}{4\pi} \frac{\sqrt{4t_2^2 - t_1^2}}{t_1^2} \cos(q(\varepsilon)D) \frac{1}{D_Z^3}, \end{aligned} \tag{5.2.4}$$

for armchair and zigzag separations respectively. Thus we should not expect to change the decay rate of the interaction by applying uniaxial strain. To study how strain affects the coupling we compare Eq. 5.2.4 with their strain-independent counterparts from Sec. 4.2 in undoped graphene as strain is ap-

plied and then increased. We define the strain-dependent amplification, β, as the ratio between the strained and unstrained couplings,

$$\beta(\varepsilon) = \frac{J_D(\varepsilon)}{J_D(\varepsilon = 0)}. \tag{5.2.5}$$

Armchair Separation

The periodicity of the coupling can be determined from Eq. 5.1.19. This is clearly independent of t_1 and t_2 at $E = 0$, and is therefore independent of strain. Thus the only effect strain can have is a distance-independent amplification or suppression. This effect arises from the $\mathcal{B}^{(1)}$ term in Eq. 5.2.3. In Fig. 5.6 a) we plot the numerically-calculated coupling between moments on the same sublattice as a function of armchair separation. This quantity is shown for zero strain (black line), and for strains of $\varepsilon = 0.05$ in the armchair (red, dashed) and zigzag (blue, dot-dashed) directions. The results, shown in log-log form, confirm that the decay rate, $\sim D^{-3}$, is unaffected as the strained cases lie parallel to the unstrained case. We note that the coupling is enhanced by zigzag strain, and suppressed by armchair strain.

To study the effect of increasing strain we calculate the amplification factor $\beta(\varepsilon)$, and find the simple analytical form for armchair separations

$$\beta_A = 3\, t_0\, \frac{t_1}{4t_2^2 - t_1^2}, \tag{5.2.6}$$

where t_0 is the unstrained hopping value. We note that this expression has the same form in terms of t_1 and t_2 for strains in both high symmetry directions, but that the t_1 and t_2 values themselves depend on the strain direction, as given by Eq. 5.1.39. In Fig. 5.6 b) we plot the analytic expression for β_A as a function of strain in both the armchair (red, solid line) and zigzag (blue, dashed line) strain directions. A monotonic decrease (increase) in the coupling for armchair (zigzag) separations consistent with the results in Fig. 5.6 a)

is observed. To confirm the analytic prediction, numerical calculations of β_A

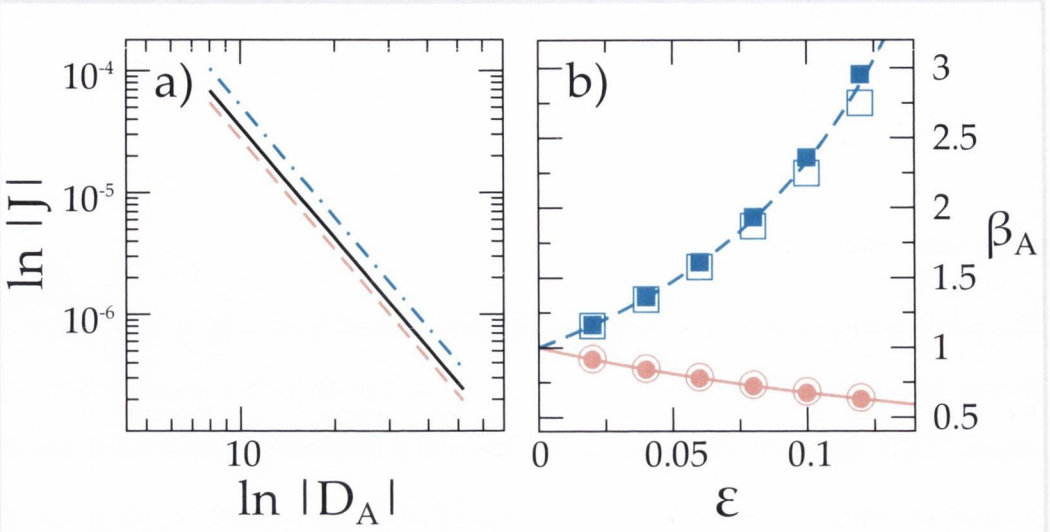


Figure 5.6: a) Log-log plot showing the numerical magnetic coupling against armchair-direction separation without strain (black, solid line) and with $\varepsilon = 0.05$ armchair (red, dashed) and zigzag (blue, dot-dashed) uniaxial strain applied.
b) Amplification factor β_A as a function of strain, ε, in the armchair (red, solid line) and zigzag (blue, dashed) directions. Filled and hollow symbols represent numerical calculations for same-sublattice and opposite sublattice cases respectively.

are performed for a fixed value of separation, $D_A = 20$. Filled and hollow symbols represent calculations performed for sites on the same or different sublattice(s) respectively. An excellent agreement with the analytic predictions is seen in all cases.

In addition to the substitutional case discussed here, numerical calculations were also performed for top-adsorbed impurities. The results (not shown) are also in perfect agreement with Eq. 5.2.6, highlighting the fact that an exact parametrisation of the magnetic impurity is not necessary to calculate the qualitative behaviour of the RKKY interaction. The identical amplification of couplings between same and opposite sublattice sites is explained by the phase factor between these couplings, which is zero for armchair direction separations [75]. For other separation directions a more complex behaviour is

expected as this phase factor is no longer zero, and the phase of the distance-dependent oscillations may also be strain dependent.

Zigzag Separation

In Fig. 5.7 a) we show the magnetic coupling as a function of zigzag separation for the unstrained case (black, solid line) and for strains of $\varepsilon = 0.05$ in the armchair (red, dashed) and zigzag (blue, dot-dashed) directions. A more complicated, non-monotonic behaviour than the armchair case is observed. This arises due to the Fermi wavevector in the zigzag direction and for unstrained graphene the oscillation has a period of $D_Z = 3$. As strain is applied, the wavevector determining the oscillation period, Eq. 5.1.23, varies as $q(\varepsilon) = q(0) + \delta k(\varepsilon)$ where $\delta k = \cos^{-1}\left(\frac{-t_2}{2t_1}\right) - \frac{4\pi}{3}$. The amplification factor in the zigzag direction, for impurities on the same sublattice, is thus

$$\beta_Z = \frac{t_0\sqrt{4t_2^2 - t_1^2}}{\sqrt{3}\,t_2^2}\,\frac{\cos^2\left(\left(q(0) + \delta k(\varepsilon)\right)D\right)}{\cos^2(q(0)\,D)}. \tag{5.2.7}$$

The amplification factor for opposite-sublattice impurities must take into account the $\frac{\pi}{2}$ phase shift from the same-sublattice case predicted for zigzag separations [75], and is equivalent to the above equation up to a prefactor (Fig. 5.7).

The first part is a distance-independent term similar to β_A which gives a monotonic increase (decrease) in the coupling for strain applied in the armchair (zigzag) direction. Viewed with the armchair results, this suggests a trend of strain perpendicular to the separation direction amplifying the coupling, and parallel to the separation direction suppressing the coupling. The second part of Eq. 5.2.7 accounts for amplification due to the change in the Fermi wavevector with strain and leads to oscillations in β_Z. The analytic expression for β_Z is plotted in Fig. 5.7 b) and c) for armchair and

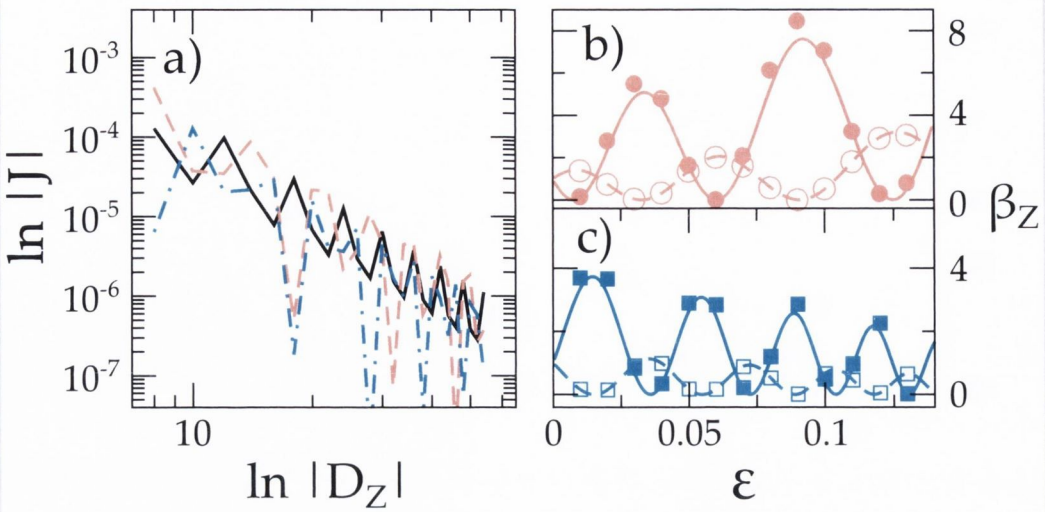


Figure 5.7: a) Log-log plot showing the numerical magnetic coupling against zigzag-direction separation without strain (solid-black line) and with $\varepsilon = 0.05$ armchair (dashed-red) and zigzag (dot-dashed-blue) uniaxial strain applied. Amplification factor β_Z as a function of b) armchair strain, and c) zigzag strain for same (solid line, filled symbols) and opposite (dashed line, hollow symbols) sublattice cases. Lines represent the analytic result and symbols the numerical calculations.

zigzag strains respectively for both same-sublattice (solid lines) and opposite-sublattice (dashed line) cases with $D_Z = 40$.

An excellent agreement is again noted with the numerical calculations represented by filled (same-sublattice) and hollow (opposite-sublattice) symbols. The oscillations in the coupling, which appear as a function of strain, are very interesting and may have significant implications for strain-tuning of the interaction. Unlike for armchair separations, a small difference in the applied strain can tune the coupling from zero to several multiples of the unstrained value. Since the same-sublattice and opposite-sublattice couplings are exactly out of phase in this direction one is switched off when the other reaches a maximum. For an arbitrary non-armchair separation the coupling will have characteristic strain values for which one of the couplings is zero but the other is not. Thus strain suggests itself as a powerful tool, not only to amplify the interaction between impurity moments, but also to switch the interaction on

and off and to control the interplay between impurities on different sublattices.

5.2.2 *Bridge-Adsorbed*

Figure 5.8 shows the coupling between two bridge-adsorbed impurities separated along the armchair and zigzag directions of unstrained graphene. The strain-dependent versions of these couplings can be calculated in a similar manner to the section above as

$$\begin{aligned} J_{D_A} &\sim V_{ex}^2 \frac{2}{\pi} \frac{t_1}{4t_2^2 - t_1^2} \frac{1}{D_A^3}, \\ J_{D_Z} &\sim -V_{ex}^2 \frac{2}{\pi} \frac{\sqrt{4t_2^2 - t_1^2}}{t_1^2} (1 - 2\cos(2q(\varepsilon)D_Z + \phi_B)) \frac{1}{D_Z^3}, \end{aligned} \tag{5.2.8}$$

where we now have a strain-dependent form of the oscillation term described in Sec. 4.2.4. The strain-independent form, previously derived by Sherafati *et al.* [75], may be used to derive this strain-dependent form. To do so we must replace the term $\frac{2\pi}{3}$, which is the strain-independent value of the Fermi vector, for zigzag separated impurities, evaluated at $E = 0$ (Eq. 4.2.23), by the strain-dependent value from Eq. 5.1.19, where $q(\varepsilon) = \cos^{-1}\left(\frac{-t_1}{2t_2}\right)$.

The analytic expressions were found to greatly underestimate the degree of suppression noted for zigzag strains for both separation directions. We emphasise however that the proper oscillatory behaviour for the coupling as a function of strain for zigzag separations is correctly predicted for both strain directions and thus Eq. 5.2.8 is a useful tool to predict the amount of strain required to turn off the coupling or change its sign. A number of representative calculations of the coupling are presented in Fig. 5.9. The top panels show the interaction between two bridge impurities as they are separated in the armchair (a) or zigzag (b) directions. We note that for the black curves, representing the unstrained case, that we now only consider every third separation

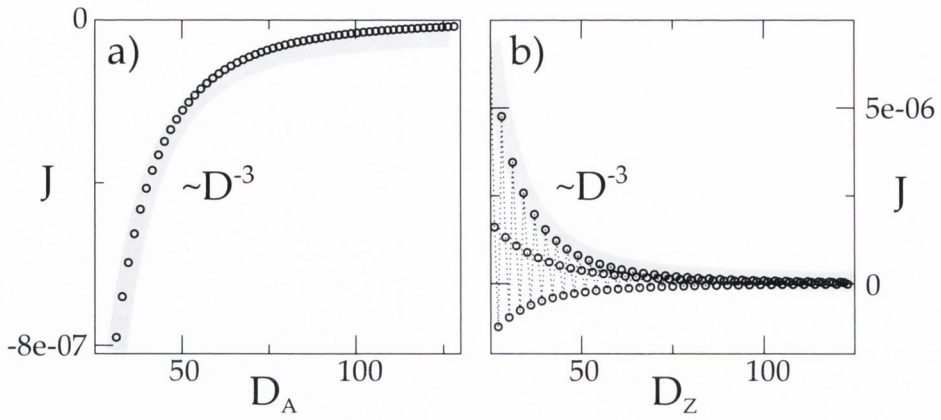


Figure 5.8: Coupling between bridge-adsorbed impurities separated along the a) armchair direction, b) zigzag direction in unstrained graphene. A monotonically decaying D^{-3} FM interaction is seen in the armchair direction (grey shading), whereas a sign-changing oscillation is observed in the zigzag direction. The phase of the oscillations is found to vary with the hopping parameter between the impurities and the carbon atoms, τ.

value in the zigzag direction in order to remove the period-3 oscillations usually seen in this direction. The red-dashed (blue dash-dotted) curve in these panels represent the interaction when armchair (zigzag) strain of strength $\varepsilon = 0.05$ is applied. In all cases, the log-log insets in panels a) and b) reveal that strain has no effect on the decay rate between bridge-adsorbed impurities, which remains at the standard D^{-3} rate for undoped graphene. For armchair separations, we note that both strains lead to a mild suppression of the coupling. This is in contrast to the prediction for substitutional impurities that parallel strain should suppress and perpendicular strain amplify the coupling. These features are also clear when we examine the change in the coupling for impurities a fixed distance $D_A = 80$ apart as armchair (c) or zigzag (d) strain is applied. Numerical calculations are shown by the red circles in c), and the solid line is the analytical result. The solid blue line in f) represents the numerical calculation for zigzag strains. In both cases only suppression of the coupling is observed until high values of strain are reached.

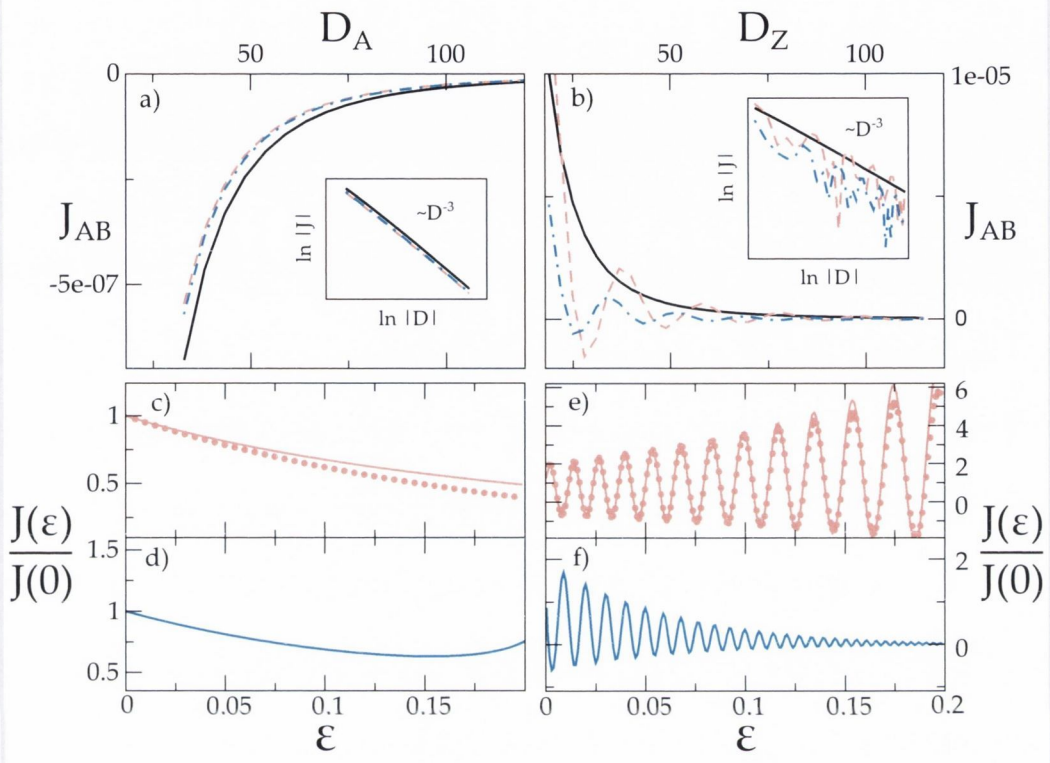


Figure 5.9: The effect of strain on the indirect exchange interaction between bridge-adsorbed impurities separated in the armchair, D_A, (left panels) and zigzag, D_Z, (right panels) direction. In all panels red (blue) plots correspond to an armchair (zigzag) direction strains. a) and b) show the separation dependence of numerically calculated interactions for unstrained (black,solid) and $\varepsilon = 0.05$ armchair (dashed-red) or zigzag (dash-dotted-blue) strains. The insets show log-log plots, confirming the persistence of the D^{-3} decay rate. The bottom panels show the change in the coupling, relative to the unstrained coupling, as a function of strain for fixed separations of $D_A = 80$ (c and d) and $D_Z = 80$ (e and f). For armchair strains (c and e) the large red dots represent numerical evaluations and the red lines the analytic predictions given in the text. Only numerical evaluations are shown for zigzag strain cases (d and f).

For zigzag separations we note that strain induces additional sign-changing oscillations as both the separation (b) and strain (e and f) are varied. The oscillations with increasing separation are in addition to the existing period-3 oscillations visible in the right panel of Fig. 5.8 for the unstrained case. For a fixed separation of $D_Z = 80$, we note that the coupling oscillates rapidly as a function of strain for both strain directions, with an overall amplification for the armchair strain (e) and suppression for the zigzag strain (f). We note that the frequency of the oscillations increases with separation. To better understand the behaviour for bridge-adsorbed impurities, it is again instructive to examine the SPA form of the Γ_{AB}, defined in Sec. 3.4.1, term entering into the expression for the coupling. The strained forms of the coefficients are

$$\begin{aligned}
N_\Gamma \overline{\mathcal{A}}_A(E,\varepsilon) &= \frac{-2\tau^2(E+t_1)}{t_1}\sqrt{\frac{2i}{\pi}}\sqrt{\frac{E}{(E^2+4t_2^2-t_1^2)\sqrt{(t_1^2-E^2)}}}, \\
q_A(E,\varepsilon) &= \pm\cos^{-1}\left(\frac{-\sqrt{t_1^2-E^2}}{t_1}\right), \\
N_\Gamma \overline{\mathcal{A}}_Z(E,\varepsilon) &= \frac{4\tau^2}{\sqrt{2i\pi}}\sqrt{\frac{E}{|t_1|(t_1-E)\sqrt{(4t_2^2-(E-t_1)^2)}}}, \\
q_Z(E,\varepsilon) &= \pm\cos^{-1}\left(\frac{-t_1+E}{2t_2}\right).
\end{aligned} \tag{5.2.9}$$

It is clear that the oscillations arising for zigzag direction separations are due to the strain-dependence of the Fermi wavevector q_Z in this direction. This is in contrast to the armchair case, where the wavevector q_A is strain-independent at $E = 0$. The anisotropy of the Fermi surface under uniaxial strain has been noted previously in the literature [112, 139] and is also the mechanism behind oscillations in the amplitude of the coupling noted previously for zigzag separated substitutional impurities.

An important difference between the bridge-adsorbed impurities and the substitutional case comes from the averaging out of sublattice dependent effects and the consequent possibility of either FM or AFM couplings, as seen in

Fig. 5.8 and in the form of the oscillatory term in Eq. 5.2.9. Including the strain dependent Fermi wavevector from Eq. 5.1.19 returns the same oscillatory behaviour as calculated numerically. In Sec. 5.2.1 we study substitutional impurities in strained systems, and we derive simple analytic expressions were derived to predict the amplification, suppression and oscillatory behaviour of $\beta = \frac{J(\varepsilon)}{J(0)}$ for the high symmetry directions of strain and separation. The accuracy of these simple expressions was as a result of the simple form of the RKKY coupling expression in terms of the off-diagonal GFs, from which the strain-dependence could be simply extracted. Although we have derived similar expressions for the Γ_{AB} function in this work, the strain dependence of the coupling amplitude is complicated significantly by the fact that the denominator in Eq. 3.4.22 relating the required GFs to these Γ terms has a non-trivial strain dependence. Focusing only on the Γ_{AB} contribution yields analytic estimates of

$$\begin{aligned} \beta_A &= \frac{3t_0 t_2}{4t_2^2 - t_1^2}\,, \\ \beta_Z &= \frac{|t_0|\sqrt{4t_2^2 - t_1^2}}{\sqrt{3}t_2^2}\frac{1 - 2\cos(2Q(\varepsilon)D + \phi_B)}{1 - 2\cos(2Q(0)D + \phi_B)}\,, \end{aligned} \tag{5.2.10}$$

for armchair and zigzag separations respectively. We note that the armchair expression is identical to that for the substitutional case, and the zigzag expression varies only in the oscillatory term. These expressions provide a reasonable approximation for armchair direction strains, and evaluations shown by solid red lines in Figs. 5.9 c) and e) match quite well with the numerical evaluations shown by the red circles. However the analytic expressions were found to greatly underestimate the degree of suppression noted for zigzag strains for both separation directions and are not shown in Figs. 5.9 d) and f). We emphasise however that the proper oscillatory behaviour for the coupling as a function of strain for zigzag separations is correctly predicted for both

strain directions and thus Eq. 5.2.10 is a useful tool to predict the amount of strain required to turn off the coupling or change its sign.

5.2.3 *Centre-Adsorbed*

Figure 5.10 shows the coupling between centre-adsorbed impurities on unstrained graphene. Using numerically evaluated GFs, we can calculate the IEC for centre-adsorbed impurities as a function of strain. The top panels of Fig. 5.11 show how the coupling between centre-adsorbed impurities a fixed distance apart varies as uniaxial strain is applied perpendicular to the separation direction. The results are normalised relative to the magnitude of the coupling in the unstrained system. We show two cases: armchair separated impurities with a zigzag strain (panel a) and zigzag separated impurities with an armchair strain (panel b). In both cases a dramatic increase in the magnitude of the coupling is observed as the strain is increased. It is worth noting that similar increases in the coupling magnitude, not shown here, are observed if parallel strains are applied. This is in contrast to the case of substitutional impurities, where parallel strains are generally associated with an overall suppression of the coupling. For the zigzag separated impurities in Fig. 5.11 b), we also note sizeable sign-changing oscillations, suggesting strain as a tool to manipulate the preferential spin alignment of a pair of centre-adsorbed impurities. A more subtle sign changing feature is also present for the armchair direction and highlighted in the zoomed inset of panel a, where we note the unstrained FM coupling switches to AFM initially, before returning to FM for larger values of strain. To understand this behaviour better, we turn to the distance dependence of the coupling in strained systems. Figure 5.11 c) shows log-log plots of the coupling as a function of distance for zigzag-separated centre-adsorbed impurities with no strain (black, solid line) and for armchair strains of $\varepsilon = 0.05$ (red, dashed) and $\varepsilon = 0.1$ (blue, dashed-dotted). It is clear

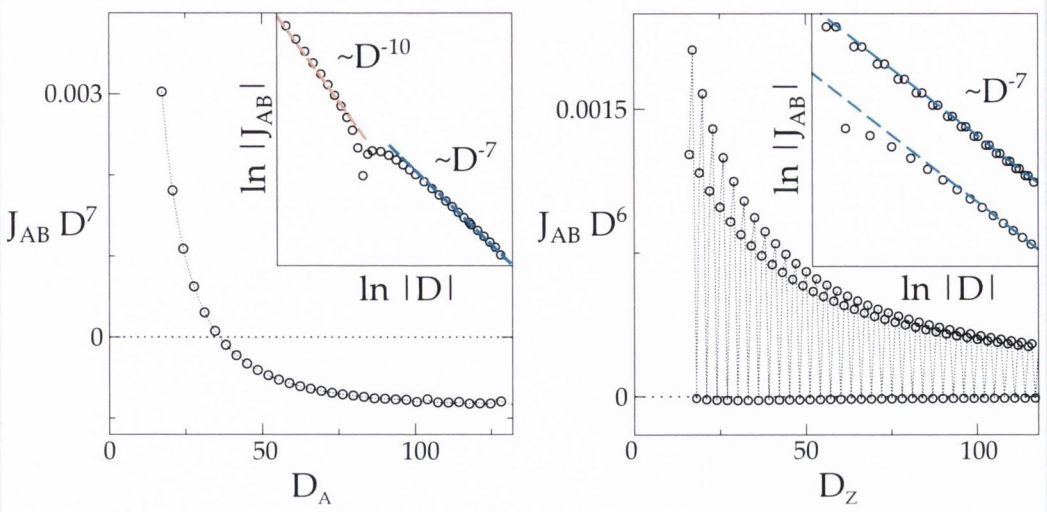


Figure 5.10: Numerical evaluation of the coupling between centre-adsorbed impurities as a function of separation, D, in the armchair and zigzag directions. The armchair (zigzag) results are multiplied by D^7 (D^6) to highlight the features discussed in the text. The dotted line at o in the main panels highlights the boundary between AFM (above) and FM (below) couplings. In the armchair direction an initial AFM interaction decays extremely rapidly as D^{-10} before a sign change to FM and a decay of D^{-7} at larger separations. Zigzag separations reveal that every third value of separation has an FM interaction approximately two orders of magnitude smaller than the AFM majority values. The insets in each case show log-log plots where dashed lines show the slopes corresponding to the relevant decay rates.

that the slopes of the three lines are different, indicating a change in the rate of decay as strain is varied. Regression fits to these curves (dotted black lines) find decay exponents of -6.8, -3.5 and -3.4 for the $\varepsilon = 0.0, 0.05, 0.1$ cases respectively. Figure 5.11 d) plots the decay exponent, α (where $J \sim D^{-\alpha}$), for a number of ε values. We see that the initial unstrained asymptotic decay rate of D^{-7} changes to the D^{-3} rate expected for substitutional and bridge impurities, shown by a dashed red line in Fig. 5.11 d), within the range $\varepsilon = 0.0 - 0.05$, and it remains constant at this value for higher values of strain. Similar transitions of the decay rate from D^{-7} to D^{-3} are noted for the other separation and strain directions, and explain the massive amplification of the coupling with strain noted in the top panels of Fig. 5.11.

To understand the behaviour of the coupling more clearly it is worth examining the strain-dependent forms of coupling, which for armchair and zigzag directions are

$$\begin{aligned} J_{D_A} &\sim \frac{t_1(t_1-t_2)^4}{t_2^4(t_1^2-4t_2^2)}\frac{1}{{D_A}^3}, \\ J_{D_Z} &\sim \frac{\sqrt{t_1^2-4t_2^2}(t_1-t_2)^4}{t_1^2t_2^4}\frac{1}{{D_Z}^3}, \end{aligned} \tag{5.2.11}$$

where we only include the strain-dependent elements arising from $\mathcal{B}^{(1)}$. It is clear that these expressions, that in the $\varepsilon = 0$ limit where $t_1 = t_2$, the numerator associated with a D^{-3} decay vanishes and J must decay at a faster rate. We recall that the decay exponent α is determined by the order of the first non-vanishing energy derivative of $\mathcal{B} = \mathcal{A}^2$ evaluated at the Fermi energy. From Eq. 5.2.1, if $\mathcal{B}^{(\ell)} \neq 0$, then $\alpha = \ell + 2$. In the unstrained case, the first four derivatives of $\mathcal{B}$ vanish, corresponding to a decay exponent of $\alpha = 5 + 2 = 7$. The zero-th derivative, $\mathcal{B}^{(0)}$, vanishes in both the strained and unstrained cases due to the presence of the E in the numerator. This is related to the vanishing density of states in graphene at the Dirac point and also occurs for substitutional and bridge-adsorbed impurities, where an $\alpha = 3$ decay is predicted for unstrained graphene. Examining the form of $\mathcal{B}^{(\ell)}(\varepsilon)$ for centre-adsorbed impurities we note that

$$\mathcal{B}^{(\ell)}(E=0) \sim (t_1-t_2)^{5-\ell} \quad \text{for} \quad \ell = 1, \cdots, 5, \tag{5.2.12}$$

so that the first four terms vanish in the unstrained case. As a uniaxial strain is applied, the quantity $t_1 - t_2$ becomes nonzero and we thus expect a decay rate of D^{-3}, corresponding to the $\ell = 1$ term in the series dominating, and indeed this is what we find numerically in the asymptotic case for larger values of strain. However, for small values of strain and small to medium separations between the impurities, the dominating term is determined by

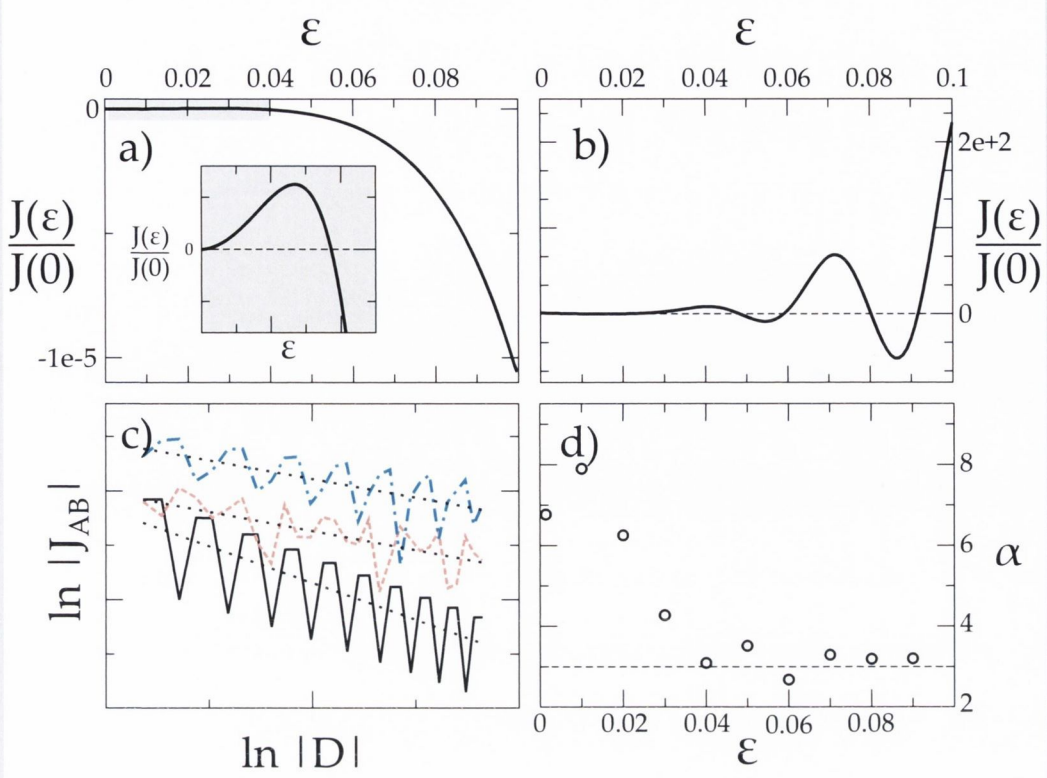


Figure 5.11: Numerically evaluated indirect exchange interaction $J(\varepsilon)$ between two centre-adsorbed impurities fixed distances apart in the a) armchair and b) zigzag direction as uniaxial strain is applied perpendicular to the separation direction. The results are normalised relative to the unstrained coupling $J(0)$. The inset in panel a) shows a close-up of the region highlighted by a grey rectangle in the main plot. c) Log-log plots of coupling against zigzag direction separation for armchair direction strains of $\varepsilon = 0.0$ (solid-black), 0.05 (dashed-red) and 0.1 (dash-dotted-blue). The black dotted lines show linear regressions with slopes of -6.8, -3.5 and -3.4 respectively. d) Plot of the decay exponent α as a function of strain for the cases shown in c) and additional values.

an interplay between the $(t_1 - t_2)^{5-\ell}$ term in the numerator and $D^{\ell+2}$ term in the denominator. Another complicating factor is the fact that the different terms in the power series expression for the coupling may have different signs. Thus, as strain is increased we should expect to see the decay rate decrease from D^{-7} to slower decays of alternating sign before settling on D^{-3} when the first non-vanishing coefficient is large enough to dominate over those of faster

decays. This is exactly the behaviour noted in the numerical results presented in the bottom panels of Fig. 5.11.

We note that in addition to the sign-changing oscillations for both armchair and zigzag directions which are associated with different terms in the coupling power series dominating the interaction, another set of sign changing oscillations emerge for zigzag separations due to the strain dependence of the Fermi surface which breaks the commensurability between the oscillation period and the lattice spacing. A similar set of oscillations, but without the sign-changing feature seen here, was noted for substitutional impurities.

5.3 STRAIN-MODIFIED INTERACTIONS IN NANOTUBES

For low-dimensional metallic structures, such as nanotubes, the exchange coupling between localized magnetic moments is predicted to decay rather slowly. In Chap. 4 we showed that it decays as D^{-1} for substitutional, top-adsorbed, and bridge-adsorbed impurities, and as D^{-5} for centre-adsorbed impurities. The long-range character of this interaction plays a significant role in determining the magnetic order of the system. In Sec. 5.2 we examined the role of uniaxial strain on the behaviour of this interaction in graphene, here we extend that work to nanotubes.

We now examine the RKKY interaction in carbon nanotubes in the presence of uniaxial strain, for the 4 common types of impurity location: substitutional, top-adsorbed, bridge-adsorbed, and centre-adsorbed impurities. The behaviour of coupling in response to strain can be extracted by comparing the coupling equation, J_D, which was calculated in Eq. 4.2.12 using the strain-independent GFs of Sec. 3.2.2, with $J_D(\varepsilon)$ which can be calculated in the same manner using the strain-dependent GFs from Sec. 5.1.4. We show that strain

is capable of amplifying or attenuating the RKKY interaction, significantly increasing certain interaction ranges, and acting as a switch: effectively turning on or off the interaction. We argue that such behaviour of the magnetic interaction in the presence of uniaxial strain can be used in future spintronic devices.

5.3.1 *Modified Interactions in Armchair Nanotubes*

Unstrained chiral nanotubes may be metallic or semiconducting. ACNTs are known to be metallic for all circumferences. These properties are due to the intersection of the discretized momentum values and the Fermi surface. The introduction of strain, ε, into the nanotube system alters the coincidence of the momentum values and the Fermi surface, this in turn alters the electronic properties of nanotubes. However, ACNTs remain metallic under strain. This can be understood by examining the BZ for ACNTs in Fig. 5.4. Since longitudinal strain shifts the Dirac points **K** and **K′**, which are located at $(0, \frac{2\pi}{3})$ and $(0, -\frac{2\pi}{3})$, only in the k_Z direction, the central line of the BZ, determined from

$$\epsilon_{\pm}(\mathbf{k}, \varepsilon) = \pm\sqrt{t_1^2 + 4t_1 t_2 \cos(k_Z)\cos\left(\frac{\pi j}{n_c}\right) + 4t_2^2\cos^2(k_Z)}, \tag{5.3.1}$$

will always cross the Dirac points leading to available states at the Fermi energy.

Although ACNTs remain metallic with strain, this does not mean that the RKKY interaction is unchanged. Figure 5.12 shows the effect of strain on the RKKY interaction for substitutional and bridge-adsorbed impurities for several separations D_Z, on an ACNT with $n_c = 21$. Top-adsorbed impurities have been omitted due to the similarity of behaviour with substitutional impurities. For both same-sublattice and opposite-sublattice interactions strain is seen to predominantly amplify the interaction. Interestingly there exist strain

values that completely shut off the opposite-sublattice interaction, whilst simultaneously maximizing the same-sublattice interaction. The overall decay rate comes from the first non-vanishing $\mathcal{B}(\varepsilon)$, which, for same-sublattice substitutional impurities, is

$$\mathcal{B}(\varepsilon)^{(0)} = \frac{1}{4n_c{}^2\left(t_1^2 - 4t_2^2\right)}. \tag{5.3.2}$$

This corresponds to a decay rate of D^{-1}, identical to that of the unstrained case. The general amplification can be understood from this term, as longitudinal strain for an ACNT is along the zigzag direction which increases the value of t_2 and decreases t_1. The equivalent opposite-sublattice term is similar.

For bridge-adsorbed impurities (Fig. 5.12 c) strain is capable of switching the sign of an interaction in a very controlled fashion. Since bridge-adsorbed impurities display a coupling with alternating sign as a function of separation, strain cannot create wholly FM or AFM interactions between multiple impurities. However, for a pair of impurities it is capable of switching the sign of the interaction. The coupling between bridge-adsorbed impurities is weakened with strain, however the decay rate is not affected. The first non-vanishing $\mathcal{B}(\varepsilon)$ is

$$\mathcal{B}(\varepsilon)^{(0)} = \frac{4}{n_c{}^2\left(t_1^2 - 4t_2^2\right)}, \tag{5.3.3}$$

corresponding to a decay rate of D^{-1}. As with bridge-adsorbed impurities in graphene, the oscillation is not easily captured within our model.

For centre-adsorbed impurities we see that the introduction of strain has a large impact on the decay rate and hence the magnitude of the interaction. Figure 5.13 shows the behaviour of the interaction between centre-adsorbed impurities with and without strain. Strain changes the interaction from being primarily antiferromagnetic to being split evenly between ferromagnetic and

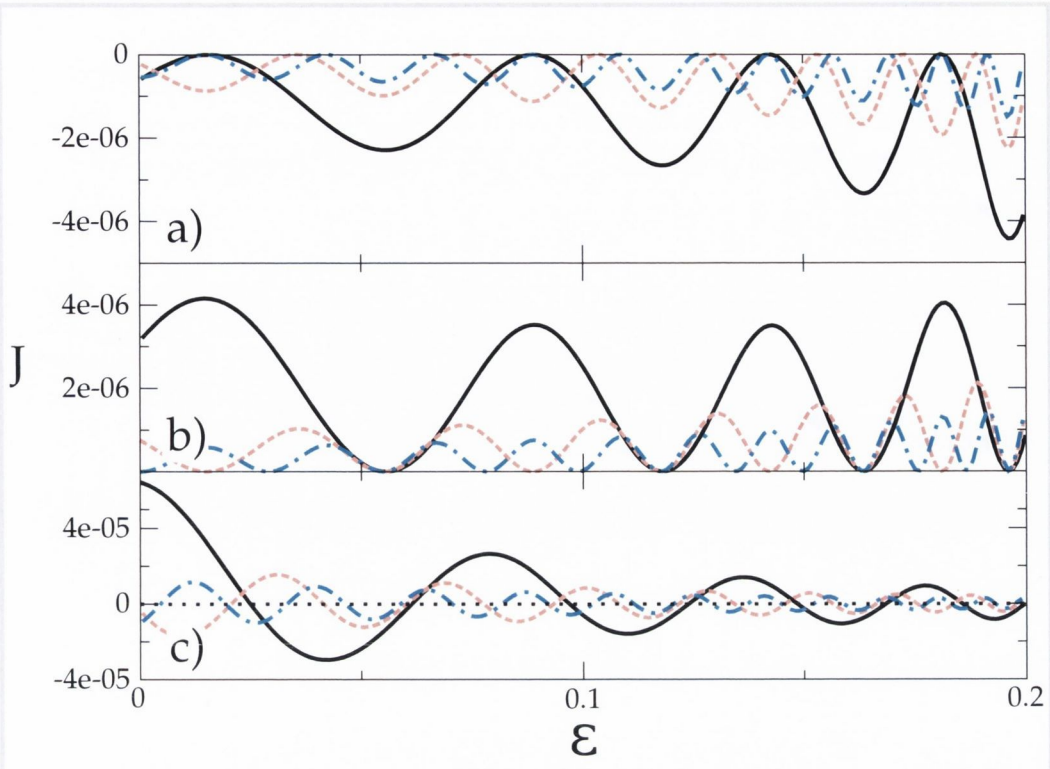


Figure 5.12: Plot of the coupling as a function of strain for ACNTs at D = 10 (black), D = 20 (dashed-red), D = 30 (dot-dashed-blue) for a) same-sublattice substitutional, b) opposite-sublattice substitutional, and c) bridge-adsorbed impurities, where the dotted-black line indicates the transition from FM to AFM.

antiferromagnetic. These impurities are known to decay rather quickly as D^{-5} (Fig. 5.13 a). This can be understood from the $\mathcal{B}(\varepsilon)^{(l)}$ terms, which are zero for $l = 0, 1, 2, 3$. The first non-zero term is found at $\mathcal{B}(\varepsilon)^{(4)}$, (it is too long to reproduce here) and thus indicates the known decay rate of D^{-5}. However, the introduction of strain breaks a key symmetry of the system massively increasing the range of the interaction. The interaction in the presence of strain decays slowly as D^{-1} (Fig. 5.13 b). The inset of figure 5.13 shows a log-log plot of the coupling between the impurities for the unstrained and strained cases. Examining the $\mathcal{B}(\varepsilon)^{(0)}$ we find an explanation for the increased range,

$$\mathcal{B}(\varepsilon)^{(0)} = \frac{(t_1 - t_2)^4 \phi(\varepsilon)}{4 n_c{}^2 t_2^4 (t_1^2 - 4t_2^2)}, \tag{5.3.4}$$

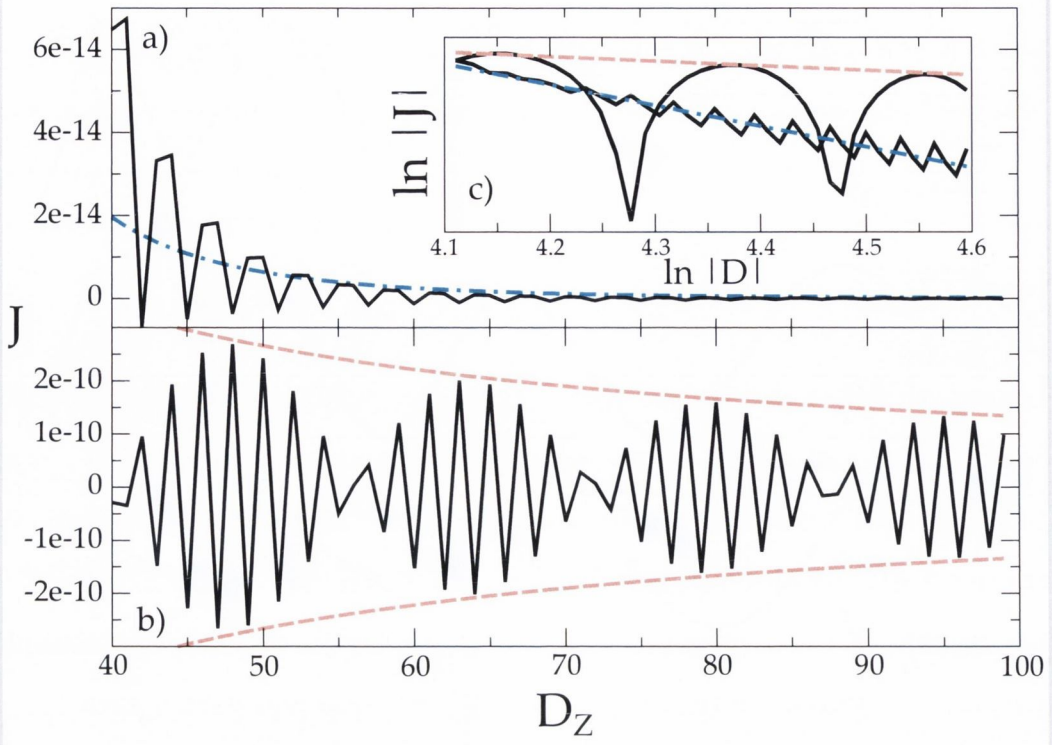


Figure 5.13: The interaction between two centre-adsorbed impurities in a) the absence of strain ($\varepsilon = 0$), and b) the presence of strain ($\varepsilon = 0.1$). c) is a normalized log-log plot of both interactions. The coloured lines show the decay rates: D^{-5} (dash-dotted-blue), D^{-1} (dashed-red).

where $\phi(\varepsilon)$ is a strain-dependent phase term. Here the numerator displays a $t_1 - t_2$ term, since the unstrained system is defined by $t_1 = t_2$ it is exactly zero only in unstrained graphene. Such a non-zero $\mathcal{B}(\varepsilon)^{(0)}$ term corresponds to a decay rate of D^{-1}. This symmetry breaking effect is analogous to that seen in graphene where the decay rate is massively reduced from D^{-7} to D^{-3} by the introduction of strain as seen in Sec. 5.2.3.

5.3.2 *Modified Interactions in Zigzag Nanotubes*

The introduction of strain, ε, into the ZZNT system alters the coincidence of the BZ and the Fermi surface. This alters the electronic properties of nanotubes by changing the number of available states at each energy. Figure 5.14

shows the density of states (DOS) of a metallic ZZNT with $n_c = 21$ as strain is applied. The initially conducting NT immediately becomes semi-conducting with slight strain, and as strain is further applied the two peaks in density of states come together and eventually merge, and the NT once again becomes metallic. This is seen in all circumferences of metallic and semi-conducting ZZNTs, where the precise value of strain required to shift the density of states away from zero around $E_F = 0$ decreases as the circumference increases. This

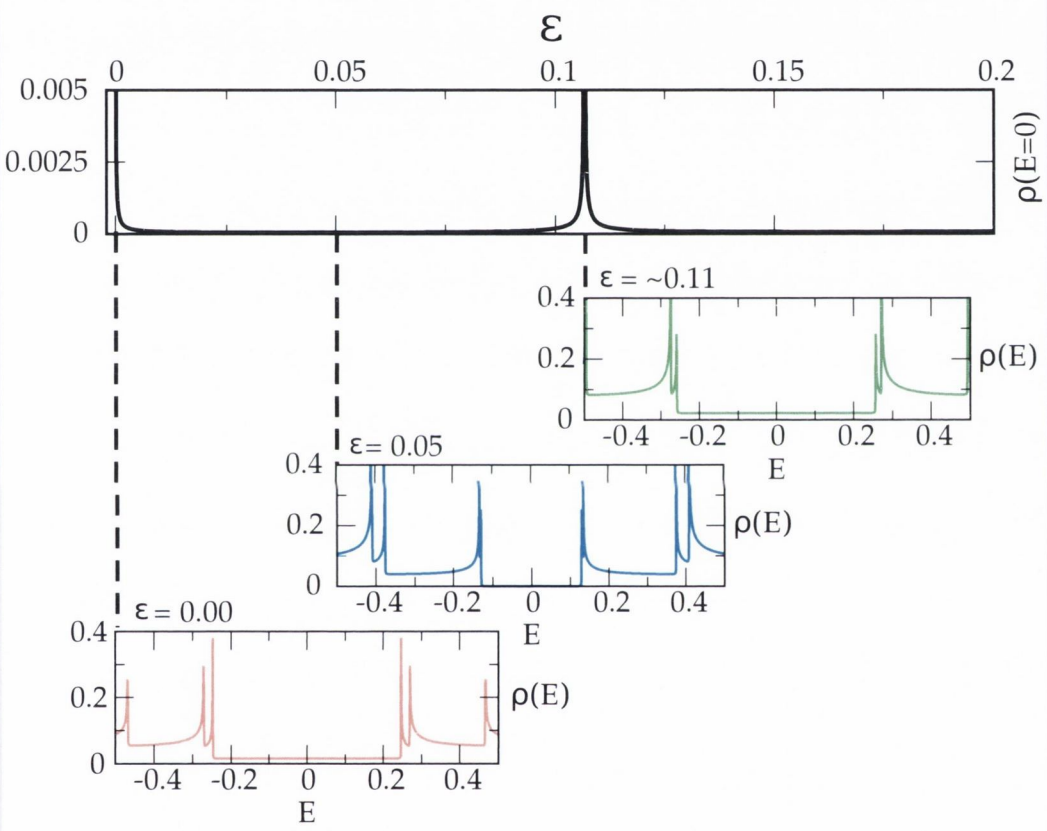


Figure 5.14: The density of states, ρ, at E = 0 for a ZZNT with $N_c = 21$ under uniaxial strain, ε. Subfigures show the density of states against energy for three strain values: $\varepsilon = 0$ (red), $\varepsilon = 0.05$ (blue), and $\varepsilon \approx 0.11$ (green).

can be understood by examining the BZ for ZZNTs in Fig. 5.4. Again, strain in the longitudinal direction shifts the Dirac points **K** and **K**′ at $\left(\pi, \frac{\pi}{3}\right)$ and

$(\pi, -\frac{\pi}{3})$ only in the k_Z direction, and to a first approximation is given by $\mathbf{K} \approx \frac{\pi}{3}\left(1 - \frac{\varepsilon(1-\sigma)}{2}\right)$ [112]. However, the discretized BZ of ZZNTs, defined by,

$$\epsilon_{\pm}(\mathbf{k}, \varepsilon) = \pm\sqrt{t_1^2 + 4t_1 t_2 \cos\left(\frac{\pi j}{n_c}\right)\cos(k_A) + 4t_2^2\cos^2\left(\frac{\pi j}{n_c}\right)}, \qquad (5.3.5)$$

will now not always intersect with the Fermi surface at $E = 0$, and only does so for certain discrete values of strain.

Since the introduction of strain changes a conducting ZZNT to a semi-conducting ZZNT the effect of strain in ZZNTs is markedly different. Figure 5.15 shows the coupling between substitutional, bridge-adsorbed, and centre-adsorbed impurities in ZZNT with $n_c = 21$ as a function of strain. Since the introduction of strain changes a ZZNT from conducting to semi-conducting the RKKY interaction in an initially conducting ZZNT goes to zero (Fig. 5.15 a). Strain also has the opposite effect on initially semi-conducting ZZNTs, taking the RKKY away from zero for precise values of strain. Similar behaviour is seen for bridge-adsorbed impurities (Fig. 5.15 b), with the key difference being the sign change that occurs around this precise strain value. What this means is that for two bridge-adsorbed impurities separated by some distance D there exists a small range of strain that can quickly turn the RKKY interaction from strongly AFM to strongly FM. This is in contrast to ACNTs where a sign change can be achieved but only gradually. The value of this precise strain value will depend on the circumference of the nanotube n_c. In addition to this the sign change occurs at all separations, meaning that it is possible that strain might be able to quickly change a system of impurities from all having the same alignment to having alternating alignments with no overall magnetic moment. The centre-adsorbed impurity (Fig. 5.15 c) shows similar behaviour, however since a key symmetry that leads to the D^{-5} decay is broken by strain the magnitude is increased massively, which gives the appearance of initially being zero.

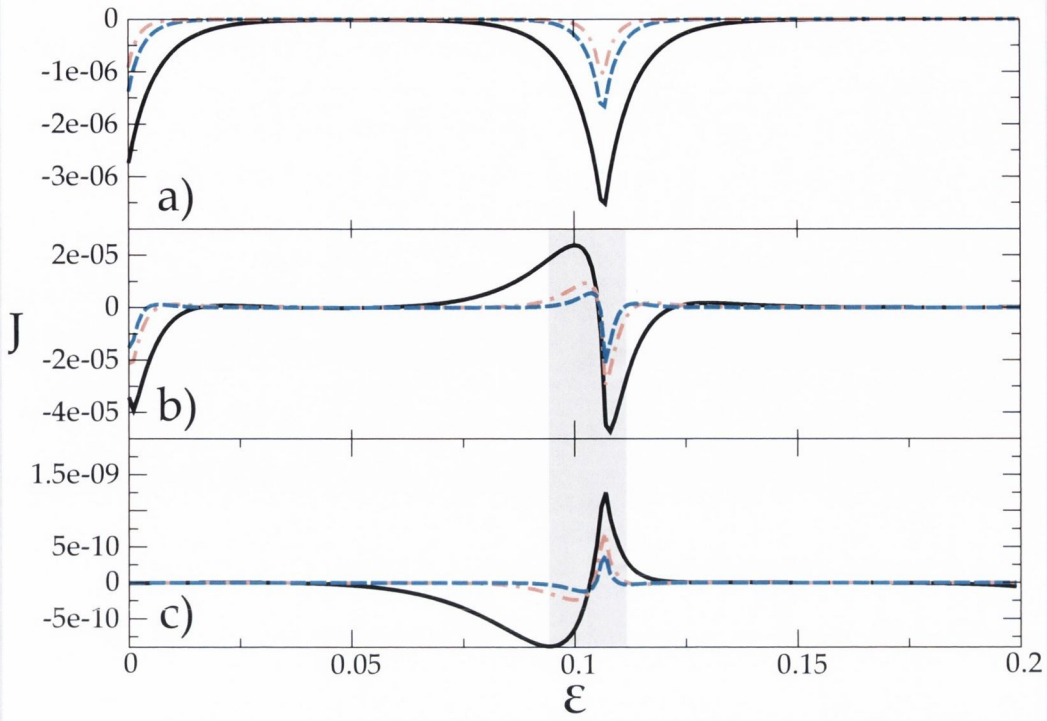


Figure 5.15: The coupling between a) substitutional, b) bridge-adsorbed, and c) centre-adsorbed impurities is plotted as a function of strain in a ZZNT with $n_c = 21$. Each coupling is plotted for three values of separation D = 10 (solid-black), D = 20 (dashed-red), D = 30 (dash-dotted-blue). The grey bands indicate the regions of sudden FM/AFM switch.

5.4 SUMMARY OF CHAPTER

In Chap. 4 we demonstrated that the features of the indirect exchange interaction between impurities in graphene and nanotubes depended primarily on their conformation. In this chapter we have extended that analysis to examine the role that strain plays in modifying the interaction between each conformation type in both systems. This was done by extending our Hamiltonian to allow the inclusion of strain in Sec. 5.1.1, and using a modified Brillouin Zone, which we discussed in Sec. 5.1.2. This allowed us to derive strain-dependent Green's functions for graphene in Sec. 5.1.3 and for nanotubes in Sec. 5.1.4. In Sec. 5.2 we examined how uniaxial strain can modify the interactions between

magnetic impurities when separated along the high symmetry directions of graphene, and in Sec. 5.3 we analysed the same thing in armchair nanotubes and zigzag nanotubes.

Our results suggest that magnetic interactions between adsorbed impurities in graphene and nanotubes can be manipulated by careful strain engineering of such systems. Since a wide range of effects, including overall moment formation and magnetotransport response, are underpinned by such interactions we predict that the ability to manipulate the coupling by applying strain may lead to interesting spintronic applications. A number of systems and conformations were analysed above, as such we find it useful at this point to summarize our results by the effects seen.

The work presented in this chapter was published in Refs. [193] and [87].

Amplification and Suppression

Some amount of strain-controlled amplification or suppression was seen in almost all systems, with all conformation types (Fig. 5.16 a, b, c). The only systems which did not show this feature were substitutional impurities in zigzag nanotubes (Fig. 5.16 d). The amplification was particularly pronounced for centre-adsorbed impurities in graphene and nanotubes where we showed that the symmetry breaking of the hexagonal lattice by uniaxial strain leads to a significantly slower decay rate between centre-adsorbed impurities: $D^{-7} \rightarrow D^{-3}$ in graphene, and $D^{-5} \rightarrow D^{-1}$ in armchair nanotubes (Figs. 5.11 and 5.16 c). An amplification effect is seen in zigzag nanotubes, but it is mostly masked by the transition from metallic to semi-conducting (Fig. 5.14). Experiments to date searching for magnetism in disordered graphene seem to suggest paramagnetic, non-interacting moments [205]. Signatures of indirect exchange interactions between such moments in graphene are very difficult to detect due to their short-ranged nature, particularly if they adopt certain adsorption con-

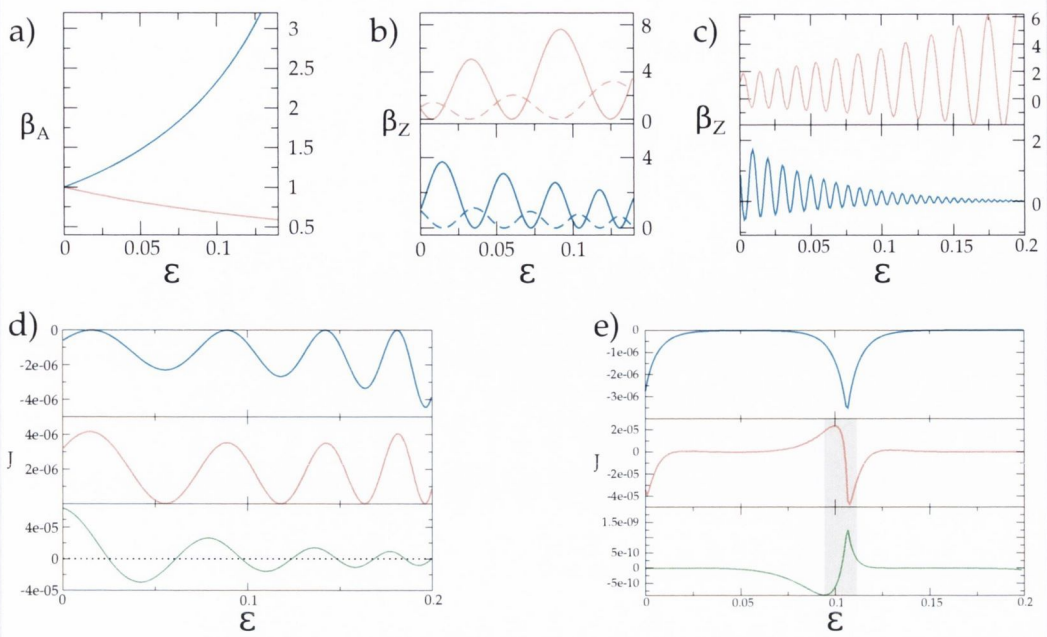


Figure 5.16: a) Amplification factor β_A as a function of strain, ε, in the armchair (red) and zigzag (blue) directions.
b) Amplification factor β_Z as a function of armchair (red) and zigzag (blue) strain for same (solid line) and opposite (dashed-line) sublattice cases.
c) Amplification factor β_Z as a function of armchair (red) and zigzag (blue) strain for zigzag separated impurities.
d) The coupling as a function of strain for ACNTs same-sublattice substitutional (blue), opposite-sublattice substitutional (red), and bridge-adsorbed impurities (green).
e) The coupling between substitutional (blue), bridge-adsorbed (red), and centre-adsorbed (green) impurities as a function of strain in a ZZNTs. The grey bands indicate the regions of sudden FM/AFM switch.

figurations, as we have demonstrated here. Amplification of these couplings using strain may provide a path to their detection in future experiments.

Sign-Changing

Sign-changing behaviour was observed in most cases, except substitutional impurities on graphene and on armchair nanotubes (Fig. 5.16 c, d, e). Only the interaction between bridge-adsorbed impurities in graphene separated along the zigzag direction, as opposed to those separated along the armchair

direction, alternates between ferromagnetic and antiferromagnetic as a function of strain. For centre-adsorbed impurities, we note that in addition to the sign-changing oscillations for both armchair and zigzag directions which are associated with different terms in the coupling power series dominating the interaction, another set of sign changing oscillations emerge for zigzag separations due to the strain dependence of the Fermi surface which breaks the commensurability between the oscillation period and the lattice spacing. Where the sign-changing behaviours are usually gradual, in ZZNTs for bridge- and centre-adsorbed impurities, they are abrupt, occurring over a range of $< 1\%$ strain (Fig. 5.16 e). This abrupt sign-change may allow strain to act as a switch in future spintronic devices.

On/Off States

In certain cases straining the system led to the coupling between impurities vanishing (Fig. 5.16 b, d). For substitutional impurities separated along the zigzag direction of graphene, and substitutional and bridge-adsorbed impurities in armchair nanotubes these on/off states transition gradually. For substitutional impurities it was found that the on/off states of same and opposite sublattice impurities were exactly out of phase such that as one was reaching a maximum the other was reaching a minimum. This presents the interesting opportunity to control the interplay between sublattices. Zigzag nanotubes were found to have a very different reaction to strain. The coupling between all impurities on zigzag nanotubes is very strain-dependent, since they are only metallic for very specific values of strain (Fig. 5.16 e). This behaviour is unique among the systems we examined, and may be useful in developing robust switches with large gaps between on and off states.

6

APPLICATION OF METHODS TO OTHER SYSTEMS

The methods we laid out in this thesis, particularly those in Sec. 4.1, were very general, and the mathematical framework can be extended to other interactions mediated by the host. In this chapter we will discuss the applications of these methods to: the RKKY between extended magnetic defects in graphene, and the asymmetric doping of graphene sublattices by Nitrogen.

Motivated by recent advances which open up the possibility of surfacing graphene with extended magnetic defects [206–209] we will first discuss extended magnetic defects in graphene (Sec. 6.1). We start by examining how the coupling between a finite number of impurities may be calculated before moving on to discuss how the coupling between an infinite number of impurities can be calculated (Sec. 6.1.1). We then show that the latter of these provides a good approximation to the former as the length of the lines increase (Sec. 6.1.2), and that these extended defects reduce the dimensionality of the system and lead to smaller decay rates and longer ranged interactions.

We will then discuss the recent theoretical and experimental work on sublattice asymmetric doping of impurities in graphene, with a focus on substitutional Nitrogen dopants (Sec. 6.2). We will start by outlining the possible uses of such doping, the current techniques of doping, and the theoretical efforts to explain the asymmetric effect. We will then provide a possible explanation for this asymmetric doping within our model of graphene. This will be accomplished by considering the change in system energy caused by Nitrogen dopants (Sec. 6.2.1), which will allow us to relate the doping effect with the concentration of dopants. From this we will then define a critical concentration of impurities, above which we expect the asymmetry to vanish

(Sec. 6.2.2). We will then use the strain-modified Green's function of Sec. 5.1.3 to analyse what effect the substrate-induced lattice distortions might have on this critical concentration (Sec. 6.2.3).

6.1 EXTENDED MAGNETIC DEFECTS

Recent studies have examined how larger structures of impurities or vacancies can be used to modify the electronic properties of graphene allotropes. One such study looks at how the controlled growth of a line of defects in graphene can be used for gate-tunable valley filtering [206], while another study looks at how transition-metal nanowires result in long-range magnetic order and magnetic anisotropy in graphyne [206, 207]. The RKKY interaction has also been recently studied in the presence of an extended line defect in graphene, where it was found to break the electron-hole symmetry and enhance the RKKY interaction by orders of magnitude [210].

The possibility and ease of depositing a line of magnetic impurities in graphene has increased with the recent work of Duesberg *et al.* [208, 209]. In these works the electronic structure of graphene is altered via folding - sometimes called graphene origami. This folding is achieved by depositing the graphene over a corrugated surface which, in conjunction with an applied magnetic field, has recently been shown to open a bandgap in graphene [211]. The ridges created during this process act as traps for magnetic impurities and open up the possibility of depositing impurities in straight parallel lines. Alternatively, increased reactivity near grain boundaries [212] or simple kinks [213] may also lead to the formation of impurity lines. A sublattice preference of the impurities along zigzag lines, as shown in Fig. 6.1, is expected due to similar behaviour predicted for zigzag edged nanoribbons [214]. Although the RKKY interaction in graphene has been intensively studied, one aspect that had not

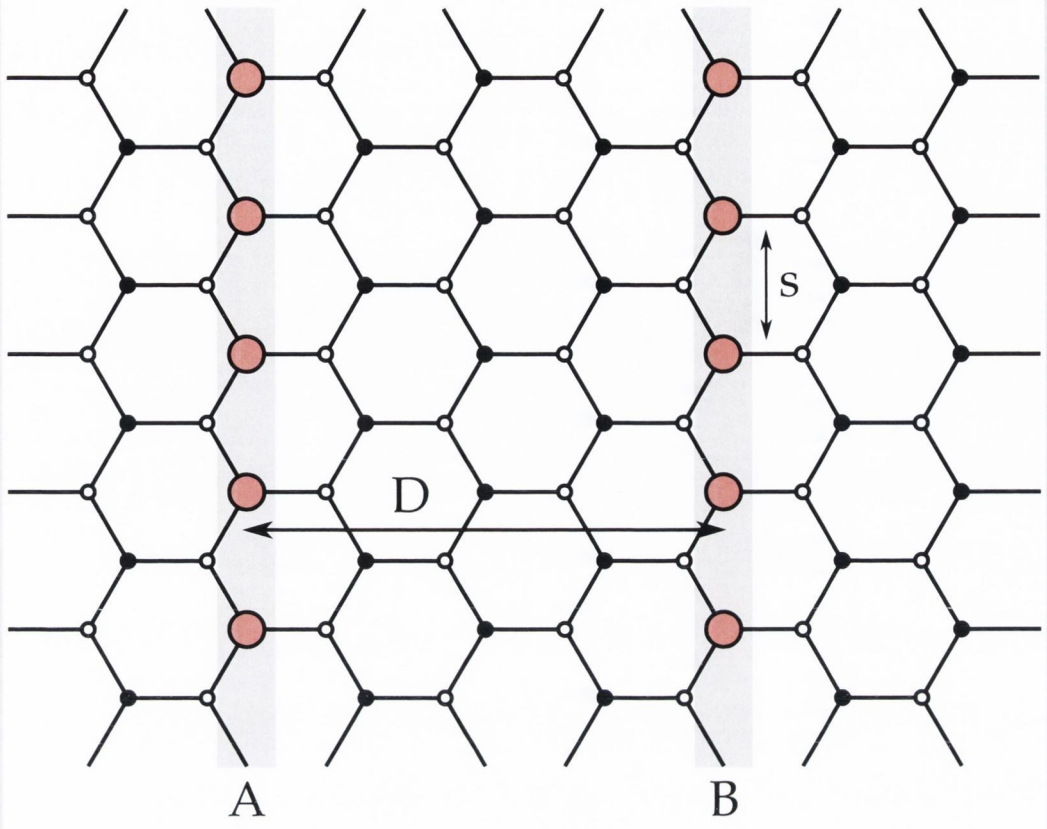


Figure 6.1: Schematic representation of the graphene lattice where the the filled and hollow symbols (•,○) represent sites on different sublattices. The red circles represent two parallel lines of magnetic impurities, A and B, separated by a distance D = 2 in the armchair direction, with a dimensionless quantity s (here s = 1) indicating the zigzag separation between moments.

been examined is how lines of impurities, which change the dimensionality of the interaction, affect the coupling.

With the motivation of understanding the magnetic interaction strength, and providing some theoretical foundation, we examined the role of dimensionality in the RKKY interaction. We applied analytical and numerical techniques to a system containing two parallel lines of magnetic impurities (Fig. 6.1). What follows is our method for calculating the coupling between lines of impurities embedded or adsorbed in a host material. Some analogues can be made between our set-up and 1D systems such as carbon nanotubes and nanoribbons [82], as well as systems with two ferromagnetic monolayers em-

bedded in a non-magnetic metal [187, 215], where the RKKY approximation can be used to derive a D^{-2} decay rate for the coupling between the ferromagnetic layers [191]. In this work we only consider a graphene host, but the method is easily generalized to other two dimensional materials.

6.1.1 *Coupling Between Lines of Defects*

The calculation of the coupling between two finite parallel lines of impurities, A and B, of length N, which we will denote J^N_{AB}, is relatively simple. However, the necessary introduction of a $2N \times 2N$ perturbation matrix $\hat{V}_I$, creates a computational problem: the matrix inversion present in the coupling calculation becomes cumbersome as N becomes large. The coupling calculation can be greatly simplified by keeping the GF partially in reciprocal space when introducing the perturbation, but this simplification comes at a cost; the lines must now be infinite. This infinite-line coupling, which we will denote $\mathcal{J}_{AB}$, allows for rapid calculation, as well as yielding an analytic form, of the coupling between two infinite parallel lines of impurities. The finite-line coupling, J^N_{AB}, and infinite-line couplings, $\mathcal{J}_{AB}$, can then be compared.

We will introduce our perturbation as a line of impurities along the y (zigzag) direction (Fig. 6.1), though a similar procedure may be used for impurities in the x (armchair) direction. When dealing with lines of impurities in the y direction, we make the projection $\langle x, k_y, \gamma|\hat{g}|x', k_y, \gamma'\rangle = g^{\gamma\gamma'}_{xx'}(k_y)$, where $\hat{g}$ is the GF of the pristine system, and γ and γ' are sublattice labels. This can be written as

$$g^{\gamma\gamma'}_{xx'}(k_y) = \frac{1}{N_x}\sum_{k_x}\frac{N_{\gamma\gamma'}(E, k_y)e^{ik_x(x'-x)}}{E^2 - |f(k_x, k_y)|^2}, \tag{6.1.1}$$

where $N_{\gamma\gamma'}$ and $f(k_x, k_y)$ have their standard forms for graphene.

For neatness we will neglect the superscripts γ and γ' from the following equations, which should be taken to be same-sublattice ($\gamma = \gamma'$), unless otherwise stated. Since we are considering two infinite parallel lines that extend in the zigzag direction the separation between these lines must necessarily be in the armchair direction. We no longer refer to the sites as x and x', but as A and B, which represent each line of impurities respectively. And the new separation is now just $D = x' - x$, since these are parallel lines separated by some distance along the x axis. The sum over k_x may be converted into an integral over the k_x direction in the Brillouin Zone, which can then be performed by contour integration. This results in an analytic form for the GF,

$$g_{AB}(k_y) = \frac{i}{4t^2} \frac{N(E, k_y) e^{iq(k_y)D}}{\cos\left(\frac{k_y}{2}\right) \sin(q(k_y))}, \tag{6.1.2}$$

with

$$q(k_y) = \pm \cos^{-1}\left[\frac{E^2 - t^2 - 4t^2 \cos^2\left(\frac{k_y}{2}\right)}{4t^2 \cos\left(\frac{k_y}{2}\right)}\right]. \tag{6.1.3}$$

Considering the Dyson equation, we may greatly reduce our analytical workload by writing our GFs as block matrices $\hat{g}_{AA} = \sum_{k_y} |A, k_y\rangle g_{AA}(k_y) \langle A, k_y|$, so that

$$\hat{I} - \hat{g}\hat{V} = \hat{I} - \begin{pmatrix} \hat{g}_{AA} & \hat{g}_{AB} & \cdots \\ \hat{g}_{BA} & \hat{g}_{BB} & \\ \vdots & & \ddots \end{pmatrix} \begin{pmatrix} \tau\hat{I} & 0 & \cdots \\ 0 & \tau\hat{I} & \\ \vdots & & 0 \end{pmatrix}, \tag{6.1.4}$$

where our perturbation, with change in onsite energy τ, has been trivially transformed to the same basis by a Fourier Transformation

$$\begin{aligned}\hat{V}_I &= \sum_n \tau|A,ns\rangle\langle A,ns| + \tau|B,ns\rangle\langle B,ns| \\ &= \frac{1}{s}\sum_{k_y} \tau|A,k_y\rangle\langle A,k_y| + \tau|B,k_y\rangle\langle B,k_y|,\end{aligned} \tag{6.1.5}$$

where s is a dimensionless quantity describing the separation of impurities along the zigzag direction as shown in Fig. 6.1, and n is summed over all sites. Since all but the first two columns are zero we can find the desired elements by just considering the 2×2 matrix multiplication. Similar identities facilitate the inversion, and our new GF, $\hat{G}$, can be calculated in a relatively transparent manner

The spin perturbation is introduced as

$$\hat{V}_s = \sum_{k_y} |B,k_y\rangle\hat{V}_\phi\langle B,k_y|, \tag{6.1.6}$$

where $\hat{V}_\phi$ is a 2D spin perturbation matrix which introduces the exchange splitting, V_{ex}, and is defined in Eq. 4.1.22.

Calculating $\hat{I} - \hat{g}\hat{V}$ for the spin perturbation is more involved, but the basic method is the same. For $\phi = \pi$ we can now write

$$\begin{aligned}\det \hat{I} - \hat{G}\hat{V}_s &= \det\left(\hat{I} - 2V_{ex}\hat{g}^{\uparrow}_{BB}\right)\left(\hat{I} + 2V_{ex}\hat{g}^{\downarrow}_{BB}\right) \\ &= \prod_{k_y}\left[\left(1 - 2V_{ex}g^{\uparrow}_{BB}(k_y)\right)\left(1 + 2V_{ex}g^{\downarrow}_{BB}(k_y)\right)\right],\end{aligned} \tag{6.1.7}$$

where all of terms are diagonal block matrices in k_y space, which allows us to write the determinant as a product.

To see the distance dependence in the coupling, we use the Dyson equation to write the coupling in terms of the spin dependent GF between each line of

impurities, $g_{AB}^{\uparrow/\downarrow}$. This is done by calculating the effect at site B of raising the energy of the down spin channel on sites A and B

$$g_{BB}^{\downarrow} = g_{BB}^{\uparrow} + 2V_{ex} g_{BB}^{\uparrow} g_{BB}^{\downarrow} + 2V_{ex} g_{BA}^{\uparrow} g_{AB}^{\downarrow}. \tag{6.1.8}$$

By rearranging this, expanding out Eq. 6.1.7, and using the properties of logarithms, we can now write the coupling per atom pair AB, $\mathcal{J}_{AB}$, in a convenient form

$$\begin{aligned} \mathcal{J}_{AB} = &-\frac{s}{N_y \pi} \mathrm{Im} \int_{-\infty}^{E_F} dE \\ &\times \sum_{k_y} \ln |1 + 4V_{ex}^2 g_{BA}^{\uparrow}(E, k_y) g_{AB}^{\downarrow}(E, k_y)|. \end{aligned} \tag{6.1.9}$$

The sum may now be converted to an integral over the Brillouin Zone in the k_y direction. We may also write $k_Z = \frac{1}{2} k_y$ to simplify, and use the analyticity of the integrand in the upper half plane to change the integration to the imaginary axis. This gives us a form of the coupling that is suitable for evaluation using numerical methods,

$$\begin{aligned} \mathcal{J}_{AB} = &\frac{2}{\pi^2} \int_{\eta}^{\infty} dy \int_{0}^{\frac{\pi}{2}} dk_Z \\ &\times \ln |1 + 4V_{ex}^2 g_{BA}^{\uparrow}(E_F + iy, k_Z) g_{AB}^{\downarrow}(E_f + iy, k_Z)|. \end{aligned} \tag{6.1.10}$$

To obtain a useful analytic form of the coupling we make several approximations which are similar in form to the RKKY approximation. We first expand the log in Eq. 6.1.9 to first order by assuming a small exchange coupling, V_{ex}. We then make the approximation $g_{AB}^{\downarrow} = g_{BA}^{\uparrow} = g_{AB}$ so that the

coupling, which we now write as $\mathscr{J}_{AB}$ to distinguish it from the numerical form above, is now given by

$$\mathscr{J}_{AB} \approx -\frac{4V_{ex}^2}{\pi^2}\mathrm{Im}\int_{-\infty}^{E_F} dE \int_{-\frac{\pi}{2}}^{\frac{\pi}{2}} dk_Z \, [g_{AB}(E, k_Z)]^2 . \tag{6.1.11}$$

At large separations the integrand oscillates quickly and only select points that contribute to the integral over k_Z. This allows us to use the SPA to write the integral in a fully analytic form. Here we use the SPA to calculate the integral over GFs that already contain impurities,

$$\int_{-\frac{\pi}{2}}^{\frac{\pi}{2}} dk_Z \, [g_{AB}(E, k_Z)]^2 = \frac{\mathcal{A}(E)e^{i2q(E)D}}{\sqrt{D}}, \tag{6.1.12}$$

where $\mathcal{A}(E)$ captures the specific sublattice dependencies, and non-contributing terms have been ignored. The symmetry in the zigzag direction allows us to use the SPA in this manner.

We can now write our coupling equation as

$$\mathscr{J}_{AB} = -\frac{4V_{ex}^2}{\pi^2}\mathrm{Im}\int_{-\infty}^{E_F} dE \, \frac{\mathcal{A}(E)e^{i2q(E)D}}{\sqrt{D}}. \tag{6.1.13}$$

The integration procedure is now identical to that for single impurities in graphene seen in Sec. 4.1.5. The functions $\mathcal{A}(E)$ and $q(E)$ are expanded around E_F and the integral can be reduced to a sum over Matsubara frequencies, which in the low temperature limit gives

$$\mathscr{J}_{AB} = V_{ex}^2 \, \mathrm{Im} \sum_{\ell} \frac{\mathcal{A}^{(\ell)}e^{i2q(E)|D|}(-1)^{\ell}}{(2iq^{(1)})^{\ell+1}D^{\ell+\frac{3}{2}}}. \tag{6.1.14}$$

The decay rate of the coupling is now determined by the first non-vanishing $\mathcal{A}^{(\ell)}$, where this notation is defined as the ℓth derivative of $\mathcal{A}$ with respect to

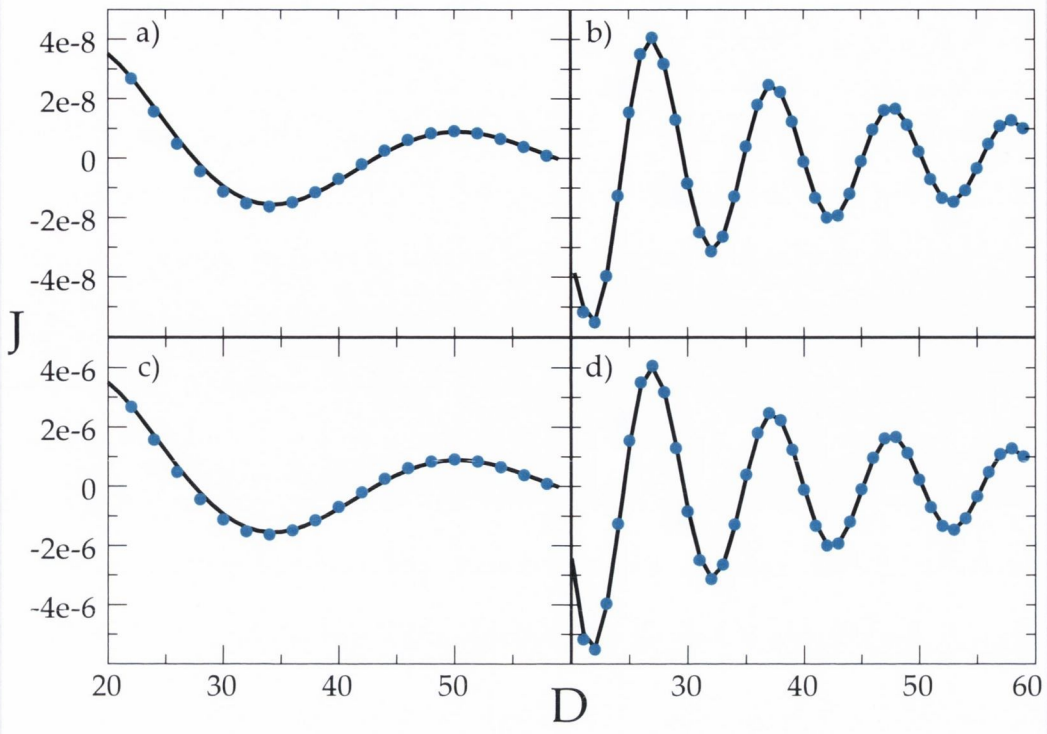


Figure 6.2: A comparison of the same-sublattice coupling, $\mathcal{J}_{AB}$ (black lines), and the SPA of coupling, $\mathscr{J}_{AB}$ (blue dots), for different exchange splittings, V_{ex}, and at different Fermi energies, E_F, a) $V_{ex} = 0.01$, $E_F = 0.1$, b) $V_{ex} = 0.01$, $E_F = 0.3$, c) $V_{ex} = 0.1$, $E_F = 0.1$, and d) $V_{ex} = 0.1$, $E_F = 0.3$.

energy evaluated at the Fermi energy. Unless otherwise specified the results that follow refer to the case $s = 1$, *i.e.*, that the impurities are separated by the minimum distance in the zigzag direction.

The SPA used in the derivation of Eq. 6.1.13 relies on the assumption of large separations between the lines of impurities, so it is important to check the accuracy of this approximation at reasonable separations. The SPA coupling, $\mathscr{J}_{AB}$, was compared against the full numerical calculation of the coupling, $\mathcal{J}_{AB}$, for a variety of Fermi energies and exchange splittings. A representative sample of these checks is shown in Fig. 6.2, where the agreement is seen to be very good even for reasonably small separations, and increases in accuracy as separation increases. The approximation is therefore concluded to be sufficiently accurate for our uses here.

6.1.2 *Comparison of Coupling Between Finite and Infinite Lines*

Figure 6.3 plots the coupling between several pairs of line segments, of length N, against an infinite pair of lines. As we increase the length of the line segments the magnitude and phase of the coupling are seen to approach that of the infinite line segment (blue dots). At a length of $N = 500$ (Fig. 6.3 d), the coupling can be seen to converge to that of an infinite line of impurities. For shorter lines, $N \sim 50$ (Fig. 6.3 c) the coupling closely resembles that between the infinite lines, with only slight discrepancies in magnitude and phase. These discrepancies increase as the line is shortened to $N \sim 10$ (Fig. 6.3 b), however even the coupling between line segments as short as $N = 10$ are seen to behave much closer to the infinite case than to the case of individual impurities (Fig. 6.3 a). Thus Eq. 6.1.14 is a useful tool for quickly calculating the coupling between finite lines of impurities since it is clear that as the length, N, of the lines increase the interaction converges to that of the infinite case.

An important feature of the coupling is its overall rate of decay with separation, $D^{-\alpha}$, which is determined from the analytic form of the coupling in Eq. 6.1.14. Here the coupling is represented as a sum of terms over ℓ, with decay rates that increase as $D^{-\ell-\frac{3}{2}}$. The decay rate is therefore determined by the first non-zero term in the series, as subsequent terms decay much more rapidly. It is the quantity $\mathcal{A}^{(\ell)}(E)$ that determines whether or not the whole term will vanish. For the case of lines of impurities occupying the same sublattice ($\gamma = \gamma'$), where the interaction is ferromagnetic, we have

$$\mathcal{A}(E)^{(0)} = -\sqrt{\frac{\pm i\pi}{(E^2+3t^2)}}\frac{E^2}{2(E^2t^2-E^4)^{\frac{3}{4}}}. \tag{6.1.15}$$

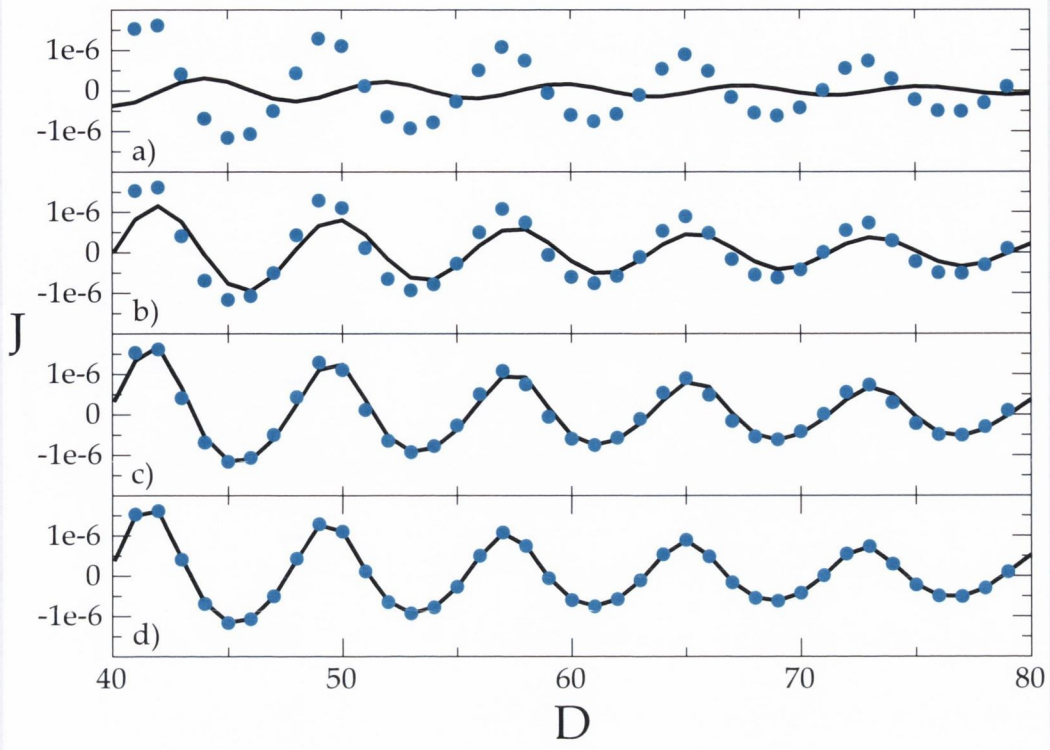


Figure 6.3: A plot of the numerical evaluation of the finite-line coupling, J^N_{AB}, against separation, D, for a pair of finite lines of length a) $N = 1$, b) $N = 10$, c) $N = 50$, d) $N = 500$. In each case the numerical evaluation of the infinite-line coupling, $\mathcal{J}_{AB}$, (Eq. 6.1.10) is represented by the blue dots.

It is clear from examination that $\mathcal{A}^{(0)}$ is non-zero whenever E is non-zero, and thus away from the Fermi energy we would expect a decay rate that goes as $\sim D^{-\frac{3}{2}}$.

In Fig. 6.4 we compare the coupling with the expected value of its decay rate at several Fermi energies. We find that for values of the Fermi energy not equal to zero ($E_F \neq 0$) that our theoretical predictions hold. At precisely $E_F = 0$, corresponding to an undoped graphene sheet, the analytical approximation no longer holds and a faster decay rate of $\sim D^{-2}$ is found. This difference of behaviour at the Dirac point is a hallmark of such interactions in graphene and is also seen for the single impurity case. However, both of the linear defect results correspond to an increased interaction range compared to single

site impurities, where we would expect to find decay rates of D^{-2} and D^{-3} for doped and undoped graphene respectively [78].

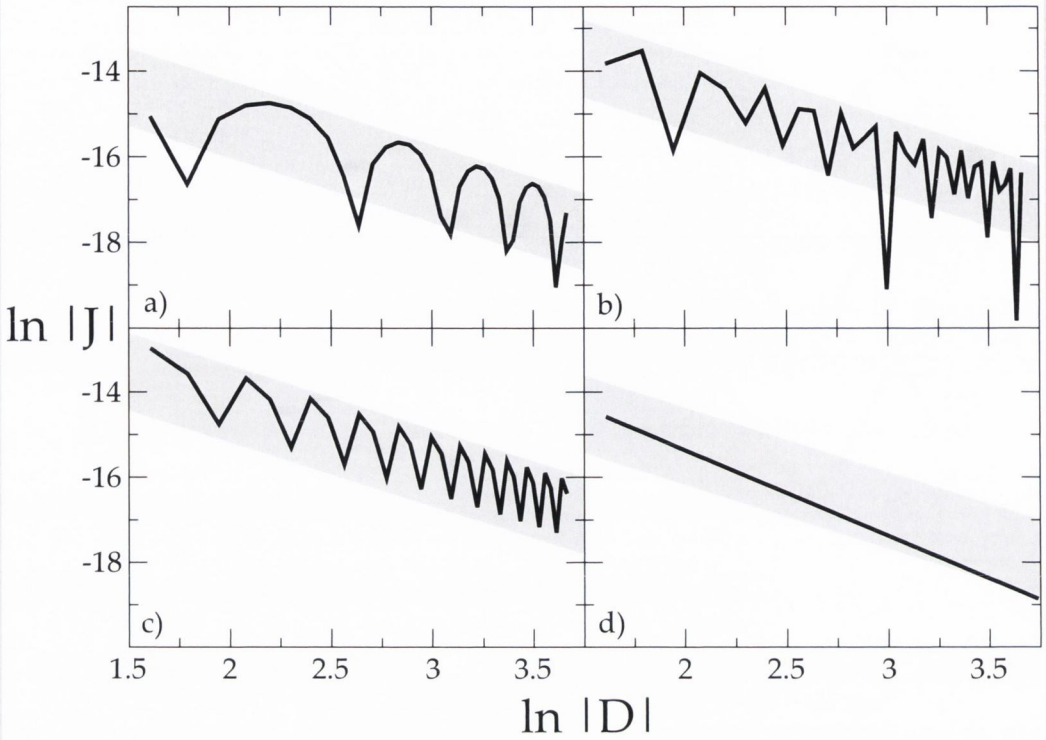


Figure 6.4: A log-log plot of the numerical evaluation of the coupling, J, between two lines of impurities as a function of their separation, D, for a) $E_F = 0.1$, b) $E_F = 0.3$, c) $E_F = 0.5$, d) $E_F = 0$. In each case the log of the coupling is represented by the solid-black line and a decay rate of 1.5 is represented by the grey shading.

These cases produced similar results to the initial case examined above in both coupling decay rate and the convergence of finite lines to the infinite case. For the cases where the impurities are spaced in the zigzag direction by a larger length $s > 1$, we again find that the coupling between lines quickly converges to that of the infinite case as N is increased.

6.2 SUBLATTICE ASYMMETRY OF IMPURITIES IN GRAPHENE

Graphene initially seems an excellent candidate for applications such as high-speed transistors and integrated circuits. However, a major problem exists with using graphene for such technologies - the absence of a band gap in the electronic structure. This would result in any field effect transistors (FETs) made using the material being unable to be switched off, rendering it useless as a logic device [100, 216, 217]. The question remains open, as to the best method to produce a sizeable band gap in graphene, thus allowing more control over the flow of current.

There are several known methods for inducing a band gap in graphene. These include systems such as stacked graphene with applied perpendicular electric fields [216, 217], 1D quantum confinement by construction of graphene nanoribbons (GNRs) [218], and deposition on a substrate [219–221], among others. None of these methods is perfect, and so alternatives are still being sought that can allow graphene to compete with silicon as a fundamental material of electronics. One such method to achieve this goal is to alter the crystal structure of graphene by introducing vacancies or dopants. Vacancies can be introduced by removing carbon atoms from the graphene lattice. It has been found that both random and periodic distributions of vacancies are capable of opening a tunable band gap in graphene, and in certain cases lead to the emergence of magnetic properties [58, 222–224]. Graphene may be substitutionally doped using Nitrogen (N) or Boron (B), which are of a similar size to Carbon and can be easily introduced to graphene via a variety of growth processes, causing a positive or negative shift in the Fermi level respectively [225]. Some early attempts at investigating doped graphene found that periodic arrangements of B or N dopants could open a band gap [226],

but the standard of precision required to produce such materials is restrictive. Random distributions of dopants may open a band gap [227], but the backscattering negatively affects the electronic properties of the device [228]. However it was found that doping the graphene sublattices asymmetrically, that is doping one sublattice more than the other, could yield such a band gap without affecting the quasi-ballistic nature of the other sublattice. Sublattice asymmetry has been predicted to open a band gap with vacancies, top-adsorbed impurities, and substitutional impurities [58–64, 224], and may pave the way to use graphene as a new species of transistor [60, 65, 66].

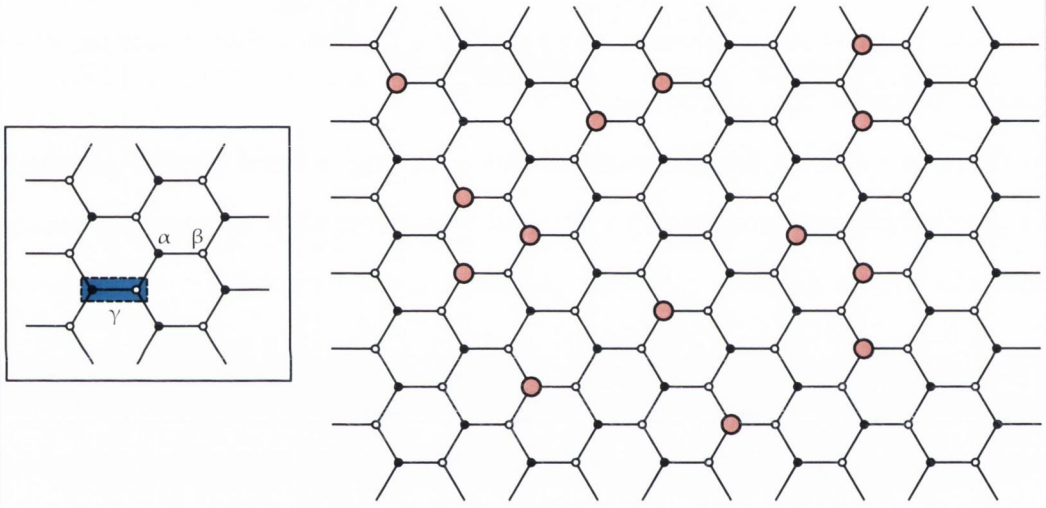


Figure 6.5: Asymmetrically doped graphene with dopants indicated by red circles all occupying sublattice α. The inset shows the unit cell, γ, and sublattice labels of graphene, α and β.

Asymmetrically doping graphene is not easy experimentally (Fig. 6.5). One method that yields a high degree of sublattice-asymmetry is the chemical vapour deposition (CVD) of graphene on Copper (Cu) with Nitrogen dopants [170, 229–231]. Despite the success of this method in producing asymmetrically doped graphene, the mechanism causing this asymmetry is unknown. It has been suggested that the preferential attachment to a sublattice on the edge of a graphene sheet, seen in DFT calculations, may lead to domains of im-

purity sublattice segregation agreeing with the crystal grain [231]. However this is not seen experimentally, where the asymmetry seems to extend beyond grain boundaries. In this section we suggest our own resolution to this puzzle. Our solution depends not on the edges of the system but on the interaction between the dopants themselves.

6.2.1 *Energetics of Dopants*

To address the issue of why substitutional impurities display such an asymmetry we will now examine the energetics of doping graphene. The sublattices of graphene, α and β (inset of Fig. 6.5) are perfectly equivalent in pristine graphene, and thus the only way that a preference may arise is via symmetry breaking. As mentioned above, edges have been suggested as this symmetry breaking agent as they are known to cause a modulation in the spatial distribution of impurities, and have been shown to make one sublattice energetically favourable in the vicinity of an edge [214]. However, these effects occur only in the close vicinity of edges, and cannot explain the experimentally observed asymmetric doping across entire samples.

We will now argue that the substitutional impurities themselves are responsible for breaking the symmetry of the lattice, and creating an energetically favourable sublattice, where we note that a similar argument has been made for adsorbed impurities [59]. To demonstrate that impurities are one of the key symmetry-breaking agents we must account for the total energy of a graphene system with many impurities. Ultimately we wish to analyse a system with a finite concentration of randomly distributed impurities. We will start by laying out the energy calculation for a single impurity, then expanding that to include two impurities, from which we will be able to see the energetics of a system with many impurities. We will continue to employ the nearest-

neighbour tight binding (NNTB) approach that we have used throughout this thesis.

The total energy change, $\Delta E(E_F)$, that results from the inclusion of a substitutional impurity can be described by the Lloyd formula [160] which we introduced in Sec. 2.4 as Eq. 2.4.19,

$$\Delta E(E_F) = \frac{1}{\pi}\mathrm{Im}\int_{-\infty}^{E_F} dE \;\; \ln\det\left(\hat{I} - \hat{g}\hat{V}\right), \tag{6.2.1}$$

where E_F is the Fermi energy of the system, $\hat{I}$ is the identity matrix, $\hat{g}$ is the Green's function (GF) matrix describing the pristine graphene lattice, and $\hat{V}$ is the perturbation matrix that we will use to introduce the substitutional impurities. We note that for a small number of dopants the Fermi energy need not be shifted from that of pristine graphene. We choose to model the substitutional impurities using a perturbation matrix that introduces a shift in energy, λ, at a site $\mathbf{r}$, that is $\hat{V} = |\mathbf{r},\gamma\rangle\lambda\langle\mathbf{r},\gamma|$, where γ is still a place holder for the sublattices α and β. So, the change in energy due to the addition of a single impurity, $\Delta E_{(1)}$, is then

$$\Delta E_{(1)}(E_F) = \frac{1}{\pi}\mathrm{Im}\int_{-\infty}^{E_F} dE \;\; \ln\det\left(\hat{I} - g_{00}^{\alpha\alpha}\lambda\right), \tag{6.2.2}$$

where we let $\mathbf{r} = 0$, since the system is translationally invariant, and we use the notation $g_{\mathbf{rr}}^{\alpha\alpha} = \langle\mathbf{r},\alpha|\hat{g}|\mathbf{r},\alpha\rangle$, as we have done throughout this work. The single-particle GF, g_{00}, carries no position dependence and therefore $\Delta E_{(1)}(E_F)$ is position independent.

Adding two impurities to the pristine system with the perturbation matrix $\hat{V} = |\mathbf{r},\gamma\rangle\lambda\langle\mathbf{r},\gamma| + |\mathbf{r}',\gamma'\rangle\lambda\langle\mathbf{r}',\gamma'|$, we can calculate the change in energy of the system from the addition of two impurities, $\Delta E_{(2)}(E_F)$, as

$$\Delta E_{(2)}(E_F) = 2\Delta E_{(1)}(E_F) + C_{\mathbf{rr}'}^{\gamma\gamma'}, \tag{6.2.3}$$

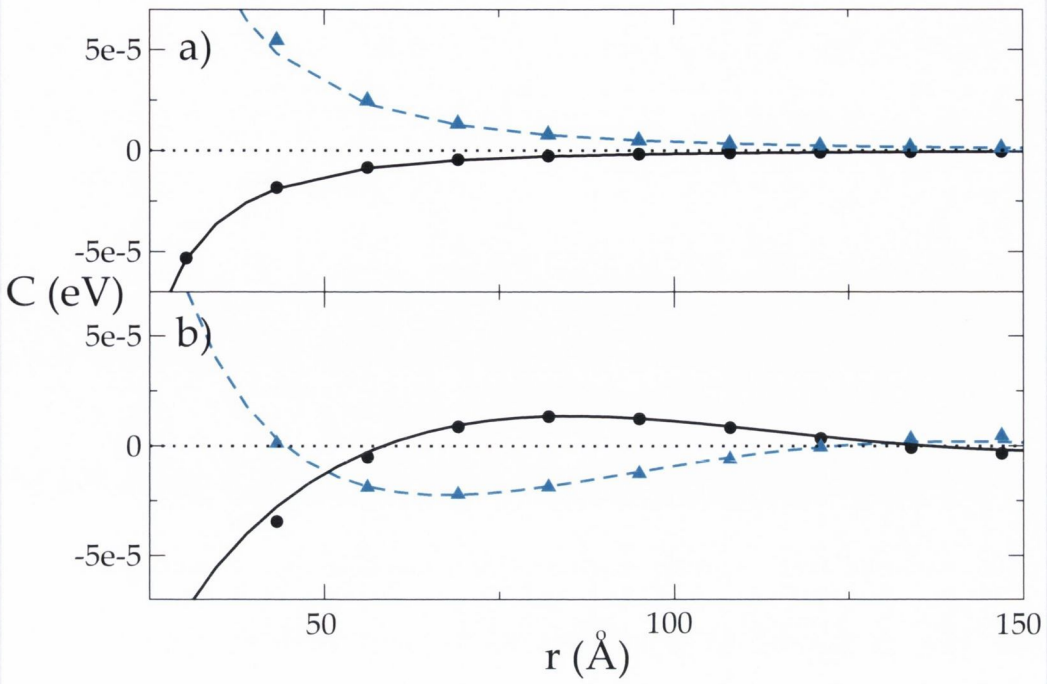


Figure 6.6: $C_{0\mathbf{r}}^{\gamma_1\gamma_2}$ plotted as a function of the separation between impurities, $\mathbf{r}$, a) $E_F = 0$; b) $E_F = 0.135$eV, both using the impurity parametrisation $\lambda = -4$eV. Solid-black (dashed-blue) lines and circular (triangular) symbols represent $C_{0\mathbf{r}}^{\alpha\alpha}$ ($C_{0\mathbf{r}}^{\alpha\beta}$). Symbols are the numerically evaluated values, whereas the lines follow the functional form $A\cos(2qD+\phi)/D^2$

which is twice the change in energy from the addition of a simple impurity, and a correction to the change in energy resulting from an interaction between the two impurities, $C_{\mathbf{r}\mathbf{r}'}^{\gamma\gamma'}$, where

$$C_{\mathbf{r}\mathbf{r}'}^{\gamma\gamma'} = \frac{2}{\pi}\mathrm{Im}\int_{-\infty}^{E_F} dE\ \ln\det\left(1-\frac{\lambda^2 g_{\mathbf{r}\mathbf{r}'}^{\gamma\gamma'} g_{\mathbf{r}'\mathbf{r}}^{\gamma'\gamma}}{(1-\lambda g_{\mathbf{r}\mathbf{r}}^{\gamma\gamma})(1-\lambda g_{\mathbf{r}'\mathbf{r}'}^{\gamma'\gamma'})}\right). \tag{6.2.4}$$

This term now depends on the relative position of the impurities, and is very similar in form to the indirect exchange coupling between two impurities derived in Sec. 4.1.2, as can be seen by expanding to lowest order in powers of λ. The term $C_{\mathbf{r}\mathbf{r}'}^{\gamma\gamma'}$ has been shown to behave as a decaying sinusoid [67, 232] of the form $C_{\mathbf{r}\mathbf{r}'}^{\gamma\gamma'} \sim A\cos(2qD+\phi)\,D^{-2}$, where A, q and ϕ are functions of the Fermi energy and D is the impurity separation as defined by $D = |\mathbf{r}'-\mathbf{r}|$.

The behaviour of this interaction term is also similar to the indirect exchange coupling in that for all separations, D, at $E_F = 0$, the interaction between impurities on the same sublattice is negative ($C^{\alpha\alpha}_{\mathbf{r}\mathbf{r}'} < 0$) and the interaction between impurities on the opposite sublattice is positive ($C^{\alpha\beta}_{\mathbf{r}\mathbf{r}'} > 0$). (This effect is due to the commensurability of the oscillation period and the lattice [67, 78, 83].) That is to say that it is more energetically favourable to accommodate two impurities on the same sublattice. Away from $E_F = 0$, the energetic favourability oscillates as a function of separation, as shown in Fig. 6.6.

For a large number of substitutional impurities, N, the perturbation will have the form

$$\hat{V} = \sum_{1}^{N} |\mathbf{r}_1, \gamma_1\rangle\lambda\langle\mathbf{r}_1, \gamma_1|. \tag{6.2.5}$$

Restricting ourselves to pairwise interactions we may approximate the change in energy of the system resulting from the addition of N impurities as

$$\Delta E_{(N)}(E_F) \approx N\Delta E_{(1)}(E_F) + \sum_{i=1}^{N}\sum_{j>i}^{N} C^{\gamma_i\gamma_j}_{\mathbf{r}_i\mathbf{r}_j}. \tag{6.2.6}$$

The second term now captures all $\frac{N(N-1)}{2}$ pairwise interactions. Although the typical magnitude of these interactions is quite small, on the order of 10^{-6}eV to 10^{-4}eV, the total sum grows as $\sim N^2$, leading to sizeable correction to the energy balance of the system for a large number of impurities.

We wish to demonstrate that asymmetric doping can be partially understood in terms of the scattering effects between pairs of impurities, to do this we must first define the number of impurities, N, not as a particular number, but instead as a concentration, *i.e.*, the percent of carbon sites that have been replaced with a substitutional impurity, where we define this concentration as ρ. Changing from a small finite number of dopants, to a concentration that is essentially infinite requires us to shift the Fermi energy. For low concentra-

tions this shift can be approximated as $E_F \sim \sqrt{|e_d|\rho}$, where is e_d the number of electrons the dopant adds to the system. This results in a pairwise interaction that is oscillatory as seen in Fig. 6.6.

The concentration ρ tells us what percent of sites are occupied, but to allow us to examine the symmetry of the doping we further define $\rho = \rho_\alpha + \rho_\beta$ where ρ_α is the concentration of impurities on the α sublattice, and likewise for β. We will now consider the two limiting doping situations - fully symmetric and full asymmetric. Fully symmetric is defined as $\rho_\alpha = \rho_\beta$, that is an equal occupation of both sublattices. Fully asymmetric is defined as $\rho_\alpha = \rho$ and $\rho_\beta = 0$ (or equivalently $\rho_\beta = \rho$ and $\rho_\alpha = 0$), that is all impurities occupying the same sublattice. We can now define a probability density of the total pairwise interaction energy between all impurities and an impurity on site $\mathbf{r}_1$ which approximations the summation over all sites. This site can be chosen as the origin, 0, without loss of generality. This essentially allows us to consider the total energy contribution from each impurity inside a ring of inner radius r and outer radius dr to a site at the origin. This ring has an area of $2\pi r dr$ and contains $2\pi\rho_\alpha r dr$ impurities on the α sublattice and $2\pi\rho_\beta r dr$ on the β sublattice. This density has two forms, depending on the sublattice occupied by the impurity at the origin. These are

$$\begin{aligned} E_\alpha &= \sum_{j\neq 1}^{N} C_{0\mathbf{r}_j}^{\alpha\gamma_j} = 2\pi\left(\rho_\alpha \int_{\sigma_{\alpha\alpha}}^{\infty} r\, C_0^{\alpha\alpha}(r)\, dr + \rho_\beta \int_{\sigma_{\alpha\beta}}^{\infty} r\, C_0^{\alpha\beta}(r)\, dr\right), \\ E_\beta &= \sum_{j\neq 1}^{N} C_{0\mathbf{r}_j}^{\beta\gamma_j} = 2\pi\left(\rho_\beta \int_{\sigma_{\beta\beta}}^{\infty} r\, C_0^{\beta\beta}(r)\, dr + \rho_\alpha \int_{\sigma_{\beta\alpha}}^{\infty} r\, C_0^{\beta\alpha}(r)\, dr\right). \end{aligned} \tag{6.2.7}$$

Here the interaction term is treated as a function of separation r, instead of having an explicit dependence on a vector $\mathbf{r}_j$, and as such the vector subscript is dropped. The lower limit, $\sigma_{\gamma\gamma'}$, is the nearest possible distance to a site on

sublattice γ' from a site on γ. Examining the symmetry of E_α and E_β we can write them in the simplified manner

$$\begin{aligned} E_\alpha &= 2\pi\left(\rho_\alpha S_1(\lambda) + \rho_\beta S_2(\lambda)\right), \\ E_\beta &= 2\pi\left(\rho_\beta S_1(\lambda) + \rho_\alpha S_2(\lambda)\right). \end{aligned} \tag{6.2.8}$$

Here S_1 and S_2 are the results of integrating over r. In practice this integral cannot be solved analytically, but we may approximate its value with a summation over all possible separations by noting that it decays as a function of r^{-2} and thus converges quickly. The total pairwise interaction energy, C_T, can now be found by summing over all impurities

$$C_T = \Delta E_N - N\Delta E_{(1)} = \sum_{i=1}^{N}\sum_{j>i}^{N} C_{\mathbf{r}_i\mathbf{r}_j}^{\gamma_i\gamma_j} = \frac{1}{2}\left(N_\alpha E_\alpha + N_\beta E_\beta\right), \tag{6.2.9}$$

where $N_\alpha = \pi R^2 \rho_\alpha$ is the number of impurities on sublattice α in a system with radius R, likewise for β. The factor of $\frac{1}{2}$ prevents the double counting of interactions.

6.2.2 *Critical Concentration*

We now wish to find the impurity segregation that minimizes the energy of the system. We can relate the quantities ρ_α and ρ_β by setting $\rho_\alpha = f\rho$, where f is the fraction of impurities occupying the α sublattice, therefore $\rho_\beta = (1-f)\rho$. The total pairwise interaction energy per unit area, C, can then be written as

$$C = \frac{C_T}{\pi R^2} = \pi\rho^2\left(2f^2(S_1 - S_2) - 2f(S_1 - S_2) + S_1\right), \tag{6.2.10}$$

where the λ dependence of $S_1(\lambda)$ and $S_2(\lambda)$ have been omitted for neatness. By taking the derivatives of this function with respect to f we find that the extrema exist at $f = 0, \frac{1}{2}, 1$. For the case $S_1(\lambda) - S_2(\lambda) > 0$ Eq. 6.2.10 has a

minimum at $f = \frac{1}{2}$, and maxima at $f = 0, 1$. This corresponds to a situation where the most energetically favourable configuration is the fully symmetric case, where the α and β sublattices are equally occupied. For the case $S_1(\lambda) - S_2(\lambda) < 0$ Eq. 6.2.10 has a maximum at $f = \frac{1}{2}$, and minima at $f = 0, 1$. This corresponds to a situation where the most energetically favourable configuration is the fully asymmetric case, where all impurities occupy the same sublattice. This suggests that impurity sublattice segregation seen in graphene is a feature of the multiple scattering effects between pairs of impurities captured in the quantities $S_1(\lambda)$ and $S_2(\lambda)$. Eq. 6.2.10 is plotted in Fig. 6.7 for

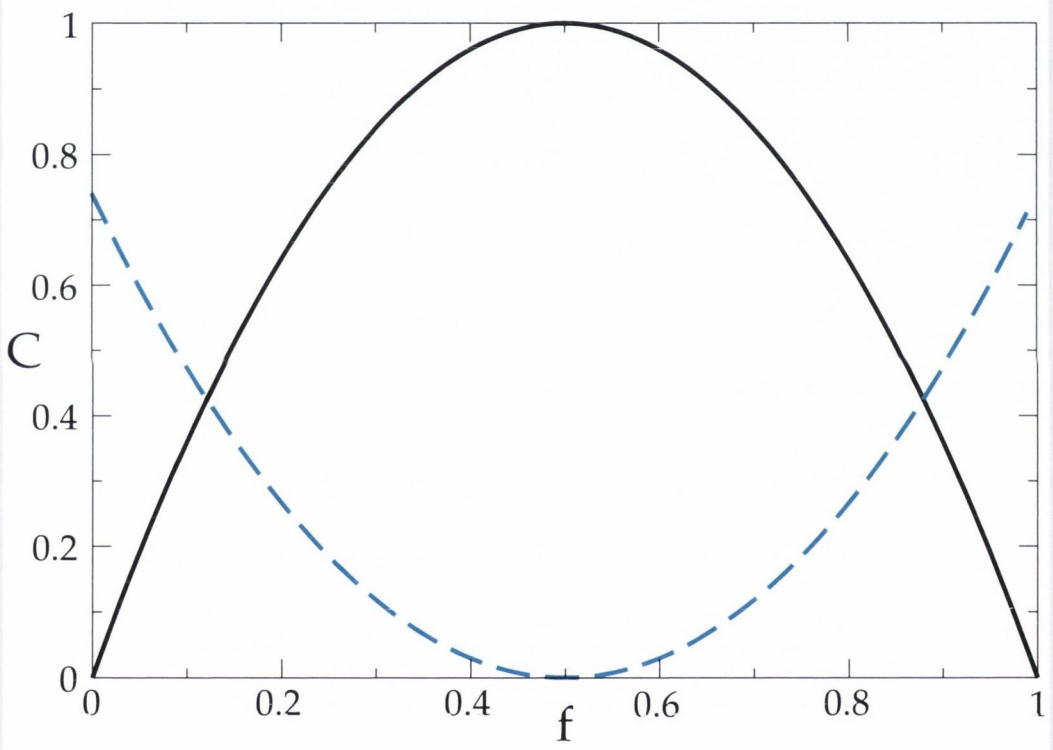


Figure 6.7: A normalized plot of the total pairwise interaction energy per unit area, C, against the fraction of impurities occupying sublattice α with $\lambda = -4eV$. The solid black (dashed-blue) line is calculated with a total concentration $\rho = 0.7\%$ ($\rho = 0.9\%$), below (above) the critical concentration ρ_c. For concentrations above ρ_c one would not expect to see sublattice segregation.

the two important cases $S_1(\lambda) - S_2(\lambda) > 0$ and $S_1(\lambda) - S_2(\lambda) < 0$ as a function of the fraction f, against a normalized total pairwise interaction energy

per unit area C. From this we can define a critical dopant concentration, ρ_c which occurs when $S_1(\lambda) - S_2(\lambda) = 0$. At concentrations above ρ_c we expect to see no sublattice asymmetry, and at concentrations below ρ_c we expect to see complete sublattice asymmetry. In physical systems the energy difference between the two states will be important to determine the stability of the asymmetry, if the energy difference is significantly smaller than the thermal fluctuations the asymmetry may arise. As C is an energy per unit area it is useful to consider the difference between the fully symmetric and fully asymmetric states over the typical area occupied by a single impurity. For example, a concentration $\rho = 0.3\%$ and parametrisation $\lambda = -4eV$ yields a difference in energy of $-880meV$.

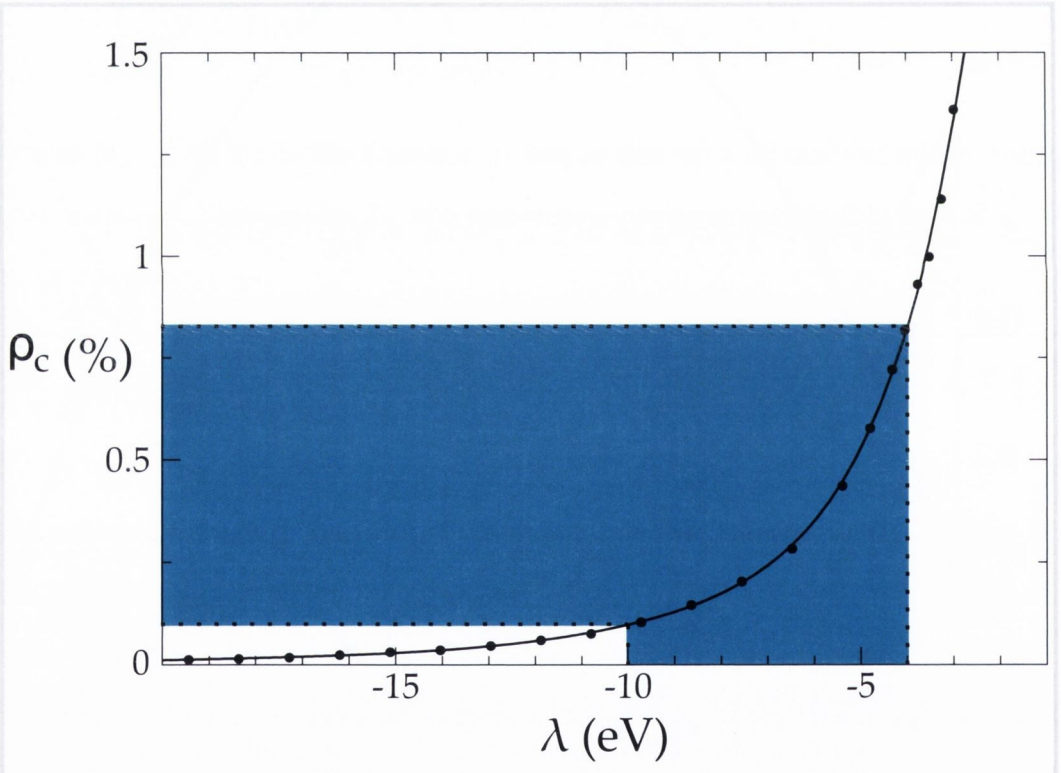


Figure 6.8: Onsite energy λ plotted against the numerically evaluated critical concentration ρ_c (dots) and fitted curve (line). Nitrogen impurities are most commonly parametrised by $\lambda = -10eV$ or $\lambda = -4eV$, corresponding to critical concentrations of 0.1% and 0.8% respectively, as indicated by the blue shaded region.

In Fig. 6.8 we plot the critical concentration, ρ_c, as a function of the onsite energy, λ, in order to gain some insight into the types of impurities and concentrations that lead to sublattice asymmetry. By way of example we will now consider the case of Nitrogen, where the onsite energy is somewhere between $\lambda_N = -10eV$ and $\lambda_N = -4eV$. These values are the two most commonly used in the literature, where the first comes from fitting the tight-binding LDOS profile to DFT results, and the second is calculated through a self-consistent tight-binding model [233, 234]. From Fig. 6.8 we see that the critical concentration for Nitrogen should be in the region between $0.1\% - 0.8\%$, where we note that the experimentally reported values for concentration where asymmetry is observed are $\sim 0.1\% - 0.3\%$ [170, 229–231]. Therefore the exact value of the critical concentration, predicted by our model, above which the sublattice asymmetry will no longer exist, does strongly depend on the choice of impurity parametrization. It is noted that Fig. 6.8 suggests the existence of a critical concentration for all values of λ, and as such provide a simple way in which the physical mechanism behind the sublattice asymmetry can be experimentally tested. Where one may conclude that the electron mediated interaction between impurities is partially responsible for the observed sublattice asymmetry if such an effect disappears when the Nitrogen concentration is increased. This work could be extended to model other impurities, where Nitrogen was especially simple to work with bonding similarly to carbon, and having only a single extra electron.

6.2.3 *Strain-Modified Critical Concentration*

As noted earlier, the substrate on which a graphene layer is deposited may significantly affect its properties. One such affect is the introduction of strain. It has been observed that graphene grown on Cu substrates using CVD may exhibit strain up to $\sim 1.5\%$. These strains may been reported as highly non-

uniform [235] or uniform [236], where the underlying factor seems to be the cooling of the substrate.

Here we attempt to understand what, if any, effect the substrate may have on the critical concentration of the material. As such, we will now briefly consider the role that a strained graphene sheet may have on the critical concentration. To do this, we apply our strain-dependent graphene GFs, which we derived in Sec. 5.1.3, to the calculation of change in energy resulting from an interaction between two impurities, Eq. 6.2.4. From this we may easily derive strain-dependent versions of the factors $S_1(\lambda, \varepsilon)$ and $S_2(\lambda, \varepsilon)$. These can then be used to calculate the strain-dependent critical concentration $\rho_c(\lambda, \varepsilon)$ in exactly the same manner as above.

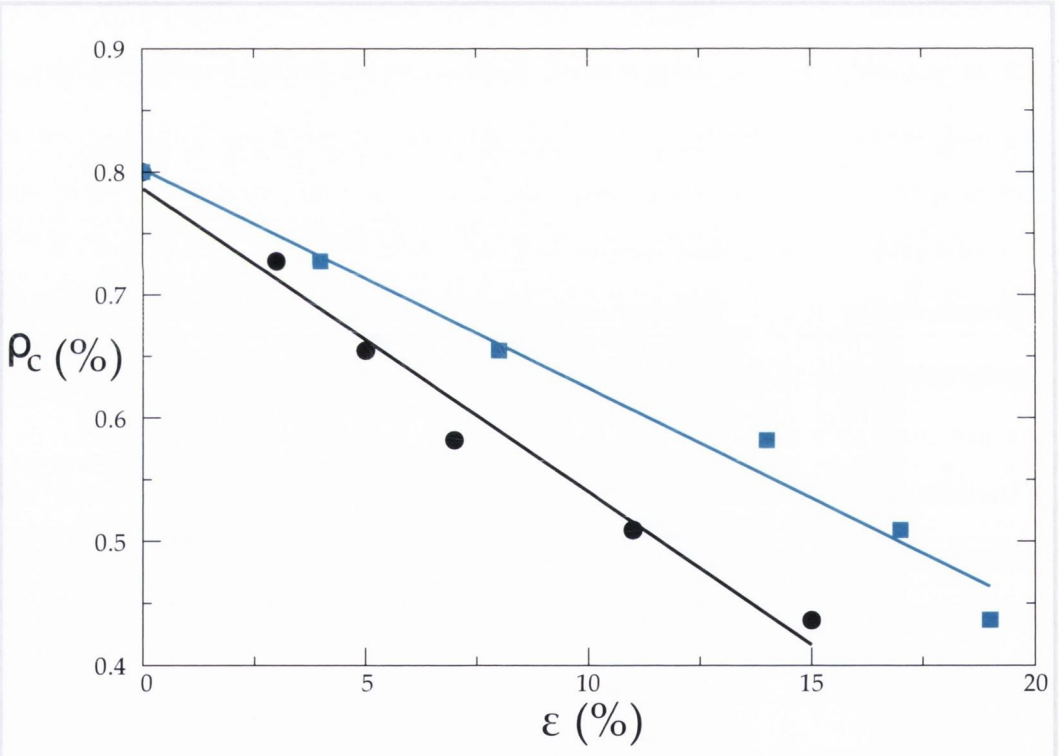


Figure 6.9: A plot of the critical concentration, ρ_c, versus strain, ε, at $\lambda = -4eV$ for both armchair (black-dots) and zigzag (blue-dots) directions of strain. The lines represent a best fit linear regression.

Figure 6.9 shows a plot of the strain-dependent critical concentration, $\rho_c(\lambda, \varepsilon)$, for Nitrogen, where we have chosen $\lambda_N = -4eV$, against an applied strain in

both the armchair and zigzag directions. Both directions of applied strain are seen to lower the critical concentration, with armchair strain slightly leading the trend. As such Fig. 6.9 is not meant to be predictive of precise responses, but rather indicative of a downward trend in the critical concentration with increased strain. Although $\rho_c(\lambda, \varepsilon)$ is calculated as the sum of strain-dependent GFs, whose oscillation periods differ from their strain-independent cousins, this downward trend can perhaps be understood in simple terms. As strain is applied it shifts the Dirac point, essentially causing a shift in the Fermi energy, E_F. Since the concentration is directly related to the Fermi energy this shift may cause a smaller concentration to act as if it were a larger concentration, which would reduce the critical concentration, all else held equal. We note at this point that we have evaluated the change in critical concentration due to strain up to physically realizable values of strain in graphene, and that the substrate induced strain would likely not reduce the critical concentration by more than 0.1% according to our model.

6.3 SUMMARY OF CHAPTER

In this chapter we examined two systems using the techniques of this thesis. In Sec. 6.1 we derived an analytic expression for the RKKY interaction in graphene between two lines of magnetic impurities separated along the armchair direction. We then showed that the coupling between lines of impurities quickly converges to the coupling of the infinite case as their length increase. The analytic form is therefore a useful way to approximate the interaction between line segments. We also used this analytic form to predict the rate of decay of this interaction, away from $E_F = 0$, which is slower than the rate of decay for two impurity interactions. Furthermore we showed that it is the reduced dimensionality of the system that increases the range of the RKKY

interaction. This increased range may ease the detection of the RKKY which is notoriously hard to examine experimentally. Since a whole range of physical features, such as magnetotransport and overall magnetic moment formation, are predicated upon the magnetic coupling, it is hoped that this work may lead to interesting spintronic applications.

In Sec. 6.2 showed that the interactions between impurities can account, at least in part, for the sublattice asymmetry of substitutional Nitrogen impurities in CVD grown graphene on Copper substrates. In Sec. 6.2.1 we used a modified form of the Lloyd formula, which we previously used to calculate the RKKY interaction, to allow us to calculate the change in energy of a system with a concentration of impurities, ρ. We further derived a critical concentration, ρ_c, in Sec. 6.2.2 that defines the limiting concentration for sublattice asymmetry to occur. In Sec. 6.2.3 we used the strain-dependent Green's functions of Sec. 5.1.3 to provide some insight into the effect that substrate induced strain might have on the critical concentration. While our simple model cannot accurately predict the exact value for this concentration, the mechanism we propose to explain the sublattice asymmetry of substitutional dopants in graphene leads can be easily tested experimentally. Our results also suggest that sublattice asymmetry could be reproduced with other impurities under certain circumstances.

The work presented in this chapter was published in Refs. [228] and [237].

7

SUMMARY AND FUTURE WORK

This thesis has considered the theoretical aspects of the interactions between magnetic and non-magnetic impurities in graphene and carbon nanotubes, where a combination of theoretical and numerical approaches were used. A strong focus was placed on how the conformation of these impurities affected the interaction with an emphasis on how conformation type reacted to uniaxial strain. Understanding how impurities interact, and how this interaction may be modified, is a vital step in the preparation of magnetically-doped graphene-related systems for spintronic applications. In this chapter we will summarize the principal methods and findings of this thesis, before suggesting useful ways this work may be extended.

7.1 SUMMARY

Chapter 1 provided a very general introduction to graphene, nanotubes, and spintronics. Here we emphasized the desire for mathematically transparent models to describe properties of interactions between magnetic impurities, and provided motivation for the work to follow.

Chapter 2 presented the mathematical methods used throughout this thesis. The focus of this chapter was a review of Green's functions and how they can be calculated and used, in conjunction with the Dyson equation and the Lloyd formula, to determine many properties of condensed matter systems. We highlighted the advantages of Green's function methods for describing systems that have been perturbed using the Dyson equation. We also exam-

ined the specific cases of using the Dyson equation to add substitutional and top-adsorbed impurities to a generic system. The Lloyd formula was also introduced here, along with a brief description of how it can be used to calculate the change of energy of a system in the presence of a perturbation. We provided a general introduction to the Stationary Phase Approximation that we would later use to write a closed-form Green's function for graphene. We also briefly discussed how integrations over Green's functions may be performed.

In chapter 3 we talked in some detail about the specific low dimensional carbon systems that we worked on throughout this thesis, namely graphene and carbon nanotubes. We introduced the nearest-neighbour tight-binding approximation Hamiltonians for these systems, and showed how their Green's functions and electronic structures could be derived. As Green's functions play a vital role in this work we spent a good deal of time deriving and simplifying the Green's function of nanotubes and graphene using contour integration and the Stationary Phase Approximation, where, in the latter case, we showed that the Stationary Phase Approximation allowed us to write a closed-form expression for graphene Green's functions along two high symmetry directions. These analytic expressions are very useful in understanding certain properties of these systems in a mathematically transparent manner. The methods we used offer advantages over numerical methods, which lack this transparency, and the linear dispersion approximation, which is only valid in a narrow energy range. We also briefly discussed the versatility of Green's functions in dealing with more difficult graphene-related materials such as semi-infinite graphene and graphene nanoribbons. We further introduced the mathematical basis needed to allow the doping of graphene and nanotubes with magnetic impurities, by expanding our Hamiltonian to allow for the inclusion of magnetic moments. And discussed the important topic of impurity conformation, how impurities adsorb to graphene and nanotubes.

In chapter 4 we combined the work of Chaps. 2 and 3, to allow us to use the Lloyd formula to calculate the Indirect Exchange Coupling between magnetic impurities. We showed that impurity conformation is one of the primary factors determining the form of the Indirect Exchange Coupling between the impurities. Important to this chapter was the ability to calculate the Indirect Exchange Coupling in an analytic fashion, so that we could derive the specific expressions for the coupling in graphene, and to determine the coupling decay rates between different impurity conformations in nanotubes. The Quantum Well method of calculating the coupling was formulated and compared to the more commonly known RKKY method, which was shown to be a second-order perturbative approximation to the coupling. Here we generalised the derivation of the decay rate in the asymptotic limit and established a formal condition for determining the decay rate. We also briefly discussed the relationship between the coupling in graphene and the coupling in nanotubes by considering the relationship between the increasing circumference of nanotubes and the decay rate of the coupling. We showed here that the Indirect Exchange Coupling behaves like that of graphene in large circumference nanotubes.

In Chap. 5 we expanded our Hamiltonian for graphene and nanotubes to allow for the inclusion of uniaxial strain. We discussed how strain modifies the electronic properties of both systems before deriving strain-dependent Green's functions. To allow for the numerical calculation of strain effects it is important to understand how the hopping integrals react to strain, which can be approximated by relating them to the interatomic carbon-carbon distance. We then extended the analysis of the RKKY interaction to examine the relationship between conformation type and strain. We found that strain had a profound effect on the RKKY interaction. It was found to be able to amplify or suppress the interaction, control its sign, or switch the interaction off entirely. It was found to affect the interaction between impurities on the

same or opposite sublattices differently, opening up the possibility to control the interplay between the sublattices and impurities. For zigzag nanotubes strain was found to have a large effect on the electronic properties, owing to that fact that strain converts semi-conducting nanotubes to metallic ones, and *vice versa*. The amplification of the RKKY interaction between centre-adsorbed impurities, which decays with separation, D, as D^{-7} and D^{-5} for graphene and nanotubes respectively, was found to be orders of magnitude larger than for other impurities. This massive increase in the RKKY can be understood directly from our transparent mathematical expressions describing the interaction, and the new decay rates of D^{-3} and D^{-1} can be easily determined.

The generality of our approach to the interaction between impurities allows us to extend the methods described in this thesis to tackle two further problems in Chap. 6. We first applied our methods to the interactions between extended magnetic defects. We showed that the interaction of finite lines can be well approximated by examining the interaction between infinite lines, where we derived an analytic expression for the RKKY interaction in graphene between two lines of magnetic impurities separated along the armchair direction. This analytic form allowed us to show that it is the reduced dimensionality of the system that leads to the slower decay rate between lines of impurities at $E_F = 0$, and may ease the detection of the RKKY which is notoriously hard to examine experimentally. We then examined the puzzle of sublattice-asymmetric nitrogen dopants in the CVD grown graphene on copper substrates. We discussed the uses of asymmetrically doping graphene before discussing some of the possible explanations of the effect. And then presented an argument that the nitrogen dopants themselves were responsible for the effect, rather than a graphene edge as has been previously suggested. To do this we used the Lloyd formula to calculate how the dopants modified the energy of the system. This was considered for a single dopant, two dopants, a finite quantity of dopants, and ultimately a concentration, ρ,

of dopants. We presented a simple model for determining the energetically favourable symmetry configuration, which allowed us to define a critical impurity conformation. This critical concentration, ρ_c, defines a concentration above which sublattice asymmetry should not occur, and may provide a useful avenue for testing our theory. The copper substrate is known to induce a strain in the graphene lattice, and so we further applied our strain-dependent model, where we determined that any induced strain would have little effect on the critical concentration of this system.

7.2 EXTENSIONS AND FUTURE WORK

There exist many possible extensions to the methods used and results obtained in this work. Recently Ref. [238] used a method related to our work in Sec. 6.1 (which was published in Ref. [237]) to examine the effect of line defects which consist of vacancies and magnetic impurities. Ref. [239] examines the effects that impurities have on electronic localization in graphene bilayers taking into account our work on impurity conformation and sublattice asymmetry, laid out in Refs. [87] and [228].

In Sec. 3.3 we mentioned that Green's functions had recently been used to describe semi-infinite graphene and graphene nanoribbons in an analytic manner [168]. These Green's functions are derived from the same Hamiltonian as pristine graphene, and so it should be possible to examine the role that strain plays in determining the properties of these materials, and in modifying the interactions of magnetic impurities adsorbed to them. Unfortunately these models cannot take into account edge-effects, which would likely become more pronounced in the presence of strain. This may lead to some discrepancies when compared with strain implemented in the standard recursive method, which is capable of capturing the edge-effects. However, a

comparison of these two methods, in the presence of strain, would give an insight into the magnitude of the change in the strained edge-effects, and could be used to determine if these strain-dependent versions of these analytic Green's functions model the systems in useful ways. Such a model may then be useful in analysing position dependent effects of dopants in graphene nanoribbons [240] in the presence of strain, which may allow an analytic investigation of the magnetoresistance of doped nanoribbon systems. This is motivated by the prospect of magnetically-doped nanoribbons providing an alternative route to spintronic devices proposed for nanoribbons with intrinsic magnetic ordering.

A recent paper has shown that it is possible to perform the Stationary Phase Approximation using the next-nearest neighbour tight-binding approximation in graphene [241]. Although it would significantly complicate the analytics it should be possible to combine the next-nearest neighbour method with the method to introduce strain, allowing for a more accurate depiction of the strain-dependent changes to the electronic structure of graphene across the entire energy band. This could also improve the accuracy of the current model of a variety of strain dependent effects.

It may also be possible to use DFT to calculate the binding energy for various impurities in graphene. This could be used to calculate the exchange splitting, V_{ex}, and hopping integral, τ, and thus examine the RKKY for specific impurities. A variation on this may also allow the strain dependence of the conformation type of various impurities to be examined. A variety of other effects could also be examined including the effect of applied magnetic fields in the presence of strain, or calculating the spin-susceptibility of impurities in strained graphene, where both are known to affect the decay rate of the indirect exchange coupling.

The above examples are just a small sample of the possible extensions that could be made using the methods set out in this thesis. Although the tech-

niques used in this thesis could be applied to a number of systems, the advantage of working with graphene-related materials is the variety of unique and interesting features that can be explored analytically, maitaining mathematical transparency, with a minimum of computational need. We hope that the work presented in thesis was enlightening and that it will be useful in future research.

A

IRREDUCIBLE GRAPHENE SECTOR: TRANSFORMATION ALGORITHM

In this section we present an algorithm for reducing the number of unique graphene Green's functions (GF) that must be calculated by recognizing the symmetries inherent in graphene and mapping the GFs into an irreducible sector. The vector describing any unit cell in graphene may be written as $\mathbf{r} = m\mathbf{a}_1 + n\mathbf{a}_2$, where $m, n \in \mathbb{Z}$, and $\mathbf{a}_1$ and $\mathbf{a}_2$ are the primitive graphene lattice vectors as seen in the inset of Fig. A.1. The GF is defined between two sites, one at $\mathbf{r}$ on sublattice $\gamma = (\alpha, \beta)$, and the other at $\mathbf{r}'$ on sublattice $\gamma' = (\alpha, \beta)$. However, since graphene is translationally invariant we may set one site to be the origin. We can also introduce the notation that

$$s = \begin{cases} +1 & \text{if } \gamma\gamma' = \alpha\beta \\ 0 & \text{if } \gamma = \gamma' \\ -1 & \text{if } \gamma\gamma' = \beta\alpha \end{cases}, \tag{A.0.1}$$

so that it now obvious that the separation between any graphene GF can be completely described by the three variables: $\mathbf{R}_i(m, n, s)$, where we will use $\mathbf{R}$ with the subscript i to denote the sector the site occupies, as seen in the inset of Fig. A.1.

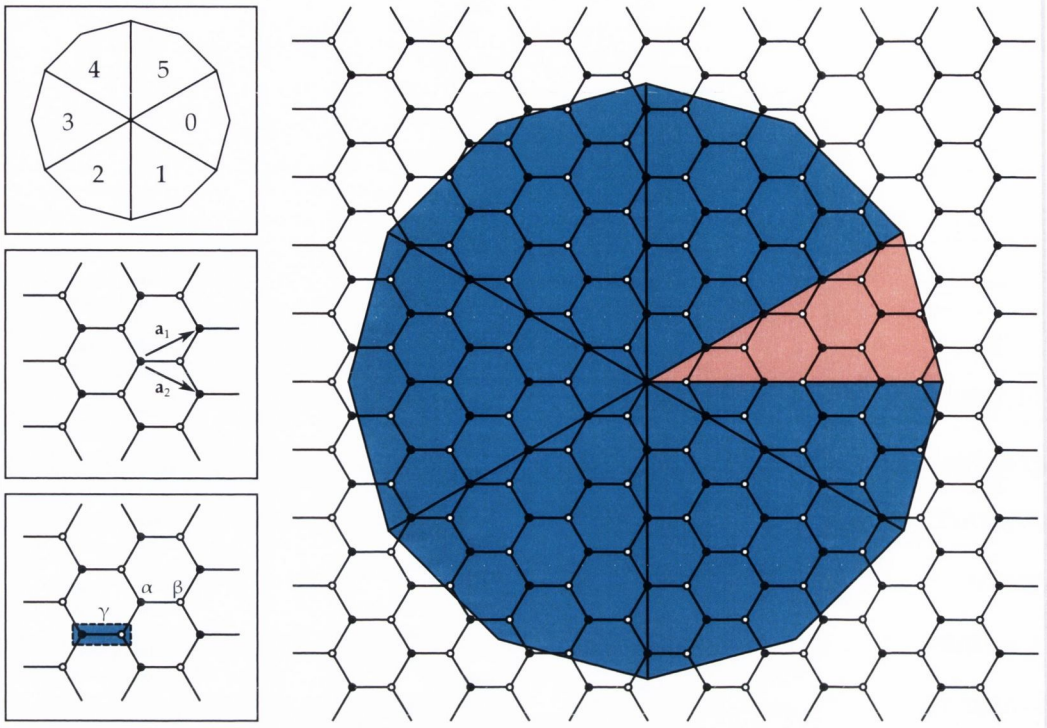


Figure A.1: A schematic representation of the irreducible graphene sector, $\mathbf{R}_{irr}$ (red), with the reducible sectors (blue). The insets shows the sector labels from 0 to 5, the primitive graphene lattice vectors $\mathbf{a}_1$ and $\mathbf{a}_2$, and the graphene unit cell γ, where the sublattices are α and β respectively.

We can immediately deal with the case $\gamma\gamma' = \beta\alpha$, and hence assume that our origin site is the on sublattice α, by applying the condition:

$$\text{if} \quad s < 1 : \qquad \mathbf{R}_i(m, n, s) = \mathbf{R}_i(-n, -m, -s), \tag{A.0.2}$$

which is just a reflection of the lattice. We can now define the conditions of each sector and how they can be transformed to sector 0:

Sector 0: if $m \geqslant 0$ and $n \geqslant 0$:

$$\mathbf{R}_0(m,n,s) = \mathbf{R}_0(m,n,s),$$

Sector 1: if $m \geqslant 0$ and $|n| \leqslant m$:

$$\mathbf{R}_1(m,n,s) = \mathbf{R}_0(-n,m+n+s,-s),$$

Sector 2: if $m \geqslant 0$ and $|n| \geqslant m$:

$$\mathbf{R}_2(m,n,s) = \mathbf{R}_0(m,-m-n-s,s),$$

Sector 3: if $m \leqslant 0$ and $n < 0$:

$$\mathbf{R}_3(m,n,s) = \mathbf{R}_0(-n,-m,-s),$$

Sector 4: if $m \leqslant 0$ and $|m| > 0$:

$$\mathbf{R}_4(m,n,s) = \mathbf{R}_0(n,-n-m-s,s),$$

Sector 5: if $m \leqslant 0$ and $|m| \leqslant 0$:

$$\mathbf{R}_5(m,n,s) = \mathbf{R}_0(-m,n+m+s,-s).$$

Following this method, all vectors $\mathbf{R}_i$ can be described by a vector in sector 0, $\mathbf{R}_0$. We may make one further reduction by noting that this $\frac{\pi}{3}$ sector, consists of two $\frac{\pi}{6}$ sectors which are mirrors of each other. We can then apply the condition

$$\begin{aligned} &\text{if} \quad n < m : \\ &\quad \mathbf{R}_{\text{irr}}(m,n,s) = \mathbf{R}_0(n,m,s), \end{aligned} \tag{A.0.3}$$

where $\mathbf{R}_{\text{irr}}$ is the irreducible sector highlighted in Fig. A.1. This method is especially useful when calculating the RKKY in systems with a large number of impurities, whether ordered or disordered, by reducing the number of unique GFs by a factor of 12.

BIBLIOGRAPHY

[1] H. W. Kroto, J. R. Heath, S. C. O'Brien, R. F. Curl, and R. E. Smalley, "C60: Buckminsterfullerene," *Nature*, vol. 318, p. 162, 1985.

[2] S. Iijima, "Helical microtubules of graphitic carbon," *Nature*, vol. 354, p. 56, 1991.

[3] S. Iijima and T. Ichihashi, "Single-shell carbon nanotubes of 1-nm diameter," *Nature*, vol. 363, no. 6430, pp. 603–605, 1993.

[4] J.-C. Charlier, X. Blase, and S. Roche, "Electronic and transport properties of nanotubes," *Reviews of Modern Physics*, vol. 79, p. 677, 2007.

[5] R. Saito, G. Dresselhaus, and M. S. Dresselhaus, *Physical Properties of Carbon Nanotubes*. London: Imperial College Press, 1998.

[6] R. Saito, M. Fujita, G. Dresselhaus, and M. S. Dresselhaus, "Electronic structure of chiral graphene tubules," *Applied Physics Letters*, vol. 60, p. 2204, 1992.

[7] K. S. Novoselov, A. K. Geim, S. V. Morozov, D. Jiang, Y. Zhang, S. V. Dubonos, I. V. Grigorieva, and A. A. Firsov, "Electric field effect in atomically thin carbon films," *Science*, vol. 11, p. 666, 2004.

[8] K. S. Novoselov, A. K. Geim, S. V. Morozov, D. Jiang, M. I. Katsnelson, S. V. Dubonos, I. V. Grigorieva, and A. A. Firsov, "Two-dimensional gas of massless Dirac fermions in graphene," *Nature*, vol. 438, p. 197, 2005.

[9] K. S. Novoselov, "Nobel lecture: Graphene: Materials in the flatland," *Rev. Mod. Phys.*, vol. 83, pp. 837–849, Aug 2011.

[10] A. K. Geim, "Nobel lecture: Random walk to graphene," *Rev. Mod. Phys.*, vol. 83, pp. 851–862, Aug 2011.

[11] A. K. Geim and K. S. Novoselov, "The rise of graphene," *Nature Materials*, vol. 6, no. 3, pp. 183–191, 2007.

[12] R. E. Peierls, "Quelques proprietes typiques des corpses solides," *Ann.I. H. Poincare*, vol. 5, no. 177, 1935.

[13] L. D. Landau, "Zur theorie der phasenumwandlungen ii," *Phys. Z. Sowjetunion*, vol. 11, no. 26, 1937.

[14] P. Blake, P. D. Brimicombe, R. R. Nair, T. J. Booth, D. Jiang, F. Schedin, L. A. Ponomarenko, S. V. Morozov, H. F. Gleeson, E. W. Hill, A. K. Geim, and K. S. Novoselov, "Graphene-Based liquid crystal device," *Nano Letters*, vol. 8, p. 1704, 2008.

[15] Y. Hernandez, V. Nicolosi, M. Lotya, F. M. Blighe, Z. Sun, S. De, M. T., B. Holland, M. Byrne, Y. K. Gun'Ko, J. J. Boland, P. Niraj, G. Duesberg, S. Krishnamurthy, R. Goodhue, J. Hutchison, V. Scardaci, A. C. Ferrari, and J. N. Coleman, "High-yield production of graphene by liquid-phase exfoliation of graphite," *Nature Nanotechnology*, vol. 3, p. 563, 2008.

[16] C. Berger, Z. Song, X. Li, X. Wu, N. Brown, C. Naud, D. Mayou, T. Li, J. Hass, A. N. Marchenkov, E. H. Conrad, P. N. First, and W. A. de Heer, "Electronic confinement and coherence in patterned epitaxial graphene," *Science*, vol. 312, p. 1191, 2006.

[17] A. H. Castro Neto, F. Guinea, and N. M. R. Peres, "Drawing conclusions from graphene," *Physics World*, vol. 19, p. 33, 2006.

[18] P. R. Wallace, "The band theory of graphite," *Physical Review*, vol. 71, p. 622, 1947.

[19] J. C. Slonczewski and P. R. Weiss, "Band structure of graphite," *Physical Review*, vol. 109, p. 272, 1958.

[20] B. Aufray, A. Kara, S. Vizzini, H. Oughaddou, C. Léandri, B. Ealet, and G. Le Lay, "Graphene-like silicon nanoribbons on ag(110): A possible formation of silicene," *Applied Physics Letters*, vol. 96, no. 18, pp. –, 2010.

[21] B. Lalmi, H. Oughaddou, H. Enriquez, A. Kara, S. Vizzini, B. Ealet, and B. Aufray, "Epitaxial growth of a silicene sheet," *Applied Physics Letters*, vol. 97, no. 22, pp. –, 2010.

[22] J. R. Brent, N. Savjani, E. A. Lewis, S. J. Haigh, D. J. Lewis, and P. O'Brien, "Production of few-layer phosphorene by liquid exfoliation of black phosphorus," *Chem. Commun.*, vol. 50, pp. 13338–13341, 2014.

[23] M. E. Dávila, L. Xian, S. Cahangirov, A. Rubio, and G. L. Lay, "Germanene: a novel two-dimensional germanium allotrope akin to graphene and silicene," *New Journal of Physics*, vol. 16, no. 9, p. 095002, 2014.

[24] C. Lee, X. Wei, J. W. Kysar, and J. Hone, "Measurement of the elastic properties and intrinsic strength of monolayer graphene," *Science*, vol. 321, p. 385, 2008.

[25] I. Meric, M. Y. Han, A. F. Young, B. Ozyilmaz, P. Kim, and K. L. Shepard, "Current saturation in zero-bandgap, top-gated graphene field-effect transistors," *Nature Nanotechnology*, vol. 3, p. 654, 2008.

[26] A. A. Balandin, S. Ghosh, W. Bao, I. Calizo, D. Teweldebrhan, F. Miao, and C. N. Lau, "Superior thermal conductivity of Single-Layer graphene," *Nano Letters*, vol. 8, p. 902, 2008.

[27] J. S. Bunch, S. S. Verbridge, J. S. Alden, A. M. van der Zande, J. M. Parpia, H. G. Craighead, and P. L. McEuen, "Impermeable atomic membranes from graphene sheets," *Nano Letters*, vol. 8, p. 2458, 2008.

[28] S. Iijima, C. Brabec, A. Maiti, and J. Bernholc, "Structural flexibility of carbon nanotubes," *The Journal of Chemical Physics*, vol. 104, no. 5, pp. 2089–2092, 1996.

[29] M.-F. Yu, B. S. Files, S. Arepalli, and R. S. Ruoff, "Tensile loading of ropes of single wall carbon nanotubes and their mechanical properties," *Phys. Rev. Lett.*, vol. 84, pp. 5552–5555, Jun 2000.

[30] M. Fujii, X. Zhang, H. Xie, H. Ago, K. Takahashi, T. Ikuta, H. Abe, and T. Shimizu, "Measuring the thermal conductivity of a single carbon nanotube," *Phys. Rev. Lett.*, vol. 95, p. 065502, Aug 2005.

[31] P. Kim, L. Shi, A. Majumdar, and P. L. McEuen, "Thermal transport measurements of individual multiwalled nanotubes," *Phys. Rev. Lett.*, vol. 87, p. 215502, Oct 2001.

[32] J. A. Misewich, R. Martel, P. Avouris, J. C. Tsang, S. Heinze, and J. Tersoff, "Electrically induced optical emission from a carbon nanotube fet," *Science*, vol. 300, no. 5620, pp. 783–786, 2003.

[33] S. M. Bachilo, M. S. Strano, C. Kittrell, R. H. Hauge, R. E. Smalley, and R. B. Weisman, "Structure-assigned optical spectra of single-walled carbon nanotubes," *Science*, vol. 298, no. 5602, pp. 2361–2366, 2002.

[34] S. J. Tans, M. H. Devoret, H. Dai, A. Thess, R. E. Smalley, L. J. Geerligs, and C. Dekker, "Individual single-wall carbon nanotubes as quantum wires," *Nature*, vol. 386, p. 474, 1997.

[35] A. H. Castro Neto, F. Guinea, N. M. R. Peres, K. S. Novoselov, and A. K. Geim, "The electronic properties of graphene," *Reviews of Modern Physics*, vol. 81, p. 109, 2009.

[36] K. S. Novoselov, A. K. Geim, S. V. Morozov, D. Jiang, M. I. Katsnelson, I. V. Grigorieva, S. V. Dubonos, and A. A. Firsov, "Two-dimensional gas of massless dirac fermions in graphene," *Nature*, vol. 438, p. 197, 2005.

[37] C. L. Kane and E. J. Mele, "Quantum spin hall effect in graphene," *Physical Review Letters*, vol. 95, p. 226801, 2005.

[38] D. Huertas-Hernando, F. Guinea, and A. Brataas, "Spin-orbit coupling in curved graphene, fullerenes, nanotubes, and nanotube caps," *Physical Review B*, vol. 74, p. 155426, 2006.

[39] H. Min, J. E. Hill, N. A. Sinitsyn, B. R. Sahu, L. Kleinman, and A. H. MacDonald, "Intrinsic and rashba spin-orbit interactions in graphene sheets," *Phys. Rev. B*, vol. 74, p. 165310, Oct 2006.

[40] D. Huertas-Hernando, F. Guinea, and A. Brataas, "Spin-Orbit-Mediated spin relaxation in graphene," *Physical Review Letters*, vol. 103, p. 146801, 2009.

[41] B. Trauzettel, D. V. Bulaev, D. Loss, and G. Burkard, "Spin qubits in graphene quantum dots," *Nature Physics*, vol. 3, p. 192, 2007.

[42] J. Fischer, B. Trauzettel, and D. Loss, "Hyperfine interaction and electron-spin decoherence in graphene and carbon nanotube quantum dots," *Physical Review B*, vol. 80, p. 155401, 2009.

[43] O. V. Yazyev, "Hyperfine interactions in graphene and related carbon nanostructures," *Nano Letters*, vol. 8, no. 4, pp. 1011–1015, 2008. PMID: 18321077.

[44] Z. Wang, C. Tang, R. Sachs, Y. Barlas, and J. Shi, "Proximity-induced ferromagnetism in graphene revealed by the anomalous hall effect," *Phys. Rev. Lett.*, vol. 114, p. 016603, Jan 2015.

[45] M. N. Baibich, J. M. Broto, A. Fert, F. N. Van Dau, F. Petroff, P. Etienne, G. Creuzet, A. Friederich, and J. Chazelas, "Giant magnetoresistance of (001)fe/(001)cr magnetic superlattices," *Physical Review Letters*, vol. 61, p. 2472, 1988.

[46] G. Binasch, P. Grünberg, F. Saurenbach, and W. Zinn, "Enhanced magnetoresistance in layered magnetic structures with antiferromagnetic interlayer exchange," *Physical Review B*, vol. 39, p. 4828, 1989.

[47] O. V. Yazyev, "Emergence of magnetism in graphene materials and nanostructures," *Reports on Progress in Physics*, vol. 73, p. 056501, 2010.

[48] S. A. Wolf, D. D. Awschalom, R. A. Buhrman, J. M. Daughton, S. von Molnár, M. L. Roukes, A. Y. Chtchelkanova, and D. M. Treger, "Spintronics: A Spin-Based electronics vision for the future," *Science*, vol. 294, p. 1488, 2001.

[49] D. D. Awschalom and M. E. Flatte, "Challenges for semiconductor spintronics," *Nature Physics*, vol. 3, p. 153, 2007.

[50] C. Chappert, A. Fert, and F. N. Van Dau, "The emergence of spin electronics in data storage," *Nature Materials*, vol. 6, p. 813, 2007.

[51] A. Fert, "Nobel lecture: Origin, development, and future of spintronics," *Reviews of Modern Physics*, vol. 80, p. 1517, 2008.

[52] D. M. Edwards, J. Mathon, R. B. Muniz, and M. S. Phan, "Oscillations in the exchange coupling of ferromagnetic layers separated by a nonmagnetic metallic layer," *Journal of Physics: Condensed Matter*, vol. 3, p. 4941, 1991.

[53] M. A. Ruderman and C. Kittel, "Indirect exchange coupling of nuclear magnetic moments by conduction electrons," *Physical Review*, vol. 96, p. 99, 1954.

[54] P. Grünberg, R. Schreiber, Y. Pang, M. B. Brodsky, and H. Sowers, "Layered magnetic structures: Evidence for antiferromagnetic coupling of fe layers across cr interlayers," *Physical Review Letters*, vol. 57, p. 2442, 1986.

[55] S. S. P. Parkin, N. More, and K. P. Roche, "Oscillations in exchange coupling and magnetoresistance in metallic superlattice structures: Co/Ru, Co/Cr, and Fe/Cr," *Physical Review Letters*, vol. 64, p. 2304, 1990.

[56] S. S. P. Parkin, "Systematic variation of the strength and oscillation period of indirect magnetic exchange coupling through the 3d, 4d, and 5d transition metals," *Physical Review Letters*, vol. 67, p. 3598, 1991.

[57] V. M. Pereira and A. H. Castro Neto, "Strain engineering of graphene's electronic structure," *Physical Review Letters*, vol. 103, p. 046801, 2009.

[58] A. Cresti, F. Ortmann, T. Louvet, D. Van Tuan, and S. Roche, "Broken symmetries, zero-energy modes, and quantum transport in disordered graphene: From supermetallic to insulating regimes," *Phys. Rev. Lett.*, vol. 110, p. 196601, May 2013.

[59] V. V. Cheianov and V. I. Fal'ko, "Friedel oscillations, impurity scattering, and temperature dependence of resistivity in graphene," *Phys. Rev. Lett.*, vol. 97, p. 226801, Nov 2006.

[60] A. Lherbier, A. R. Botello-Méndez, and J.-C. Charlier, "Electronic and transport properties of unbalanced sublattice n-doping in graphene," *Nano Letters*, vol. 13, no. 4, pp. 1446–1450, 2013.

[61] P. Rani and V. K. Jindal, "Designing band gap of graphene by b and n dopant atoms," *RSC Advances*, vol. 3, no. 3, p. 802, 2013.

[62] C. Popovici, O. Oliveira, W. de Paula, and T. Frederico, "Charge confinement and klein tunneling from doping graphene," *Phys. Rev. B*, vol. 85, p. 235424, Jun 2012.

[63] H. Park, A. Wadehra, J. W. Wilkins, and A. H. Castro Neto, "Spin-polarized electronic current induced by sublattice engineering of graphene sheets with boron/nitrogen," *Phys. Rev. B*, vol. 87, p. 085441, Feb 2013.

[64] P. Rakyta, A. Kormanyos, and J. Cserti, "Effect of sublattice asymmetry and spin-orbit interaction on out-of-plane spin polarization of photoelectrons," *Phys. Rev. B*, vol. 83, p. 155439, Apr 2011.

[65] Y.-M. Lin, K. A. Jenkins, A. Valdes-Garcia, J. P. Small, D. B. Farmer, and P. Avouris, "Operation of graphene transistors at gigahertz frequencies," *Nano Letters*, vol. 9, no. 1, pp. 422–426, 2008.

[66] S. V. Morozov, K. S. Novoselov, M. I. Katsnelson, F. Schedin, D. C. Elias, J. A. Jaszczak, and A. K. Geim, "Giant intrinsic carrier mobilities in graphene and its bilayer," *Phys. Rev. Lett.*, vol. 100, p. 016602, Jan 2008.

[67] S. R. Power and M. S. Ferreira, "Indirect exchange and rkky interactions in magnetically-doped graphene," *Crystals*, vol. -, pp. –, - 2013.

[68] M. A. H. Vozmediano, M. P. López-Sancho, T. Stauber, and F. Guinea, "Local defects and ferromagnetism in graphene layers," *Physical Review B*, vol. 72, p. 155121, 2005.

[69] V. K. Dugaev, V. I. Litvinov, and J. Barnas, "Exchange interaction of magnetic impurities in graphene," *Physical Review B*, vol. 74, p. 224438, 2006.

[70] S. Saremi, "RKKY in half-filled bipartite lattices: Graphene as an example," *Physical Review B*, vol. 76, p. 184430, 2007.

[71] L. Brey, H. A. Fertig, and S. D. Sarma, "Diluted graphene antiferromagnet," *Physical Review Letters*, vol. 99, p. 116802, 2007.

[72] E. H. Hwang and S. Das Sarma, "Screening, kohn anomaly, friedel oscillation, and RKKY interaction in bilayer graphene," *Physical Review Letters*, vol. 101, p. 156802, 2008.

[73] J. E. Bunder and H. Lin, "Ruderman-Kittel-Kasuya-Yosida interactions on a bipartite lattice," *Physical Review B*, vol. 80, p. 153414, 2009.

[74] A. M. Black-Schaffer, "RKKY coupling in graphene," *Physical Review B*, vol. 81, p. 205416, 2010.

[75] M. Sherafati and S. Satpathy, "RKKY interaction in graphene from the lattice green's function," *Physical Review B*, vol. 83, p. 165425, 2011.

[76] B. Uchoa, T. G. Rappoport, and A. H. Castro Neto, "Kondo quantum criticality of magnetic adatoms in graphene," *Physical Review Letters*, vol. 106, p. 016801, 2011.

[77] A. M. Black-Schaffer, "Importance of electron-electron interactions in the RKKY coupling in graphene," *Physical Review B*, vol. 82, p. 073409, 2010.

[78] S. R. Power and M. S. Ferreira, "Electronic structure of graphene beyond the linear dispersion regime," *Physical Review B*, vol. 83, p. 155432, 2011.

[79] M. Sherafati and S. Satpathy, "Analytical expression for the RKKY interaction in doped graphene," *Physical Review B*, vol. 84, p. 125416, 2011.

[80] E. Kogan, "RKKY interaction in graphene," *Physical Review B*, vol. 84, p. 115119, 2011.

[81] H. Lee, J. Kim, E. R. Mucciolo, G. Bouzerar, and S. Kettemann, "Rkky interaction in disordered graphene," *Phys. Rev. B*, vol. 85, p. 075420, Feb 2012.

[82] J. Klinovaja and D. Loss, "RKKY interaction in carbon nanotubes and graphene nanoribbons," *Physical Review B*, vol. 87, p. 045422, Jan. 2013.

[83] A. T. Costa, D. F. Kirwan, and M. S. Ferreira, "Indirect exchange coupling between magnetic adatoms in carbon nanotubes," *Physical Review B*, vol. 72, p. 085402, 2005.

[84] D. F. Kirwan, C. G. Rocha, A. T. Costa, and M. S. Ferreira, "Sudden decay of indirect exchange coupling between magnetic atoms on carbon nanotubes," *Physical Review B*, vol. 77, p. 085432, 2008.

[85] D. F. Kirwan, *Theoretical Studies of Carbon Nanotubes Interacting with Magnetic Atoms*. PhD thesis, School of Physics, Trinity College Dublin, Dublin, 2009.

[86] D. F. Kirwan, V. M. de Menezes, C. G. Rocha, A. T. Costa, R. B. Muniz, S. B. Fagan, and M. S. Ferreira, "Enhanced spin-valve effect in magnetically doped carbon nanotubes," *Carbon*, vol. 47, p. 2533, 2009.

[87] P. D. Gorman, J. M. Duffy, M. S. Ferreira, and S. R. Power, "Rkky interaction between adsorbed magnetic impurities in graphene: Symmetry and strain effects," *Phys. Rev. B*, vol. 88, p. 085405, Aug 2013.

[88] V. Krstiċ, C. P. Ewels, T. Wågberg, M. S. Ferreira, A. M. Janssens, O. Stèphan, and M. Glerup, "Indirect magnetic coupling in light-element-doped single-walled carbon nanotubes," *ACS Nano*, vol. 4, p. 5081, 2010.

[89] E. J. G. Santos, A. Ayuela, and D. Sánchez-Portal, "First-principles study of substitutional metal impurities in graphene: structural, electronic and magnetic properties," *New Journal of Physics*, vol. 12, p. 053012, 2010.

[90] P. Venezuela, R. B. Muniz, A. T. Costa, D. M. Edwards, S. R. Power, and M. S. Ferreira, "Emergence of local magnetic moments in doped graphene-related materials," *Physical Review B*, vol. 80, p. 241413, Dec. 2009.

[91] E. J. G. Santos, D. Sánchez-Portal, and A. Ayuela, "Magnetism of substitutional co impurities in graphene: Realization of single π vacancies," *Physical Review B*, vol. 81, p. 125433, 2010.

[92] I. C. Gerber, A. V. Krasheninnikov, A. S. Foster, and R. M. Nieminen, "A first-principles study on magnetic coupling between carbon adatoms on graphene," *New Journal of Physics*, vol. 12, p. 113021, Nov. 2010.

[93] F. Meier, L. Zhou, J. Wiebe, and R. Wiesendanger, "Revealing magnetic interactions from single-atom magnetization curves," *Science*, vol. 320, pp. 82–86, Apr. 2008. PMID: 18388289.

[94] A. A. Khajetoorians, J. Wiebe, B. Chilian, S. Lounis, S. Blügel, and R. Wiesendanger, "Atom-by-atom engineering and magnetometry of tailored nanomagnets," *Nature Physics*, vol. 8, pp. 497–503, June 2012.

[95] L. Zhou, J. Wiebe, S. Lounis, E. Vedmedenko, F. Meier, S. Blügel, P. H. Dederichs, and R. Wiesendanger, "Strength and directionality of surface Ruderman-Kittel-Kasuya-Yosida interaction mapped on the atomic scale," *Nature Physics*, vol. 6, pp. 187–191, Mar. 2010.

[96] C. F. Hirjibehedin, C. P. Lutz, and A. J. Heinrich, "Spin coupling in engineered atomic structures," *Science*, vol. 312, pp. 1021–1024, May 2006. PMID: 16574821.

[97] M. Y. Han, B. Özyilmaz, Y. Zhang, and P. Kim, "Energy band-gap engineering of graphene nanoribbons," *Phys. Rev. Lett.*, vol. 98, p. 206805, May 2007.

[98] E. Suárez Morell, R. Vergara, M. Pacheco, L. Brey, and L. Chico, "Electronic properties of twisted bilayer nanoribbons," *Phys. Rev. B*, vol. 89, p. 205405, May 2014.

[99] J. Bai, X. Zhong, S. Jiang, Y. Huang, and X. Duan, "Graphene nanomesh," *Nature nanotechnology*, vol. 5, pp. 190–194, Mar. 2010.

[100] Y. Zhang, T.-T. Tang, C. Girit, Z. Hao, M. C. Martin, A. Zettl, M. F. Crommie, Y. R. Shen, and F. Wang, "Direct observation of a widely

tunable bandgap in bilayer graphene," *Nature*, vol. 459, pp. 820–823, June 2009.

[101] A. Ayuela, W. Jaskólski, H. Santos, and L. Chico, "Electronic properties of graphene grain boundaries," *New Journal of Physics*, vol. 16, no. 8, p. 083018, 2014.

[102] T. Ohta, A. Bostwick, T. Seyller, K. Horn, and E. Rotenberg, "Controlling the electronic structure of bilayer graphene," *Science*, vol. 313, no. 5789, pp. 951–954, 2006.

[103] Z. Luo, P. M. Vora, E. J. Mele, A. T. C. Johnson, and J. M. Kikkawa, "Photoluminescence and band gap modulation in graphene oxide," *Applied Physics Letters*, vol. 94, no. 11, pp. –, 2009.

[104] H. Santos, M. C. Muñoz, M. P. López-Sancho, and L. Chico, "Interplay between symmetry and spin-orbit coupling on graphene nanoribbons," *Phys. Rev. B*, vol. 87, p. 235402, Jun 2013.

[105] E. V. Castro, K. S. Novoselov, S. V. Morozov, N. M. R. Peres, J. M. B. L. dos Santos, J. Nilsson, F. Guinea, A. K. Geim, and A. H. C. Neto, "Biased bilayer graphene: Semiconductor with a gap tunable by the electric field effect," *Phys. Rev. Lett.*, vol. 99, p. 216802, Nov 2007.

[106] H. C. Schniepp, J.-L. Li, M. J. McAllister, H. Sai, M. Herrera-Alonso, D. H. Adamson, R. K. Prud'homme, R. Car, D. A. Saville, and I. A. Aksay, "Functionalized single graphene sheets derived from splitting graphite oxide," *The Journal of Physical Chemistry B*, vol. 110, no. 17, pp. 8535–8539, 2006. PMID: 16640401.

[107] F. Liu, P. Ming, and J. Li, "*Ab initio* calculation of ideal strength and phonon instability of graphene under tension," *Phys. Rev. B*, vol. 76, p. 064120, Aug 2007.

[108] T. M. G. Mohiuddin, A. Lombardo, R. R. Nair, A. Bonetti, G. Savini, R. Jalil, N. Bonini, D. M. Basko, C. Galiotis, N. Marzari, K. S. Novoselov, A. K. Geim, and A. C. Ferrari, "Uniaxial strain in graphene by raman spectroscopy: g peak splitting, grüneisen parameters, and sample orientation," *Phys. Rev. B*, vol. 79, p. 205433, May 2009.

[109] Z. H. Ni, T. Yu, Y. H. Lu, Y. Y. Wang, Y. P. Feng, and Z. X. Shen, "Uniaxial strain on graphene: Raman spectroscopy study and band-gap opening," *ACS Nano*, vol. 2, no. 11, pp. 2301–2305, 2008.

[110] K. S. Kim, Y. Zhao, H. Jang, S. Y. Lee, J. M. Kim, K. S. Kim, J. Ahn, P. Kim, J. Choi, and B. H. Hong, "Large-scale pattern growth of graphene films for stretchable transparent electrodes," *Nature*, vol. 457, p. 706, 2009.

[111] V. M. Pereira and A. H. Castro Neto, "Strain engineering of graphene's electronic structure," *Phys. Rev. Lett.*, vol. 103, p. 046801, Jul 2009.

[112] V. M. Pereira, A. H. Castro Neto, and N. M. R. Peres, "Tight-binding approach to uniaxial strain in graphene," *Physical Review B*, vol. 80, p. 045401, 2009.

[113] F. Guinea, M. I. Katsnelson, and A. K. Geim, "Energy gaps and a zero-field quantum hall effect in graphene by strain engineering," *Nature Physics*, vol. 6, no. 1, pp. 30–33, 2010. Cited By (since 1996): 150.

[114] A. Sharma, V. N. Kotov, and A. H. Castro Neto, "Effect of uniaxial strain on ferromagnetic instability and formation of localized magnetic states on adatoms in graphene," *Physical Review B*, vol. 87, p. 155431, Apr. 2013.

[115] N. Ferralis, R. Maboudian, and C. Carraro, "Evidence of structural strain in epitaxial graphene layers on 6h-sic(0001)," *Phys. Rev. Lett.*, vol. 101, p. 156801, Oct 2008.

[116] J. Borysiuk, R. Bozek, W. Strupinski, A. Wysmolek, K. Grodecki, R. Stepniewski, and J. M. Baranowski, "Transmission electron microscopy and scanning tunneling microscopy investigations of graphene on 4h-sic(0001)," *Journal of Applied Physics*, vol. 105, no. 2, p. 023503, 2009.

[117] S. Jun, "Density-functional study of edge stress in graphene," *Phys. Rev. B*, vol. 78, p. 073405, Aug 2008.

[118] B. Huang, M. Liu, N. Su, J. Wu, W. Duan, B.-l. Gu, and F. Liu, "Quantum manifestations of graphene edge stress and edge instability: A first-principles study," *Phys. Rev. Lett.*, vol. 102, p. 166404, Apr 2009.

[119] G. F. Sun, J. F. Jia, Q. K. Xue, and L. Li, "Atomic-scale imaging and manipulation of ridges on epitaxial graphene on 6h-sic(0001)," *Nanotechnology*, vol. 20, no. 35, p. 355701, 2009.

[120] M. Neek-Amal and F. Peeters, "Strain-engineered graphene through a nanostructured substrate. ii. pseudomagnetic fields," *Physical Review B*, vol. 85, no. 19, pp. 1–6, 2012.

[121] J. W. González, M. Pacheco, P. Orellana, L. Brey, and L. Chico, "Electronic transport of folded graphene nanoribbons," *Solid State Communications*, vol. 152, no. 15, pp. 1400 – 1403, 2012. Exploring Graphene, Recent Research Advances.

[122] W. Bao, F. Miao, Z. Chen, H. Zhang, W. Jang, C. Dames, and C. N. Lau, "Controlled ripple texturing of suspended graphene and ultrathin graphite membranes," *Nat Nano*, vol. 4, pp. 562–566, 2009.

[123] S. H. R. Sena, J. M. P. Jr, G. A. Farias, F. M. Peeters, and R. N. C. Filho, "The electronic properties of graphene and graphene ribbons under simple shear strain," *Journal of Physics: Condensed Matter*, vol. 24, no. 37, p. 375301, 2012.

[124] B. Verberck, B. Partoens, F. M. Peeters, and B. Trauzettel, "Strain-induced band gaps in bilayer graphene," *Phys. Rev. B*, vol. 85, p. 125403, Mar 2012.

[125] C. P. Chang, B. R. Wu, R. B. Chen, and M. F. Lin, "Deformation effect on electronic and optical properties of nanographite ribbons," *Journal of Applied Physics*, vol. 101, no. 6, p. 063506, 2007.

[126] G. Gui, J. Li, and J. Zhong, "Band structure engineering of graphene by strain: First-principles calculations," *Phys. Rev. B*, vol. 78, p. 075435, Aug 2008.

[127] M. Farjam and H. Rafii-Tabar, "Comment on "band structure engineering of graphene by strain: First-principles calculations"," *Phys. Rev. B*, vol. 80, p. 167401, Oct 2009.

[128] G. Gui, J. Li, and J. Zhong, "Reply to "comment on 'band structure engineering of graphene by strain: First-principles calculations' "," *Phys. Rev. B*, vol. 80, p. 167402, Oct 2009.

[129] L. Sun, Q. Li, H. Ren, H. Su, Q. W. Shi, and J. Yang, "Strain effect on electronic structures of graphene nanoribbons: A first-principles study," *The Journal of Chemical Physics*, vol. 129, no. 7, p. 074704, 2008.

[130] M. Mohr, K. Papagelis, J. Maultzsch, and C. Thomsen, "Two-dimensional electronic and vibrational band structure of uniaxially strained graphene from *ab initio* calculations," *Phys. Rev. B*, vol. 80, p. 205410, Nov 2009.

[131] O. Hod and G. E. Scuseria, "Electromechanical properties of suspended graphene nanoribbons," *Nano Letters*, vol. 9, no. 7, pp. 2619–2622, 2009. PMID: 19505116.

[132] K. Alam, "Uniaxial strain effects on the performance of a ballistic top gate graphene nanoribbon on insulator transistor," *Nanotechnology, IEEE Transactions on*, vol. 8, no. 4, pp. 528–534, July.

[133] F. M. D. Pellegrino, G. G. N. Angilella, and R. Pucci, "Strain effect on the optical conductivity of graphene," *Phys. Rev. B*, vol. 81, p. 035411, Jan 2010.

[134] S.-M. Choi, S.-H. Jhi, and Y.-W. Son, "Effects of strain on electronic properties of graphene," *Phys. Rev. B*, vol. 81, p. 081407, Feb 2010.

[135] R. Rasuli, H. Rafii-Tabar, and A. I. zad, "Strain effect on quantum conductance of graphene nanoribbons from maximally localized wannier functions," *Phys. Rev. B*, vol. 81, p. 125409, Mar 2010.

[136] M. Poetschke, C. G. Rocha, L. E. F. Foa Torres, S. Roche, and G. Cuniberti, "Modeling graphene-based nanoelectromechanical devices," *Phys. Rev. B*, vol. 81, p. 193404, May 2010.

[137] M. Z. Hossain, "Quantum conductance modulation in graphene by strain engineering," *Applied Physics Letters*, vol. 96, no. 14, p. 143118, 2010.

[138] Y. Lu and J. Guo, "Band gap of strained graphene nanoribbons," *Nano Research*, vol. 3, pp. 189–199, 2010.

[139] A. L. Kitt, V. M. Pereira, A. K. Swan, and B. B. Goldberg, "Lattice-corrected strain-induced vector potentials in graphene," *Phys. Rev. B*, vol. 85, p. 115432, Mar 2012.

[140] D. A. Abanin and D. A. Pesin, "Interaction-induced topological insulator states in strained graphene," *Phys. Rev. Lett.*, vol. 109, p. 066802, Aug 2012.

[141] N. Levy, S. A. Burke, K. L. Meaker, M. Panlasigui, A. Zettl, F. Guinea, A. H. C. Neto, and M. F. Crommie, "Strain-induced pseudo-magnetic fields greater than 300 tesla in graphene nanobubbles," *Science*, vol. 329, no. 5991, pp. 544–547, 2010.

[142] H. Yan, Y. Sun, L. He, J.-C. Nie, and M. H. W. Chan, "Observation of landau-level-like quantization at 77 k along a strained-induced graphene ridge," *Phys. Rev. B*, vol. 85, p. 035422, Jan 2012.

[143] M. M. Fogler, F. Guinea, and M. I. Katsnelson, "Pseudomagnetic fields and ballistic transport in a suspended graphene sheet," *Phys. Rev. Lett.*, vol. 101, p. 226804, Nov 2008.

[144] F. Guinea, A. K. Geim, M. I. Katsnelson, and K. S. Novoselov, "Generating quantizing pseudomagnetic fields by bending graphene ribbons," *Phys. Rev. B*, vol. 81, p. 035408, Jan 2010.

[145] M. Neek-Amal, L. Covaci, and F. M. Peeters, "Nanoengineered nonuniform strain in graphene using nanopillars," *Phys. Rev. B*, vol. 86, p. 041405, Jul 2012.

[146] N. N. Klimov, S. Jung, S. Zhu, T. Li, C. A. Wright, S. D. Solares, D. B. Newell, N. B. Zhitenev, and J. A. Stroscio, "Electromechanical properties of graphene drumheads," *Science*, vol. 336, no. 6088, pp. 1557–1561, 2012.

[147] L. Gerhard, E. Moyen, T. Balashov, I. Ozerov, M. Portail, H. Sahaf, L. Masson, W. Wulfhekel, and M. Hanbucken, "A graphene electron lens," *Applied Physics Letters*, vol. 100, no. 15, p. 153106, 2012.

[148] W. S. Su, "Electronic and structural properties of carbon nanotubes modulated by external strain," *Journal of Applied Physics*, vol. 113, p. 244308, June 2013.

[149] Y. R. Chen, C. I. Weng, and S. J. Sun, "Electronic properties of zigzag and armchair carbon nanotubes under uniaxial strain," *Journal of Applied Physics*, vol. 104, p. 114310, Dec. 2008.

[150] L. Yang and J. Han, "Electronic structure of deformed carbon nanotubes," *Physical Review Letters*, vol. 85, pp. 154–157, July 2000.

[151] S. Sreekala, X. Peng, P. M. Ajayan, and S. K. Nayak, "Effect of strain on the band gap and effective mass of zigzag single-wall carbon nanotubes: First-principles density-functional calculations," *Physical Review B*, vol. 77, p. 155434, Apr. 2008.

[152] A. Pullen, G. L. Zhao, D. Bagayoko, and L. Yang, "Structural, elastic, and electronic properties of deformed carbon nanotubes under uniaxial strain," *Physical Review B*, vol. 71, p. 205410, May 2005.

[153] J. W. Ding, X. H. Yan, J. X. Cao, D. L. Wang, Y. Tang, and Q. B. Yang, "Curvature and strain effects on electronic properties of single-wall carbon nanotubes," *Journal of Physics: Condensed Matter*, vol. 15, p. L439, July 2003.

[154] Y. He, C. Zhang, C. Cao, and H. P. Cheng, "Effects of strain and defects on the electron conductance of metallic carbon nanotubes," *Physical Review B*, vol. 75, p. 235429, June 2007.

[155] M. A. Cullinan and M. L. Culpepper, "Carbon nanotubes as piezoresistive microelectromechanical sensors: Theory and experiment," *Physical Review B*, vol. 82, p. 115428, Sept. 2010.

[156] Y. Yoon and J. Guo, "Analysis of strain effects in ballistic carbon nanotube FETs," *IEEE Transactions on Electron Devices*, vol. 54, pp. 1280–1287, June 2007.

[157] E. D. Minot, Y. Yaish, V. Sazonova, J. Y. Park, M. Brink, and P. L. McEuen, "Tuning carbon nanotube band gaps with strain," *Physical Review Letters*, vol. 90, p. 156401, Apr. 2003.

[158] H. Fang, R. Z. Wang, M. Yan, S. Y. Chen, and B. Wang, "Strain-induced metal to semiconductor transition in ultra-small diameter single-wall carbon nanotubes," *Physics Letters A*, vol. 375, pp. 1200–1204, Feb. 2011.

[159] D. Orlikowski, M. Buongiorno Nardelli, J. Bernholc, and C. Roland, "Theoretical STM signatures and transport properties of native defects in carbon nanotubes," *Physical Review B*, vol. 61, pp. 14194–14203, May 2000.

[160] P. Lloyd, "Wave propagation through an assembly of spheres: ii. the density of single-particle eigenstates," *Proceedings of the Physical Society*, vol. 90, p. 207, 1967.

[161] R. Courant and D. Hilbert, *Methods of mathematical physics 1 (2nd revised ed.)*. New York: New York Interscience Publishers, second ed., 1953.

[162] A. K. Geim and K. S. Novoselov, "The rise of graphene," *Nature Materials*, vol. 6, p. 183, 2007.

[163] O. V. Yazyev, "Magnetism in disordered graphene and irradiated graphite," *Physical Review Letters*, vol. 101, p. 037203, 2008.

[164] C. T. White and T. N. Todorov, "Carbon nanotubes as long ballistic conductors," *Nature*, vol. 393, p. 240, 1998.

[165] G. W. Semenoff, "Condensed-matter simulation of a three-dimensional anomaly," *Phys. Rev. Lett.*, vol. 53, pp. 2449–2452, Dec 1984.

[166] P. Avouris, Z. Chen, and V. Perebeinos, "Carbon-based electronics," *Nature Nanotechnology*, vol. 2, pp. 605–615, Oct. 2007.

[167] L. Chico, H. Santos, M. C. Muñoz, and M. P. López-Sancho, "Intrinsic spin-orbit interaction in carbon nanotubes and curved nanoribbons," *Solid State Communications*, vol. 152, no. 15, pp. 1477 – 1482, 2012. Exploring Graphene, Recent Research Advances.

[168] J. M. Duffy, P. D. Gorman, S. R. Power, and M. S. Ferreira, "Variable range of the RKKY interaction in edged graphene," *Journal of Physics: Condensed Matter*, vol. 26, p. 055007, Feb. 2014.

[169] D. M. Eigler and E. K. Schweizer, "Positioning single atoms with a scanning tunnelling microscope," *Nature*, vol. 344, pp. 524–526, Apr. 1990.

[170] R. Lv, Q. Li, A. R. Botello-Mendez, T. Hayashi, B. Wang, A. Berkdemir, Q. Hao, A. L. Elias, R. Cruz-Silva, H. R. Gutierrez, Y. A. Kim, H. Muramatsu, J. Zhu, M. Endo, H. Terrones, J.-C. Charlier, M. Pan, and M. Terrones, "Nitrogen-doped graphene: beyond single substitution and enhanced molecular sensing," *Scientific Reports*, vol. 2, Aug. 2012.

[171] L. Tapasztó, G. Dobrik, P. Nemes-Incze, G. Vertesy, P. Lambin, and L. P. Biró, "Tuning the electronic structure of graphene by ion irradiation," *Phys. Rev. B*, vol. 78, p. 233407, Dec 2008.

[172] L. Tsetseris, B. Wang, and S. T. Pantelides, "Substitutional doping of graphene: The role of carbon divacancies," *Physical Review B*, vol. 89, no. 3, p. 035411, 2014.

[173] S. B. Fagan, R. Mota, R. Baierle, A. J. da Silva, and A. Fazzio, "Energetics and structural properties of adsorbed atoms and molecules on silicon-doped carbon nanotubes," *Materials Characterization*, vol. 50, no. 2-3, pp. 183–187, 2003. Brazilian Materials Research Society Symposia: Current Trends in Nanostructured Materials, Semiconductor Materials, Thin Films, and Biomaterials.

[174] T. Eelbo, M. Wasniowska, P. Thakur, M. Gyamfi, B. Sachs, T. O. Wehling, S. Forti, U. Starke, C. Tieg, A. I. Lichtenstein, and R. Wiesendanger, "Adatoms and clusters of 3d transition metals on graphene: Electronic and magnetic configurations," *Physical Review Letters*, vol. 110, p. 136804, Mar. 2013.

[175] K. T. Chan, J. B. Neaton, and M. L. Cohen, "First-principles study of metal adatom adsorption on graphene," *Physical Review B*, vol. 77, p. 235430, June 2008.

[176] Y. Mao, J. Yuan, and J. Zhong, "Density functional calculation of transition metal adatom adsorption on graphene," *Journal of Physics: Condensed Matter*, vol. 20, p. 115209, Mar. 2008.

[177] T. O. Wehling, A. I. Lichtenstein, and M. I. Katsnelson, "Transition-metal adatoms on graphene: Influence of local coulomb interactions on chemical bonding and magnetic moments," *Physical Review B*, vol. 84, p. 235110, Dec. 2011.

[178] S. B. Fagan, R. Mota, A. J. R. da Silva, and A. Fazzio, "*Ab initio* study of an iron atom interacting with single-wall carbon nanotubes," *Phys. Rev. B*, vol. 67, p. 205414, May 2003.

[179] P. O. Lehtinen, A. S. Foster, A. Ayuela, A. Krasheninnikov, K. Nordlund, and R. M. Nieminen, "Magnetic properties and diffusion of adatoms on a graphene sheet," *Physical Review Letters*, vol. 91, p. 017202, June 2003.

[180] A. V. Krasheninnikov, K. Nordlund, P. O. Lehtinen, A. S. Foster, A. Ayuela, and R. M. Nieminen, "Adsorption and migration of carbon adatoms on carbon nanotubes: Density-functional \textit{ab initio} and tight-binding studies," *Physical Review B*, vol. 69, p. 073402, Feb. 2004.

[181] B. Kappes and C. Ciobanu, "Bandgap opening in metallic carbon nanotubes due to silicon impurities," *Computers, Materials and Continua*, vol. 38, no. 1, 2013.

[182] K. Nakada and A. Ishii, *DFT Calculation for Adatom Adsorption on Graphene*. ISBN: 978-953-307-556-3, InTech, DOI: 10.5772/20477, Aug. 2011.

[183] C. F. Majkrzak, J. W. Cable, J. Kwo, M. Hong, D. B. McWhan, Y. Yafet, J. V. Waszczak, and C. Vettier, "Observation of a magnetic antiphase domain structure with long-range order in a synthetic gd-y superlattice," *Phys. Rev. Lett.*, vol. 56, pp. 2700–2703, Jun 1986.

[184] T. Kasuya, "A theory of metallic ferro- and antiferromagnetism on zener's model," *Progress of Theoretical Physics*, vol. 16, p. 45, 1956.

[185] K. Yosida, "Magnetic properties of Cu-Mn alloys," *Physical Review*, vol. 106, p. 893, 1957.

[186] D. M. Edwards, J. Mathon, R. B. Muniz, and M. S. Phan, "Oscillations of the exchange in magnetic multilayers as an analog of de Haas - van Alphen effect," *Physical Review Letters*, vol. 67, p. 493, 1991.

[187] P. Bruno and C. Chappert, "Oscillatory coupling between ferromagnetic layers separated by a nonmagnetic metal spacer," *Physical Review Letters*, vol. 67, p. 1602, 1991.

[188] M. Ferreira, J. d. e Castro, D. Edwards, and J. Mathon, "Non-rkky oscillations of exchange coupling in magnetic multilayers," *Journal of magnetism and magnetic materials*, vol. 154, no. 1, pp. L1–L6, 1996.

[189] M. S. Ferreira, J. d'Albuquerque e Castro, D. M. Edwards, and J. Mathon, "Fundamental oscillation periods of the interlayer exchange coupling beyond the rkky approximation," *Journal of Physics: Condensed Matter*, vol. 8, p. 11259, 1996.

[190] M. S. Ferreira, R. B. Muniz, J. d'Alberquerque e Castro, and D. M. Edwards, "The nature and validity of the RKKY limit of exchange coupling in magnetic trilayers," *Journal of Physics: Condensed Matter*, vol. 6, p. L619, 1994.

[191] J. d'Albuquerque e Castro, M. S. Ferreira, and R. B. Muniz, "Theory of the exchange coupling in magnetic metallic multilayers," *Physical Review B*, vol. 49, p. 16062, 1994.

[192] M. P. López Sancho, M. C. Muñoz, and L. Chico, "Coulomb interactions in carbon nanotubes," *Phys. Rev. B*, vol. 63, p. 165419, Apr 2001.

[193] S. R. Power, P. D. Gorman, J. M. Duffy, and M. S. Ferreira, "Strain-induced modulation of magnetic interactions in graphene," *Phys. Rev. B*, vol. 86, p. 195423, Nov 2012.

[194] F. Peng and W. Hongbin, "Strain enhanced exchange interaction between impurities in graphene," *Physica B: Condensed Matter*, vol. 407, no. 17, pp. 3434 – 3436, 2012.

[195] O. L. Blakslee, D. G. Proctor, E. J. Seldin, G. B. Spence, and T. Weng, "Elastic constants of compression-annealed pyrolytic graphite," *Journal of Applied Physics*, vol. 41, no. 8, pp. 3373–3382, 1970.

[196] J. C. Slater and G. F. Koster, "Simplified lcao method for the periodic potential problem," *Phys. Rev.*, vol. 94, no. 1498, 1954.

[197] W. A. Harrison, *Elementary Electronic Structure*. New York Interscience Publishers, 1999.

[198] G. Grosso and C. Piermarocchi, "Tight-binding model and interactions scaling laws for silicon and germanium," *Physical Review B*, vol. 51, pp. 16772–16777, June 1995.

[199] D. A. Papaconstantopoulos, M. J. Mehl, S. C. Erwin, and M. R. Pederson, *Tight-Binding Approach to computational Material Science*. Materials Research Society, 1998.

[200] A. H. Castro Neto and F. Guinea, "Electron-phonon coupling and raman spectroscopy in graphene," *Phys. Rev. B*, vol. 75, p. 045404, Jan 2007.

[201] E. J. G. Santos, A. Ayuela, and D. Sánchez-Portal, "Strain-tunable spin moment in ni-doped graphene," *The Journal of Physical Chemistry C*, vol. 116, no. 1, pp. 1174–1178, 2012.

[202] B. Huang, J. Yu, and S.-H. Wei, "Strain control of magnetism in graphene decorated by transition-metal atoms," *Phys. Rev. B*, vol. 84, p. 075415, Aug 2011.

[203] A. V. Krasheninnikov, P. O. Lehtinen, A. S. Foster, P. Pyykkö, and R. M. Nieminen, "Embedding Transition-Metal atoms in graphene: Structure, bonding, and magnetism," *Physical Review Letters*, vol. 102, p. 126807, 2009.

[204] E. Machado-Charry, P. Boulanger, L. Genovese, N. Mousseau, and P. Pochet, "Tunable magnetic states in hexagonal boron nitride sheets," *Applied Physics Letters*, vol. 101, no. 13, p. 132405, 2012.

[205] M. Sepioni, R. R. Nair, S. Rablen, J. Narayanan, F. Tuna, R. Winpenny, A. K. Geim, and I. V. Grigorieva, "Limits on intrinsic magnetism in graphene," *Physical Review Letters*, vol. 105, p. 207205, Nov. 2010.

[206] J. Chen, G. Autés, N. Alem, F. Gargiulo, A. Gautam, M. Linck, C. Kisielowski, O. V. Yazyev, S. G. Louie, and A. Zettl, "Controlled growth of a line defect in graphene and implications for gate-tunable valley filtering," *Physical Review B*, vol. 89, p. 121407, Mar. 2014.

[207] J. He, P. Zhou, N. Jiao, S. Y. Ma, K. W. Zhang, R. Z. Wang, and L. Z. Sun, "Magnetic exchange coupling and anisotropy of 3d transition metal nanowires on graphyne," *Scientific Reports*, vol. 4, Feb. 2014.

[208] S. Winters, T. Hallam, H. Nolan, and G. S. Duesberg, "Production of 3D-shaped graphene via transfer printing," *physica status solidi (b)*, vol. 249, pp. 2515–2518, Dec. 2012.

[209] T. Hallam, M. T. Cole, W. I. Milne, and G. S. Duesberg, "Field emission characteristics of contact printed graphene fins," *Small*, vol. 10, pp. 95–99, Jan. 2014.

[210] L. Jiang, X. Zhao, and Y. Zheng, "RKKY interaction in graphene with a line defect," *Journal of Physics: Condensed Matter*, vol. 27, p. 046003, Feb. 2015.

[211] A. T. Costa, M. S. Ferreira, T. Hallam, G. S. Duesberg, and A. H. Castro Neto, "Origami-based spintronics in graphene," *EPL (Europhysics Letters)*, vol. 104, p. 47001, Nov. 2013.

[212] A. Salehi-Khojin, D. Estrada, K. Y. Lin, M.-H. Bae, F. Xiong, E. Pop, and R. I. Masel, "Polycrystalline graphene ribbons as chemiresistors.," *Advanced materials (Deerfield Beach, Fla.)*, vol. 24, pp. 53–7, 52, Jan. 2012.

[213] J. T. Rasmussen, T. Gunst, P. Bøggild, A.-P. Jauho, and M. Brandbyge, "Electronic and transport properties of kinked graphene.," *Beilstein journal of nanotechnology*, vol. 4, pp. 103–10, Jan. 2013.

[214] S. R. Power, V. M. de Menezes, S. B. Fagan, and M. S. Ferreira, "Model of impurity segregation in graphene nanoribbons," *Physical Review B*, vol. 80, p. 235424, 2009.

[215] P. Bruno and C. Chappert, "Ruderman-kittel theory of oscillatory interlayer exchange coupling," *Physical Review B*, vol. 46, p. 261, 1992.

[216] Y. Lin, K. A. Jenkins, A. Valdes-Garcia, J. P. Small, D. B. Farmer, and P. Avouris, "Operation of graphene transistors at gigahertz frequencies," *Nano Letters*, vol. 9, p. 422, 2008.

[217] F. Schwierz, "Graphene transistors," *Nature Nanotechnology*, vol. 5, pp. 487–496, July 2010.

[218] X. Li, X. Wang, L. Zhang, S. Lee, and H. Dai, "Chemically derived, ultrasmooth graphene nanoribbon semiconductors," *Science*, vol. 319, p. 1229, 2008.

[219] K. Novoselov, "Graphene: Mind the gap," *Nature Materials*, vol. 6, pp. 720–721, Oct. 2007.

[220] S. Y. Zhou, G.-H. Gweon, A. V. Fedorov, P. N. First, W. A. de Heer, D.-H. Lee, F. Guinea, A. H. Castro Neto, and A. Lanzara, "Substrate-induced bandgap opening in epitaxial graphene," *Nature Materials*, vol. 6, pp. 770–775, Oct. 2007.

[221] C.-K. Chang, S. Kataria, C.-C. Kuo, A. Ganguly, B.-Y. Wang, J.-Y. Hwang, K.-J. Huang, W.-H. Yang, S.-B. Wang, C.-H. Chuang, M. Chen, C.-I. Huang, W.-F. Pong, K.-J. Song, S.-J. Chang, J.-H. Guo, Y. Tai, M. Tsujimoto, S. Isoda, C.-W. Chen, L.-C. Chen, and K.-H. Chen, "Band gap engineering of chemical vapor deposited graphene by in situ BN doping," *ACS Nano*, vol. 7, no. 2, pp. 1333–1341, 2012.

[222] R. Martinazzo, S. Casolo, and G. F. Tantardini, "Symmetry-induced band-gap opening in graphene superlattices," *Phys. Rev. B*, vol. 81, p. 245420, Jun 2010.

[223] J. J. Palacios, J. Fernández-Rossier, and L. Brey, "Vacancy-induced magnetism in graphene and graphene ribbons," *Physical Review B*, vol. 77, p. 195428, 2008.

[224] V. M. Pereira, J. M. B. Lopes dos Santos, and A. H. Castro Neto, "Modeling disorder in graphene," *Physical Review B*, vol. 77, p. 115109, 2008.

[225] M. S. Islam, K. Ushida, S. Tanaka, T. Makino, and A. Hashimoto, "Effect of boron and nitrogen doping with native point defects on the vibrational properties of graphene," *Computational Materials Science*, vol. 94, pp. 35–43, Nov. 2014.

[226] S. Casolo, R. Martinazzo, and G. F. Tantardini, "Band engineering in graphene with superlattices of substitutional defects," *J. Phys. Chem. C*, vol. 115, no. 8, pp. 3250–3256, 2011.

[227] A. Lherbier, X. Blase, Y.-M. Niquet, F. m. c. Triozon, and S. Roche, "Charge transport in chemically doped 2d graphene," *Phys. Rev. Lett.*, vol. 101, p. 036808, Jul 2008.

[228] J. A. Lawlor, P. D. Gorman, S. R. Power, C. G. Bezerra, and M. S. Ferreira, "Sublattice imbalance of substitutionally doped nitrogen in graphene," *Carbon*, vol. 77, no. 0, pp. 645 – 650, 2014.

[229] L. Zhao, M. Levendorf, S. Goncher, T. Schiros, L. Pálová, A. Zabet-Khosousi, K. T. Rim, C. Gutiérrez, D. Nordlund, C. Jaye, M. Hybertsen, D. Reichman, G. W. Flynn, J. Park, and A. N. Pasupathy, "Local atomic and electronic structure of boron chemical doping in monolayer graphene," *Nano Letters*, vol. 13, no. 10, pp. 4659–4665, 2013.

[230] L. Zhao, R. He, K. T. Rim, T. Schiros, K. S. Kim, H. Zhou, C. Gutiérrez, S. P. Chockalingam, C. J. Arguello, L. Pálová, D. Nordlund, M. S. Hybertsen, D. R. Reichman, T. F. Heinz, P. Kim, A. Pinczuk, G. W. Flynn, and A. N. Pasupathy, "Visualizing individual nitrogen dopants in monolayer graphene," *Science*, vol. 333, pp. 999–1003, Aug. 2011.

[231] A. Zabet-Khosousi, L. Zhao, L. PÃ¡lovÃ¡, M. S. Hybertsen, D. R. Reichman, A. N. Pasupathy, and G. W. Flynn, "Segregation of sublattice

domains in nitrogen-doped graphene," *Journal of the American Chemical Society*, vol. 136, no. 4, pp. 1391–1397, 2014.

[232] J. A. Lawlor, S. R. Power, and M. S. Ferreira, "Friedel oscillations in graphene: Sublattice asymmetry in doping," *Physical Review B*, vol. 88, p. 205416, Nov. 2013.

[233] P. Lambin, H. Amara, F. Ducastelle, and L. Henrard, "Long-range interactions between substitutional nitrogen dopants in graphene: Electronic properties calculations," *Phys. Rev. B*, vol. 86, p. 045448, Jul 2012.

[234] T. G. Pedersen and J. G. Pedersen, "Self-consistent tight-binding model of b and n doping in graphene," *Phys. Rev. B*, vol. 87, p. 155433, Apr 2013.

[235] R. He, L. Zhao, N. Petrone, K. S. Kim, M. Roth, J. Hone, P. Kim, A. Pasupathy, and A. Pinczuk, "Large physisorption strain in chemical vapor deposition of graphene on copper substrates," *Nano Letters*, vol. 12, no. 5, pp. 2408–2413, 2012.

[236] V. Yu, E. Whiteway, J. Maassen, and M. Hilke, "Raman spectroscopy of the internal strain of a graphene layer grown on copper tuned by chemical vapor deposition," *Physical Review B*, vol. 84, p. 205407, Nov. 2011.

[237] P. D. Gorman, J. M. Duffy, S. R. Power, and M. S. Ferreira, "Rkky interaction between extended magnetic defect lines in graphene," *Phys. Rev. B*, vol. 90, p. 125411, Sep 2014.

[238] L. Jiang, X. Zhao, and Y. Zheng, "Rkky interaction in graphene with a line defect," *Journal of Physics: Condensed Matter*, vol. 27, no. 4, p. 046003, 2015.

[239] H. P. Ojeda Collado, G. Usaj, and C. A. Balseiro, "Impurities and electronic localization in graphene bilayers," *Phys. Rev. B*, vol. 91, p. 045435, Jan 2015.

[240] S. R. Power, V. M. de Menezes, S. B. Fagan, and M. S. Ferreira, "Magnetization profile for impurities in graphene nanoribbons," *Physical Review B*, vol. 84, p. 195431, Nov. 2011.

[241] J. A. Lawlor and M. S. Ferreira, "Green functions of graphene: An analytic approach," *Physica B: Condensed Matter*, vol. 463, pp. 48–53, Jan. 2015.